Reactive Absorption Kinetics of CO_2 in Alcoholic Solutions of MEA: Fundamental Knowledge for Determining Effective Interfacial Mass Transfer Area

by

Louis Jacobus du Preez

Dissertation presented for the Degree

of

DOCTOR OF PHILOSOPHY
(Chemical Engineering)

in the Faculty of Engineering
at Stellenbosch University

Supervisor

Prof. J.H. Knoetze

Co-Supervisor

Dr. L.H. Callanan

April 2014

Declaration

By submitting this dissertation electronically, I declare that the entirety of the work contained therein is my own, original work, that I am the sole author thereof (save to the extent explicitly otherwise stated), that reproduction and publication thereof by Stellenbosch University will not infringe any third party rights and that I have not previously in its entirety or in part submitted it for obtaining any qualification.

L.J. du Preez — 19 February 2014

Signature — Date

Summary

The reactive absorption rate of CO_2 into non-aqueous solvents containing the primary amine, mono-ethanolamine (MEA) is recognised as a suitable method for measuring the effective interfacial mass transfer area of separation column internals such as random and structured packing. Currently, this method is used under conditions where the concentration of MEA in the liquid film is unaffected by the reaction and the liquid phase reaction is, therefore, assumed to obey pseudo first order kinetics with respect to CO_2. Under pseudo first order conditions, the effect of surface depletion and renewal rates are not accounted for. Previous research indicated that the effective area available for mass transfer is also dependent upon the rate of surface renewal achieved within the liquid film. In order to study the effect of surface depletion and renewal rates on the effective area, a method utilising a fast reaction with appreciable depletion of the liquid phase reagent is required.

The homogeneous liquid phase reaction kinetics of CO_2 with MEA n-Propanol as alcoholic solvent was investigated in this study. A novel, *in-situ* Fourier Transform Infra-Red (FTIR) method of analysis was developed to collect real time concentration data from reaction initiation to equilibrium. The reaction was studied in a semi-batch reactor set-up at ambient conditions (T = 25°C, 30°C and 35°C, P = 1 atm (abs)). The concentration ranges investigated were [MEA]:[CO_2] = 5:1 and 10:1. The concentration range investigated represents conditions of significant MEA conversion.

The reaction kinetic study confirmed the findings of previous research that the reaction of CO_2 with MEA is best described by the zwitterion reactive intermediate reaction mechanism. Power rate law and pseudo steady state hypothesis kinetic models (proposed in literature) were found to be insufficient at describing the reaction kinetics accurately. Two fundamentally derived rate expressions (based on the zwitterion reaction mechanism) provided a good quality model fit of the experimental data for the conditions investigated. The rate constants of the full fundamental model were independent of concentration and showed an Arrhenius temperature

dependence. The shortened fundamental model rate constants showed a possible concentration dependence, which raises doubt about its applicability.

The specific absorption rates (mol/m^2.s) of CO_2 into solutions of MEA/n-Propanol (0.2 M and 0.08 M, T = 25°C and 30°C, P = ±103 kPa) were investigated on a wetted wall experimental set-up. The experimental conditions were designed for a fast reaction in the liquid film to occur with a degree of depletion of MEA in the liquid film. Both interfacial depletion and renewal of MEA may be considered to occur. The gas phase resistance to mass transfer was determined to be negligible. An increase in liquid turbulence caused an increase in the specific absorption rate of CO_2 which indicated that an increase in liquid turbulence causes an increase in effective mass transfer area. Image analysis of the wetted wall gas-liquid interface confirmed the increase in wave motion on the surface with an increase in liquid turbulence. The increase in wave motion causes an increase in both interfacial and effective area.

A numerical solution strategy based on a concentration diffusion equation incorporating the fundamentally derived rate expressions of this study is proposed for calculating the effective area under conditions where surface depletion and renewal rates are significant. It is recommended that the reaction kinetics of CO_2 with MEA in solvents of varying liquid properties is determined and the numerical technique proposed in this study used to calculate effective area from absorption rates into these liquids. From the absorption data an effective area correlation as a function of liquid properties may be derived in future.

Opsomming

Die reaktiewe absorpsie van CO_2 in nie-waterige oplossings van die primêre amien, mono-etanolamien (MEA) word erken as 'n geskikte metode om die effektiewe massaoordragsarea van gepakte skeidingskolomme te bepaal. Tans word die metode gebruik onder vinnige pseudo eerste orde reaksietoestande met betrekking tot CO_2. Die pseudo eersteorde aanname beteken dat die konsentrasie van MEA in die vloeistoffilm onbeduidend beïnvloed word deur die reaksie en effektief konstant bly. Onder pseudo eerste orde toestande word oppervlakverarming- en oppervlakvernuwingseffekte nie in ag geneem nie, juis as gevolg van die konstante konsentrasie van MEA in die vloeistoffilm. Daar is voorheen bevind dat oppervlakverarming en oppervlakvernuwing 'n beduidende invloed het op die beskikbare effektiewe massaoordragsarea. Hierdie invloed kan slegs bestudeer word met 'n vinnige reaksie in die vloeistoffilm wat gepaard gaan met beduidende oppervlakverarming van die vloeistoffase reagens.

Die homogene vloeistoffase reaksiekinetika van CO_2 met MEA in die alkohol oplosmiddel, n-Propanol, is in hierdie studie ondersoek. 'n Nuwe, *in-situ* Fourier Transform Infra-Rooi (FTIR) metode van analiese is ontwikkel in hierdie ondersoek. Die reaksie is ondersoek in 'n semi-enkelladings reaktor met MEA wat gevoer is tot die reaktor om met die opgeloste CO_2 te reageer. Die FTIR metode meet spesiekonsentrasie as 'n funksie van tyd sodat die konsentrasieprofiele van CO_2, MEA en een van die soutprodukte van die reaksie gebruik kan word om verskillende reaksiesnelheidsvergelykings te modelleer. Die reaksie is ondersoek onder matige toestande (T = 25°C, 30°C and 35°C, P = 1 atm (abs)). Die konsentrasiebereik van die ondersoek was [MEA]:[CO_2] = 5:1 en 10:1. Hierdie bereik is spesifiek gebruik sodat daar beduidende omsetting van MEA kon plaasvind. Die reaksiekinetieka studie het, ter ondersteuning van bestaande teorie, bevind dat die reaksie van CO_2 met MEA in nie-waterige oplosmiddels soos alkohole, beskyf word deur 'n zwitterioon reaksiemeganisme. Die bestaande reaksiesnelheids modelle (eksponensiële wet en pseudo gestadigde toestand hipotese) kon nie die eksperimentele data met genoegsame akuraatheid beskryf nie. Twee nuwe

reaksiesnelheidsvergelykings, afgelei vanaf eerste beginsels en gebaseer op die zwitterioon meganisme, word voorgestel. Hierdie volle fundamentele model het goeie passings op die eksperimentele data getoon oor die volledige temperatuur en konsentrasiebereik van hierdie studie. Die reaksiekonstantes van die fundamentele model was onafhanklik van konsentrasie en tipe oplosmiddel en het 'n Arrhenius temperatuurafhanklikheid. Die verkorte fundamentele model se reaksiekonstantes het 'n moontlike konsentrasieafhanlikheid gewys. Dit plaas onsekerheid op die fundamentele basis van hierdie model en kan dus slegs as 'n eerste benadering beskou word.

Die spesifieke absorpsietempos (mol/m^2.s) van CO_2 in MEA/n-Propanol oplossings (0.2 M en 0.08 M MEA, T = 25°C and 30°C, P = ±103 kPa) is ondersoek met 'n benatte wand ('wetted wall') eksperimentele opstelling. Die eksperimentele toestande is gekies sodat daar 'n vinnige reaksie in die vloeistoffilm plaasgevind het, met beide beduidende en nie-beduidende MEA omsetting. Die doel met hierdie eksperimentele ontwerp was om die invloed van intervlakverarming en intervlakvernuwing op die spesifieke absorpsietempo te ondersoek. Gas fase weerstand was nie-beduidend onder die eksperimentele toestande nie. Beide intervlakverarming en intervlakvernuwing gebeur gelyktydig en is waargeneem vanuit die eksperimentele data. 'n Beeldverwerkingstudie van die gas-vloeistof intervlak van die benatte wand het bevind dat daar 'n toename in golfaksie op die vloeistof oppervlak is vir 'n toename in vloeistof turbulensie. Hierdie golfaksie dra by tot oppervlakvernuwing en 'n toename in effektiewe massaoordragsarea.

'n Numeriese metode word voorgestel om die effektiewe area van beide die benatte wand en gepakte kolomme te bepaal vanaf reaktiewe absorpsietempos. Die metode gebruik die fundamentele reaksiesnelheidsvergelykings, bepaal in hierdie studie, in a konsentrasie diffusievergelyking sodat oppervlakverarming en vernuwing in ag geneem kan word. Daar word voorgestel dat die reaksiekinetika van CO_2 met MEA in oplossings met verskillende fisiese eienskappe (digtheid, oppervlakspanning en viskositeit) bepaal word sodat die numeriese metode gebruik kan word om 'n effektiewe area korrelasie as 'n funksie van hierdie eienskappe te bepaal.

Acknowledgements

This project would not have been possible without the assistance given by colleagues, friends and family. I would like to acknowledge the contributions of the following people especially:

- **Prof. Hansie Knoetze** and **Dr. Linda Callanan**, my supervisors. Thank you for the seemingly bottomless reservoir of advice, motivation and guidance that you offered me through the course of this project. Thinking back on the time spent in the developing stages through to the experimental and modelling phase of the project, I can hardly believe that we managed to achieve most of the goals we aimed for. It has been an honour to work with you on this project.
- **Dr. J.P. Barnard** and **Ms. C. Yzelle** for your assistance in developing the Matlab® algorithms used in this study. The work that you did truly helped in revealing the core contribution of this body of work. J.P., my friend, you have amazing skill in coding an algorithm in such a way that it is computationally efficient and elegant in its structure. Your work, in this regard, has been essential to the contributing value of this project. Corne, thank you for your contribution to this project through the coding of the image analysis algorithm. It may have played a small role in this project, but it will feature more and more as the results obtained in this study are further explored in future work.
- **Jannie Barnard**, **Anton Cordier**, **Vincent Carolissen**, **Oliver Jooste** and **Alvin Petersen.** The personnel in the work shop of the department of Process Engineering at University Stellenbosch have contributed significantly to the success of this project. Without your help, the construction of both experimental set-ups used in this study would not have been possible. There were a seemingly countless number of obstacles to overcome in the manufacturing and construction of two highly complicated and specialized experimental set-ups. Precision work was required during the construction phase and the results achieved were nothing short of amazing. Thank you for all your help and the good laughs we shared whilst toiling away in the work shop. I shall cherish those moments forever.

- **Ms. Hanlie Botha**, senior analyst in our analytical laboratories. Thank you for your help with both the titration and GC methods used in this study.
- **Liaan Kritzinger** and **Nico-Ben Janse van Rensburg**. Thank you for your help in the reaction kinetic study and wetted wall study respectively. It is always better to work with someone in the lab, especially in the early morning hours. You guys were assigned to work under my guidance for your final year projects and I must say that I am impressed with your dedication to the work at hand. Thank you for sometimes being my soundboard to bounce ideas off of. I appreciate your help, very much and I wish you good fortune in life.
- **Dr. Cathy Dowding** of Department Soil Sciences. Thank you for allowing me to initially test the feasibility of my reaction system on the FTIR at Department Geology. I enjoyed working there and made many friends. Your help with regards to getting me started on the FTIR was invaluable to the results obtained in this project. I also wish you the best of luck for your future research.
- **Jacques du Preez**, my brother and one of my house mates for most of this project. I love you and I will never be able to thank you enough for being such a great brother and friend to me all my life. You are an inspiration in my life and for that I thank you, because that is what helped me get through tough times or enjoy the good times to the fullest. See you in the line-up at Llandudno.
- **Ursula Theron (du Preez)**, my sister. Thank you so much for being a fantastic big sister and always encouraging me when I feel down. You have a beautifully pure heart, but a head that knows the real world and that is a rare combination to have. You inspire me to focus on the brighter side of things, always, whether you intended to or not. I love you very much.
- **Louis and Annelien du Preez**, my loving parents. I love you. You have supported me and are continuing that support through my entire life. Without you, I would not have existed, so everything that I achieve in my life, I dedicate to you, everything. Thank you for all that you are and that you raised a brother and sister to support and love me too. You did a great job, thus far, and I believe you can be proud of the children that you

raised under the guidance and protection of the mercy provided by God and His Son, Jesus. Thank you, God, for my parents. You truly blessed me with and amazing family and I am grateful that You preserved our family as a unit through the years.

Table of Contents

Declaration i

Summary ii

Opsomming iv

Acknowledgements vi

Table of Contents ix

List of Figures in Body Text xv

List of Tables in Body Text xx

Glossary xxii

Chapter 1 Introduction and Project Outline 1

1.1 Separation Column Internals: A Brief Introduction 1

1.1.1 Trays 2

1.1.2 Random Packing 3

1.1.3 Structured Packing 4

1.2 Effective Interfacial Area Background 6

1.3 CO_2-Amine Systems: A Brief Introduction 7

1.4 Project Scope and Objectives 8

1.5 Thesis Layout 12

Chapter 2 Physical and Reactive Absorption Theory 14

2.1 Physical Gas-Liquid Mass Transfer Theory 15

2.1.1 Film Theory 15

2.1.2 Penetration Theory 17

2.1.3 Surface Renewal Theory 19

2.1.4 Eddy Diffusivity Theory 20
2.2 Mass Transfer with Chemical Reaction 21
2.2.1 Irreversible Reactions 24
2.2.2 Reversible Reactions 32
Chapter 3 Reaction Kinetics: Theory and Method Development 38
3.1 The Reaction of CO_2 with Amines 38
3.1.1 Proposed Reaction Mechanism for Primary Amines in Non-aqueous Solvents 39
3.1.2 Existing Rate Expressions for the CO_2/Amine Reaction in Non-Aqueous Solvents 42
3.2 Amine and Solvent Selection Criteria 45
3.3 Introduction to an In-situ FTIR Method of Analysis 47
3.3.1 Brief Description of FTIR Spectroscopy (Sherman Hsu, 1997) 48
3.3.2 IR Energy Absorption vs. Species Concentration 50
3.3.3 Feasibility of FTIR for CO_2/MEA systems 50
3.4 Experimental Method Development 52
3.4.1 ATR combined with FTIR 52
3.4.2 Semi-Batch Reactor Set-up 56
3.5 Calibration Procedures and Method Validation 59
3.5.1 OMNIC® Software Settings 60
3.5.2 MEA Calibration 60
3.5.3 RNH_3^+ Equilibrium Analysis and Calibration via Conductometric Titration 63
3.5.4 MEA Interference with RNH_3^+ Spectra and Subsequent Calibration 67
3.5.5 CO_2 Calibration 71
3.5.6 Validation of FTIR method 78
3.6 Experimental Design 81

3.7 Experimental Procedure 83
3.8 Collecting and Processing Continuous Time Data 86
3.8.1 Carbon Balance to Calculate the Zwitterion Concentration 88
3.8.2 FTIR Measurement Repeatability Study 89
3.8.3 Molar Amount vs. Time Profiles 92
3.8.4 Effect of MEA Molar Flow Rate 95
3.8.5 Analysis of Equilibrium Data 97
3.9 Chapter Conclusions 102
Chapter 4 Reaction Kinetics Results and Modelling 103
4.1 Modelling of Semi-batch Reaction Kinetic Data 103
4.1.1 Semi-batch Reactor Design Equations 104
4.1.2 Modelling Procedure 105
4.2 Existing Rate Expressions 109
4.2.1 Power Rate Law Model 110
4.2.2 Pseudo Steady State Hypothesis Model 114
4.2.3 Pseudo First Order Model 118
4.3 Proposed Rate Expressions 119
4.3.1 Fundamental Model 120
4.3.2 Shortened Fundamental (Equilibrium) Model 130
4.4 Comparison of Model Fits 137
4.5 Chapter Conclusions 138
Chapter 5 Existing Mass Transfer Area Theory and Correlations 140
5.1 Hydraulic and Geometry Based Correlations 142
5.1.1 Correlations of Shi and Mersmann 143

5.1.2 Studies by Shetty and Cerro 145
5.1.3 SRP Model 148
5.1.4 Billet and Schultes Model 150
5.1.5 Delft Model 152
5.1.6 Correlations Proposed by Del Carlo et al. 156
5.1.7 CFD and X-Ray CT Approach 158
5.2 The Chemical Method 160
5.2.1 Pseudo First Order Conditions 161
5.2.2 Specific Absorption Rate Approach 163
5.2.3 Series Resistance Approach 164
5.2.4 Most Popular Absorption Systems Used for Calculating Interfacial Area 166
5.2.5 Equipment used in Specific Absorption Rate Studies 167
5.2.6 Correlations Resulting from the Chemical Method 170
5.3 Comparison of Existing Effective Area Correlations 173
5.4 Chapter Conclusions 183
Chapter 6 Reactive Absorption Study 185
6.1 The Wetted Wall Experimental Set-up 185
6.1.1 The Wetted Wall Column 186
6.1.2 Piping and Instrumentation of the Wetted Wall Experimental Set-up 190
6.1.3 Measuring Liquid Film Thickness and Capturing the Interfacial Profile on Video 193
6.1.4 Solvent Regeneration 194
6.1.5 Experimental Procedure 195
6.2 Reactive Absorption Study Experimental Design and Methods of Analysis 196
6.2.1 Gas Phase Method of Analysis 196

6.2.2 GC Method of Analysis 197
6.2.3 Specific Absorption Rates Experimental Design 199
6.2.4 Gas Phase Mass Transfer Resistance Considerations 203
6.2.5 Gas-Liquid Contact Time 206
6.3 Reactive Absorption Rate Results and Discussion 207
6.3.1 Equipment Validation Results 207
6.3.2 Total Absorption Rate Results 209
6.3.3 Specific Absorption Rate Results 213
6.4 Image Analysis of the Gas-Liquid Interface 227
6.4.1 Waves on Falling Liquid Films 227
6.4.2 Image Analysis Procedure 231
6.4.3 Image Analysis Results 235
6.5 Chapter Conclusions 239
Chapter 7 Conclusions and Recommended Future Work 241
7.1 Conclusions from the Reaction Kinetic Study 241
7.2 Conclusions from the Reactive Absorption Study 243
7.3 Novel Contributions 244
7.4 Recommended Future Work 246
References 248
Appendix A Property Data and Sample Calculations 265
A.1 Species Properties 265
A.2 Calculating Wetted Wall Absorption Rate Measurement Error Range 266
A.3 Evaluating the Gas side Mass Transfer Coefficient and Gas Phase Mass Transfer Resistance of the Wetted Wall 267

Appendix B Basis for a New Effective Area Theory and Numerical Method of Calculation 273

B.1 Formulation of the Proposed Approach to Determine Effective Interfacial Mass Transfer Area 273

B.1.1 The Fundamental Reactive Diffusion Equations 274

B.1.2 Physiochemical Properties and Initial and Boundary Conditions 278

B.2 Solving the Reactive Diffusion Equation Numerically in Matlab® 279

B.3 Estimating the Required Physiochemical Properties for the Use in the New Effective Area Theory 284

B.4 Examples of Initial and Boundary Conditions Values for Determining the Effective Mass Transfer Area of the Wetted Wall Column 288

B.5 Conclusions and Future Work Identified 289

Appendix C Mechanical Drawings and Schematics of the Equipment Used 290

Appendix D Equipment Specifications 294

D.1 Nicolet 6700 Spectrometer Specifications 294

D.2 Axiom DPR-207 IR Probe Inspection and Test Report 297

D.3 1188HD Camera CCU and 1188 Camera Head with Coupler 298

D.4 Hauppauge Colossus Recording Card 300

D.5 CO_2 Concentration Analyser Calibration Certificate 303

Appendix E Data of the Reaction Kinetic Study 304

E.1 Derivation of the Pseudo Steady State Hypothesis Reaction Rate Expression 304

E.2 Reaction Kinetic Experimental Parameters 305

E.3 Fundamental Model Estimated Rate Constants 306

Appendix F Data of The Reactive Absorption Study 310

F.1 Wetted Wall Experimental Data 310

List of Figures in Body Text

Figure 1.1 The Three Fields of Research in Separation Technology 9

Figure 2.1 Schematic of Film Theory Diffusive Mass Transfer 16

Figure 2.2 Schematic of Diffusive Mass Transfer Assuming Penetration Theory to Apply 19

Figure 2.3 Schematic of Diffusive Mass Transfer Showing Eddy Diffusivity Renewing the Interface with Bulk Liquid 21

Figure 2.4 Schematic of Diffusive Mass Transfer with Chemical Reaction 22

Figure 3.1 Formation of the Zwitterion Reactive Intermediate in the Reaction of a Primary Amine (Mono-ethanolamine) with CO_2 39

Figure 3.2 A Primary Amine (MEA) Acting as a Brønsted-Lawry base 40

Figure 3.3 Simplified Schematic of a Typical FTIR Spectrometer 49

Figure 3.4 Schematic Illustrating ATR Technology 53

Figure 3.5 Schematic Diagram of the ATR Probe (used with permission from (Axiom, 2010)) .. 55

Figure 3.6 The Semi-Batch Reactor. All Dimensions in mm 56

Figure 3.7 The Semi-batch Reactor Experimental Set-up 59

Figure 3.8 Spectra of 0.334 mol/dm^3 of MEA Dissolved in n-Propanol at 30°C and 1 atm Showing the RNH_2 Wagging Peak at 944.949 cm^{-1} 61

Figure 3.9: MEA Calibration Data in n-Propanol at 25^{o}C 62

Figure 3.10 A Section of an Equilibrium Spectrum Showing the RNH_3^+ Peak at 1492.657 cm^{-1} Noticed During the Reaction of CO_2 and MEA in n-Propanol 64

Figure 3.11 Typical Titration Curve for Determining RNH_3^+ concentration 66

Figure 3.12 Calibration Curve for MEA IR Activity in the Region of RNH_3^+ absorption. Calibration Curve for n-Propanol at 35°C 67

Figure 3.13 RNH_3^+ Calibration Curve for n-Propanol at 35°C and 1 atm. [MEA]:[CO_2] = 10:1 ... 69

Figure 3.14 Sample Cylinder for Mass Based Loading of CO_2 72

Figure 3.15 256 Scan Background Spectrum of n-Propanol at a Resolution of 32 cm^{-1} and 30°C 73

Figure 3.16 CO_2 Peak at 2337.339 cm^{-1} for 0.489g CO_2 dissolved in n-Propanol at 25°C and 1 atm 74

Figure 3.17 Spectra of the CO_2 Peak Height Decreasing with Each nPropanol Injection in a Calibration Dilution Series 75

Figure 3.18 CO_2 Calibration Curve in n-Propanol at 30 ^oC 76

Figure 3.19 MEA Peak Height Behaviour Validation at 25°C 79

Figure 3.20 MEA Peak Height Behaviour Validation at 30°C 79

Figure 3.21 Typical Peak Area Profiles of CO_2, MEA and RNH_3^+/MEA Obtained During Data Collection. Reaction Conditions: 35°C, [MEA]:[CO_2] = 10:1 and an MEA molar flow rate of 0.011 mol/s. The x-axis denotes Time in seconds and the y-axis Peak Height (displayed as Intensity). 87

Figure 3.22 Repeatability of CO_2 Concentration Profiles at 35°C and [MEA]:[CO_2] = 10:1 92

Figure 3.23 Molar amount vs. Time Profiles for the First 40 seconds of Data Collection at 35°C, 1 atm, [MEA]:[CO_2] = 10:1 and F_{MEA} = 0.0112 mol/s 93

Figure 3.24 Data Scatter Reduction in the Molar Amount profiles. Data Collection at 35°C, 1 atm, [MEA]:[CO_2] = 10:1 and F_{MEA} = 0.0112 mol/s 95

Figure 3.25 Effect of MEA Molar Flow Rate on the CO_2 Concentration vs. Time Profiles. Data Collection at 35°C, 1 atm 96

Figure 3.26 Average K_C Values as a Function of Temperature 100

Figure 3.27 Change in K_C with Time for an experimental run at 25°C and [MEA]:[CO_2] = 5:1 .. 101

Figure 4.1 Flow Diagram of Modelling Procedure 108

Figure 4.2 Power Rate Law Model Fit for the Reaction of CO_2 with MEA in n-Propanol at 30°C, [MEA]:[CO_2] = 10:1 (run#: 30_10_1) 111

Figure 4.3 PSSH Rate Law Model Fit for the Reaction of CO_2 with MEA in n-Propanol at 35°C, [MEA]:[CO_2] = 5:1 (run# 35_5_2) 115

Figure 4.4 PSSH Rate Law Model Fit for the Reaction of CO_2 with MEA in n-Propanol at 25°C, [MEA]:[CO_2] = 10:1 (run# 25_10_2) 116

Figure 4.5 Fundamental Rate Model Fit for the Reaction of CO_2 with MEA in n-Propanol at 30°C, [MEA]:[CO_2] = 10:1 (run# 30_10_3) 122

Figure 4.6 Fundamental Rate Model Fit for the Reaction of CO_2 with MEA in n-Propanol at 35°C, [MEA]:[CO_2] = 5:1 (run# 35_5_2) 124

Figure 4.7 Arrhenius Plot of Fundamental Rate Expression for n-Propanol 128

Figure 4.8 Calculated and Estimated Fundamental Rate Expression Constants of n-Propanol 129

Figure 4.9 Shortened Fundamental Rate Model Fit for the Reaction of CO_2 with MEA in n-Propanol at 25°C, [MEA]:[CO_2] = 10:1 (run# 25_10_3) 132

Figure 4.10 Shortened Fundamental Rate Model Fit for the Reaction of CO_2 with MEA in n-Propanol at 30°C, [MEA]:[CO_2] = 5:1 (run# 30_5_1) 133

Figure 4.11 Arrhenius Plot of Short Fundamental Rate Expression for n-Propanol..... 136

Figure 4.12 Comparison of the Quality of the Model Fits Obtained (run#30_10_3) 137

Figure 5.1 Schematic of a Liquid Rivulet Flowing from a Point Source Down an Inclined Flat Plate 144

Figure 5.2 Schematic of Periodic Surfaces Studied by Cerro et al. (1997) 146

Figure 5.3: Geometry of a Triangular Gas-Liquid Flow Channel (Redrawn with permission from (Olujic, et al., 1999))..... 152

Figure 5.4 Comparison of Effective Area Correlations for Mellapak™ 125Y Structured Packing 176

Figure 5.5 Comparison of Effective Area Correlations for Mellapak™ 250Y Structured Packing 177

Figure 5.6 Comparison of Effective Area Correlations for Mellapak™ 500Y Structured Packing 178

Figure 5.7 Comparison of Effective Area Correlations for Water and Alcohol (n-Propanol) Type Liquid Properties for Mellapak™ 125Y Structured Packing 181

Figure 5.8 Comparison of Effective Area Correlations for Water and Alcohol (n-Propanol) Type Liquid Properties for Mellapak™ 250Y Structured Packing 182

Figure 5.9 Comparison of Effective Area Correlations for Water and Alcohol (n-Propanol) Type Liquid Properties for Mellapak™ 500Y Structured Packing 183

Figure 6.1 Fully Assembled Wetted Wall Column Set-up..... 187

Figure 6.2 Sectioned Drawing of the Fully Assembled Wetted Wall Reactor 188

Figure 6.3 Wetted Wall Exit Collar 189

Figure 6.4 P&ID of the Wetted Wall Experimental Set-up 191

Figure 6.5 GC arrangement for analyzing liquid phase MEA and CO_2 197

Figure 6.6 GC Chromatogram Indicating the Presence of CO_2 in the Sample 198

Figure 6.7 Gas Phase Residence Time Distribution Curve of the Wetted Wall Dome Set-up ... 208

Figure 6.8 Validation Results of Wetted Wall Experimental Set-up 209

Figure 6.9 Total Reactive Absorption Rates into 0.2 M MEA in n-Propanol as a Function of CO_2 Partial Pressure 210

Figure 6.10 Total Reactive Absorption Rates into 0.08 M MEA in n-Propanol as a Function of CO_2 partial pressure 212

Figure 6.11 Specific Reactive Absorption Rates into 0.2 M MEA in n-Propanol as a Function of CO_2 partial pressure 215

Figure 6.12 Specific Reactive Absorption Rates into 0.08 M MEA in n-Propanol as a Function of CO_2 partial pressure 216

Figure 6.13 Specific Reactive Absorption Rates into 0.2 M MEA in n-Propanol as a Function of Liquid Reynolds Number 220

Figure 6.14 Specific Reactive Absorption Rates into 0.08 M MEA in n-Propanol as a Function of Liquid Reynolds Number 221

Figure 6.15 Erasmus Correlation (Equation 6.15) fitted on Specific Reactive Absorption Rates into 0.08 M MEA in n-Propanol 222

Figure 6.16 Parity Plot of Equation 6.18 225

Figure 6.17 Parity Plot of Equation 6.19 Fitted on the Experimental Data of Erasmus (2004). 226

Figure 6.18 Schematic Diagram of Waves in a Falling Film (Redrawn from (Yu, et al., 2006)) . 229

Figure 6.19 User Selection Screen where the Region for Image Analysis of the Gas-Liquid Interface may be selected 233

Figure 6.20 Image Pixel Inspection to Find the Contrast of the Gas-liquid Boundary 234

Figure 6.21 Preview of a Selected Gas-liquid Boundary at a Threshold Value of 160 235

Figure 6.22 Typical Re-recording of the Processed Image Analysis at a Flow Rate of 1.345 cm^3/s Indicating the Three types of Waves Found in Falling Liquid Films 237

Figure 6.23 Image Analysis of the Gas-liquid Interfacial Profile of n-Propanol Flowing Down a Cylindrical Wetted Wall at 0.874 cm^3/s 237

Figure 6.24 Image Analysis of the Gas-liquid Interfacial Profile of n-Propanol Flowing Down a Cylindrical Wetted Wall at 1.016 cm^3/s 238

Figure 6.25 Image Analysis of the Gas-liquid Interfacial Profile of n-Propanol Flowing Down a Cylindrical Wetted Wall at 1.345 cm^3/s 238

List of Tables in Body Text

Table 1.1 Examples of Random Packing Elements for Each Generation (Lamprecht, 2010) 4

Table 1.2 Examples of Structured Packing Elements for Each Generation (Lamprecht, 2010) 6

Table 3.1 IR Absorption Wave Numbers for Reagents and Products in Equation 3.3 (Silverstein & Bassler, 1967; Bellamy, 1976; Aruldhas, 2007; Jackson, et al., 2009; Derks, et al., 2011; Richner & Puxty, 2012) 51

Table 3.2 MEA Calibration Factors 63

Table 3.3 True Salt Peak Height Calibration Factor Consistency Test at 25°C 70

Table 3.4 True Salt Peak Height Calibration Factors 71

Table 3.5 Normalised CO_2 Calibration Equations 77

Table 3.6 Experimental Design Parameters..... 83

Table 3.7 Experimental Parameters for Repeatability Study at 35°C and [MEA]:[CO_2] = 10:1... 91

Table 3.8 Summary of Reaction Kinetic Data 97

Table 3.9 Calculated Equilibrium Constants..... 99

Table 4.1 Power Rate Law Rate Constant for n-Propanol 112

Table 4.2 Pseudo Steady State Hypothesis Rate Law Rate Constants for n-Propanol..... 117

Table 4.3 Initial Guesses for the Fundamental Model Fit 122

Table 4.4 Fundamental Model Rate Law Rate Constants for n-Propanol..... 125

Table 4.5 Temperature Investigation Data for n-Propanol showing Activation Energies and Arrhenius Constants for the Estimated Rate Constants of the Fundamental Model..... 128

Table 4.6 Initial Guesses for the Shortened Fundamental Model Fit..... 132

Table 4.7 Shortened Fundamental Model Rate Law Rate Constants for n-Propanol 134

Table 4.8 Temperature Dependence of the Short Fundamental Rate Expression Rate Constants for n-Propanol..... 135

Table 5.1 Summary of Absorption Equipment Used to Conduct Kinetic Studies (Charpentier, 1981) 168

Table 5.2 Summary of Some of the Effective Area Correlations Presented in Chapter 5..... 174

Table 5.3 Packing Type and Properties Used for Effective Area Correlations Comparison 175

Table 6.1 Validation Study Experimental Design (Erasmus, 2004)..... 199

Table 6.2 Results Validating the Fast Reaction Regime for the Reactive Absorption Experimental Conditions..... 201

Table 6.3 Experimental Design..... 202

Table 6.4 Liquid Film Thickness Measurements..... 214

Glossary

Symbol	Description	SI Units
A	Cross Sectional Area	m^2
A_i	Arrhenius Constant	same units as k_i
C_i	Concentration of *i*	mol/dm^3
$D_{i,L}$	Liquid Phase Diffusivity of *i*	m^2/s
$D_{i,G}$	Gas Phase Diffusivity of *i*	m^2/s
E	Enhancement Factor	-
E_a	Activation Energy	J/mol
F_i	Molar Flow Rate	mol/s
F_{SE}	Surface Texture Factor	-
H_i	Henrys Law Constant of *i*	$m^3/(Pa.kmol)$
K_G	Overall Mass Transfer Coefficient	$kmol/(m^2.Pa.s)$
K	Equilibrium Constant	-
L (eq. 5.2)	Liquid Phase Molar Flow Rate	mol/s
L_P	Wetted Perimeter in Cross Sectional Slice of Packing	m
N_i (eq 4.1 – 4.4)	Number of Moles	mol

N_i	Specific Absorption Rate	mol/(m^2.s)
P	Pressure	Pa
P_i	Partial Pressure	Pa
R	Universal Gas Constant	J/(mol.K)
S	Packing Side Dimension	m
T	Temperature	K
V	Volume	cm^3 or dm^3 or m^3
V (eq. 5.2)	Vapour Phase Molar Flow Rate	mol/s
$\dot{V}$	Volumetric Flow Rate	m^3/s
$\bar{V}$	Molal Volume	cm^3/mol
X_i	Conversion of *i*	-
a_e	Effective Interfacial Mass Transfer Area	m^2 or m^2/m^3
a_i	Gas-Liquid Interfacial Area	m^2
a_p	Packing Specific Area	m^2/m^3
d_h	Hydraulic Diameter	m
e_d	Eddy Movement/Diffusivity Factor	s^{-1}
g	Gravitational Acceleration	m/s^2
h_L	Fractional Liquid Hold-up	-

k_L	Liquid Phase Mass Transfer Coefficient	m/s
k_L'	Modified Liquid Phase Mass Transfer Coefficient	kmol/(m^2.Pa.s)
k_G	Gas Phase Mass Transfer Coefficient	m/s or kmol/(m^2.Pa.s)
k_i	Reaction Rate Constant	units dependent upon expression
m	reaction order	-
n	reaction order	-
n_i	Molar Absorption Rate of *i*	mol/s
r_j	Reaction Rate	mol/(dm^3.s)
s	surface renewal rate factor	s^{-1}
t	time variable	s
t_c	Contact Time	s
u_L	Superficial Liquid Velocity	m/s
u_G	Superficial Vapour Velocity	m/s
u_{eff}	Effective Velocity	m/s
x	Space Variable	m
x (eq. 6.8)	Mass Fraction	-
y	Space Variable	m
z	Space Variable	m

ρ_L	Liquid Density	kg/m^3
ρ_G	Vapour Density	kg/m^3
θ	Packing Corrugation Angle	°
δ	Film Thickness	m
σ	Surface Tension	N/m
ν	Kinematic Viscosity	m^2/s
μ_L	Liquid Dynamic Viscosity	Pa.s
μ_G	Vapour Dynamic Viscosity	Pa.s
γ	Contact Angle	°
ε	Void Fraction	m^3/m^3
ϖ (eq 5.44)	Slope of the Steepest Descendent Line Relative to the Horizontal Axis	°
ξ_{G-L}	Gas-Liquid Friction Factor	-
φ (eq. 5.28)	Fraction of Triangular Flow Channel Occupied with Liquid	-
λ	Wavelength	m

Chapter 1 INTRODUCTION AND PROJECT OUTLINE

Tray and packed columns are extensively used in industry to create a gas-liquid interface area required for separation of various components in either the gas or liquid phase. These columns are thus used for distillation, absorption, desorption and extraction, etc. (Wang, et al., 2005). Despite the thermodynamic inefficiency of this method of separation (Shetty & Cerro, 1997), it is still primarily used in industry. The need will therefore forever exist to improve on the efficiency of this vital separation technology. This may, for example, be achieved by improving on column internal design in order to maximize the effective interfacial mass transfer area created by the type of tray or packing. Before this improvement can be implemented, an accurate method of measurement and calculation of the effective interfacial mass transfer area achieved by the different column internals must firstly be developed.

1.1 Separation Column Internals: A Brief Introduction

The gas-liquid contact area required for the above mentioned separation processes is achieved with the use of various column internals. The mechanism of the process is very simple and may briefly be described as follows: Liquid enters at the top of the column and flows down under the influence of gravity. The liquid is distributed over column internals to increase the gas-liquid contact area and contact time by inducing a volume of liquid hold-up in the column. The gas flows either co-currently or more often counter-currently with respect to the liquid inside the column and makes contact with the liquid volume in hold-up on the surface of the column internals. It is during gas-liquid contact that mass transfer is achieved and the efficiency of the transfer achieved, depends on various factors, one of which is the effective interfacial mass transfer area between the contacting gas and liquid. The way in which the efficiency of mass transfer is calculated is discussed in section 1.2.

There are three main types of internals currently employed in industrial applications, namely Trays, Random Packing and Structured Packing. A brief discussion on these types of column internals will be presented here.

1.1.1 Trays

In tray columns, the liquid phase flows over a series of horizontally orientated perforated plates, whilst the gas phase travels through the perforations and disperses through the liquid phase in the form of bubbles. The type of perforation on the tray surface, determines the type of try. There are mainly three types of trays used in separation columns, namely sieve trays, bubble cap trays and valve trays. Sieve trays are, as the name suggests, made from flat plates with circular perforations. The main advantage in such a simple tray design, is the lower manufacturing cost compared with valve or bubble cap trays (Seader & Henley, 1998). Bubble cap and valve trays do, however, have the advantage of a higher turn-down ratio than sieve trays (Kister, 1992). The turn-down ratio indirectly indicates the vapour flow rate range that may be used to ensure the most efficient tray column operation. The efficiency of the separation achieved by the tray is dependent upon the degree of liquid entrainment and liquid weeping. The turn down ratio is defined in terms of these effects.

Entrainment occurs when the gas flow rate is high enough to overcome the influence of gravity on a liquid droplet and carries it up to the tray above. Entrainment of liquid to the upper trays decreases the overall mass transfer efficiency. At high enough liquid entrainment conditions, the column may be flooded with liquid, making it nearly impossible of the gas phase to disperse in the liquid phase and the pressure drop over the tray section increases sharply. At higher liquid flow rates or lower gas flow rates, the influence of gravity on the liquid droplets exceeds the upward drag force of the gas and the liquid droplets short circuits by dripping (or weeping) down to the tray below. This short circuiting of the liquid phase also decreases mass transfer efficiency. The turn down ratio of a tray type, may be defined as the ratio of the gas flow rate, just before entrainment occurs, to the minimum gas flow rate required to prevent weeping.

Valve trays have a higher turn-down ratio than sieve trays (Lockett, 1986). This is achieved by placing a flat plat cap, confined within vertical risers, over the perforation in the plate. The gas flow lifts the cap (valve) to allow for the vapour to come into contact with the liquid phase. The gas flow rate determines the degree of the valve opening, thus, preventing excessive liquid weeping at low gas flow rates. Bubble cap trays have inverted cups, positioned over the tray perforations, with risers inside the cup to prevent the liquid on the tray from weeping through the perforations. This gives the bubble cap trays an even higher turn-down ratio than valve trays, but both are significantly more expensive than sieve trays (Lockett, 1986).

1.1.2 Random Packing

A random packing element is a separation column internal of a specific geometrical design, which is simply dumped in the column shell, along with several identical elements. The packing elements are thus randomly distributed in the column with respect to orientation. The flow paths of both the liquid and vapour phases are disrupted constantly and forced to change direction rapidly, which increases both hold-up and turbulence of both phases, which is beneficial for mass transfer purposes (Yu, et al., 2006).

Random packing was developed in four distinct generations (Lamprecht, 2010). The first and second generation random packing were mainly of ring or saddle shaped geometry. The ring shape would increase mass transfer, whilst the saddle shape would facilitate easier gas flow conditions, which would decrease the pressure drop over the packed bed. The third generation random packing merged the saddle and ring design to form hybrid shapes (Schultes, et al., 2010). The hybrid shape would contain tongues for increased droplet formation, which increases interfacial area, but also pressure drop and liquid entrainment at higher gas flow rates.

The fourth generation random packing abandoned the ring/saddle hybrid shape and replaced it with new wave shaped geometry (Lamprecht, 2010). The material elements shaped like sinus waves would be connected together at the two ends of the packing element, whilst bulging in the middle of the element to form an oval or egg like shape that has a large void fraction to

keep the pressure drop minimal. The wave shaped connectors increases the turbulence in flow, yet reduces droplet formation, which is beneficial for both mass transfer and pressure drop considerations.

Random packing was developed before structured packing, but is still preferred over structured packing for column operation under high pressure (> 14 bar) and high liquid flow rates (> 45 $m^3/(m^2 \cdot hr)$) (Kister, 1992). The four generations of Random Packing is tabulated in **Table 1.1**.

Table 1.1 Examples of Random Packing Elements for Each Generation (Lamprecht, 2010)

First generation (1895-1950s)	Second generation (1950s-1970s)	Third generation (1970s-late 1990s)	Fourth Generation (late 1990s-present)
Raschig Ring	Intalox® Saddle	IMTP®	Raschig Super Ring
Lessing Ring	Super Intalox® packing	CMR®	Intalox® Ultra™
Berl Saddle	Pall® Ring	Levapak	
	Hy-Pak packing	Nutter Rings™	
		FLEXIMAC™	
		Hiflow® Ring	
		Intalox® Snowflake	

1.1.3 Structured Packing

Structured packing material consists of corrugated sheets, pressed in manufacturing to obtain a modular shape and then stacked together in an ordered arrangement. The ordered arrangement permits the formation of channels for two phase flow, inducing phase contact for mass transfer. The sections of packing material within the bed may be arranged at 90° with respect to one another, causing the flow direction of both gas and liquid to change rapidly. This is done to improve mixing of the phase through increased turbulence (Olujic, et al., 1999). The ordered arrangement of the flow channels within the packed bed, results in a decrease in pressure drop compared to random packing and trays (Erasmus, 2004; Tsai, 2010)

Structured Packing was developed and improved over four generations. The first and second generation consisted of wire gauze material, which showed a drastic decrease in pressure drop, but a marked increase in cost relative to the random packing available at the time (Billet, 1995)

The introduction of sheet metal structured packing, as a third generation packing, cemented the presence of structured packing as a high capacity, low pressure drop, high efficiency, lower sensitivity to solids and lower cost separation column internal (Kister, 1992). As mentioned in section 1.1.2, structured packing has a lower efficiency than random packing at higher liquid flow rates. This is due to the sharp directional change in flow rate encountered at the packing section interface. A fourth generation, high capacity packing was developed to improve the efficiency of structured packing at high liquid flow rates. The higher capacity packing would have larger flow channels and these flow channels curves towards the packing section interface to channel the liquid with less resistance through the directional change at the interface. The smoother directional change in liquid flow rate prevents the onset of flooding under higher liquid flow rates (Olujic, et al., 2001).

Structured packing is classified in accordance with its properties. These classification properties include, but are not limited to:

- Material Type
- Void Fraction
- Geometric Surface Area
- Flow Channel Geometry and Angle
- Surface Texture

Examples of the types of structured packing associated with each of the four generations during development are tabulated in **Table 1.2**.

Table 1.2 Examples of Structured Packing Elements for Each Generation (Lamprecht, 2010)

First generation (1940s-1950s)	Second generation (1950s-1970s)	Third generation (1970s- late 1990s)	Fourth Generation (late 1990s-present)
Panapak	Goodloe®	Sulzer Mellapak™®	Mellapak™plus®
	Hyperfil®	Koch Flexipac®	Sulzer Optiflow®
	Sulzer, Koch BX	Montzpak-B®	Flexiapk®HC™
		Gempak®	Montz-PakM®
			Raschig Super-Pak

1.2 Effective Interfacial Area Background

Effective interfacial mass transfer area is one of the most important efficiency parameters for characterizing the performance of any separation column internal (Shi & Mersmann, 1985; Wang, et al., 2005; Tsai, et al., 2008). Whether one deals with trays, random- or structured packing as the column internal, the effective interfacial mass transfer area (a_e) directly influences the calculation of the efficiency parameter, HETP (Olujic, et al., 1999). The HETP, or height equivalent to a theoretical plate, is an indication of the height of the packed bed that represents one equilibrium stage. One of the main aims in separation column design is thus to minimize the HETP required for the specified degree of separation. It now becomes clear that in order to be able to achieve the optimum column design, accurate knowledge of a_e is vital.

There have been many publications on the topic of accurately determining a_e (Shi & Mersmann, 1985; Wang, et al., 2005) but according to Shultes (Shultes, 2010) there is still room for vast improvements on the accuracy and application range of the existing correlations for estimating a_e. Shultes reports an up to 80% discrepancy in the various model predictions. This is an alarming figure, but may in part be attributed to the variety of methods and systems used to derive a_e correlations (Sridharan & Sharma, 1976; Shi & Mersmann, 1985; Shetty & Cerro, 1997; Tsai, 2010).

The two most popular methods implemented, may be separated on the basis of their main assumptions. The first method is based on physical liquid distribution theory (Shi & Mersmann,

1985; Shetty & Cerro, 1997) and assumes that the entire gas liquid interfacial area is effective for the purpose of mass transfer. The other method, involving the reactive absorption of a gas into a liquid, assumes the existence of interfacial areas that do not take part in mass transfer. These so-called dead zones do exist (Joosten & Danckwerts, 1973), which means that the chemical method may be more accurate in its a_e estimation than the physical one. Care must, however, be taken to ensure that the chemical method is applied correctly and there is still room for improvement regarding the fundamental understanding of the method. The chemical method has the great advantage of being a method for measuring effective interfacial mass transfer area via an actual mass transfer process. The method is based on reactive absorption theory utilizing a fast reaction in the liquid film to render the absorption rate to be independent of the physical liquid phase mass transfer coefficient (Danckwerts, 1970; Charpentier, 1981; Tsai, et al., 2008). The absorption rate is, therefore, controlled by the liquid phase reaction kinetics and the effective area available for mass transfer. One such chemical method will be investigated and developed in this study.

1.3 CO_2-Amine Systems: A Brief Introduction

One of the chemical methods used to measure effective interfacial mass transfer area involves the absorption of CO_2 into either aqueous or non-aqueous solutions containing an amine or a mixture of amines (Sridharan & Sharma, 1976). The details of the method used in this study will be discussed in Chapter 3 and Chapter 4, but it is worth mentioning now, since this system has various other applications as well. Currently the reactive absorption of CO_2 into a solution containing either one amine or mixtures of amines is an industrial scale process for capturing CO_2 in combustion emissions and aiding in the sequestration of this greenhouse gas. The capturing takes place in an absorber/stripper packed column configuration (Tsai, 2010) which means that the effective area of the column internals used, is vital knowledge towards the efficiency of the process.

As mentioned, the capture is achieved through reactive absorption. CO_2 thus reacts with the amine present in the solvent. The reaction kinetics of this system is vital for both a_e determination and CO_2 sequestration applications. Accurate knowledge of the reaction kinetics

of CO_2 with amines has, therefore, formed part of many previous investigations (Hikita, et al., 1976; Danckwerts, 1979; Alvarez-Fuster, et al., 1981; Barth, et al., 1984; Sada, et al., 1985; Versteeg & van Swaaij, 1988; Davis & Sandall, 1993). Since this is a gas-liquid system, all previous researchers, apart from Hikita, et al. (1976), have derived the reaction kinetics of the system using methods where gaseous CO_2 absorbs and reacts. It is, however, well known that under ambient conditions, the reaction only occurs in the liquid phase (Hikita, et al., 1976). It is further known that the reaction rate expression and the reaction order is dependent on the type of solvent as well, whether it be aqueous or non-aqueous (Alvarez-Fuster, et al., 1981). A homogeneous liquid phase study of this reaction should yield a more accurate description of the rate expression governing this system and these rate expressions should be valid over a wider range of operating conditions. This will improve on the fundamental understanding of this important reactive absorption process. The reaction kinetic theory will be discussed in further detail in Chapter 3.

1.4 Project Scope and Objectives

This project forms part of the greater science of separation technology, specifically to the application of separation column internals. Separation technology may be divided into three main fields of research with definite overlap. **Figure 1.1** gives visual representation to the above mentioned research fields and their area of overlap.

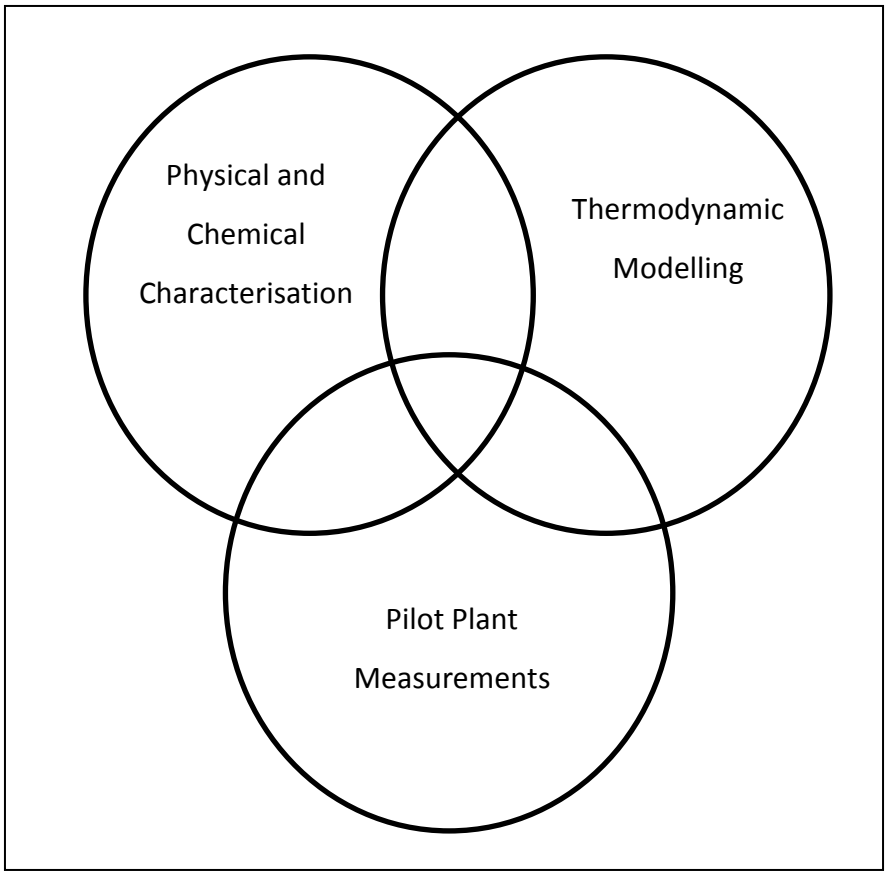

Figure 1.1 The Three Fields of Research in Separation Technology

The work done in this study lies in the overlap between 'Physical and Chemical Characteristics Investigation' and 'Pilot Plant Measurements' although more of the focus will be on the former. The physical and chemical characterization of separation column internals is vital for the derivation and improvement of fundamental theory governing the design and operation of separation columns. The thermodynamic modelling of separation systems falls outside the scope of this study.

Reactive absorption under fast pseudo first order reaction conditions is currently the accepted chemical method for measuring interfacial mass transfer area of separation column internals such as random and structured packing material (Tsai, 2010). Under pseudo first order reaction conditions, the liquid phase undergoes insignificant surface depletion due to the reaction and, thus, the surface renewal rate of such a liquid phase is infinite. No depletion of the components involved in the mass transfer process at the gas liquid interface and an infinite

surface renewal rate of the liquid phase may not always be obtained under normal separation column operation. Diffusivity rates of the active liquid phase component to the surface may be slowed down significantly in higher viscosity liquids (Reid & Sherwood, 1966), for example. This means that, due to the slower surface renewal rate, there is a decrease in effective interfacial mass transfer area, even though the interfacial area remained unaffected. Liquid properties, such as density, viscosity and surface tension influence the hydraulic behaviour of the liquid film (Shi & Mersmann, 1985; Shetty & Cerro, 1997), including the onset and degree of turbulence.

Surface renewal rate is a function of liquid side turbulence (Lamourelle & Sandall, 1972), which is one of the reasons why an increased mass transfer rate is noticed under turbulent liquid conditions (Yu, et al., 2006). The increase in mass transfer rate may be attributed to the increase in effective interfacial mass transfer area, brought on by the turbulent liquid increasing the transport of species to and from the gas-liquid interface, whilst also increasing the rate of departure of inert components from the interface. This effect cannot be investigated using a method that relies on an infinite surface renewal rate, with no surface depletion. The same argument of a fast reaction controlling the absorption rate at the interface may be used to derive a method for measuring effective interfacial mass transfer area under conditions where surface depletion and surface renewal rates are significant. The reaction kinetics in the liquid phase will, however, no longer be able to be approximated by a pseudo first order rate expression. A more fundamentally consistent reaction rate expression will be needed, which is applicable over the concentration range where surface depletion of the reagent in the liquid film is appreciable.

The main objectives of this study may, therefore, be summarized as follows:

1. To find a chemical system where the fast reaction of CO_2 with a primary amine can be used to measure effective interfacial mass transfer area. The reactive absorption of CO_2 in alcoholic solutions of mono-ethanolamine (MEA) has been proposed as a suitable method (Charpentier, 1981; Erasmus, 2004). This system will be investigated in this study

2. To develop a method for measuring the reaction kinetics of this system under conditions where surface depletion of MEA is significant. A homogeneous liquid phase reaction kinetic study, employing a non-intrusive method of analysis to measure the concentration profiles as a function of real time during the reaction progress must, therefore, be developed. n-Propanol as representative alcoholic solvent will be investigated in this study
3. The existing reaction rate expressions will be investigated for feasibility in the concentration ranges where surface depletion of the primary amine is significant. If the existing rate expressions are not feasible, then a new, fundamentally derived reaction rate expression must be proposed and fitted on the experimental data.
4. To perform reactive absorption experiments of CO_2 into an assumed known interfacial area of MEA/alcohol of different concentrations. A wetted wall column absorber experimental set-up was used in this study to perform such experiments. With the variation of liquid flow rate and column height, the specific absorption rate (mol/m^2.s) of CO_2 as a function of contact time and liquid Reynolds number can be investigated. Reactive absorption experiments under conditions where interfacial depletion of the amine is appreciable must be performed. The reactive absorption data can then be discussed in terms of the existence of interfacial depletion and renewal rates and how it may affect the effective area available for an assumed known interfacial mass transfer area. The data can be used to show that a new numerical method to calculate effective interfacial mass transfer area is necessary in order to be able to account for surface depletion and renewal rates. The new method will employ the best representative reaction rate expression for the concentration ranges where appreciable surface depletion of the amine exists and will be applicable for use on both random and structured packing material. It will also be useful for determining the true effective area of the assumed known interfacial area of the wetted wall column.

A secondary objective of this study was to capture video footage of the gas-liquid interface on the wetted wall column absorber. In future, image analysis of the gas-liquid interface may provide insight into the true interfacial area achieved by the wetted wall column through

studying the profiles of the wave motion on the liquid surface, as a function of liquid turbulence. The chemical method developed in this study, measures the effective interfacial mass transfer area, which can then be compared to the interfacial area determined from the image analysis. The degree of liquid turbulence should also be factored in to determine the surface renewal rate achieved by the wetted wall column.

1.5 Thesis Layout

Chapter 2	In Chapter 2 the existing mass transfer theory is discussed, including reactive absorption theory. The chapter gives insight into the different approaches followed in incorporating reaction kinetics into diffusive mass transfer theory. It discusses both reversible and irreversible reaction kinetic rate expressions, since both reaction mechanisms are of importance to this study
Chapter 3	In Chapter 3 the reaction kinetics of CO_2 with the primary amine, mono-ethanolamine (MEA) is investigated. A literature review revealed the current rate expressions used to describe the liquid phase reaction kinetics of this system. An *in-situ* FTIR method of analysis is developed to measure the real time concentration profiles of the reagents and one of the products of this reactive system. The data collected may be used to model existing and newly derived rate expressions
Chapter 4	In Chapter 4 the modelling of the real time data, collected via the method developed in Chapter 3, is performed. The existing rate expressions are evaluated for feasibility in the use of a new method for measuring effective interfacial mass transfer area under conditions where surface depletion of MEA is aprreciable. New, fundamentally derived, rate expressions are also investigated
Chapter 5	In Chapter 5 the existing effective interfacial mass transfer area theory and correlations are presented. Interfacial area correlations based on the

	geometry of the packing material and liquid distribution models is investigated. The chemical method for measuring interfacial area directly from the absorption rate of a reacting gas, is also presented and the predictions of the various correlations compared and discussed.
Chapter 6	In Chapter 6 the method development and results of a reactive absorption study of the CO_2/MEA/n-Propanol system is presented. The study was conducted on a cylindrical wetted wall column to try and obtain a known interfacial area for the gas to absorb into. Experiments were conducted under conditions where a degree of MEA depletion in the liquid film occurred, yet under fast reaction conditions, in order for the absorption measurements to be viable for effective area calculation. The experimental set-up was also designed to enable the capture of video footage of the gas-liquid interface on the wetted wall column. Image analysis of the gas liquid interface was performed in Matlab®, illustrating the wave motion on the liquid surface.
Chapter 7	Chapter 7 contains the main conclusions drawn from this study. Based on the conclusion, future work is identified and recommended. The novel contributions of this study are also summarised in Chapter 7
Appendix B	Appendix B introduces the basis for a newly proposed method for calculating effective interfacial mass transfer area under conditions where surface depletion and renewal rates become significant. The method comprises of solving a system of partial differential equations numerically, given the appropriate initial and boundary conditions. Since pseudo first order reaction kinetics are not valid under these conditions, the fundamentally derived rate expressions from Chapter 4 are proposed for use in the system of equations. The method for calculating the initial and boundary condition values are also provided.

Chapter 2 PHYSICAL AND REACTIVE ABSORPTION THEORY

The reactive absorption of CO_2 into alcoholic solutions containing a primary amine such as mono-ethanolamine (MEA) is an example of a mass transfer process accompanied with a chemical reaction in the liquid phase (Danckwerts, 1970). Reactive absorption is a special case of physical absorption and thus the applicable theory on both of these processes will be presented in this chapter.

Physical and reactive absorption are two examples of mass transfer processes. Mass transfer will occur whenever there is contact between two phases that are either not in physical or chemical equilibrium (Astarita, 1967). The concentration difference of the species undergoing mass transfer through the phases provides the driving force for the mass transfer process, whilst the physical and hydrodynamic properties of the two phases induce a resistance to the potential mass transfer. The rate of mass transfer may therefore be expressed as (Tsai, 2010):

$$\text{Rate of Transport} = \frac{\text{Driving Force}}{\text{Resistance}}$$

This relationship may best be represented mathematically as (refer to **Figure 2.1** on page 16 for annotation and the glossary on page xxii for symbol definitions):

$$\left(N_A\right)_x = \frac{n_A}{a_e} = K_G\left(P_{A,0} - P_{A,L}\right) = k_G\left(P_{A,0} - P_{A,i}\right) = k_L\left(C_{A,i} - C_{A,L}\right) = \frac{k_L}{H_A}\left(P_{A,i} - P_{A,L}\right) \qquad 2.1$$

From equation 2.1 the partial pressure and concentration differences represent the driving force of the absorption, whilst the reciprocals of the transfer coefficients represent the resistance to mass transfer. The overall resistance may be calculated as a series of gas-side and liquid-side resistance:

$$\frac{1}{K_G} = \frac{1}{k_G} + \frac{H_A}{k_L} \qquad 2.2$$

The theory developed for both physical and reactive absorption is based on this relationship and the mathematics derived to describe these mass transport phenomena. It always considers both the driving force and resistance simultaneously in order to make sense of the experimentally measured transport rate. An understanding of especially the nature of the mass transfer resistance encountered is of utmost importance in simplifying the sometimes monstrous analytical solutions proposed for especially reactive absorption processes (Astarita, 1967). Here, the nature of the reaction is of great interest, since different reaction rates will influence the relationship between the absorption driving force and the mass transfer resistance encountered.

This chapter will introduce the existing theory that was developed for describing both physical mass transfer as well as mass transfer accompanied by a chemical reaction. The latter is of more importance to the scope of this research, since the use of a reactive absorption process will form the basis for deriving a new theory for calculating both interfacial – and effective interfacial mass transfer area.

2.1 Physical Gas-Liquid Mass Transfer Theory

There exist four main theories describing the mechanism of a gas absorbing into a liquid. All theories agree that the driving force behind physical absorption is due to a concentration gradient of the absorbing species across a boundary layer that connects the two contacting phases. This is the first principle whereupon the oldest of these theories, Film Theory, is based.

2.1.1 Film Theory

Film Theory (Lewis & Whitman, 1924) is the oldest relevant mass transfer theory available. It assumes four regions forming whenever gas (*A*) and liquid (*B*) comes into contact (**Figure 2.1**). The bulk liquid and bulk gas regions are uniform in concentration, since perfect convective mixing is assumed for these regions. A boundary layer is formed on both sides of the gas-liquid

interface. The boundary layer consists of a stagnant liquid film in contact with a stagnant vapour film and only steady state molecular diffusion of species along a concentration gradient is assumed to occur.

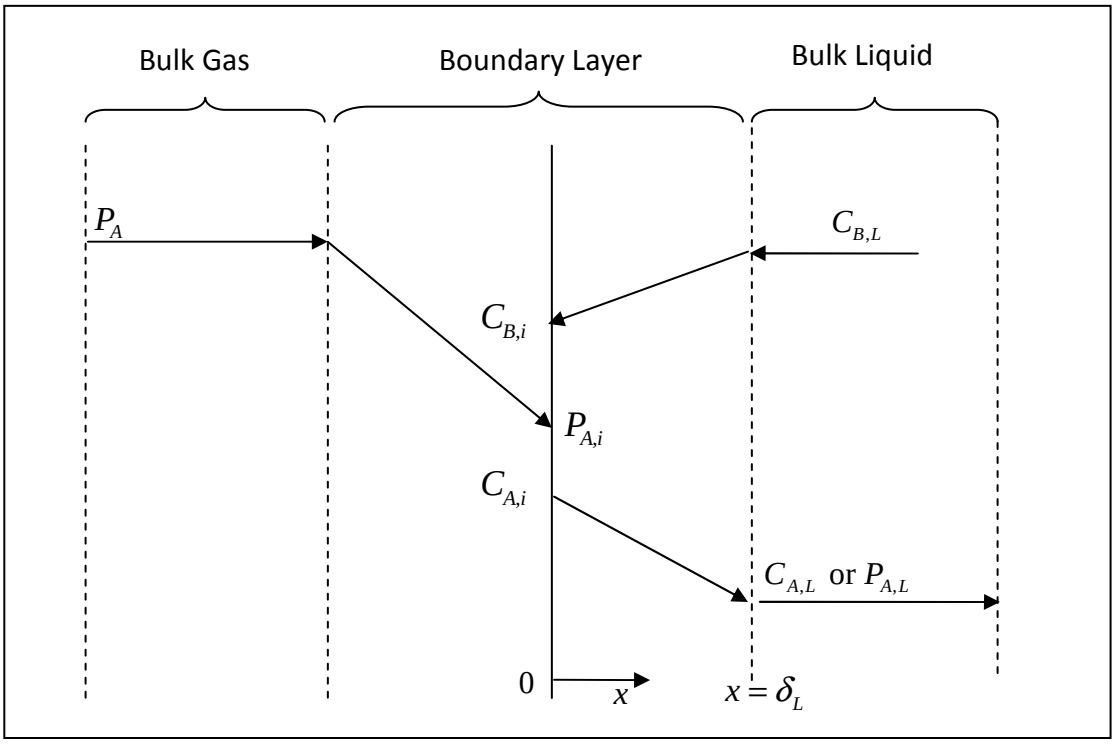

Figure 2.1 Schematic of Film Theory Diffusive Mass Transfer

The steady state rate of diffusion for the film theory may be expressed as (Danckwerts, 1970; Charpentier, 1981):

$$D_{A,L}\frac{d^2C_A}{dx^2} = 0 \qquad 2.3$$

where x is the direction of diffusion and absorption, as illustrated in **Figure 2.1** and $D_{A,L}$ is the diffusivity of species *A* in the liquid phase. Applying the assumption of two stagnant films of different phases in contact, the rate of mass transfer of gaseous species *A* along its concentration gradient at the interface may be determined from

$$\left(N_A\right)_x = \frac{n_A}{a_e} = -D_{A,L}\left(\frac{dC_A}{dx}\right)_{x=0} \qquad 2.4$$

where a_e is the effective interfacial mass transfer area and n_A the average rate of absorption per unit of effective area. Film theory assumes a linear concentration gradient for species *A* from its interfacial concentration, C_A^*, to its bulk liquid concentration, $C_{A,L}$, during absorption. When this linear profile is integrated for a liquid film thickness of δ_L, equation 2.5 results:

$$n_A = a_e\left(\frac{D_{A,L}}{\delta_L}\right)\left(C_{A,i} - C_{A,L}\right) \qquad 2.5$$

Equation 2.5 is analogous in form to the basic absorption equation incorporating the liquid side mass transfer coefficient, k_L (Charpentier, 1981)

$$\left(N_A\right)_x \cdot a_e = n_A = k_L a_e\left(C_{A,i} - C_{A,L}\right) \qquad 2.6$$

Based on the analogy, it now may be deduced from basic film theory that

$$k_L = \frac{D_{A,L}}{\delta_L} \qquad 2.7$$

Experimental evidence , however, suggests that there is not a direct proportionality between k_L and $D_{A,L}$ (Astarita, 1967; Danckwerts, 1970; Tsai, 2010). The proportionality is better described by $D_{A,L}^{0.5}$. This discovery prompted the development of more accurate and representative mass transfer theories, namely the penetration theory, surface renewal theory and eddy diffusivity theory.

2.1.2 Penetration Theory

Penetration theory (Higbie, 1935; Charpentier, 1981; Tsai, 2010) assumes that each liquid element is exposed for an equal time to the absorbing gas, before being replaced by an identical element from the bulk liquid phase. It is thus a non-steady state absorption model of

gas diffusing into a liquid film of infinite depth and is described by the following differential equation:

$$D_{A,L}\frac{\partial^2 C_A}{\partial x^2}-\frac{\partial C_A}{\partial t}=0 \qquad 2.8$$

Equation 2.8 may be solved for unsteady state conditions assuming the following boundary conditions (Astarita, 1967):

$$@\, x \geq 0,\ t=0\ :\ C_A = C_{A,0}$$
$$@\, x=0,\ \mathrm{t}>0\ :\ C_A = C_{A,i}$$
$$@\, x \to \infty,\ t>0\ :\ C_A = C_{A,L}$$

which results in the following expression for the absorption rate of the solute gas:

$$n_A = 2\left(\frac{D_{A,L}}{\pi t_c}\right)^{0.5}\cdot a_e\left(C_{A,i}-C_{A,L}\right) \qquad 2.9$$

where t_c is the average contact time of each of the liquid elements with the gas phase. From the analogy of equation 2.9 with equation 2.6 it may be seen that

$$k_L = 2\sqrt{\frac{D_{A,L}}{\pi t_c}} \qquad 2.10$$

which is a more representative mass transfer theory according to the experimental evidence. A schematic of diffusive mass transfer assuming penetration theory is shown in **Figure 2.2**.

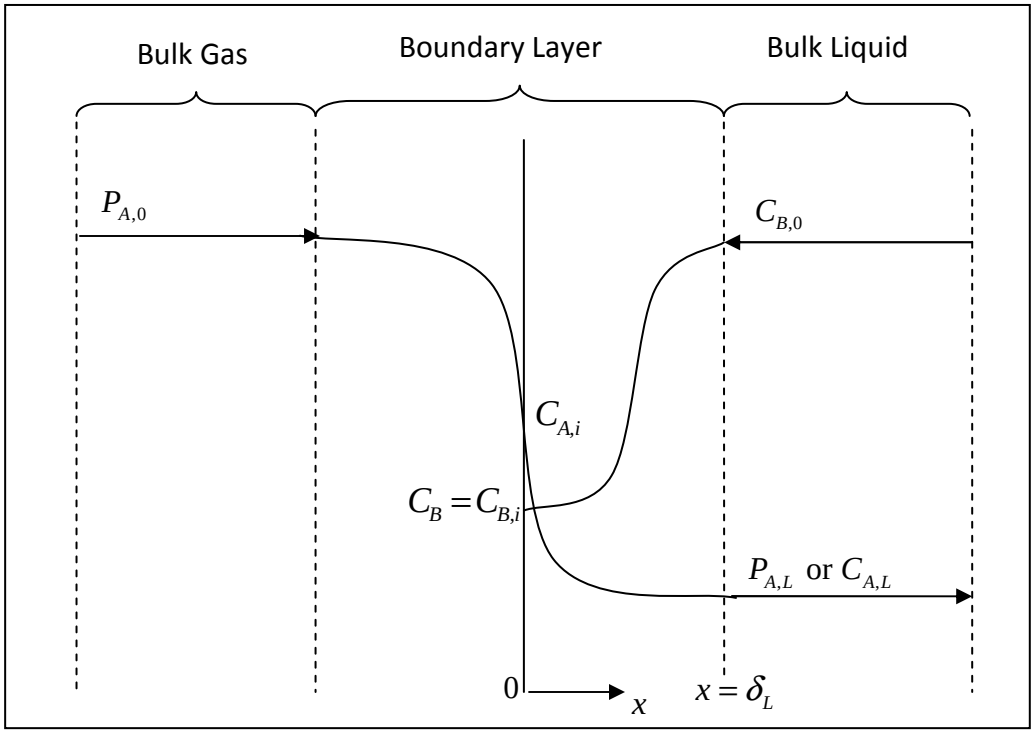

Figure 2.2 Schematic of Diffusive Mass Transfer Assuming Penetration Theory to Apply

2.1.3 Surface Renewal Theory

Surface renewal theory (Danckwerts, 1951) is an attempt to improve on the accuracy of the equal exposure time assumption of the penetration theory. The surface renewal theory rejects the assumption that all liquid elements spend equal times exposed to the gas phase. The surface renewal theory basically states that there exists an equal probability that an element will be replaced in a certain time, $t_c + dt$ or that it will remain exposed.

It follows that only a fraction of the liquid surface is renewed in equal time segments (Danckwerts, et al., 1963). This model is a more realistic mass transfer model, since perfect liquid mixing is not possible, especially in large gas-liquid contactors. The fraction of liquid renewed in each time segment is denoted by s and the resulting expression for the mass transfer coefficient based on the surface renewal theory is expressed as (Charpentier, 1981):

$$k_L = \sqrt{D_{A,L} s} \qquad 2.11$$

which is, similarly to the penetration theory, in agreement with experimental evidence. It should be noted that for the surface renewal theory to be applied accurately, knowledge of the surface renewal rate is needed, which is not always easy to obtain (Charpentier, 1981). A form of the surface renewal rate has been proposed as a function of liquid Reynolds number (Lamourelle & Sandall, 1972):

$$s = 0.115 \cdot \mathrm{Re}_L^{1.678} \qquad 2.12$$

One of the advantageous of the method used in this study is that a more realistic idea of the surface renewal rate may be approximated with the use of a reactive absorption process under the fast reaction regime for which the liquid phase reaction kinetics is well known. The development of this method will be discussed in Chapter 7. The surface renewal theory is the most realistic theory to date and must be explored and validated to enhance our understanding of mass transfer processes. Surface renewal theory may be interpreted as having a similar schematic representation as in **Figure 2.2**, since the same transport equations are solved as for the penetration theory. The only difference is in the formulation of the mass transfer coefficient.

2.1.4 Eddy Diffusivity Theory

Eddy Diffusivity Theory (King, 1966) moves away from the concept of diffusion being time dependant and replaces it with a liquid convection theory. It assumes that at the gas-liquid interface diffusion is the dominant means of molecular movement, while convective liquid movement in the form of “eddies” provide the driving force for mixing in the bulk liquid phase. The eddy movements, denoted by e_d in the model equations are implemented as factors to achieve closure and solvability of unsteady state Navier-Stokes equations (Bird, et al., 2002). The eddy diffusivity factors are formulated to obtain the correct relation between k_L and $D_{A,L}$. The governing differential equation for the Eddy Diffusivity model is depicted as (Lamourelle & Sandall, 1972):

$$\frac{\partial}{\partial x}\left[\left(D_{A,L} + e_d x^2\right)\frac{\partial C_A}{\partial x}\right] = 0 \qquad 2.13$$

With the liquid side mass transfer coefficient expressed as

$$k_L = \frac{2}{\pi}\sqrt{D_{A,L} e_d} \qquad 2.14$$

A schematic illustrating the role of eddies enhancing surface renewal in the liguid phase is shown in diffusivity in

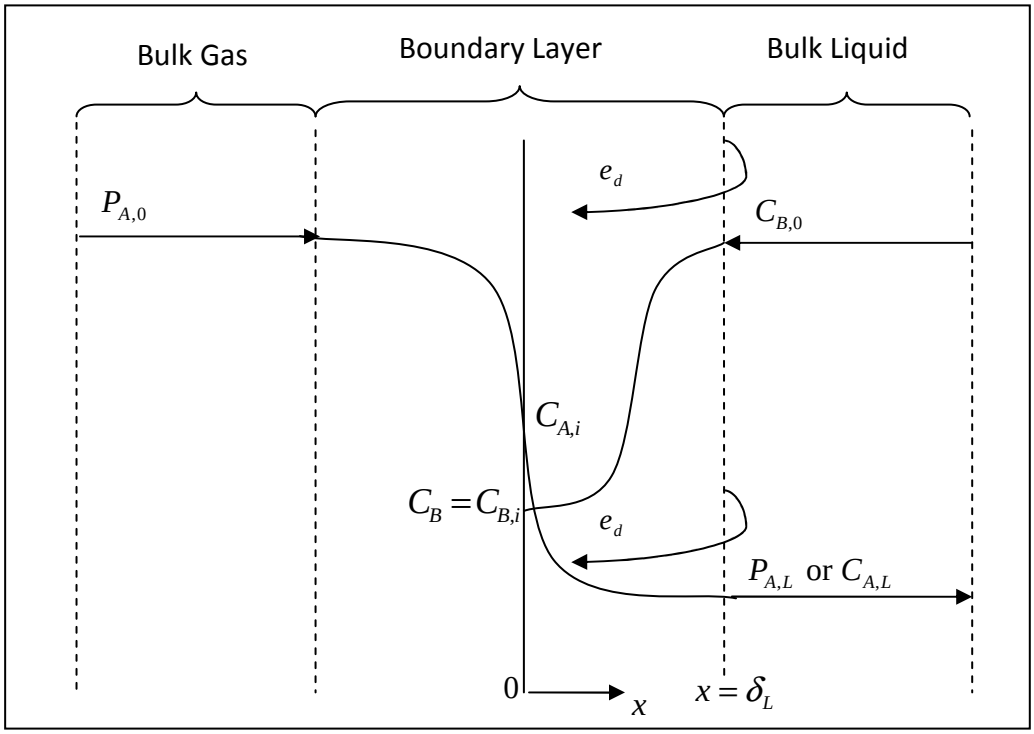

Figure 2.3 Schematic of Diffusive Mass Transfer Showing Eddy Diffusivity Renewing the Interface with Bulk Liquid

The eddy diffusivity theory matches the other three theories within 5% (Tsai, 2010). In .

2.2 Mass Transfer with Chemical Reaction

If two phases, which are not in chemical equilibrium, come into contact the mass transfer between the phases is accompanied by a chemical reaction. A similar boundary layer schematic to the one proposed for the film theory (**Figure 2.1**) is usually assumed (Astarita, 1967; Danckwerts, 1970; Charpentier, 1981) with a significant difference in the shape of the

concentration profiles within the mass transfer zone. A representative schematic of mass transfer accompanied by a chemical reaction is depicted in **Figure 2.4**.

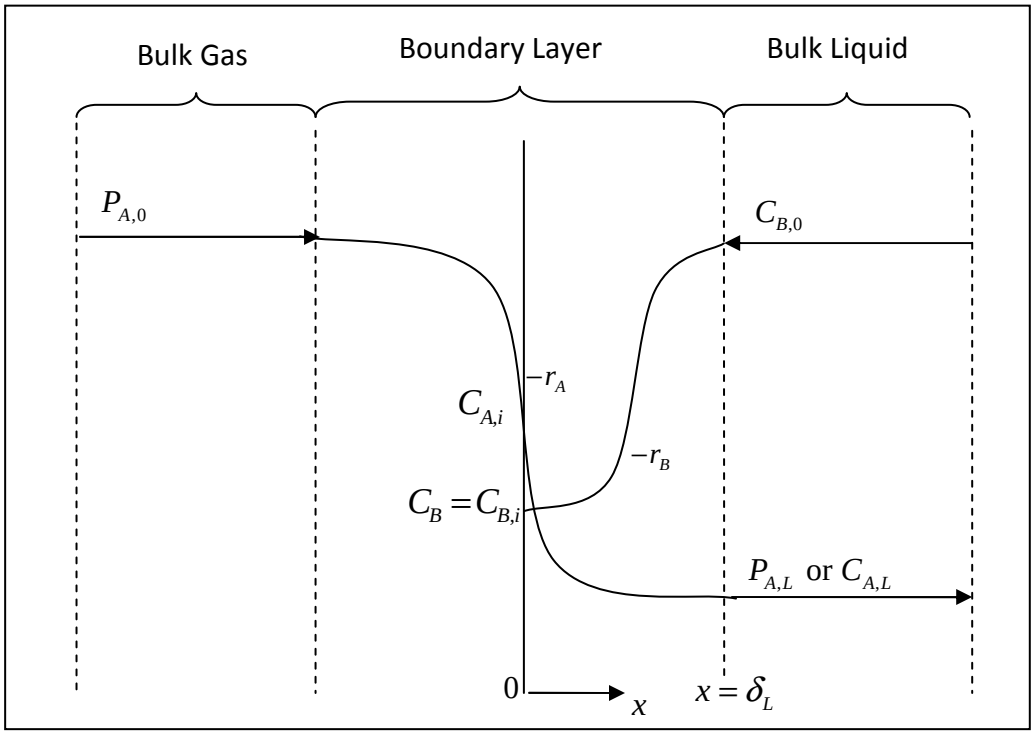

Figure 2.4 Schematic of Diffusive Mass Transfer with Chemical Reaction

The governing equation is derived from the unsteady state diffusion equation forming the basis of the penetration and surface renewal theories (equation 2.8) with the addition of the reaction rate expression governing the liquid phase reaction kinetics between the absorbing gas (A) and the liquid component (B):

$$D_j \frac{\partial^2 C_j}{\partial x^2} = \frac{\partial C_j}{\partial t} + r_j \qquad 2.15$$

where j represents all species in the mixture and r_j the nett reaction rate expression for each of the reacting species. Inert components are all lumped with the solvent and are assumed to have no added significant effect on the diffusivities of the reacting species.

Equation 2.15 was derived from first principles and forms the basis for most existing models. The difference between the models is the assumptions made regarding the nature of the reaction in the liquid phase. There are three types of reactions considered in literature: Slow, Fast and Instantaneous. There are of course instances when a reaction may be considered to be in the transition zone between either slow and fast or fast and instantaneous, but for the sake of deriving the base line theory for different reactive absorption reactions, only the three distinct cases will be presented.

A reactive absorption process may be considered to fall in the slow reaction category when the reaction time greatly exceeds the diffusion time. This implies that the absorption rate is controlled by the physical properties of the species present and the reaction kinetics is confined to the bulk liquid phase. These systems are ideal for determining the liquid side mass transfer coefficient, k_L (Neelakantan & Gehlawat, 1982). Since the slow reaction type falls outside the scope of this study, it will not be investigated further.

At the other end of the spectrum, a reaction may be considered to occur at such a fast rate that it consumes both reaction species within the liquid boundary layer. The rate of absorption for this type of instantaneous irreversible reaction is dependent on the diffusion rate of species to the thin reaction zone and the reaction kinetics is therefore considered insignificant (Astarita, 1967). The stoichiometry of the reaction may be used to determine the thickness of the reaction zone in the liquid boundary layer, which indicates that the type of reaction will enhance the absorption rate by a constant factor. This type of reaction also falls outside the scope of this study and will not be discussed in further detail.

The reaction type of interest to this study falls within the fast reaction category. Under conditions where gas phase mass transfer resistance may be considered to be negligible, the absorption rate is controlled by the liquid phase reaction and is therefore independent of k_L. Referring to equation 2.6, this then logically forms the basis for deriving theory for determining both interfacial area and effective interfacial area The theory used to calculate effective interfacial mass transfer area rests strongly on the reaction mechanism and kinetics assumed to be valid under the reactive absorption conditions.

Mass transfer with chemical reaction is best represented by a rate based model which includes a rate expression describing the reaction kinetics of the liquid phase reaction (Astarita, 1967; Van Swaaij & Versteeg, 1992). The rate expression is of course a strong function of the reaction type and mechanism. For most reactive absorption systems, the governing rate based models are derived under conditions where the reaction is assumed to obey simple kinetics such as an irreversible power rate law or pseudo first order kinetics. As the rate expressions increase in complexity, so do the resulting analytical solutions of the differential equations.

With the limited computational power and techniques available to previous researchers, it made sense to simplify the kinetics as far as possible. It is, however, of great interest to be able to model a reactive absorption process on its fundamental merits, in order for the resulting models to be more robust over a wider range of reactive absorption conditions. Great advances are being made in computational techniques to solve complex differential and partial differential equations, which contributes to developing solutions for the fundamentally derived reactive absorption models.

All rate based models assuming penetration theory are derived from equation 2.15. The simplest models are derived for irreversible reactions with a marked increase in model complexity for reversible reactions. Both will be presented here, based on the derivations and solution strategies found in literature.

2.2.1 Irreversible Reactions

Irreversible reaction mechanisms are often encountered in industrial absorbers (Astarita, 1967; Danckwerts, 1970; Charpentier, 1981; Tsai, 2010). Under conditions where one of the reactants is in great excess, even a reversible reaction may be approximated to obey irreversible reaction kinetics. This seems to contradict the fundamental knowledge of the reaction mechanism itself, but in order to simplify the rate based model structure; previous researchers had no other choice but to implement these simplifying assumptions.

The reaction investigated in this study (CO_2 with an amine) is one of the main examples of a reversible system, subject to irreversible kinetics in order to simplify the mathematics. Some of

the model structures used to describe its reactive absorption behaviour is discussed in section 3.1.2. It is, therefore, worthwhile to present the rate based model derived for an irreversible reaction.

An irreversible reaction proceeds in only one direction and may be presented as:

$$aA + bB \xrightarrow{k} cC \qquad 2.16$$

The reactive absorption of CO_2 (A) with an amine (B) will be discussed as an example system throughout the derivation of the general analytical solutions. This is done in order to illustrate the methods and theories used to determine the reaction kinetic parameters of this reactive system. One may apply either the film theory or penetration theory to express the reactive absorption of A into B in terms of differential equations. For the sake of improved model accuracy, the penetration theory will be presented instead of the simpler, less accurate film theory. For the derivation of the film theory expression, refer to either (Astarita, 1967) or (Danckwerts, 1970). The penetration theory expressions are (Onda, et al., 1972):

$$D_A \frac{\partial^2 C_A}{\partial x^2} - \frac{\partial C_A}{\partial t} = k C_A^m C_B^n = -r_A \qquad 2.17$$

$$D_B \frac{\partial^2 C_B}{\partial x^2} - \frac{\partial C_B}{\partial t} = \frac{b}{a}(-r_A) \qquad 2.18$$

Where b/a is the ratio of the stoichiometric coefficients of B and A in equation 2.16. Equations 2.17 and 2.18 may be solved analytically subject to certain boundary conditions applicable to the penetration theory. At the gas-liquid interface the concentration of the absorbing gas is equal to its solubility in the liquid phase for the specified partial pressure $(P_{A,i})$ at the gas-liquid interface. For a reacting gas, this is a difficult parameter to determine and is best approximated with an analogy.

For CO_2 the best analogous gas to use for amine systems is the non reacting gas, N_2O, since they share similar molecular structure and identical molecular weight (Alvarez-Fuster, et al., 1981; Laddha & Danckwerts, 1981; Wang, et al., 1992; Li & Lai, 1995). The N_2O analogy, along

with the approximations used to estimate the solubility and diffusivity of CO_2 in amine solutions will further be discussed in Chapter 6 and Appendix B. Since the liquid component is assumed to be non-volatile, it has a transport of zero across the interface. This assumption will be upheld for all liquid species in a reaction mixture. The measured absorption rate of the gas may be presented in the form of equation 2.4. The initial and boundary conditions are expressed mathematically as:

$$@\ x \geq 0,\ t = 0\ :\ \left\{ \begin{matrix} C_A = C_{A,0} = 0 \\ C_B = C_{B,0} = C_{B,L} \end{matrix} \right\} \qquad 2.19$$

$$@\ x = 0,\ \mathrm{t} > 0\ :\ \left\{ \begin{matrix} C_A = C_{A,i} = \dfrac{P_{A,i}}{H_A} \\ \dfrac{\partial C_B}{\partial x} = 0 \\ C_B = C_{B,i} \end{matrix} \right\} \qquad 2.20$$

$$@\ x \to \infty,\ t > 0\ :\ \left\{ \begin{matrix} C_A = C_{A,L} \\ C_B = C_{B,L} \end{matrix} \right\} \qquad 2.21$$

with

$$\frac{n_A}{a_e} = -D_{A,L}\left(\frac{\partial C_A}{\partial x}\right)_{x=0} \qquad 2.22$$

Equation 2.22 contains the concentration gradient term of the absorbing gas at the gas-liquid interface $(x=0)$ and it is a function of time. A linear approximation of $-r_A$ is required in order to be able to simplify the resulting analytical solution. The approximation as proposed by Hikita and Asai (Danckwerts, 1970) is:

$$-r_A = \frac{2}{m+1} k_{m.n} C_{A,i}^{m-1} C_{B,i}^{n} C_A \equiv \xi C_A \qquad 2.23$$

The linearization of the rate expression reduces it to a similar form of a pseudo first order rate expression. This special case will be discussed later in this section. The analytical solution obtained after linearization of the rate expression is long and of a high degree of complexity and will thus not be presented here. It may be found elsewhere (Onda, et al., 1972). It may, however, be noted that if the limitations of instantaneous reaction or slow reaction is applied to the solution, it corresponds well to the solutions proposed by other researchers who focused on these limiting cases. The analytical solution obtained for the irreversible reaction mechanism therefore serves as a good approximation under certain, limiting absorption conditions.

Analytical solutions are impossible to obtain for reactive absorption conditions where more complex reaction kinetics prevails and, thus, numerical strategies are called for (Van Swaaij & Versteeg, 1992). This is one of the reasons why many previous researchers have tried to conduct experiments under conditions where the reaction may not only be considered to be irreversible, but that it obeys simple elementary reaction kinetics as well. The major drawback to this approach is the limitation of the model prediction range and validity. Once the operating conditions inside the absorber falls outside the narrow range of conditions where the irreversible model was derived, it fails to predict absorption rates accurately.

In an attempt to simplify the numerical approach and save on computational time, previous researchers have resorted to implementing an enhancement factor to account for the enhancement in absorption in the presence of a chemical reaction (Danckwerts, 1970; Van Swaaij & Versteeg, 1992; Vas Bhat, et al., 2000; Meldon, et al., 2007). The enhancement factor is defined as the ratio of the absorption rate in the presence of a chemical reaction to that without a reaction in the liquid film for identical physical conditions:

$$E = \frac{N_{A,\text{ with chemical reaction}}}{N_{A,\text{without chemical reaction}}} \qquad 2.24$$

The absorption rate in the presence of a chemical reaction may now be expressed as:

$$\left(N_A\right)_x \cdot a_e = n_A = Ek_L a_e \left(C_{A,i} - C_{A,L}\right) \qquad 2.25$$

The enhancement factor is a function of the reaction rate expression assumed for the reaction in the liquid film. Analytical solutions for the enhancement factor assuming different reaction rate expressions to apply have been determined by Danckwerts. An example of such a solution for the m,nth order reaction of equation 2.17 is (Danckwerts, 1970):

$$E = \frac{\mathrm{Ha}\left[\left(E_i - E\right)\Big/\left(E_i - 1\right)\right]^{n/2}}{\tanh\left\{\mathrm{Ha}\left[\left(E_i - E\right)\Big/\left(E_i - 1\right)\right]^{n/2}\right\}} \qquad 2.26$$

where Ha is the Hatta number(Van Swaaij & Versteeg, 1992), which in this case is defined as:

$$\mathrm{Ha} = \frac{\sqrt{\left(\frac{2}{m+1}\right)\left(k_{m,n} D_A C_{A,i}^{m-1} C_{B,L}^{n}\right)}}{k_L} \qquad 2.27$$

and E_i is the enhancement factor for an instantaneous reaction defined as:

$$E_i = 1 + \left(\frac{a \cdot D_B}{b \cdot D_A}\right)\left(\frac{C_{B,L}}{C_{A,i}}\right) \qquad 2.28$$

Where a and b are the stoichiometric coefficients in equation 2.16. For the reaction to safely be approximated as fast pseudo m,nth order, the following criteria must be met (Danckwerts, 1970; Alvarez-Fuster, et al., 1980; de Brito, et al., 1994; Charpentier, 1981):

For a reaction in the moderately fast reaction regime, the Hatta number lies within the following region (Charpentier, 1981):

$$0.3 < \mathrm{Ha} < 3 \qquad 2.29$$

Under these conditions, the concentration of the reactively absorbing gas (A) decreases sharply within the reaction zone (the liquid film boundary layer in **Figure 2.2**) and reaches concentrations approaching zero at the boundary of the reaction zone and the bulk liquid. There is surface depletion of the liquid phase reactant (B) (Charpentier, 1981). Under this fast

reaction regime, the absorption rate is most strongly influenced by the available effective mass transfer area and is thus an appropriate chemical method to use for measuring effective area from reactive absorption rates where surface depletion and renewal rates are significant.

A special case of a fast, pseudo m,nth order reaction occurs when the following criteria are met:

$$3 < \mathrm{Ha} < 0.5E_i \qquad 2.30$$

Under the conditions of equation 2.30 the reaction may be considered to be fast pseudo first order with respect to the reactively absorbing gas (de Brito, et al., 1994; Tsai, et al., 2008; Charpentier, 1981). The pseudo first order approximation becomes valid because under these conditions there is insignificant depletion of the liquid phase reactant in the reaction zone within the liquid film. Its concentration remains constant as the bulk liquid concentration and may be lumped with the reaction rate constant to represent a pseudo first order rate constant. Under pseudo m,nth order and pseudo first order conditions, the following approximation becomes valid (Tsai, 2010):

$$E \approx \mathrm{Ha} \qquad 2.31$$

If experiments are conducted on a device with an assumed known interfacial mass transfer area and the entire interfacial area is assumed to be effective, then a combination of equation 2.1 and equation 2.25 will yield:

$$\left(N_A\right)_x = \frac{n_A}{a_e} = k_G\left(P_{A,0} - P_{A,i}\right) = \mathrm{Ha}\cdot k_L\left(C_{A,i} - C_{A,L}\right) = \frac{\mathrm{Ha}\cdot k_L}{H_A}\left(P_{A,i} - P_{A,L}\right) \qquad 2.32$$

Assuming gas phase resistance to be significant and expressing the absorption in terms of a series of gas-side and liquid side resistances (equation 2.2) the following expression is obtained (Alvarez-Fuster, et al., 1981):

$$\frac{n_A}{a_{\text{contact device}}} = \frac{\left(P_{A,0} - P_{A,L}\right)}{\frac{1}{k_G} + \frac{H_A}{\left[\left(\frac{2}{m+1}\right)\left(k_{m,n}D_A C_{A,i}^{m-1} C_{B,L}^{n}\right)\right]^{0.5}}} \qquad 2.33$$

Since the gas-side mass transfer resistance is in most cases calculated with an empirical correlation with inherent inaccuracy (Tsai, 2010), it is best to work under conditions where gas-side resistance is negligible. Under such conditions, equation 2.33 reduces to:

$$n_A = a_{\text{contact device}}\left(C_{A,i} - C_{A,L}\right)\sqrt{\left(\frac{2}{m+1}\right)\left(k_{m,n}D_A C_{A,i}^{m-1}C_{B,L}^{n}\right)} \qquad 2.34$$

Since equation 2.34 is independent of k_L, it forms the basis of the absorption equation used to derive the m,nth order reaction rate constant, $k_{m,n}$ provided that C_A^* and D_A are known. This was the approach used by some previous researchers to derive the kinetic parameters of the reaction of CO_2 with various amines in both aqueous and non-aqueous solvents (Alvarez-Fuster, et al., 1981). For this purpose, it was assumed that the CO_2/amine system obeyed irreversible reaction kinetics. A more in depth review of the existing CO_2/amine reaction mechanisms and rate expressions is presented in section 3.1.

Another, more popular approach to deriving the kinetic parameters for the CO_2/amine system is to collect absorption data under conditions where a pseudo first order rate expression is assumed. The enhancement factor is once again used, since the pseudo first order rate expression is a simplified version of the pseudo m,nth order expression. Along with the restriction of equation 2.30, constant amine concentration at the interface is assumed to be maintained if (Laddha & Danckwerts, 1981):

$$\left(N_A\right)_x << \frac{1}{2}k_L C_{B,i}\sqrt{\frac{D_B}{D_A}} \qquad 2.35$$

If the concentration of amine in the liquid phase is assumed to suffer insignificant depletion due to its reaction with CO_2, its concentration is lumped with the rate constant to give:

$$-r_A = k_{m,n}C_A^m C_B^n \approx k_{m,0}C_A^m \qquad 2.36$$

Under the same assumption of insignificant gas-phase mass transfer resistance, equation 2.34 reduces to

$$n_A = a_{\text{contact device}} \left(C_{A,i} - C_{A,L}\right) \sqrt{\left(\frac{2}{m+1}\right)\left(k_{m,0} D_A C_{A,i}^{m-1}\right)} \qquad 2.37$$

Equation 2.37 represents the general form of the absorption expression under pseudo mth order reaction conditions with insignificant gas-phase resistance. Many authors believe the reaction order with respect to CO_2 is unity under these conditions, regardless of the type of amine it reacts with or which solvent is used (Sada, et al., 1985; Luo, et al., 2012). For $m = 1$, equation 2.37 reduces to:

$$n_A = a_{\text{contact device}} \left(C_{A,i} - C_{A,L}\right) \sqrt{k_{1,0} D_A} = a_{\text{contact device}} \frac{\left(P_{A,i} - P_{A,L}\right)}{H_A} \sqrt{k_{1,0} D_A} \qquad 2.38$$

The pseudo first order rate constant, $k_{1,0}$ may now be obtained with the knowledge of D_A and H_A. As mentioned earlier, these parameters are estimated with the use of the N_2O analogy. Equation 2.37 will form the basis for deriving the theory on which the chemical method is based for estimating interfacial mass transfer area. This will be discussed further in Chapter 5.

Although the enhancement factor approach has several advantages with regards to decreasing computational time required to obtain an approximate solution, it may still only be regarded as an approximation. The use of the enhancement factor has several disadvantages in modelling reactive absorption processes (Brinkmann, et al., 1998):

- First order reactions provide an analytical solution for E, whilst higher order reactions are subject to complex mathematical solutions only valid in a narrow range of limiting cases. These limiting cases are based on simplifying assumptions such as irreversible reaction ($C_{A,L} = 0$), negligible gas phase mass transfer resistance and equal diffusivities.
- The enhancement factor calculated for higher order reactions is a function of the bulk liquid concentrations. Since the bulk liquid concentrations are in most cases dependent system variables, the enhancement factor is not known in advance and is dependent on the operating conditions.

- When film theory is applied, there may be multiple solutions for the enhancement factor when consecutive reactions are considered. This means that the system is not uniquely defined inasmuch as different mass transfer rates are obtained for the different solutions of the enhancement factor. Surface renewal theory provides a unique solution for the mass transfer rates but results in highly complex expressions for E.

Based on the above mentioned disadvantages, caution should be applied when using the enhancement factor for modelling a reactive absorption process under conditions where irreversible pseudo (m,n)th order kinetic conditions are no longer valid.

2.2.2 Reversible Reactions

Rate based models based on reversible reactions have gained in popularity due its firmer fundamental basis of derivation and wider application range (Onda, et al., 1972; Bosch, et al., 1989; Vas Bhat, et al., 1997; Brinkmann, et al., 1998; Vas Bhat, et al., 2000; Meldon, et al., 2007; Versteeg, et al., 1990). The analytical solutions are of a higher degree of complexity compared to irreversible reaction mechanisms, but numerical solutions are available and are proving to be accurate (Aboudheir, et al., 2003). This section will discuss the strategies followed by previous researchers to obtain a solution to a reactive absorption process accompanied by a reversible chemical reaction.

There are various types of reversible chemical reactions. An elementary reaction occurs in one step and is the simplest form of a reversible reaction. Elementary reactions are, however, not encountered often. The most applicable reaction mechanism for reactive absorption processes found in industry is probably consecutive and parallel reversible reactions (Onda, et al., 1972). In this study a consecutive reversible reaction with a reactive intermediate is investigated. The generalized reaction expression for this type of reversible chemical reaction with unit stoichiometric coefficients is:

$$A + B \underset{k_2}{\overset{k_1}{\rightleftharpoons}} C$$
$$C + B \underset{k_3}{\overset{k_2}{\rightleftharpoons}} D + E \qquad 2.39$$

Once again the more accurate penetration (Vas Bhat, et al., 2000) or surface renewal theory (Brinkmann, et al., 1998) may be applied to solve the following set of differential equations:

$$\frac{\partial C_j}{\partial t} = D_j \frac{\partial^2 C_j}{\partial x^2} - r_j \quad \text{j} \in \{A, B, C, D, E\} \qquad 2.40$$

with r_j being the nett reaction rate for each of the species in the mechanism. Knowledge of the nett reaction rate expression for each of the species in the mechanism as well as the diffusivity of each component, will allow for fast model convergence and accurate prediction of the absorption rate per effective area. Under conditions where there is appreciable surface depletion of the liquid phase reactant and the effective mass transfer area becomes dependent upon the surface renewal rate achieved, irreversible pseudo (m,n)th order kinetics may no longer be valid. These conditions must be investigated with the use of a fast reversible reaction system to be able to take the interfacial depletion into account.

If absorption experiments are carried out on a device with a known interfacial area, the effective area model based on fast reversible reaction kinetics will show what percentage of the interfacial area is actually effective for the purpose of mass transfer. With surface renewal rates varying with hydrodynamic conditions and the type of separation column internal used, situations may arise where the effective area is larger than the interfacial area. Under conditions where surface depletion rates are higher than surface renewal rates, the effective area will be less than the interfacial area.

The boundary conditions are determined through common sense intuition of the conditions at the various boundaries in **Figure 2.2**. The liquid phase is assumed to be free of gas component, *A*, initially. The initial and boundary conditions are similar to equations 2.19 - 2.21, but may be expressed in a more general form as follows:

$$@\, x \geq 0,\ t = 0\ :\ \left\{ \begin{matrix} C_A = C_{A,0} = 0 \\ C_j = C_{j,0} \end{matrix} \right\}\ j \in \{B, C, D, E\} \qquad 2.41$$

$$@\, x = 0,\ \mathrm{t} > 0\ :\ \left\{ \begin{matrix} C_A = C_{A,i} = \dfrac{P_{A,i}}{H_A} \\ \dfrac{\partial C_j}{\partial x} = 0 \end{matrix} \right\}\ j \in \{B, C, D, E\} \qquad 2.42$$

$$@\, x \to \infty,\ t > 0\ :\ \left\{ \begin{matrix} C_B = C_{B,L} \\ C_j = C_{j,L} \end{matrix} \right\}\ j \in \{A, C, D, E\} \qquad 2.43$$

with equation 2.22 still relevant:

$$\frac{n_A}{a_e} = -D_{A,L} \left(\frac{\partial C_A}{\partial x} \right)_{x=0} \qquad 2.22$$

Another time domain boundary condition that may be used, if it is assumed to be valid, is based on the gas-liquid contact time achieved by the experimental device. For the fast reaction regime, it is preferable that the contact time is at least of the same order of magnitude as the reaction time, preferably longer. This will ensure that the reaction reaches its state of equilibrium within the contact time which gives rise to the following boundary condition:

$$@\, x \to \infty,\ t = t_c\ :\ C_q = C_{q,\,\mathrm{equilibrium}}\quad q \in \{A, B, C, D, E\} \qquad 2.44$$

For the surface renewal theory, boundary condition 2.44 will be subject to the probability of each liquid element spending equal times at the surface. The absorption rate must therefore be weighted with an age distribution function, $p(t)$ (Brinkmann, et al., 1998):

$$(N_A)_x = \frac{n_A}{a_e} = \int_0^\infty \left[-D_{A,L} \left(\frac{dC_A}{dx} \right)_{x=0} \right] \cdot p(t)\, dt \qquad 2.45$$

with the age distribution function derived from surface renewal theory, assuming complete mixing in both liquid and gas phases (similar to an ideal CSTR), to be(Brinkmann, et al., 1998):

$$p(t) = \frac{1}{\tau} e^{-t/\tau} \qquad 2.46$$

with τ representing the mean residence time of each liquid element at the surface. If τ is the mean residence time, then $1/\tau$ is the fractional rate of surface renewal, s (Danckwerts, et al., 1963), which results in the surface renewal theory age distribution function:

$$p(t) = s \cdot e^{-st} \qquad 2.47$$

Estimation of the value of the fractional rate of surface renewal is a difficult prospect (Danckwerts, et al., 1963; Charpentier, 1981) compared to the assumption of Higbie that each liquid element spends equal time at the surface. Attempts at correlating the surface renewal rate as a function of liquid turbulence have been made (see equation 2.12). If perfect mixing is assumed and equation 2.45 is valid, the mean residence time may be estimated in accordance with the contact time achieved on the experimental absorption set-up. If the contact time is in the order of 1 - 3 seconds, the mean residence time may be in the order of 0.01 - 0.5 seconds (Brinkmann, et al., 1998).

According to Dankwerts, the choice in model comes down to a matter of convenience and the most convenient choice is the Higbie assumption regarding the age distribution function:

$$\begin{aligned} p(t) &= \frac{1}{\theta}, \quad 0 < t < \theta \\ p(t) &= 0, \quad t > 0 \end{aligned} \qquad 2.48$$

In many cases, it is assumed that the reaction is fast enough for all species to be at their equilibrium concentrations for any $t > 0$ (Astarita, 1967). Since reactive absorption data is preferably recorded under steady state conditions, an average absorption rate based on equal exposure times should provide for a valid first approximation. The mean residence time may be estimated to be nearly equal to the exposure time and the age distribution function calculated accordingly.

Enhancement factors for reversible reactions have been derived by previous researchers (DeCoursey, 1982; Van Swaaij & Versteeg, 1992; Vas Bhat, et al., 2000; Meldon, et al., 2007) to try and find approximate analytical solutions to various limiting conditions. DeCoursey derived enhancement factors for a reversible reaction system with unit stoichiometric coefficients and equal diffusivities taking the following form (DeCoursey, 1982):

$$M + N \underset{k_2}{\overset{k_2}{\rightleftharpoons}} P + W \qquad 2.49$$

His strategy involved the use of "s-multiplied" Laplace transforms of the system of differential equations represented by 2.40. He further assumed a second order rate expression of the following form:

$$r_A = k_2 \left(C_M C_N - \frac{C_P C_W}{K} \right) \qquad 2.50$$

with K representing the equilibrium constant of equation 2.49:

$$K = \frac{C_P C_W}{C_M C_N} \qquad 2.51$$

The equilibrium constant was used by other researchers as well (Vas Bhat, et al., 2000; Aboudheir, et al., 2003) in order to make predictions of the absorption rates at different reagent and product concentrations. In their studies, the equilibrium constant was used to calculate the equilibrium concentrations of the product species that could not be analysed for. They therefore applied the assumption that the reaction time in the liquid film is short enough to assume fast reaction equilibrium to be obtained. The equilibrium constant further enabled the calculation of enhancement factors for a range of reagent and product concentration ratios. In order to be able to use the equilibrium constant accurately in modelling reactive absorption systems, the reaction time and gas-liquid contact time must be known. If the reaction is not fast enough to reach equilibrium during the time of exposure, then the use of the equilibrium constant may result in inaccurate predictions. The researchers that employed the equilibrium constant assumed the reaction to reach equilibrium within the absorption time, since this method was only applied to fast reaction regimes.

Due to the complexity of the mathematical solutions and restricted application range, the use of an enhancement factor for modelling the reversible reaction of this study will not be explored. Numerical techniques for solving partial differential equations given well estimated initial and boundary conditions provides model solutions that are applicable over a wide range of conditions and are therefore fundamentally consistent (Brinkmann, et al., 1998). This will form the basis of the method proposed for determining effective interfacial mass transfer area under conditions where surface depletion and surface renewal of the active agent in the liquid phase becomes significant. For this method to be applied, the liquid phase reaction kinetics must be known, which is why a homogeneous liquid phase reaction kinetic study was undertaken in this body of research.

The liquid phase reaction kinetics of CO_2 with MEA in alcoholic solvents will be investigated in Chapter 3 and Chapter 4 of this study. Based on the results of this study, the most appropriate reaction rate expression governing the reaction in the fast reaction regime will be determined. The reaction rate expression will reveal whether the reaction may be considered to be an irreversible or reversible reaction system, which will influence the way in which it is incorporated into a method for determining effective interfacial mass transfer area under conditions where surface depletion and renewal rates are significant.

Reactive absorption experiments using a wetted wall experimental set-up will be conducted and the most applicable theory presented in this chapter will be used to interpret the reactive absorption results. The implementation of the best representative rate expression into either penetration or surface renewal theory will form the basis of the method for calculating effective interfacial mass transfer area from reactive absorption data.

Chapter 3 REACTION KINETICS: THEORY AND METHOD DEVELOPMENT

Chapter 2 revealed the existing theory used to attempt to understand and describe both physical and reactive absorption. It was discovered that reactive absorption under the fast reaction regime provides the necessary conditions for mass transfer to occur independent of the physical liquid phase mass transfer coefficient, k_L. This theory then becomes the basis for measuring both the interfacial area and effective interfacial area for mass transfer directly from the rate of absorption of some reacting gas. The reactive absorption of CO_2 with primary amines, in both aqueous and non-aqueous solvents is an example of suitable systems for measuring effective area via the chemical method (Sridharan & Sharma, 1976).

This chapter will briefly re-introduce the existing theory of the reaction of CO_2 with primary amines and will then focus on the reaction kinetic theory in non-aqueous solvents. A discussion of the most suitable reaction mechanism in non-aqueous solvents will be followed by an in-depth investigation into the selection criteria of the most appropriate primary amine and type of organic solvent to use. Once the selection of both amine and solvent is complete, the novel development of an *in-situ* Fourier Transform Infra-Red (FTIR) method used for determining the homogeneous liquid phase reaction kinetics will be discussed in detail.

3.1 The Reaction of CO_2 with Amines

Under certain conditions, the absorption of CO_2 into solutions of amines is accompanied by a fast reaction in the liquid film (Astarita, 1967; Danckwerts, 1970; Sada, et al., 1986). If gas phase mass transfer resistance is negligible, the absorption rate is controlled by the reaction in the liquid film (Astarita, 1967; Sridharan & Sharma, 1976; Tsai, 2010). This reactive system was identified as one of the feasible systems to investigate in order to calculate effective area from the absorption rate of CO_2. As discussed in Chapter 1, the reactive absorption of CO_2 into both

aqueous and non-aqueous solutions of amines has further industrial significance, since it is currently one of the more mature technologies available for implementation in the sequestration process of this acid gas (Kritzinger, 2013). The reaction kinetics of this system has, therefore, been one of the major research topics of the last 6 decades.

3.1.1 Proposed Reaction Mechanism for Primary Amines in Non-aqueous Solvents

Currently, there exists some debate over the exact reaction mechanism governing the reaction of CO_2 with amines. There are mainly two mechanisms considered, the zwitterion mechanism and the termolecular mechanism. The zwitterion mechanism (Caplow, 1968) first introduced by Caplow and later confirmed by Danckwerts and others to describe the reaction most accurately (Versteeg & van Swaaij, 1988; Littel, et al., 1992(a)) will be discussed first. It involves the formation of a reactive intermediate from the reaction of CO_2 with an amine as illustrated in **Figure 3.1**. The neucleophilic nitrogen atom of the amine attacks the delta positively charged carbon atom of CO_2 causing the oxygen atom to shift one of its double bonded electrons into a vacant valence orbital (McMurry, 2004). The nitrogen atom attaches to the carbon atom and gains a positive charge, which is balanced by the induced negative charge of the oxygen atom, resulting in molecular neutrality. **Figure 3.1** depicts the reaction of CO_2 with the primary amine, mono-ethanolamine.

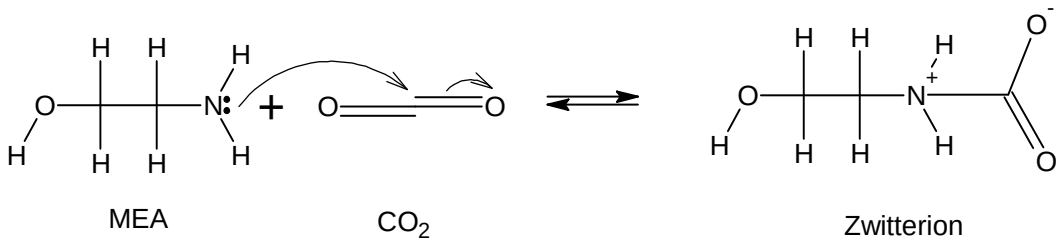

Figure 3.1 Formation of the Zwitterion Reactive Intermediate in the Reaction of a Primary Amine (Mono-ethanolamine) with CO_2

The zwitterion is, however, considered to be unstable and either decomposes back to its original reagent species or is readily deprotonated by a nearby base. Due to the two available electrons on its nitrogen atom, both primary and secondary amines have the potential to act as

a classic Brønsted-Lawry base (McMurry, 2004). This is best illustrated in **Figure 3.2**. This means that, even if there are no stronger bases present, the amine itself can act as the deprotonating base.

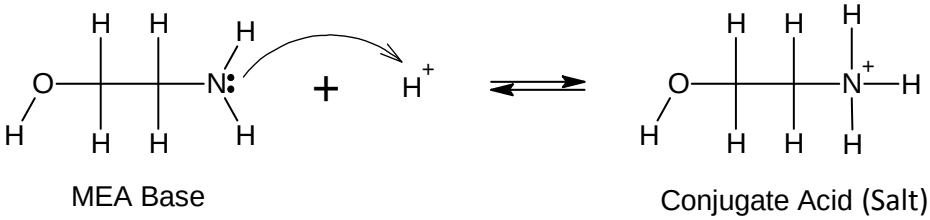

Figure 3.2 A Primary Amine (MEA) Acting as a Brønsted-Lawry base

It was the deprotonation reaction that sparked great interest in deriving the most representative rate expressions for this reaction. It is now known that the choice of solvent greatly influences the rate expression, since the chosen solvent may also take part in the deprotonation step of the reaction mechanism (Versteeg & van Swaaij, 1988). The general form of the zwitterion mechanism may thus be considered to be:

$$1)\ CO_2 + R'R''NH \underset{k_2}{\overset{k_1}{\rightleftharpoons}} R'R''NH^+COO^-$$
$$2)\ R'R''NH^+COO^- + B \underset{k_4}{\overset{k_3}{\rightleftharpoons}} R'R''NCOO^- + BH^+ \qquad 3.1$$

where *R* represents various functional groups attached to the nitrogen atom of the amine and *B* denotes any base that may deprotonate the zwitterion. The molecular structure of *B* now also influences the structure of one of the ionic salt products of reaction 2 in equation 3.1.

One of the greatest challenges in deriving the reaction kinetic rate expression for aqueous solvent systems was to consider the reactivity of the hydroxide ions of water with the zwitterion reactive intermediate. Many authors have resorted to lumping the effect of all the bases present into a single term in the derived rate expression (Danckwerts, 1979; Versteeg & van Swaaij, 1988; Littel, et al., 1992(a)). This has great impact on certain amine systems where the deprotonation reaction has a significant influence on the overall reaction rate (Littel, et al., 1992(a)). Further discussion of the multi-base effect on the deprotonation reaction is

considered to fall outside the scope of this study, since only non-aqueous solvent systems are investigated.

In the non-aqueous systems where only the amine is considered to be responsible for deprotonating the zwitterion reactive intermediate (Davis & Sandall, 1993), the degree of deprotonation is reduced (Sada, et al., 1985). This simplifies equation 3.1 to give

$$\begin{aligned} &1)\ CO_2 + R'R''NH \underset{k_2}{\overset{k_1}{\rightleftharpoons}} R'R''NH^+COO^- \\ &2)\ R'R''NH^+COO^- + R'R''NH \underset{k_4}{\overset{k_3}{\rightleftharpoons}} R'R''NCOO^- + R'R''NH_2^+ \end{aligned} \qquad 3.2$$

It may be noticed that if there is a stronger base than the amine in the liquid phase, the reaction order with respect to the amine remains close to unity. If, however, the amine is responsible for most to all of the deprotonation of the zwitterion, the order of reaction with respect to the amine shifts to within the region of 1 – 2 (Sada, et al., 1986). The presence of a stronger base in aqueous solvents, along with the fact that the zwitterion is more stable in aqueous solvents (Littel, et al., 1992(a)) leads to a higher overall reaction rate noticed for aqueous solvents (Davis & Sandall, 1993). Nevertheless, the reaction rate in alcoholic solvents is still considered to fall in the fast reaction category, since the criteria presented for this regime to apply (see section 2.2.1), can easily be obtained. Alcoholic solvents are therefore suitable for effective area determination (Sridharan & Sharma, 1976).

If equation 3.2 is further simplified to the case of CO_2 reacting with a primary amine in an inert non-aqueous solvent system (such as an alcoholic solvent system), the mechanism may be given by (Sada, et al., 1985)

$$\begin{aligned} &1)\ CO_2 + RNH_2 \underset{k_2}{\overset{k_1}{\rightleftharpoons}} RNH_2^+COO^- \\ &2)\ RNH_2^+COO^- + RNH_2 \underset{k_4}{\overset{k_3}{\rightleftharpoons}} RNHCOO^- + RNH_3^+ \end{aligned} \qquad 3.3$$

Equation 3.3 will form the basis for deriving the rate expressions investigated in this study, which will ultimately form the foundation of the newly derived effective interfacial mass transfer area theory.

The second proposed reaction mechanism, only to be briefly discussed here, is known as the termolecular mechanism, originally introduced by Crooks and Donnelan (Crooks & Donnellan, 1989). It postulates that the reaction occurs in one step, where the amine reacts both with CO_2 and a nearby base simultaneously to produce the ionic salt products. The termolecular mechanism results in a greatly simplified rate expression, since consecutive reaction steps are eliminated. In aqueous solvent systems, under conditions where the deprotonation rate of the zwitterion intermediate may be considered to be instantaneous, the termolecular mechanism is a good approximation (Aboudheir, et al., 2003). The termolecular mechanism is, most likely, fundamentally incorrect as 3rd or higher order elementary reactions are extremely unlikely to occur (Fogler, 1999).

The termolecular mechanism has been implemented in the rate based model of Aboudheir (Aboudheir, et al., 2003) to describe the absorption kinetics of CO_2 into loaded solutions of relatively concentrated MEA/water systems. It must be mentioned that Aboudheir et al. investigated both the zwitterion and termolecular reaction mechanisms, but could only achieve model convergence using the termolecular mechanism as basis for deriving the rate expressions. Whenever there is a reduction in the zwitterion deprotonation rate, the termolecular mechanism does not account for all the observed reaction kinetics (Littel, et al., 1992(b)). Since this was the case for non-aqueous solvent systems (Sada, et al., 1985) the termolecular mechanism was rejected for the purpose of this investigation. The validity of this rejection is discussed after modelling of the reaction kinetic data in Chapter 4 of this study.

3.1.2 Existing Rate Expressions for the CO_2/Amine Reaction in Non-Aqueous Solvents

The zwitterion reaction mechanism (equations 3.2 and 3.3) is considered to be the mechanism that best describes the reaction of CO_2 with amines in non-aqueous solvent systems (Sada, et al., 1985; Versteeg & van Swaaij, 1988; Davis & Sandall, 1993). The reason previous researchers used for not considering the termolecular mechanism for non-aqueous solvents is because the deprotonation rate of the zwitterion is slower in inert solvents compared to aqueous solvents (Davis & Sandall, 1993). For this reason a non-elementary rate expression is considered to be best for describing the liquid phase reaction kinetics in inert non-aqueous solvents. This rate

expression was derived from the pseudo steady state hypothesis (PSSH) applied to the zwitterion and it reads (refer to Appendix E.1 for derivation):

$$-r_{CO_2} = \frac{k'''[CO_2][RNH_2]^2 - k_4\left[RNH_3^+\right]^2}{1 + k''[RNH_2]} \qquad 3.4$$

for the primary amine, MEA, where $k'' = \frac{k_3}{k_2}$ and $k''' = k_1 k''$.

The reason for applying the PSSH is twofold:

1. The overall reaction is considered to fall in the fast reaction category, thus reaction equilibrium is achieved quickly. The deprotonation rate of the zwitterion is further considered to still be fast enough for its nett reaction rate at equilibrium, as a reactive intermediate, to be effectively zero. This is the basis of the pseudo steady state hypothesis (Fogler, 1999).
2. The reaction kinetics of CO_2 with amines was predominantly determined from heterogeneous absorption experiments. These experiments had an inherent limitation in the amount of measurable information. Mostly, only the absorption rate of CO_2 into a liquid of assumed known interfacial area containing a known amount of amine was measured.

This lack of information forced previous researchers to make more simplifying assumptions. Since it was impossible to analyse for the ionic salt product in the reaction (2) of equations 3.2 and 3.3, they assumed the reaction to be irreversible. This assumption simplifies equation 3.4 to:

$$-r_{CO_2} = \frac{[CO_2][RNH_2]}{\frac{1}{k_1} + \frac{1}{k_1 k''[RNH_2]}} = \frac{k_1 k''[CO_2][RNH_2]^2}{1 + k''[RNH_2]} \qquad 3.5$$

The absorption experiments were further, mostly carried out under conditions where irreversible, pseudo mth order kinetics was assumed (see section 2.2.1). If the absorption

experiments were carried out using a device with a known interfacial area, such as a wetted wall column or a stirred tank absorber, then the apparent reaction rate constants may be determined indirectly from the rate of absorption (Sada, et al., 1986):

$$C_{B,0}\left(\frac{C_{A,i}D_{A,L}^{0.5}}{N_A}\right)=\frac{1}{k_1}+\frac{1}{k_1k''}\cdot\frac{1}{C_{B,0}} \qquad 3.6$$

where $C_{A,i}$ is the concentration of CO_2 at the gas-liquid interface and is calculated from solubility data as in equation2.20. $C_{B,0}$ is the concentration of the amine in the liquid phase and remains constant under pseudo mth order conditions. N_A is the absorption rate of CO_2 per unit interfacial area and a plot of $C_{B,0}\left(C_{A,i}D_{A,L}^{0.5}/N_A\right)$ vs. $C_{B,0}^{-1}$ will yield a straight line at high enough amine concentrations for pseudo mth order conditions to be considered valid. The rate constants were derived from the intercept and the slope of the straight line.

Another popular rate expression for the reaction of CO_2 with amines in non-aqueous solvents is the power rate law expression. This expression once again assumes the second reaction in the mechanism to be irreversible, therefore, referring to equation 3.5 there are two possibilities for which the power rate law is assumed to be applicable (Alvarez-Fuster, et al., 1981):

1. Overall second order kinetics are assumed to occur when $k''[RNH_2]<<1$. The rate expression for CO_2 with MEA is given as:

$$-r_{CO_2}=k_1[CO_2][RNH_2] \qquad 3.7$$

2. Overall third order kinetics are assumed if $k''[RNH_2]>>1$. Under these circumstances the rate expression is given as:

$$-r_{CO_2}=k_1[CO_2][RNH_2]^2 \qquad 3.8$$

Case 1 is applicable when the zwitterion deprotonation rate is fast enough to be approximated as instantaneous. This case arises in solvent systems where there are stronger bases present than the amine only and all bases present take part in the deprotonation reaction of the

zwitterion. The most common example of such a system is an aqueous system. Case 2 arises when only a weak base is present and the zwitterion deprotonation rate is slowed down appreciably. In alcoholic solvent systems, the amine alone is responsible for the deprotonation and thus its reaction order increases from 1 – 2 (Sada, et al., 1985).

The PSSH and power rate law rate expressions serve as good approximations under conditions where there is insignificant depletion of amine at the gas-liquid interface. There is, however, a fundamental flaw in the assumption of an irreversible reaction. This flaw is illustrated in the fact that solvent regeneration is possible by driving off the loaded CO_2 from amine solvents under elevated temperatures (Astarita, 1967; Erasmus, 2004; Kritzinger, 2013). The reaction of CO_2 with amines is, therefore, fundamentally reversible and thus an irreversible reaction rate expression will only be valid under limiting conditions. One of the aims of this study is to use the fast reaction of CO_2 with MEA under conditions where interfacial depletion is appreciable, in order to propose a method for calculating effective interfacial mass transfer area taking surface depletion and renewal rates into consideration. This will be a more representative effective area calculation and will require the derivation of a fundamentally correct reaction rate expression, since the assumption of pseudo m^{th} order reaction kinetics will no longer be valid.

3.2 Amine and Solvent Selection Criteria

In deciding on the most appropriate amine and solvent to investigate in this study, various selection criteria were considered. The selection was done in tandem, since some of the criteria created overlap between the properties of both the amine and the solvent. The first criteria considered, was the reactivity of the amine.

It is well known that under the appropriate circumstances, CO_2 reacts with an amine under the fast reaction regime. The rate of reaction is to a certain degree dependent on the degree of steric hindrance associated with the complexity of the amine molecule. For example, one would expect a primary amine to be more reactive than a secondary amine, because the nitrogen atom on a primary amine has less steric hindrance than the equivalent atom on a

secondary amine (McMurry, 2004). Since there is no reaction between CO_2 and tertiary amines in non-aqueous solvents (Versteeg & van Swaaij, 1988(b)) the choice was made to use a primary amine in this study.

The type of amines that are most widely used in industry are alcohol amines (Alvarez-Fuster, et al., 1981; Aboudheir, et al., 2003). The simplest primary alcohol amine is known as mono-ethanolamine (MEA). Both aqueous and non-aqueous solutions of MEA have been used to derive interfacial area correlations under the pseudo-first order assumption (see section 5.2.4) (Sridharan & Sharma, 1976; Erasmus, 2004). Before the choice of MEA can be finalized, the criteria for solvent selection have to be considered.

It has been suggested that organic solvents are considered for the use in amine based CO_2 sequestration methods for various advantageous reasons (Sada, et al., 1985). This has sparked the investigation of the reactive absorption kinetics of CO_2 with amines in non-aqueous solvents. For the purpose of effective area determination, the liquid phase should adhere to certain physical properties. The first of which is that the solvent should have a low vapour pressure at the experimental conditions in order to minimize solvent loss due to evaporation. Evaporative solvent loss would result in unknown reagent and product concentrations in the liquid phase, influencing the reaction kinetics in an indeterminate manner. This would cause the collapse of the theory derived to calculate effective area, since it relies on the reaction kinetics to be well known. The second, equally important criterion is to make sure that both MEA and CO_2 are readily soluble in the solvent.

Based on the above mentioned criteria and existing literature data (Alvarez-Fuster, et al., 1981; Sada, et al., 1986), it was decided that C_3 alcohols are suitable solvents for investigation in this study. n-Propanol was chosen as representative alcoholic solvent, since specific absorption data for CO_2 into solutions of MEA/n-Propanol exists from a previous study (Erasmus, 2004) and since it further adheres to a secondary criteria, which will influence the applicability of the method to be used on a larger scale, namely cost and hazardous properties. All alcohol amines are toxic and corrosive, but experiments can be designed to minimize the amine concentration, thereby controlling the hazards associated with corrosiveness. Both C_3 alcohols are flammable,

but this hazard can be overcome by correct experimental and separation column equipment design as well as working under an inert atmosphere. The solvents are also relatively inexpensive. Furthermore, if one considers the fact that the loaded solvents can be regenerated (due to the reversibility of the CO_2/MEA reaction) at lower energy consumption than its equivalent aqueous solvent systems (Sada, et al., 1985), the economic impact becomes even less of a concern.

Another advantage of organic solvents over water is their lower surface tension resulting in improved liquid distribution across the packing material inside the separation column. Improved liquid distribution leads to an increase in interfacial area which will cause an increase in effective interfacial area as well. Liquid properties such as density, viscosity and surface tension have an influence on effective interfacial mass transfer area (Tsai, et al., 2008). The viscosity and density of alcoholic solvents may be altered by using mixtures of alcohols. This was not investigated in this study, since the focus of this study was mainly on method development. Altering the physical properties of the alcoholic solvent used in this study to determine its effect on the effective mass transfer achieved will be investigated in future research.

3.3 Introduction to an In-situ FTIR Method of Analysis

In order to be able to confirm or reject the zwitterion reaction mechanism for the reaction of CO_2 with the primary amine, MEA in an alcoholic solvent system (equation 3.3) a method of analysis must be designed to study the reaction homogeneously in the liquid phase. This will have the great advantage of eliminating gas phase mass transfer resistance from the process and will allow the study of the reaction across all fast reaction regimes and will not only be limited to the pseudo-first order regime, as all current heterogeneous studies are (see section 3.1.2).

From a pure reaction kinetics point of view, it is further advantageous to study the reaction in real time and to collect data in short time intervals, with the measurement having no influence on the kinetics itself. This conclusions was made from previous investigations attempting to

derive the homogeneous liquid phase reaction kinetics of CO_2 with MEA in 2-Propanol (Du Preez, et al., 2009). These previous studies were conducted in a continuous stirred tank reactor (CSTR) set-up and relied on stopping the reaction after short residence times by scavenging the unreacted MEA with an excess of benzoyl chloride. One of the limitations of this approach was that the data can only be presented in terms of residence time and not continuous time. Another disadvantage was that the effect of intruding on the reaction kinetics by using a scavenging agent was unknown. A continuous time, rapid data collecting, non-intrusive method was thus considered to overcome these limitations.

Fourier Transform Infra Red (FTIR) is a feasible method for monitoring the progress of a chemical reaction *in-situ* (Carter, et al., 2010; Parikh, et al., 2008). It uses the amount of absorbed or transmitted infrared energy as the basis for its analytical capability, which means that the analysis is fast (Parikh, et al., 2008) , down to nanosecond scale if required (Johnson, et al., 1993), non intrusive, sensitive and has a high degree of repeatability (Sherman Hsu, 1997) under optimum operating conditions.

3.3.1 Brief Description of FTIR Spectroscopy (Sherman Hsu, 1997)

FTIR is one of the most common spectral techniques used by organic chemists to perform species identification studies. In most basic terms, Infra-red spectroscopy relies on the absorption of infra-red energy by the various organic functional groups of molecules in a sample placed in the path of an infra-red beam. Different functional groups absorb energy at different frequencies, which allows for the identification of a number of different functional groups in one sample.

In order to be able to understand how a spectral image is generated, a basic understanding of how a FTIR spectrometer works is required (Sherman Hsu, 1997). A simplified schematic of the layout of a typical FTIR is shown in **Figure 3.3**. The spectrometer consists of an infrared source, a beam splitter, two mirrors situated perpendicular to each other, of which one is stationary and the other moving and, finally, a detector. IR energy from the source (in a certain spectral frequency range) is directed to the potassium bromide (KBr) coated beam splitter, which splits

the IR beam and directs one part of the IR beam to the fixed mirror and the other to the moving mirror. The mirrors then reflect the beam back to the beam splitter, where they are combined and directed through the sample to the detector.

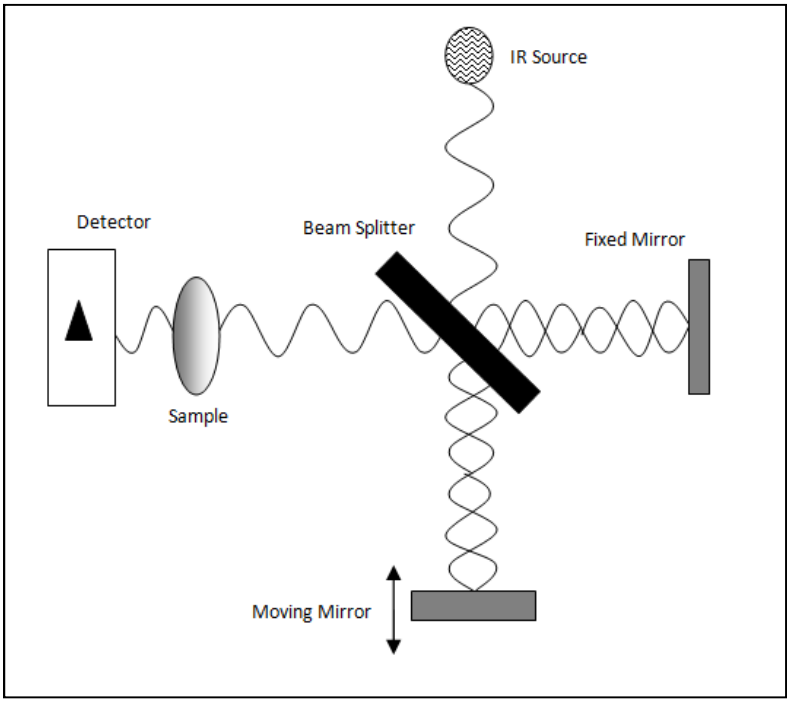

Figure 3.3 Simplified Schematic of a Typical FTIR Spectrometer

By moving one mirror relative to the other, an interference pattern (known as an interferogram) in the combined IR beam is created due to the different optical path lengths followed by each of the IR beams. The interference is both of a constructive and destructive nature and, since the source produces a broad band of sine waves at different frequencies, the interferogram contains information of all the frequencies in the spectral region investigated.

As the beam then passes through the sample, some of the energy at some of the frequencies is absorbed. When the time domain interferogram signal is Fourier transformed to the frequency domain, a spectral image of the amount of IR energy absorbed in each frequency is obtained. The amount of energy absorbed is always measured relative to a reference (or background) spectrum and is displayed as peaks in an FTIR spectrum. The peaks are always presented as

either absorption or transmittance as a function of wavenumber (cm^{-1}). Wavenumber is just the number of waves per unit length and is proportional to frequency as well as the IR energy of that frequency.

3.3.2 IR Energy Absorption vs. Species Concentration

The definition of the temperature of a certain substance is associated with the average kinetic energy of all the molecules of that substance (Aruldhas, 2007). This means that at temperatures above absolute zero, all molecules are vibrating and moving. Different functional groups vibrate at different frequencies (Bellamy, 1976). If IR energy is directed to a certain molecule, the functional groups of that molecule will absorb the IR energy of equal frequency to their vibration frequencies. Since different types of vibrations (bending, scissoring, stretching etc.) are possible due to molecular structure, the same functional group can absorb IR energy at various different frequencies or wavenumbers (Sherman Hsu, 1997).

It now seems logical that the amount of IR energy absorbed by a certain functional group in a sample is proportional to the concentration of that functional group in the sample. This proportionality is best described by Beer's Law (Grffiths, 2002). At low concentrations of functional groups, Beer's Law is approximated as a linear relationship between IR energy absorption and the concentration of the functional group. At higher concentrations, chemical deviations may occur due to a higher degree of molecular interaction (intermolecular attractive and repulsive forces cause the mixture to deviate from ideal behaviour).

In order to obtain the correct proportionality of IR energy absorbed vs. concentration, a series of calibration experiments of the species of interest should be done. The calibration procedure is for the most part relatively simple and is discussed in detail in section 3.5.

3.3.3 Feasibility of FTIR for CO_2/MEA systems

As mentioned in section 3.3.1, various different organic functional groups absorb IR energy at various different wavenumbers. In order to be able to use FTIR to study the reaction of CO_2 with MEA in alcoholic solvents, the absorption wavenumbers of the various components in the

reaction mixture must first be obtained. A literature review on the absorption wavenumbers of the functional groups in equation 3.3 is tabulated in **Table 3.1**.

Table 3.1 IR Absorption Wave Numbers for Reagents and Products in Equation 3.3 (Silverstein & Bassler, 1967; Bellamy, 1976; Aruldhas, 2007; Jackson, et al., 2009; Derks, et al., 2011; Richner & Puxty, 2012)

Functional Group	Wave Number Absorbing (cm^{-1})	Band Type and Strength*
CO_2	2300 – 2400	(s)
$-NH_3^+$	3380 and 3280	Stretching Bands (s)
	3100 – 2600	
	1550 – 1485	Symmetrical Bend (s)
	1660 – 1610	Asymmetrical Bend (w)
$-COO^-$	1610 – 1550	Asymmetrical Stretch (s)
	1420 – 1300	Symmetrical Stretch (w)
$-NH_2$	3500	Free Asymmetrical Stretch (s)
	3400-3300	Free Symmetrical Stretch (s)
	1650 – 1580	Scissoring (m)
	960 – 666	Wagging (m)
$-OH$	3550 – 3650	Stretch (b,s)
	3400 – 3300	

*(s) = strong; (m) = medium; (w) = weak; (b) = broad

From **Table 3.1** it may be noticed that the wagging band of MEA at 960 - 666 cm^{-1} and the symmetrical bending band of RNH_3^+ at 1550 – 1485 cm^{-1} may be used to study the species concentration, since it would appear that there are no spectral overlaps for those regions. A speciation study in aqueous solvent systems revealed the wagging band of MEA to behave in accordance with the proposed reaction mechanism (equation 3.1) and even showed that MEA and CO_2 reacts in a 2:1 stoichiometric ratio (Richner & Puxty, 2012). The same study confirmed that the salt product of equation 3.3, RNH_3^+, absorbs IR energy in the region of 1550 - 1485 cm^{-1}.

CO_2 is well known to be strongly IR active and absorbs IR energy in a band far removed from the other components of interest. Mapping the CO_2 concentration during the reaction progress is therefore easily accomplished under optimal purge conditions. Confirmation and validation of the FTIR method of analysis is presented in section 3.5.6. With the feasibility of the FTIR method in place, an experimental set-up to study the reaction of CO_2 with MEA in alcoholic solvents must be designed, built and commissioned.

3.4 Experimental Method Development

One of the main aims of this study was to develop a method for monitoring the reaction of CO_2 with the primary amine, MEA in non-aqueous, alcoholic, solvent systems. FTIR has been shown to be a feasible analytical option for collecting real time data in the liquid phase as the concentration of the reagent and product species in equation 3.3 change with reaction time.

3.4.1 ATR combined with FTIR

Referring to **Table 3.1**, it is noticeable that the spectral region of interest lies within the mid-IR wavenumber range (4000 – 200 cm^{-1}) (Sherman Hsu, 1997). The spectral data for this study were collected using a Nicolet 6700 mid-IR spectrometer supplied by Thermofisher Scientific® (Refer to Appendix D for specifications). The spectral data used in this study was collected with the use of the complimentary IR technology, attenuated total reflectance (ATR).

ATR has previously been used to collect real time data during the progress of a reaction (Sherman Hsu, 1997; Krishnan & Flanagan, 2000; Parikh, et al., 2008). It has previously been used to determine the liquid phase speciation of an equilibrium mixture of CO_2/amine/water (Derks, et al., 2011). It had not, however, previously been used to monitor the liquid phase reaction kinetics of CO_2 with a primary amine. The mechanism of ATR used in combination with an FTIR spectrometer is illustrated in **Figure 3.4**.

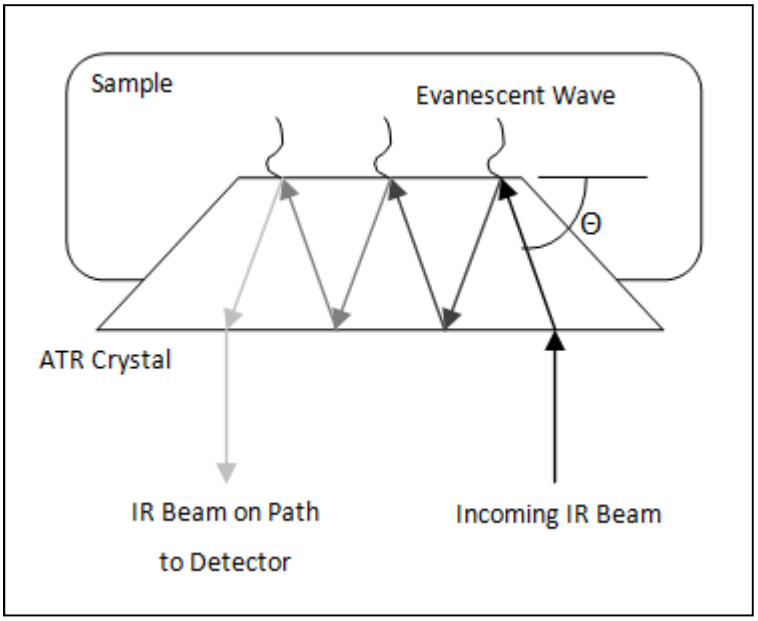

Figure 3.4 Schematic Illustrating ATR Technology

ATR occurs when the incident angle (θ) of a beam of light exceeds the critical angle of incidence for the medium it is travelling through. At incidence angles exceeding θ, most of the beam is reflected with only a small percentage travelling a short distance (µm scale) into the less dense medium. The fraction of the beam entering the less dense medium is known as the evanescent wave. ATR can be coupled with FTIR as shown in **Figure 3.4**. The IR beam now, instead of passing through a sample, comes into contact with the sample molecules through the evanescent wave emitted by the ATR crystal. The intensity of the IR beam is affected by the absorption of IR energy by the sample molecules from the evanescent wave and the change in IR intensity is once again detected by a suitable detector.

There are various types of ATR elements or crystals available, each with physical properties (pH tolerance, detection windows, resistance to corrosion etc.) making them suitable for a variety of applications. The ATR element used in this study was a Zinc Selenide (ZnSe) crystal manufactured to achieve 2 internal reflections of the IR beam. ZnSe was identified as the best suited crystal material based on its physical properties and cost. Physical properties such as crystal hardness, refractive index, evanescent wave penetration depth and chemical reactivity with the sample, were considered. According to the physical properties provided by one of the

suppliers of ATR elements, PIKE® (PIKE, 2013), ZnSe has a crystal hardness of 120 (which is low, meaning the crystal can break easily) a refractive index of 2.4 (ideal for organic solutions), a penetration depth of 2 µm and a pH range of operation of 5 – 9. ZnSe is thus unsuited for use in acidic solutions, but since the solutions used in this study are all weakly basic (McMurry, 2004), ZnSe was determined to be suitable. Another crystal material worth considering was germanium (Ge). Although it is more chemically inert, it is more expensive than ZnSe, with a shorter evanescent wave penetration depth.

The crystal was allowed to come into contact with the reagent mixture inside the reactor by fitting it to the tip of a probe. The probe used was a DPR-207 probe supplied by Axiom Analytical®. A schematic of the probe is illustrated in **Figure 3.5**. The probe utilises gold plated light guides to minimise IR beam energy loss as it is directed from the beam splitter via a series of KBr plated mirrors to the ZnSe crystal in the probe tip and back via the same mirrors to the detector.

ATR is unfortunately notorious for its low IR energy efficiency, meaning a significant amount of energy is absorbed in the crystal itself, which then never reaches the detector. It is therefore of utmost importance that the most sensitive detector be used in combination with ATR, especially if low concentration mixtures are analysed. During the course of the method development, various detectors were tested for feasibility. The detector that gave the most satisfactory results was found to be a liquid nitrogen cooled, high definition, Mercury Cadmium Telluride (MCT-D*) detector also supplied by Thermofisher Scientific®.

In order to be able to achieve the most sensitive measurements possible with an ATR system coupled with a MCT-D* detector, various other factors must also be considered. These factors along with the sensitivity in detection are discussed in section 3.8.2.

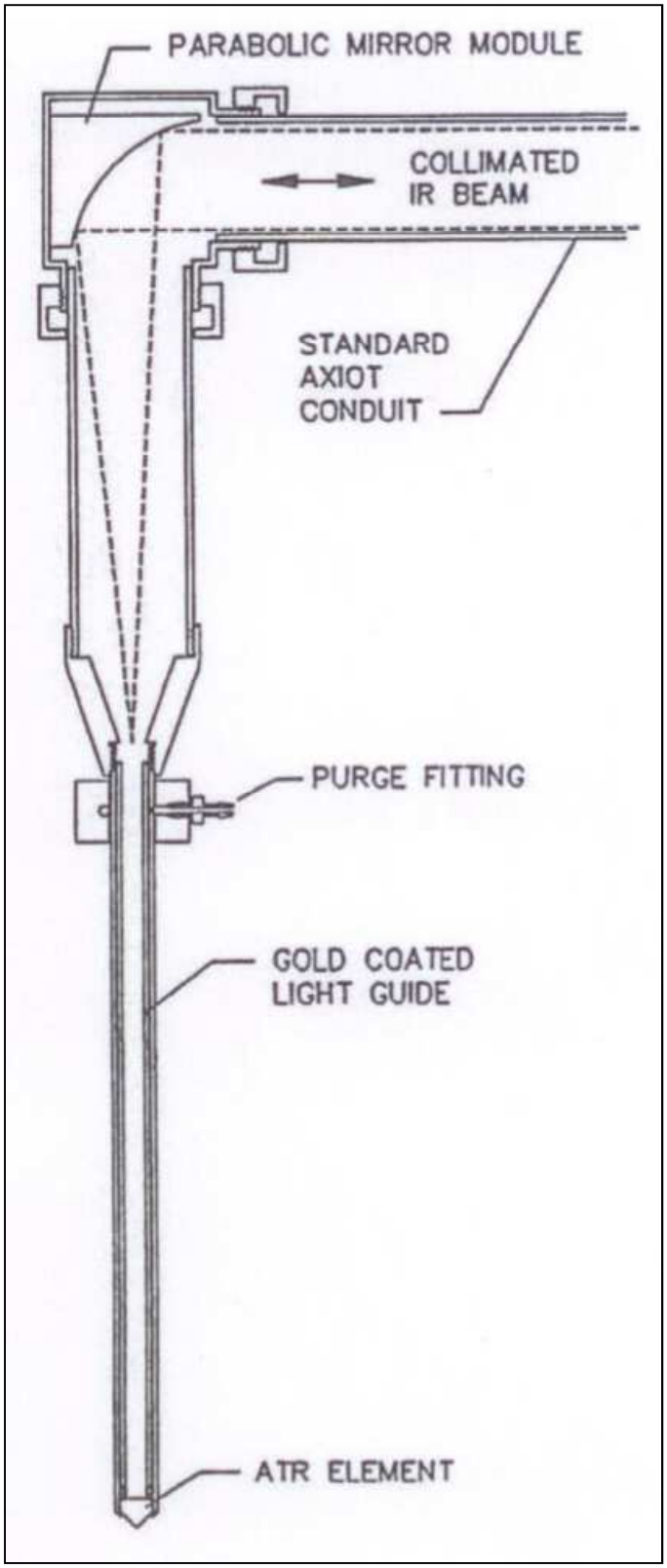

Figure 3.5 Schematic Diagram of the ATR Probe (used with permission from (Axiom, 2010))

3.4.2 Semi-Batch Reactor Set-up

ATR coupled with FTIR has made it possible to bring the IR energy into contact with the reagent mixture inside a reaction vessel. Real time kinetic studies, similar to the one proposed in this study are best conducted using a batch or semi-batch reactor (Fogler, 1999).

Since the reaction of CO_2 with MEA is fast, a semi-batch reactor seems to be the favourable choice. Besides the advantage of being able to slow the reaction down by controlling one of the reagent's feed rates to the system, the semi-batch reactor has additional benefits compared to a batch reactor. The exothermic nature of the reaction of MEA with CO_2 (Hikita, et al., 1976) has the potential to cause sharp temperature spikes inside the reactor. Since it was desirable to conduct the experiments at a constant specified temperature, the addition rate of one of the solvents will aid in moderating the exothermic effect (Fogler, 1999). The other advantages become clear as the method development unfolds.

A schematic of the reactor used in the kinetic study is illustrated in **Figure 3.6**.

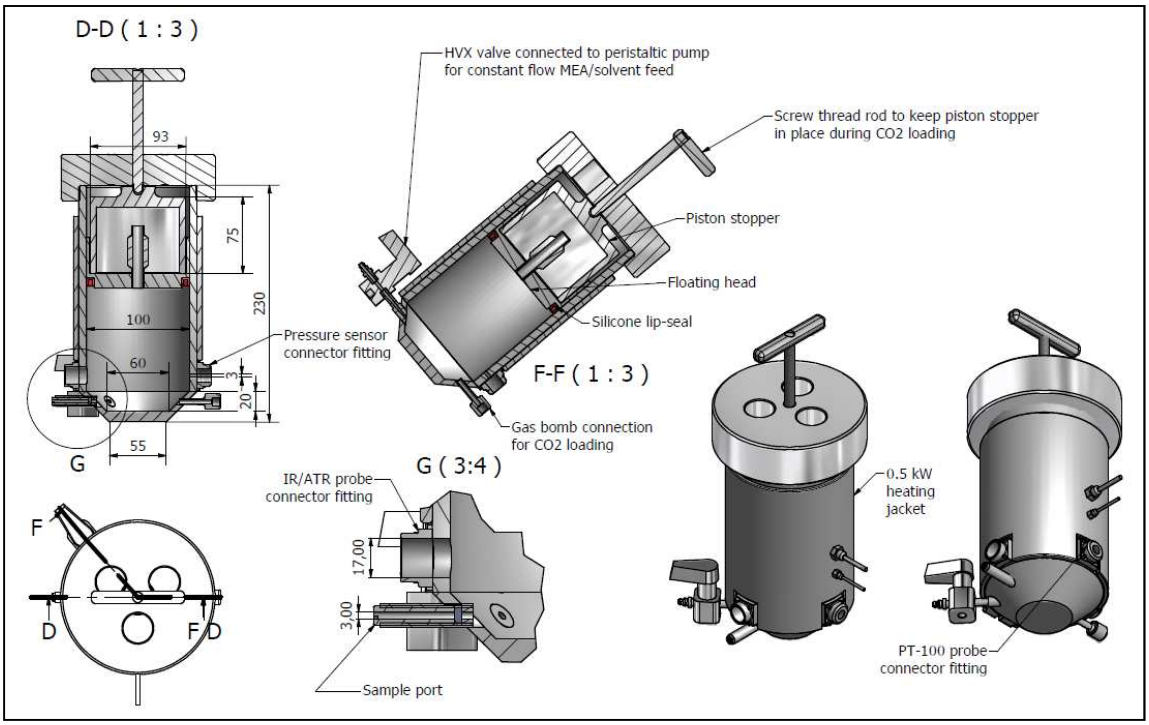

Figure 3.6 The Semi-Batch Reactor. All Dimensions in mm

The conditions where effective interfacial mass transfer area measurements are usually made is near ambient (P = 1 atm (abs), T = 20 - 40°C) (Tsai, 2010). The reactor was, therefore, designed to be suitable for use at these near ambient experimental conditions. The temperature and pressure inside the reactor was constantly monitored with a PT-100 temperature probe (accuracy = ±0.5°C) and Endress and Hauser® Cerebar S Pressure sensor (accuracy: 0.075% of reading value) respectively. The semi-batch reactor was designed to have a floating head to meet the pressure constraint. As liquid is pumped into the reactor, the floating head will rise, keeping the pressure balanced with atmospheric pressure. The exact required pressure to initiate the movement of the floating head could not be determined, since it was smaller than 100 Pa and fell outside the resolution of the pressure sensor used. The fact that the required pressure was less than 0.1% of the operating pressure, suggests that the moving head moves smoothly. It moved smoothly with a constant pressure reading in the order of 100 kPa (±3 kPa) under the influence of the liquid being pumped into the reactor The temperature of the reagent mixture was controlled with a 0.5 kW electric heating jacket. A constant temperature profile within the measurement accuracy of the temperature probe (±0.5°C) was obtained for all experimental runs.

The experimental concept is now briefly presented. The reactor was designed to easily accommodate an initial solvent volume of 500 cm^3. After loading the solvent into the reactor (on a mass basis), the floating head was allowed to rest flush with the liquid. The valve on the floating head was shut, sealing the solvent inside. The solvent was heated under magnetic stirring until the desired temperature was reached. CO_2 was then charged to the reactor on a mass basis (see section 3.5.2) and allowed to dissolve. The floating head was fitted with a silicone lip seal to prevent any gas leaking from the reactor. Silicone was chosen, since MEA does not affect it. The dissolution rate of CO_2 was enhanced by creating an over pressure with a screw thread rod pushing down on the floating head, keeping it flush with the liquid. The lip seal was leak tested by forcing it down with only air inside the reactor, compressing the air and raising the pressure inside the reactor to above 2 bar. The piston head was kept in this position and the pressure reading monitored. It was found that for the entire duration of the leak test (1 hour) the pressure inside the reactor remained constant, indicating no gas leaks.

Due to the fact that the stainless steel (316) cylindrical reactor is precision machined to have the floating head fit snugly, but move smoothly, no welding was allowed on the reactor body. Special fittings had to be constructed to fit the sensors and IR probe to the reactor. These fittings were made to hug the outside curvature of the reactor and were screwed into the outside reactor wall to stay in place. A sheet of cork between the fitting and reactor outer wall provided the necessary inert seal.

The bottom of the reactor was conically shaped to aid with liquid mixing using a magnetic stirrer. The bottom was fitted with a sample port containing a septum through which samples may be withdrawn with a syringe. It was also fitted with a port for CO_2 loading and a Hamilton® HVX two-way valve with a 3 mm bore diameter. The MEA, diluted with solvent, would be pumped from a reservoir (a gas tight 100 cm^3 Hamilton® syringe) with a peristaltic pump at a constant flow rate via the two-way valve into the reactor. Whilst the MEA/solvent mixture is pumped into the reactor, real time data was collected in the form of IR absorbance spectra spaced in small time increments for the duration of the reaction. A photograph of the semi-batch reactor set-up is illustrated in **Figure 3.7**. Refer to section 3.8 for a detailed description of the data collection parameters and procedure.

Another advantage of the semi-batch reactor set-up was to allow for the MEA to be diluted with solvent before being pumped into the reactor. MEA concentration spikes were noticed when pure MEA was pumped into the reactor. This effect may be due to the high viscosity of MEA preventing it from being easily dispersed, creating tiny MEA 'pockets' that were stirred around and when one of these 'pockets' came into contact with the probe tip a spike in MEA concentration was recorded. Since MEA is 20 times more viscous than water, diluting it before pumping it into the reactor allows the mixture to be more easily dispersed by the stirrer inside the reactor.

Once the reaction had enough time to proceed to equilibrium, the data collection was stopped. A sample could then be withdrawn from the reactor and analysed for the equilibrium concentration of one of the salt products, RNH_3^+. The analysis of the salt product was achieved using a conductometric titration method also developed in this study. Refer to section 3.5.3 for

a detailed discussion on this method of analysis. The spectral data could then be converted to concentration vs. time data with the use of the species calibration curves.

Refer to Appendix C for the detailed mechanical drawing of the semi-batch reactor in **Figure 3.6**.

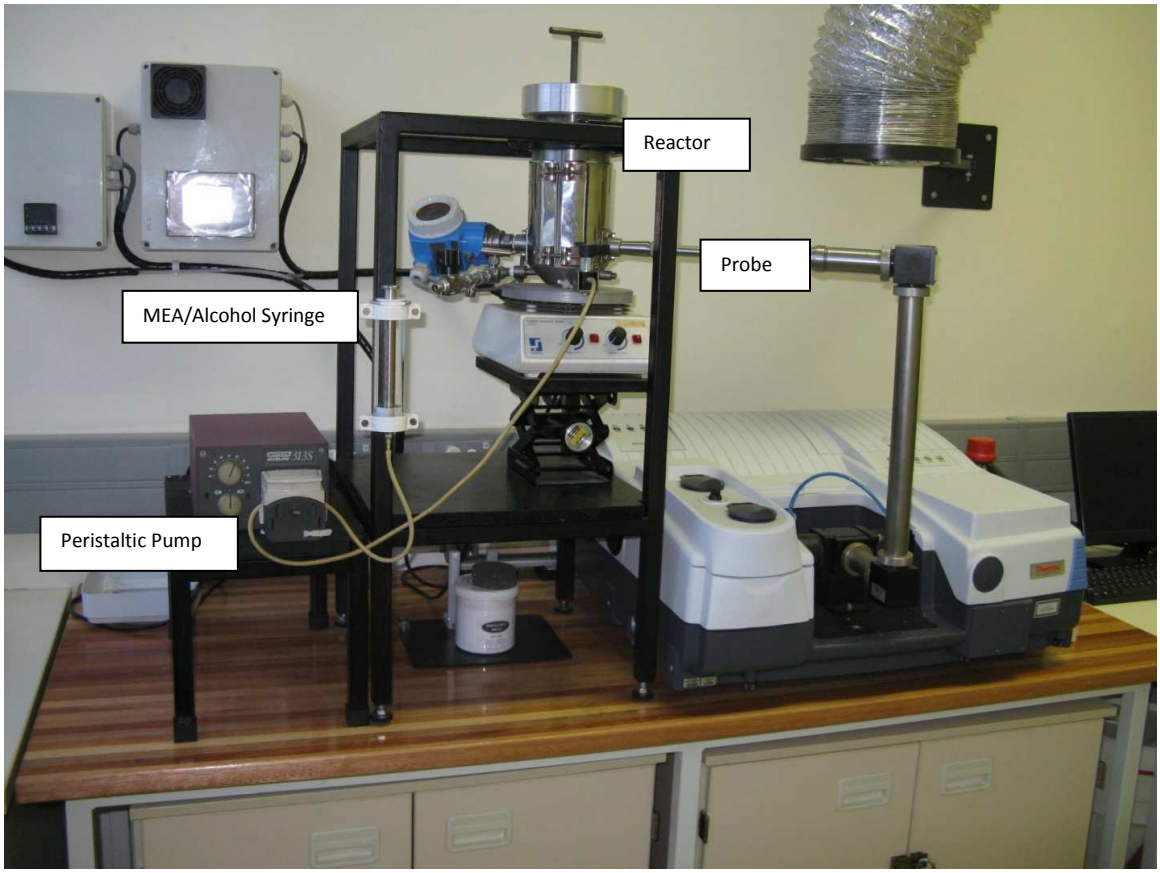

Figure 3.7 The Semi-batch Reactor Experimental Set-up

3.5 Calibration Procedures and Method Validation

In order to be able to convert the FTIR absorbance data collected for each reaction, the reactant and product species must firstly be calibrated. This section will give a detailed account on how the calibrations were performed and the experimental design that followed.

3.5.1 OMNIC® Software Settings

Before any calibration or experimental run could be performed, the optimal settings in the FTIR software package, OMNIC® (supplied by Thermofisher Scientific®), had to be found:

It was firstly desirable to collect as many data points as possible during the reaction time, without sacrificing too much accuracy. It was found that if the Series® software (an add on package to OMNIC® specifically designed to collect time series data) was set to 'kinetics' mode and 1 scan at a resolution of 32 cm^{-1} were collected, it would produce a data point for every 0.08 seconds elapsed. In order to optimize the accuracy in data collection (maximizing signal to noise ratio), the collected spectra were reference to a background file consisting of 256 scans with atmospheric and ATR correction employed. All scans were treated to 2 levels of zero filling, Happ-Genzel apodization and Mertz phase correction.

All calibration and experimental spectra were collected at the above mentioned software settings.

3.5.2 MEA Calibration

The calibration of MEA was achieved by injecting known masses of MEA and collecting a 10 second series file after each injection. The series file contained 137 spectra, for which the peak height at 944.949 cm^{-1} (baseline 975.804 – 898.666 cm^{-1}) were averaged. Each calibration point thus represents the average of 137 peak height measurements. A part of one of the spectra taken from the series data set at 0.334 mol/dm^3 MEA at 30°C and 1 atm with n-Propanol as solvent is illustrated in **Figure 3.8**.

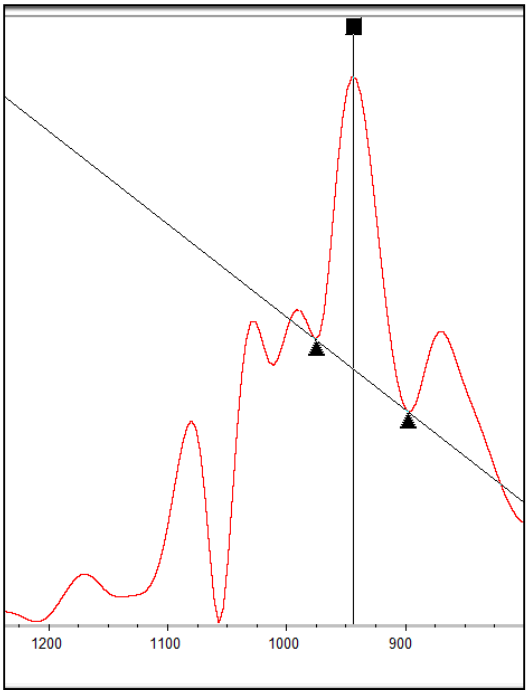

Figure 3.8 Spectra of 0.334 mol/dm^3 of MEA Dissolved in n-Propanol at 30°C and 1 atm Showing the RNH_2 Wagging Peak at 944.949 cm^{-1}

From **Figure 3.8** the wagging absorption band of MEA shows peak activity in the range of 960 - 800 cm^{-1}. It was found that when using peak height as a calibration entity, no baseline correction was necessary. No smoothing operations were performed. An investigation was done to determine whether the peak identified for monitoring the MEA concentration was representative of the $–NH_2$ functional group. The test consisted of monitoring the behaviour of the MEA peak when it reacts with CO_2. This test was done by loading the reactor with MEA and monitoring the peak behaviour with the addition of CO_2. It was found that the peak height increased with the addition of MEA and decreased with the addition of CO_2. This was in agreement with the proposed reaction mechanism (equation 3.3) and the peak behaviour reported in literature (Jackson, et al., 2009; Richner & Puxty, 2012). The magnitude of the decrease in peak height with the addition of CO_2 is presented in section 3.5.6 to validate the equilibrium stoichiometric ratio of the reaction.

Three MEA calibrations were performed for each temperature. Two of the calibrations were performed on the same day and the third, 5 days later to verify the repeatability of the calibration. The calibration data of the three calibrations at 25°C are illustrated in **Figure 3.9**.

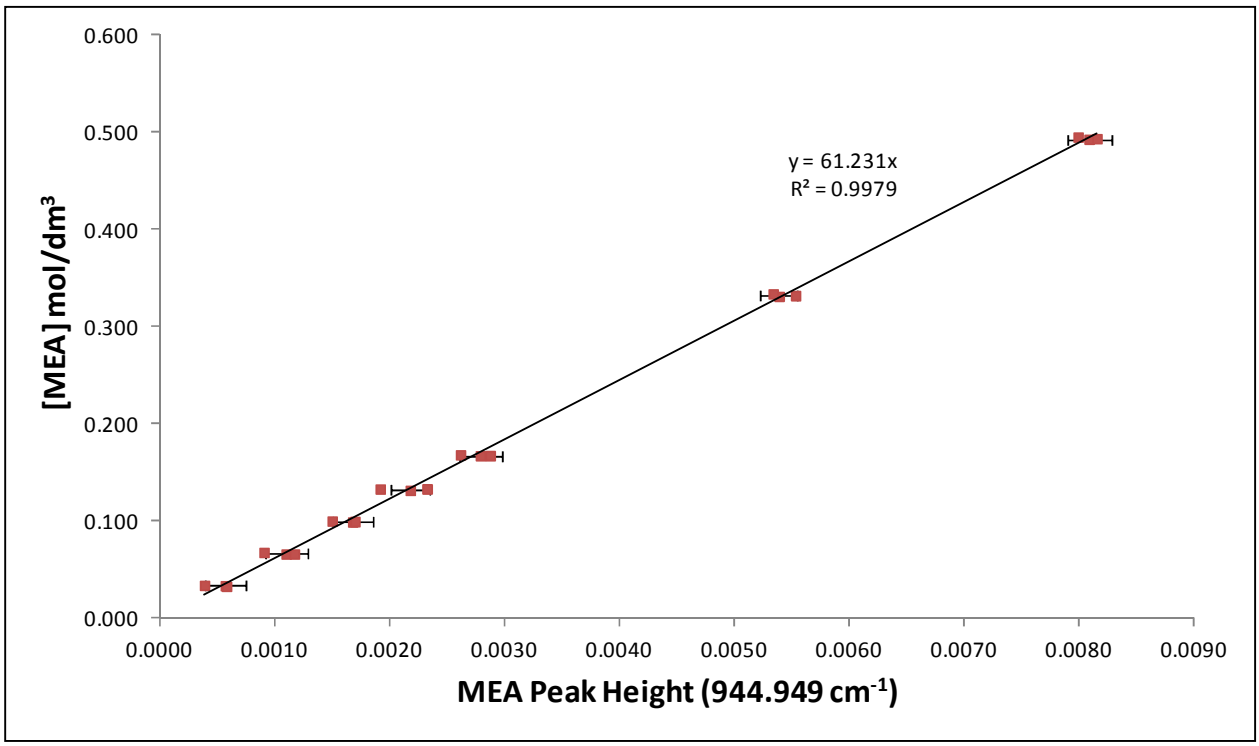

Figure 3.9: MEA Calibration Data in n-Propanol at 25°C

It may be noticed from **Figure 3.9** that MEA exhibits a linear correlation between measured peak area and concentration. The three data points at each MEA concentration represent the three calibrations performed at each temperature. The data indicates that good repeatability of the measured MEA peak height could be obtained for the temperature and concentration range investigated in this study. The error bars for one of the calibration data sets are included in **Figure 3.9**. The error bars represent the standard deviation in the 137 peak height measurements made for each calibration point. The calibration factors for MEA at 25°C, 30°C and 35°C are tabulated in **Table 3.2**.

Table 3.2 MEA Calibration Factors

Temperature (°C)	MEA Calibration Factor	Pearson's R^2
25	61.231	0.9979
30	60.237	0.9988
35	58.653	0.9965

The calibration factor data in **Table 3.2** show that at each temperature a linear correlation passing through the origin was obtained. This is in agreement with Beer's law at low concentrations (Grffiths, 2002). The calibration curves were forced through the origin for the fundamental reason that at zero concentration the average measured peak height should, fundamentally, be zero. The Pearson's R^2 values of more than 0.99 for each of the calibration curves serves to validate this assumption. The calibration factors of **Table 3.2** were multiplied with the peak height data of a reaction run to obtain the concentration data for MEA.

An effect of temperature on the calibration factor may be noticed. This effect was not investigated, since all experimental runs were performed at each of the temperatures tabulated in **Table 3.2**, for which a specific calibration factor was determined. The effect of temperature on the calibration factor was, therefore irrelevant with regards to the aims of this study.

3.5.3 RNH_3^+ Equilibrium Analysis and Calibration via Conductometric Titration

One of the reaction products in equation 3.3 is a bound amine salt, RNH_3^+. According to **Table 3.1** the typical absorption range due to symmetrical bending of the molecule for compounds containing - NH_3^+ functional groups is 1550 – 1485 cm^{-1}. The formation of the salt product species was investigated by allowing a reaction of CO_2 and MEA to occur inside the reactor and monitoring the region of 1550 – 1485 cm^{-1} for peak activity. A part of one of the equilibrium spectra of this investigation is illustrated in **Figure 3.10**. The spectrum is that of reaction equilibrium at 30°C for which the equilibrium MEA to CO_2 concentration ratio is 10:1. The choice of concentration ratios selected for investigation in this study is discussed in section 3.6. It was noticed that a peak at 1492.657 cm^{-1} (baseline: 1525 – 1467 cm^{-1}) grew along with

the reaction progress. This peak behaviour for RNH_3^+ is in agreement with findings in literature (Richner & Puxty, 2012).

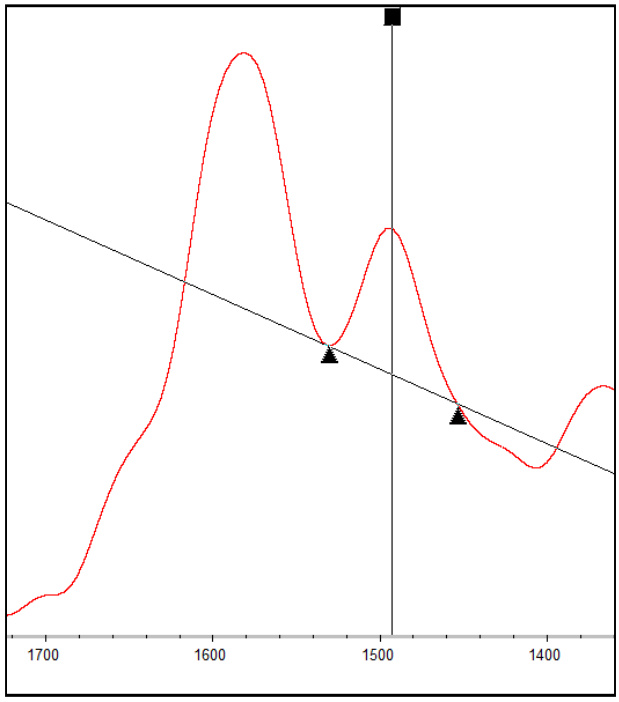

Figure 3.10 A Section of an Equilibrium Spectrum Showing the RNH_3^+ Peak at 1492.657 cm^{-1} Noticed During the Reaction of CO_2 and MEA in n-Propanol

A conductometric titration method of analysis has been proposed by previous researchers (Van Meurs & Dahmen, 1959; Cummings, et al., 1990) to determine the concentration of proton bound amines (RNH_3^+) in CO_2 sequestration mixtures of aqueous systems. The concentration of these salts is determined through titration with a diluted (±0.1 mol/dm^3) strong base such as NaOH or KOH. The challenge in this study was to translate the method to be used for a non-aqueous (alcoholic) system. Since KOH is more soluble in the alcohols of this study, than NaOH, it was chosen as the titration base responsible for removing the proton from the bound amine and revealing the product salt concentration.

A temperature controlled titration vessel was designed to conduct the product concentration analysis. It consists of a glass vessel, jacketed for heated water circulation, fitted with a lid that

seals the vessel contents from the atmosphere. It was purged with N_2 before injecting the sample, withdrawn from the semi-batch reactor. The KOH/alcohol mixture (concentration = ± 0.09 mol/dm^3) was introduced as either 1 cm^3 or 0.1 cm^3 volume aliquots, depending on whether the expected RNH_3^+ concentration was above or below 0.007 mol/dm^3. The expected RNH_3^+ concentration could easily be calculated via a dilution series. The conductivity of the mixture was recorded after every dose and a plot of conductivity vs. volume of KOH/alcohol drawn up. An example of such a plot is illustrated in **Figure 3.11**.

The titration end-point was calculated as follows: The slope of the titration curve changes as the solution passes through a titration end point (as seen in **Figure 3.11**). The intercept of the slope lines indicates the volume of titrant needed to reach the end-point of the titration (Cummings, et al., 1990). If the volume of titrant needed is known, along with the concentration of the titrant and the stoichiometric ratio of the titration reaction, the concentration of the protonated amine salt is easily calculated:

$$\left[RNH_3^+\right] = \frac{\left[KOH\right] \cdot V_{KOH}}{V_{\text{Sample}}}$$

The amine salt calibration was carried out by allowing a reaction mixture to reach equilibrium inside the reactor. After collecting a spectrum, a 40 cm^3 sample was withdrawn from the reactor, further diluted with n-Propanol to 95 cm^3 and analysed via titration. The amine salt calibration curve was obtained by diluting the salt in the reactor with the addition of more solvent.

The method was tested by doing an experiment with MEA in great excess relative to CO_2 (90:1). A sample was withdrawn and analysed as described above. By noting the amounts of MEA and CO_2 charged to the system, and assuming that 99% of the CO_2 reacted, it was possible to estimate the titration end-point. The 99% CO_2 reacted assumption was based on the high CO_2 conversion (in the order of 99%) achieved when it reacted with MEA in a 90:1 ratio. The end-point estimation proved to be accurate and the worst case mass balance closure achieved was within 6% of the estimated end point. The measured salt concentration was always lower than

the estimated concentration, indicating that even with an excess amount of MEA, the CO_2 never reacts completely or the zwitterion never decomposes completely.

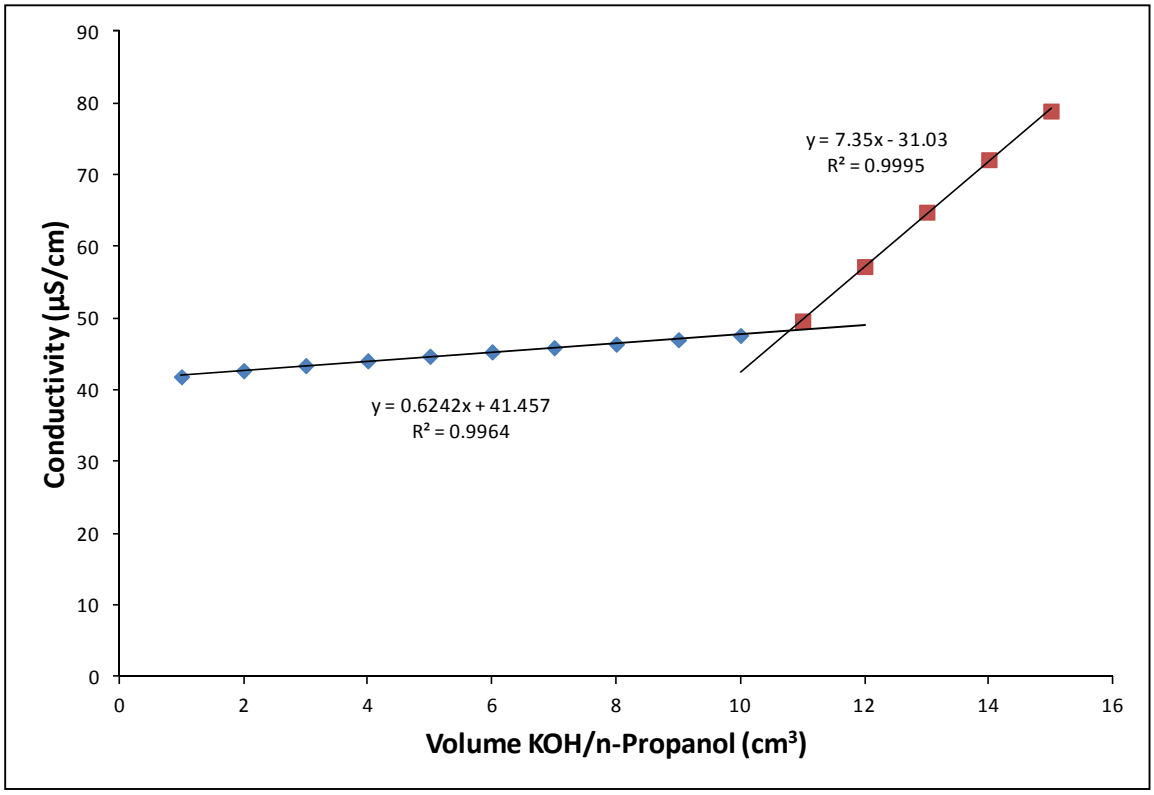

Figure 3.11 Typical Titration Curve for Determining RNH_3^+ concentration

The KOH/n-Propanol mixture used as titrant was standardised using the standard potassium hydrogen phthalate (KHP) method. KHP is deprotonated by KOH in a 1:1 stoichiometric ratio, making it suitable for standardisation purposes. Since KHP needs to be dissolved in water for the procedure, some concern arose, since the dissociation of KOH in alcohol may be affected by the addition of water, influencing the actual concentration of OH^- ions available for titration. The standardisation was confirmed by using benzoic acid dissolved in alcohol as a calibration standard, revealing near exact OH^- ion concentrations to that of KHP in water.

Since KOH has an affinity for atmospheric CO_2, it was decided to test the degradation of the KOH solution with time. 4 standardisations of freshly prepared KOH/n-Propanol revealed a concentration of 0.0916 mol/dm^3. The mixture was sealed for 7 days, apart from exposing it to

the atmosphere once daily. This once daily atmospheric exposure was in accordance with the procedure followed on a day of experimentation. Standardisation analysis of the rested KOH/n-Propanol revealed a concentration of 0.0911 mol/dm^3. This indicates that no appreciable degradation due to atmospheric contamination occurred in the batch life time.

3.5.4 MEA Interference with RNH_3^+ Spectra and Subsequent Calibration

One of the main reasons for inaccurate measurement in FTIR studies is peak interference from one or multiple other compounds (Sherman Hsu, 1997). In analyzing the preliminary experimental results of this study, it was discovered that MEA absorbs small amounts of IR energy in exactly the region identified to monitor the RNH_3^+ product concentration. From the series MEA calibration data (see section 3.5.2), calibration curves to determine the magnitude of the MEA interference in the RNH_3^+ region was constructed for all temperatures. For example, the calibration curve at 30°C is illustrated in **Figure 3.12**.

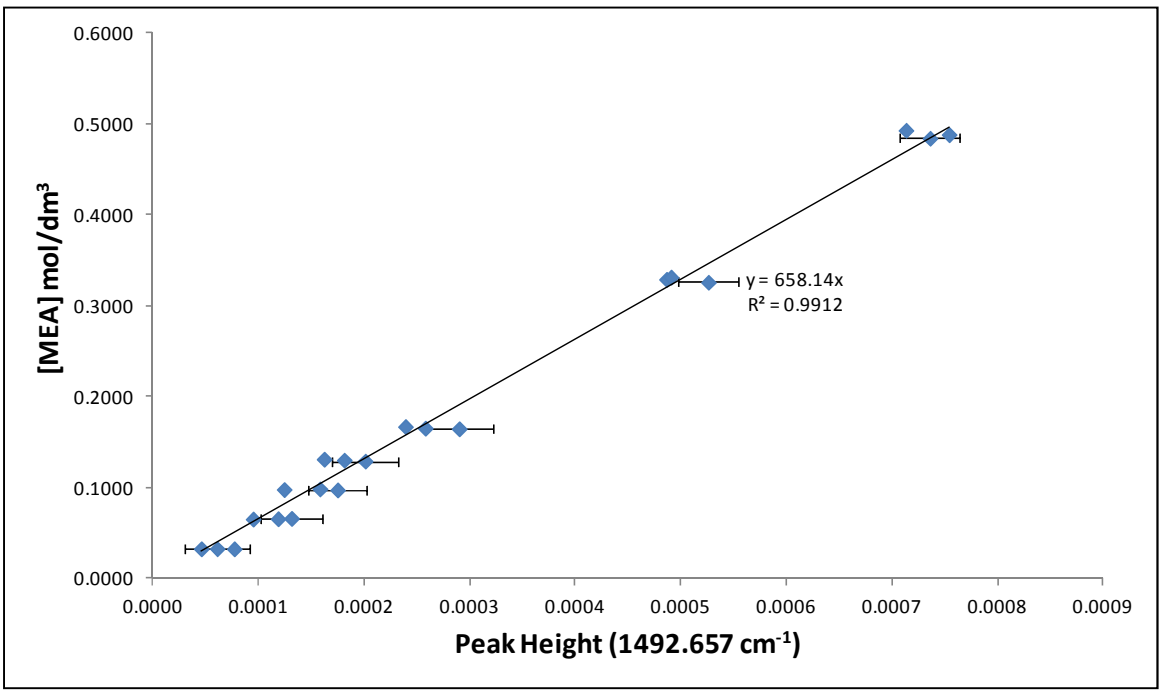

Figure 3.12 Calibration Curve for MEA IR Activity in the Region of RNH_3^+ absorption.

Calibration Curve for n-Propanol at 35°C

A linear correlation with a steep slope passing through the origin may be noticed in **Figure 3.12**. The steepness of the slope indicates weak IR activity of MEA in this region. The weak activity is also why there is more scatter noticed in the calibration data than compared with an MEA calibration. Care must be taken to ensure that the calibration data is measured under optimum purge conditions, since atmospheric water content could influence the position and peak height of the peak at 1492.657 cm^{-1}, resulting in larger data scatter and inaccurate calibration. It was, however, found that the large data scatter had no significant influence on the calculated salt calibration factor. Due to the linear trend noticed and the weak IR activity, it was assumed that the measured peak height in the region 1550 – 1485 cm^{-1} is the sum of the MEA and RNH_3^+ peak heights. This assumption allows the calculation of the true RNH_3^+ concentration as follows:

The peak height of the peak at 1492.657 cm^{-1} is measured over the reaction time. The equilibrium concentration of RNH_3^+ is determined by conductometric titration. The concentration of MEA is determined from the peak height shown in **Figure 3.8**. A dilution series was prepared and a series data set, containing 137 spectra, collected after each n-Propanol injection. The peak height contribution of MEA was subtracted from the measured peak height to obtain the peak height of the product species RNH_3^+. A typical calibration curve for RNH_3^+ that is obtained from this operation is illustrated in **Figure 3.13**

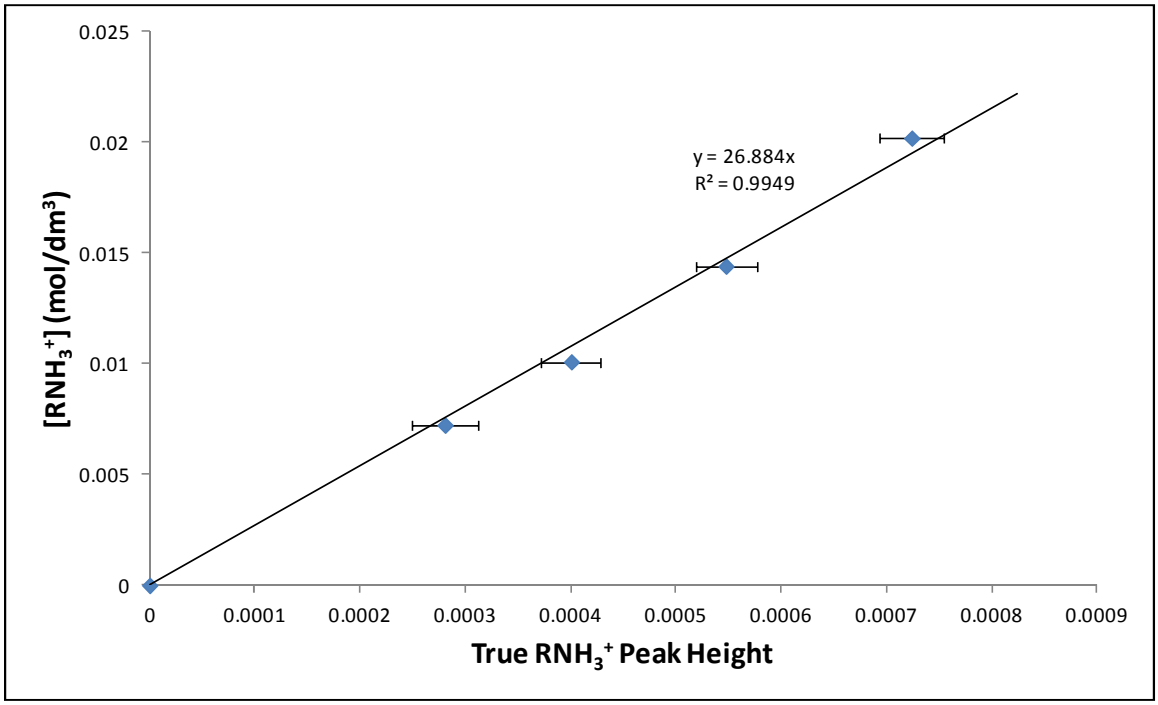

Figure 3.13 RNH_3^+ Calibration Curve for n-Propanol at 35°C and 1 atm. [MEA]:[CO_2] = 10:1

From **Figure 3.13** a linear correlation passing through the origin may once again be noticed. The error bars represent the standard deviation of the 137 peak height measurements made after each injection in the dilution series. A linear correlation was noticed throughout the temperature range investigated in this study. Not all dilution series to calibrate the salt concentration were successful. The unsuccessful measurements were attributed to water vapour contamination of the spectrometer atmosphere causing inaccurate peak height measurement. These experiments were discarded and repeated when purge conditions were once again optimal.

A consistency test of the true salt peak height calibration was performed at 25°C. The consistency test consisted of comparing the true salt peak height calibration factor for three experimental runs at similar conditions to see whether an average calibration factor can be used. The results of the consistency test are tabulated in **Table 3.3**.

The results of the consistency test showed that an average of the true salt peak height calibration factor may be used for all experimental runs at the same conditions. The variation

in the calibration factors had no significant impact on the equilibrium stoichiometric ratio obtained for each of the three runs at the same conditions. The significance of this finding is that during data collection under similar conditions, it may be assumed that it is only necessary to perform a dilution series for one of the experimental runs to obtain the true salt calibration factor for the given experimental conditions.

Table 3.3 True Salt Peak Height Calibration Factor Consistency Test at 25°C

Temperature (°C)	[MEA]:[CO_2]	Experimental Run #	Calibration Factor	Average Calibration Factor
25	5	25_5_1	32.08	31.69
		25_5_2	29.81	
		25_5_3	33.18	
	10	25_10_1	26.31	24.76
		25_10_2	24.04	
		25_10_3	23.94	

This finding saves on both experimental time and solvent use. It was tested for the 30°C and 35°C experimental runs and it was found that the true salt peak height calibration factor determined for one of the three runs was accurate enough to be used as the representative calibration factor for all three of the runs, since all three showed similar stoichiometric ratios at equilibrium. This is, furthermore a testament to the repeatability of the data collection method, which will be discussed in further detail in section 3.8.2.

As shown in **Table 3.3**, it was found that the calibration factors for RNH_3^+ were influenced by the MEA concentration. However, since the RNH_3^+ concentration may be measured with titration, a calibration factor of RNH_3^+ was determined for each set of experimental runs at the same temperature and relative concentration. In this way, the RNH_3^+ is exactly calibrated for the specific experimental run conditions. This was tested and confirmed in this study and is recommended as the preferred procedure for future experimental work. The true salt peak height calibration factors used in this study is tabulated in **Table 3.4**

Table 3.4 True Salt Peak Height Calibration Factors

Temperature (°C)	[MEA]:[CO_2]	Calibration Factor	Pearson's R^2
25	5	31.69	0.99
	10	24.76	0.99
30	5	29.21	0.99
	10	24.63	0.99
35	5	31.17	0.99
	10	26.88	0.99

3.5.5 CO_2 Calibration

The fact that CO_2 is highly IR active (Aruldhas, 2007) was one of the first considerations when investigating FTIR as a feasible method of analysis for this study. However, due to the compressibility of a gas, any volumetrically based calibration procedure would be highly tedious to perform accurately. The only method that would leave little room for error would be one that is performed on a mass basis.

The mass based loading of CO_2 was achieved with the use of a 'gas bomb' as shown in **Figure 3.8**. A 'gas bomb' is basically a high pressure sample cylinder with a needle valve at both ends. The sample cylinder is connected to a CO_2 cylinder with a dipstick inside in order to withdraw from the denser liquid phase inside the cylinder. The sample cylinder is sealed off with the CO_2 inside and the loaded 'bomb' is weighed. All weighing in this study was done on a Precisa® EP 920M balance with a capacity of 920g and an accuracy of 0.001g. After noting the mass of the loaded 'bomb', it was connected to the reactor as shown in **Figure 3.14**.

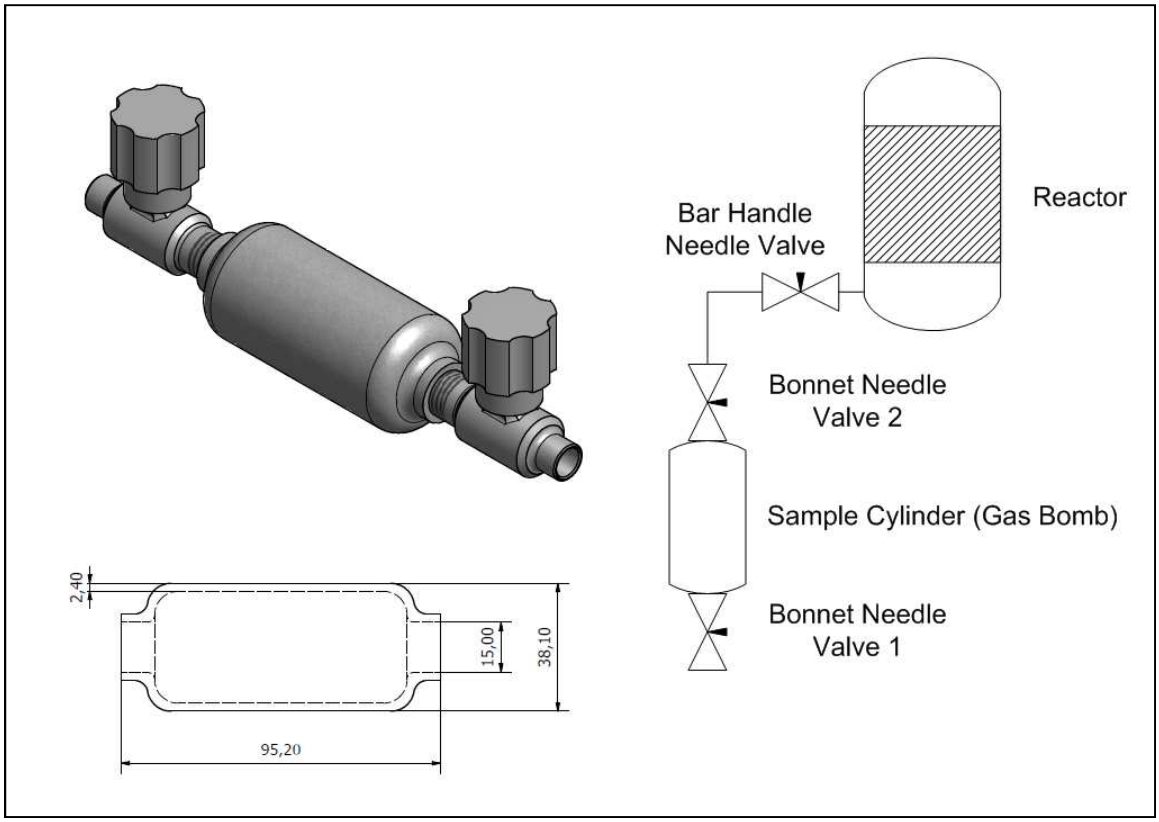

Figure 3.14 Sample Cylinder for Mass Based Loading of CO_2

The procedure for charging a known mass of CO_2 to a reactor has been used previously at Stellenbosch University for studying supercritical phase behaviour (Schwarz & Nieuwoudt, 2003) giving testimony to the accuracy of the method. The method may be described as follows: All needle valves must be shut to begin with. The tubing between bonnet needle valve 2 and the bar handle needle valve is filled with CO_2 by opening and closing bonnet needle valve 2. In order to minimize the dead volume in the tubing and valves between the 'bomb' and the reactor, all voids were fitted with Teflon bushings, machined to fit snugly. The bushings had a 1 mm hole drilled through the centre for the gas to flow through. The CO_2 was charged to the reactor by opening and closing the bar handle needle valve repeatedly. The gas bomb is fitted to the reactor set-up with a face seal fitting between bonnet needle valve 2 and the bar handle needle valve. The difference in the mass of the gas bomb before and after loading the reactor was the mass of CO_2 charged to the reactor.

Before any CO_2 was charged to the reactor, a background consisting of 256 scans at a resolution of 32 cm^{-1} was taken after purging the instrument with dry, baseline grade N_2 for between 4 and 5 hours at a constant flow rate of 20 sft^3/hr which relates to 157 cm^3/s or 9.44 L/min. This is a lower purge rate than the user manual recommended purge rate of 14 L/min. It was, however found that this flow rate was sufficient for purging and more economical, since less N_2 was required. Higher purge flow rates with CO_2 and H_2O free air should be investigated in future.

When the instrument went unpurged for a time, a whole day of purging was allowed, before any analysis was performed. This was necessary to obtain the lowest and most constant possible CO_2 and water vapour concentrations in the FTIR atmosphere during analysis. The background was also taken with the solvent inside the reactor at the desired temperature. Baseline grade N_2 contains less CO_2 than technical grade, making it a more suitable purge gas for this study. A typical background spectra at 30°C with n-Propanol as solvent is illustrated in **Figure 3.15**.

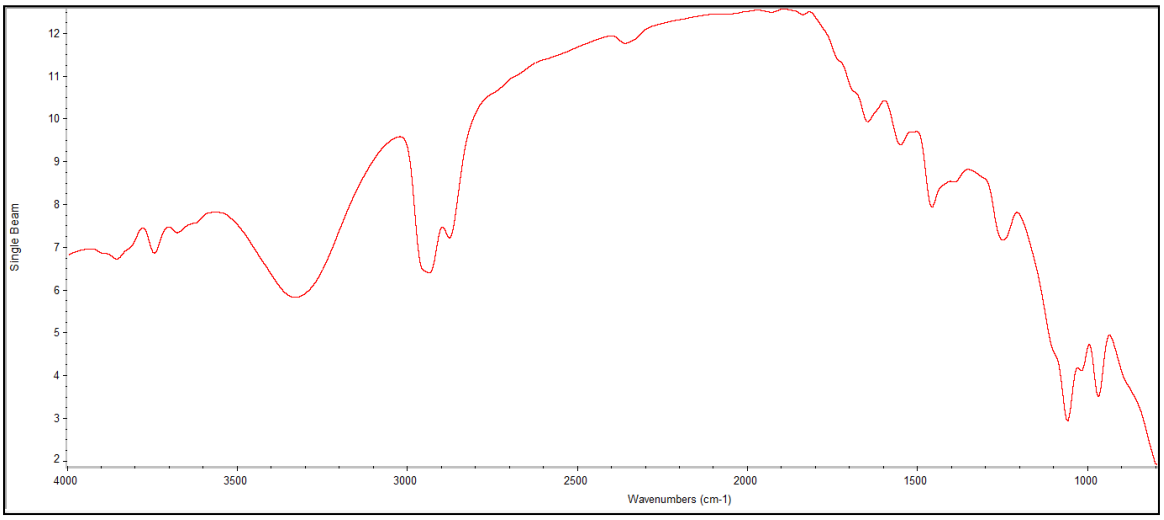

Figure 3.15 256 Scan Background Spectrum of n-Propanol at a Resolution of 32 cm^{-1} and 30°C

Once the CO_2 was loaded, its peak in the region of 2300 – 2400 cm^{-1} appeared and kept growing as the CO_2 dissolved in the alcohol. The CO_2 peak investigated in this study appeared at

2337.339 cm^{-1}. An example of the CO_2 peak for 0.489 g of CO_2 loaded in 0.5 dm^3 n-Propanol at 25°C is illustrated in **Figure 3.16**.

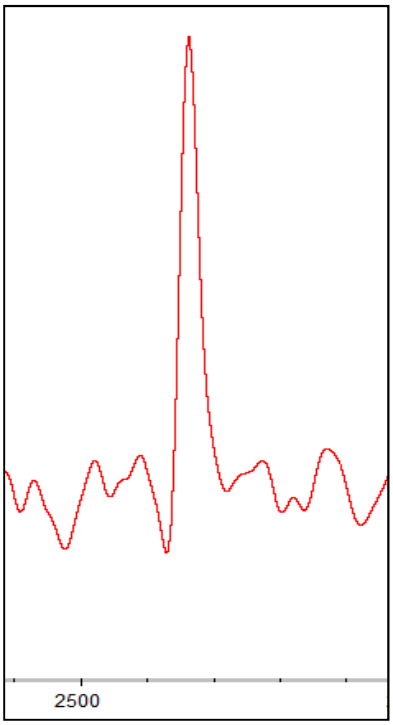

Figure 3.16 CO_2 Peak at 2337.339 cm^{-1} for 0.489g CO_2 dissolved in n-Propanol at 25°C and 1 atm

In preliminary peak behaviour confirmation studies, it was confirmed that the CO_2 peak height decreased as MEA was fed to the reactor. Once MEA was in great excess, the peak height of CO_2 became of similar order in magnitude of the instrumental noise surrounding it. This meant that accurately determining the equilibrium concentration of CO_2 after a reaction with excess MEA was very difficult. It was, therefore decided to monitor the CO_2 peak as it grows negatively with the reaction progress. This was achieved by loading the reactor with a known mass of CO_2, allowing it to dissolve and taking a background of the CO_2/n-Propanol mixture. As MEA was pumped into the reactor, the CO_2 peak height became increasingly negative, making a negative peak height measurement more accurate than a decreasing positive peak height.

In order to quantitively study a negative peak, a calibration procedure had to be devised. It was decided to use a dilution series approach. A known mass of CO_2 (close to 0.5 g CO_2 to be similar to the masses of CO_2 used in the reaction kinetic study) was dissolved in the reactor and a background collected. Known masses of n-Propanol were injected in small increments to keep the floating head flush with the liquid level to achieve dilution of the CO_2 inside the reactor. The volume of n-Propanol injected was calculated using density data from literature (Valtz, et al., 2004). A series data set of 137 spectra was collected after each injection. After each injection, a measured mass of the CO_2/n-Propanol mixture was extracted from the reactor by using the piston stopper to push the liquid into the syringe, thereby keeping the floating head flush with the liquid. A mass balance calculation was performed to calculate the CO_2 concentration after each extraction/injection cycle. The typical decrease in CO_2 peak height after dilution is illustrated in **Figure 3.17**

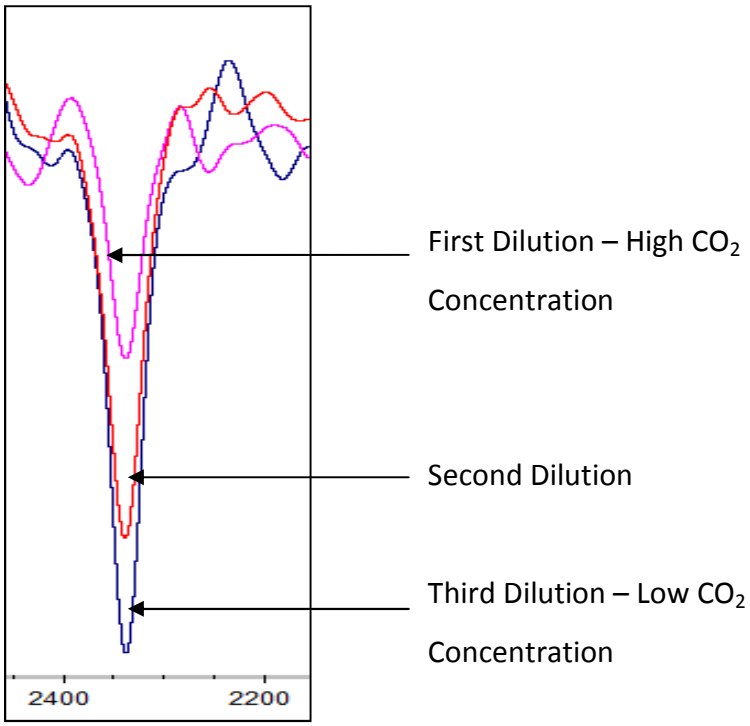

Figure 3.17 Spectra of the CO_2 Peak Height Decreasing with Each nPropanol Injection in a Calibration Dilution Series

A test was performed to ensure that the concentration of CO_2 inside the reactor remained unchanged after each extraction. This consisted of collecting a series data set after each extraction and comparing the average peak height measurement with the data set collected before the extraction. It was found that the average peak height after extraction remained within the standard deviation (error range) of the peak height collected before the extraction. This confirmed that the concentration of CO_2 was not affected by the extraction.

In order to obtain a generalised calibration curve for CO_2, the calculated CO_2 concentrations in the dilution series were fractionalised. This was done by dividing the calculated concentration by the initial concentration. The result of this was a linear calibration curve with a positive slope intercepting the y-axis at 1. A plot of the fractional CO_2 concentrations of two calibrations vs. peak height at 2337.339 cm^{-1} (baseline: 2364.338 cm^{-1} – 2314.197 cm^{-1}) in n-Propanol at 30°C and 1 atm is shown in **Figure 3.18**.

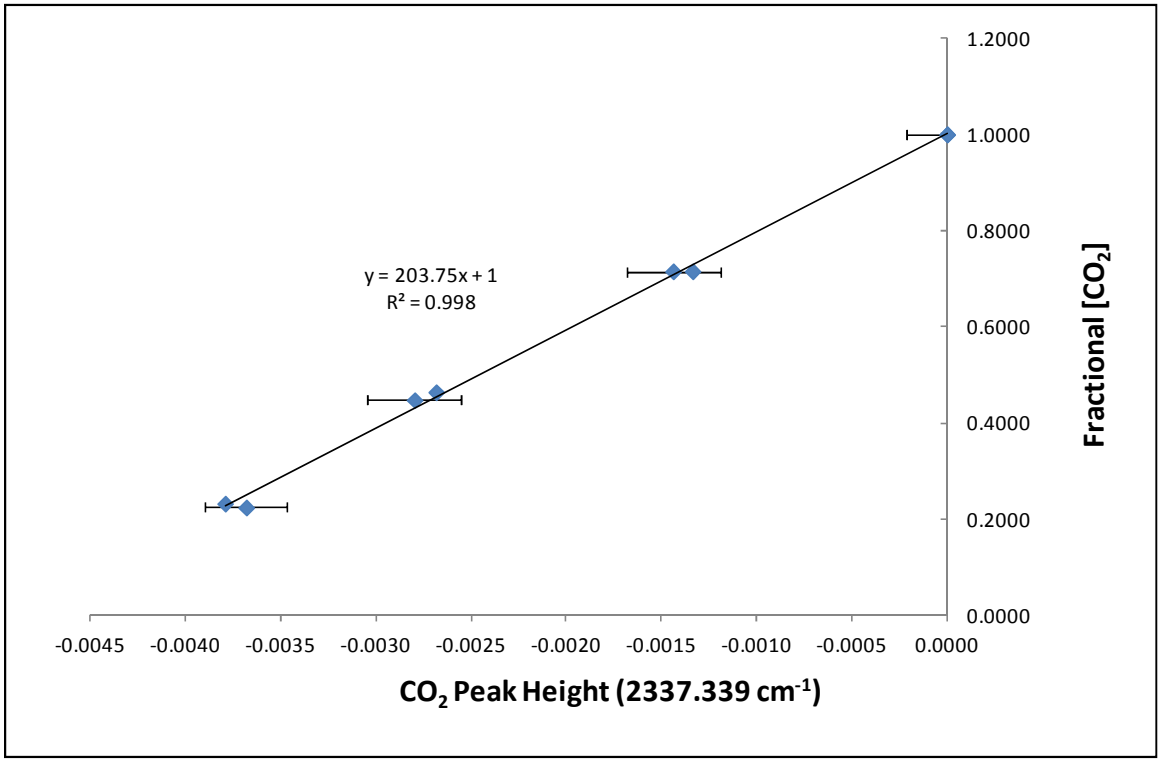

Figure 3.18 CO_2 Calibration Curve in n-Propanol at 30 °C

It may be noticed from **Figure 3.18** that a linear correlation exists between normalised CO_2 concentration and peak height with a Pearson's R^2 = 0.99 for this particular calibration. Calibration 1 and 2 were performed on different days with different background files and from the combined data plot the same linear correlation was noticed, proving the repeatability of the procedure and the instrumental measurements under optimum purge conditions. Care must be taken to ensure that the calibration data is measured under optimum purge conditions, since atmospheric CO_2 content could influence the peak height of the peak at 2337.339 cm^{-1}, resulting in larger data scatter and inaccurate calibration. The error bars in **Figure 3.18** represent the standard deviation in peak height measurement for the 137 spectra collected at each calibration point. The error bars for the CO_2 calibration are larger than that of MEA due to larger variances in the measured peak height for different calibrations. A sensitivity analysis of its effect on especially the equilibrium concentrations of CO_2 is presented in section 3.8.5.

The calibration curve was forced to intercept the y-axis at 1, since that is the initial fractional concentration of the calibration. The Pearson's R^2 obtained supports this action. The CO_2 calibration factors obtained for the three temperatures investigated in this study is tabulated in **Table 3.5**.

Table 3.5 Fractionalised CO_2 Calibration Equations

Temperature (°C)	CO_2 Calibration Equation	Pearson's R^2
25	$201.23x[CO_2]_{frac}$ +1	0.9972
30	$203.75x[CO_2]_{frac}$ +1	0.998
35	$207.27x[CO_2]_{frac}$ +1	0.990

It may firstly be noticed from **Table 3.5** that the linearity of the CO_2 calibration curves are consistent for the temperature range investigated. This is once again in agreement with Beer's law for low concentration solutions. The CO_2 calibration equations were used to calculate the fractional concentration of CO_2. The true concentration of CO_2 was obtained by multiplying the

calculated fractional concentration with the initial CO_2 concentration of that specific experimental run.

A temperature dependence of the calibration equation may be noticed, but as with the MEA calibration factors, it was not deemed necessary to investigate, since it had no impact on the results of this study.

3.5.6 Validation of FTIR method

Validation of the FTIR method of analysis was accomplished via a two part test. The first of which was to make sure that the representative peaks behaved in accordance with the reaction mechanism in equation 3.3. This was achieved by firstly loading the reactor with MEA, after which two or three charges of CO_2 were made. When charging the MEA, its peak at 944.945 cm^{-1} appeared along with the RNH_3^+ peak at 1492.657 cm^{-1}. After the charges of CO_2, the MEA peak height decreased and the RNH_3^+ peak height increased. This was in complete agreement with the mechanism in equation 3.3. It had to be confirmed that the decrease in MEA peak area was consistent with its calibration curve. The MEA concentration was calculated by once again assuming that 99% of the CO_2 reacted in a 2:1 ratio with MEA. The experiment was conducted at both 25°C and 30°C and the results are illustrated in **Figure 3.19** and **Figure 3.20**.

The data shows that the decrease in MEA peak height fell on the calibration curves. The difference may be attributed to the assumption of 99% CO_2 reaction and exactly 2:1 reaction ratio, which may not in fact be the case, but is acceptable for a validation study. This serves to prove that the MEA peak behaves in accordance with the reaction mechanism proposed in equation 3.3. As expected, the CO_2 peak height increased with addition of CO_2 and decreased with addition of MEA. The peak height of RNH_3^+ kept increasing with the addition of both MEA and CO_2 but showed a stabilization (only a slight increase due to the MEA effect) once the CO_2 in the system became depleted with excess MEA addition. The error bars in **Figure 3.19** and **Figure 3.20** represent the standard deviation of the 137 spectra collected per data point.

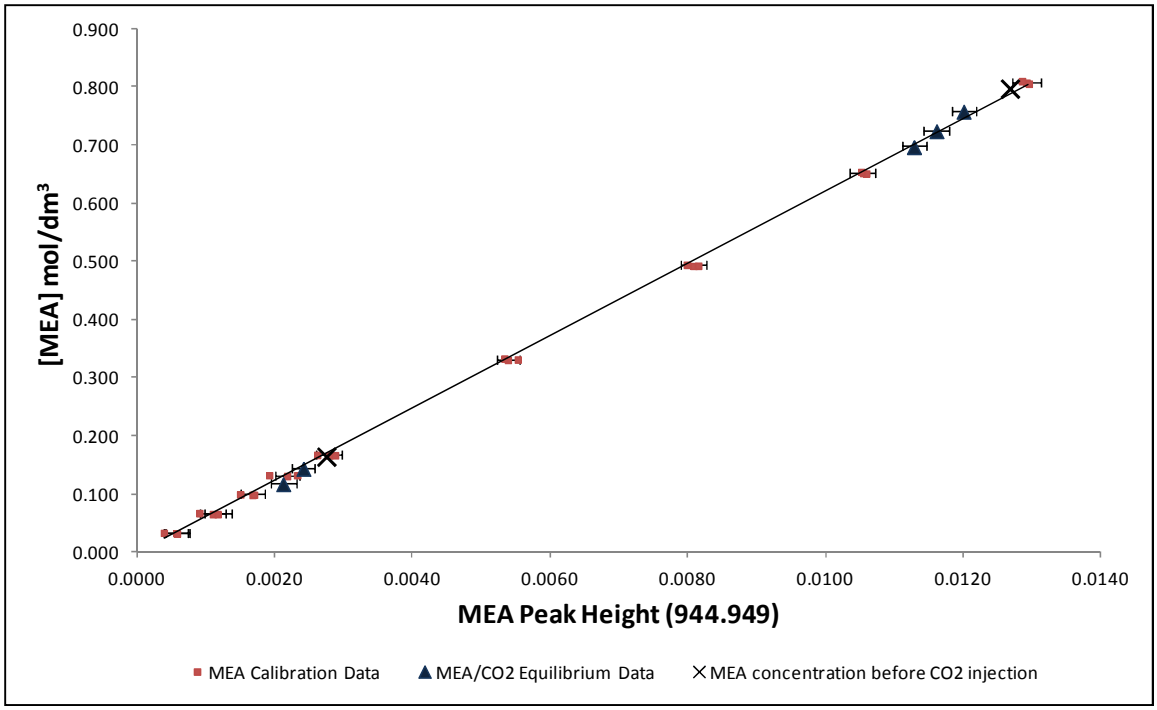

Figure 3.19 MEA Peak Height Behaviour Validation at 25°C

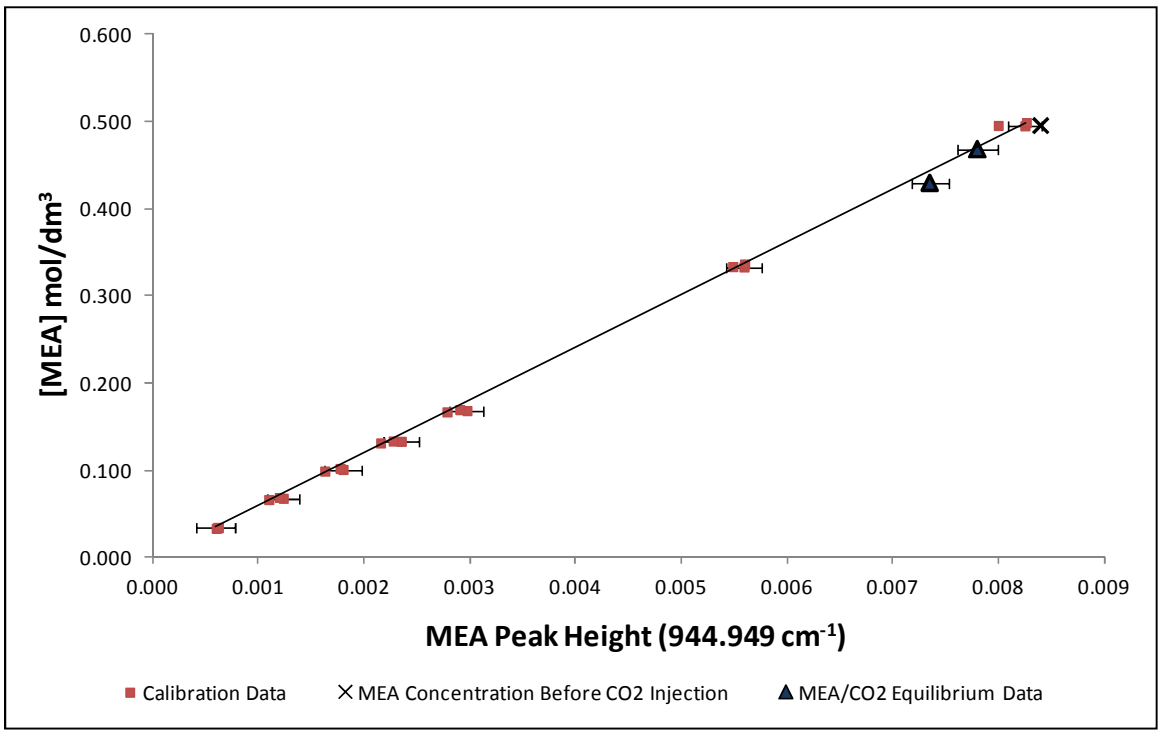

Figure 3.20 MEA Peak Height Behaviour Validation at 30°C

The second part in the validation test was to ensure that the equilibrium stoichiometry in equation 3.3 was satisfied. Test runs over a range of MEA:CO_2 (5:1 and 10:1) relative concentrations were performed and it was found that if the required purge conditions as discussed in section 3.5.5 were satisfied that the stoichiometric coefficients achieved fell within the following ranges:

$$n_{\text{MEA, reacted}} : n_{CO_2\text{, reacted}} = 2.0 \pm 0.1$$
$$n_{\text{MEA, reacted}} : n_{RNH_3^+\text{, formed}} = 2.0 \pm 0.1$$
$$n_{CO_2\text{, reacted}} : n_{RNH_3^+\text{, formed}} = 1.0 \pm 0.1$$

These specified coefficient ranges are in accordance with the equilibrium stoichiometric coefficients of the zwitterion reaction mechanism. The coefficients were calculated from the average of the equilibrium data (the plateau region in the concentration profile). Taking an average of the equilibrium data points should, however, still be as close to the actual expected stoichiometric ratio as possible in order for the experiment to be considered successful for modelling purposes. The coefficients achieved once again agree with the proposed mechanism in equation 3.3. This finding is consistent with the hypothesis that the zwitterion mechanism is the most appropriate mechanism for non-aqueous solvent systems. It is also in agreement with previous research (Versteeg & van Swaaij, 1988).

Under improper purge conditions there may be a shift in the MEA CO_2 peak location. These shifts were never more than 5 cm^{-1}, but may be attributed to the influence of atmospheric CO_2 and water vapour. Peak shifts may also occur as concentration increases (Richner & Puxty, 2012) but this was checked during calibration and it was found that for the concentration range investigated in this study, there was no noticeable peak shift. A peak shift causes inaccurate peak height measurements relating to inaccurate concentrations. If the equilibrium stoichiometric ratio obtained in an experiment fell outside the above mentioned range, that experimental run was discarded and repeated with an improved background file, taken when purge conditions were optimal.

3.6 Experimental Design

This section will discuss all aspects considered during the design of the experimental work conducted in this study. The experimental design was done in order to satisfy both a study dealing with deriving the most accurate reaction kinetic parameters as well as being suitable for determining both interfacial and effective interfacial mass transfer area.

As mentioned in section 2.2.1 all heterogeneous studies on the reaction kinetics of CO_2 with amines in both aqueous and non-aqueous solvents were conducted under conditions where the reaction may be considered to be pseudo m,nth order or pseudo first order with respect to the concentration of CO_2. Operating under pseudo first order conditions for the purpose of determining the reaction kinetics were necessary, since it was only possible to measure the amount of CO_2 absorbed and in some cases the amount of amine left at reaction equilibrium. The limitations in analysis have therefore impeded previous researcher's ability to study the reaction in accordance with the proposed mechanisms.

The novel FTIR method proposed in this study has two main advantages over previous methods. It firstly surpasses the heterogeneous barrier by studying the reaction in the liquid phase only, which is where the reaction takes place. This eliminates the possibility of mass transfer resistance in both the gas and liquid phase to influence the reaction rate in the liquid film. Mass transfer resistance must be taken into account when deriving reaction kinetic parameters during heterogeneous studies. This incurs error on the calculated parameters. The other main advantage is that all species in the reaction mechanism may be accounted for via either direct measurement or indirect calculation via a material balance. This allows for fundamental reaction rate expressions to be modelled which will be applicable over all concentration ranges.

A further implication of studying the reaction under pseudo first order conditions is the assumption of irreversibility. The zwitterion reaction mechanism, which is the most widely accepted mechanism in literature, is a mechanism proposing a reversible reaction. The reversibility of the reaction has been proven in as much as the amine solvents used for CO_2

capture, may be regenerated via heating. This implies that the pseudo first order assumption, although valid under certain conditions, is not a true representation of the reaction kinetics under all operating conditions.

Regarding interfacial area studies, the assumption of pseudo first order conditions is crucial to the current method of determining the interfacial area directly from gas absorption. The measurement of interfacial area is a good start and may be used for preliminary equipment design. The design may, however, be improved if the method for measuring interfacial area could be improved to determine effective interfacial area. This means being able to account for a reduction in effective area due to interfacial depletion along with an increase in effective area due to surface renewal of the liquid film. This may be achieved by studying the reactive absorption into a known gas-liquid interface, but under conditions where the interface becomes subject to depletion and surface renewal. Under these conditions the assumption of pseudo first order kinetics is no longer valid.

The first consideration in the experimental design was temperature. As mentioned in section 3.4.2, the majority of interfacial area studies have been conducted at ambient temperatures and pressures. Since the solubility of CO_2 in alcohols decreases with an increase in temperature (Tokunaga, 1975) it was decided to not exceed 35°C in this study. Therefore the temperatures under investigation in this study were 25°C, 30°C and 35°C. The pressure was kept at 1 atm (abs) for all experiments.

The next consideration was the concentration range. One of the aims of this study was to propose reaction rate expressions that are valid for a large concentration range. The range under investigation should be such that it still has industrial application in mind, which means that MEA should always be in excess. It was decided to investigate the following two relative concentrations ([MEA]:[CO_2]): 5:1, 10:1. Since the reaction is studied in a semi-batch reactor, the reaction will occur as MEA is pumped into the reactor, i.e. when MEA:CO_2 < 5:1. It is, therefore not necessary to investigate higher [MEA]:[CO_2]. The concentration ratios selected here represents the ratios investigated on the wetted wall experimental set-up (see Chapter 6) where the absorption of CO_2 causes appreciable interfacial depletion of MEA. Under these

conditions a pseudo first order reaction kinetics assumption is not valid and a fundamentally derived rate expression is desired. This study is aimed at deriving such a rate expression.

It is important to note that these relative concentrations are based on when all reactants are inside the reactor. The concentration of MEA inside the 100 cm^3 syringe reservoir, before being pumped into the reactor, will naturally be higher. The experimental design parameters are tabulated in **Table 3.6**. Refer to **Table E 1** in Appendix E for the actual amounts (mass basis) of reagents used for the successful data sets selected for modelling purposes.

Table 3.6 Experimental Design Parameters

Successful Experimental Run #	[MEA]:[CO_2]	Temperature (°C)
25_5_1	5	25
25_5_2		
25_5_3		
25_10_1	10	
25_10_2		
25_10_3		
30_5_1	5	30
30_5_2		
30_5_3		
30_10_1	10	
30_10_2		
30_10_3		
35_5_1	5	35
35_5_2		
35_5_3		
35_10_1	10	
35_10_2		
35_10_3		

3.7 Experimental Procedure

The experimental procedure for the homogeneous liquid phase reaction kinetic study of CO_2 with MEA in n-Propanol was as follows:

- The purge rate of dry, baseline N_2 to the spectrometer was firstly set to 20 sft^3/hr (157 cm^3/s) after which liquid N_2 was poured into the jacket surrounding the MCT-D* detector to cool it down to the optimal temperature.
- The n-Propanol was purged with dry N_2 to drive off any dissolved CO_2. The solvent was then placed in a temperature controlled water bath to obtain the desired reaction temperature before it was loaded into the reactor. The MEA to be used in the day's experiments were also placed in the water bath. Pre-heating of the liquids achieved three goals. It firstly decreased the heating time required by the reactor heating jacket. It secondly ensured that the volume of liquid loaded into the reactor went through minimal thermal expansion in reaching the experimental temperature and finally ensured that the n-Propanol and MEA injected into the reactor for both reaction and dilution purposes were at the desired temperature.
- The reactor was also purged with dry N_2 to ensure an inert atmosphere and also to purge the reactor from the previous experiment. The ZnSe ATR crystal was rinsed with acetone and the acetone evaporated with dry N_2.
- 500 cm^3 of CO_2 free solvent was then measured off on a mass basis and loaded into the purged reactor. The volume of solvent was calculated by taking the density of n-Propanol at the reaction temperature into consideration. The density data of n-Propanol was taken from literature (Valtz, et al., 2004). The floating head was lowered into place, flush with the liquid and secured with the piston stopper.
- The magnetic stirrer was switched on and set to the desired stirring rate. The heating jacket was set to the desired temperature.
- Whilst waiting for the proper purge conditions of the spectrometer, the balance was calibrated and the titration station prepared for the day's experiments. If the KOH/n-Propanol titrant was in need of standardization, it was done during this time as well.
- Once thermal equilibrium, proper purge conditions and detector equilibrium was reached, a background file was collected and saved.

- The desired mass (±0.5g for this study) of CO_2 was loaded into the reactor as described in section 3.5.5. The CO_2 was allowed to dissolve under elevated pressure for about 60 – 90 min after which the pressure stabalised at around 1.1-1.2 atm. The reason for the slightly elevated pressure was because the floating head was forced down a quater turn of the piston stopper on the liquid surface. A quater turn release of the piston stopper brought the floating head back to its position on the liquid surface before CO_2 loading and the pressure decreased to 1.02 – 1.04 atm.
- After CO_2 loading was complete, a background file was collected and the desired concentration of MEA prepared in the 100 cm^3 syringe. This was achieved by loading the syrring with the desired mass of MEA and filling the syringe to approximately 60 cm^3 with n-Propanol. The exact volume of the n-Propanol/MEA mixture was calculated from the mass of the solutions and the densities of MEA (Wang, et al., 1992) and n-Propanol. It was found through experiment (see section 6.2.5), that MEA and n-Propanol form an ideal solution at the MEA concentrations investigated. Volume change with mixing, may, therefore, be considered negligible. The solution density could thus be calculated from:

$$\frac{1}{\rho_{\text{MEA/n-Prop}}} = \frac{x_{\text{MEA}}}{\rho_{\text{MEA}}} + \frac{1 - x_{\text{MEA}}}{\rho_{\text{n-Prop}}} \qquad 3.9$$

- The syringe was connected to the reactor via a peristaltic pump. 10 cm^3 of the MEA/alcohol mixture was bled to ensure that the tubing connected to the reactor is filled with the mixture. The mass of solution bled was calculated assuming a 10 cm^3 volume and the solution density of equation 3.9. The syringe now contained approximately 50 cm^3 of reagent mixture.
- The Series software was prompted to collect a time series data file. Collection was started along with a stopwatch. The piston stopper was released, the two-way valve opened and after approximately 6 - 10 seconds of collection time, the pump was switched on to pump approximately 40 cm^3 of the MEA/n-Propanol mixture into the reactor, initiating the reaction. The approximately 10 cm^3 left inside the syringe was weighed to determine the exact mass of MEA/n-Propanol pumped into the reactor.

- The flow rate of the peristaltic pump was measured by timing equal volume segments of the 100 cm^3 syringe. It was found that a constant flow rate could be achieved with this dosing method. The molar flow rate of MEA into the reactor could be calculated from the concentration of the mixture being pumped in and the volumetric flow rate delivered by the pump.
- The Series software was prompted to stop data collection after 70 seconds. A 40 cm^3 sample was withdrawn from the reactor and weighed. It was diluted to 95 cm^3 with n-Propanol and weighed. The solution was then injected into the titration vessel and titrated for the equilibrium RNH_3^+ concentration.
- If the stoichiometric ratios in section 3.5.6 were satisfied, the experiment was regarded as a success. A dilution series of the product mixture was prepared by injecting 200 cm^3 of n-Propanol (mass basis), taking a spectrum and extracting 200 cm^3 for double titration. Repetition of the injection and extraction process produces the dilution series. In order to save on solvent use, the dilution series was only prepared if an experiment was deemed a success.
- The reagent mixture was removed from the reactor and the procedure repeated for the next experimental run. It is of utmost importance to do as many experiments as possible once the instrument has reached optimal purge conditions in order to maximize the chance of an experimental run being successful.

3.8 Collecting and Processing Continuous Time Data

The relevant reaction kinetic points of discussion that will be addressed in this section are:

- The collection and processing of real time reaction kinetic data for the homogeneous liquid phase reaction of CO_2 with MEA in n-Propanol.
- Material balances to calculate the concentration of reaction species not detected by FTIR.
- The behaviour and stoichiometry of reagent and product species concentration profiles during the course of the reaction and at equilibrium
- The effect of MEA molar flow rate on the concentration vs. time profiles

- An analysis of the reaction equilibrium to the accuracy allowed by the collected data

During the OMNIC Series® data collection procedure mentioned in section 3.7 the software were prompted to create peak height profiles for the three species, CO_2, MEA and RNH_3^+ during the reaction progress. An example of one of these sets of profiles is illustrated in **Figure 3.21**. The example is at 35°C, [MEA]:[CO_2] = 10:1 and an MEA molar flow rate of 0.011 mol/s.

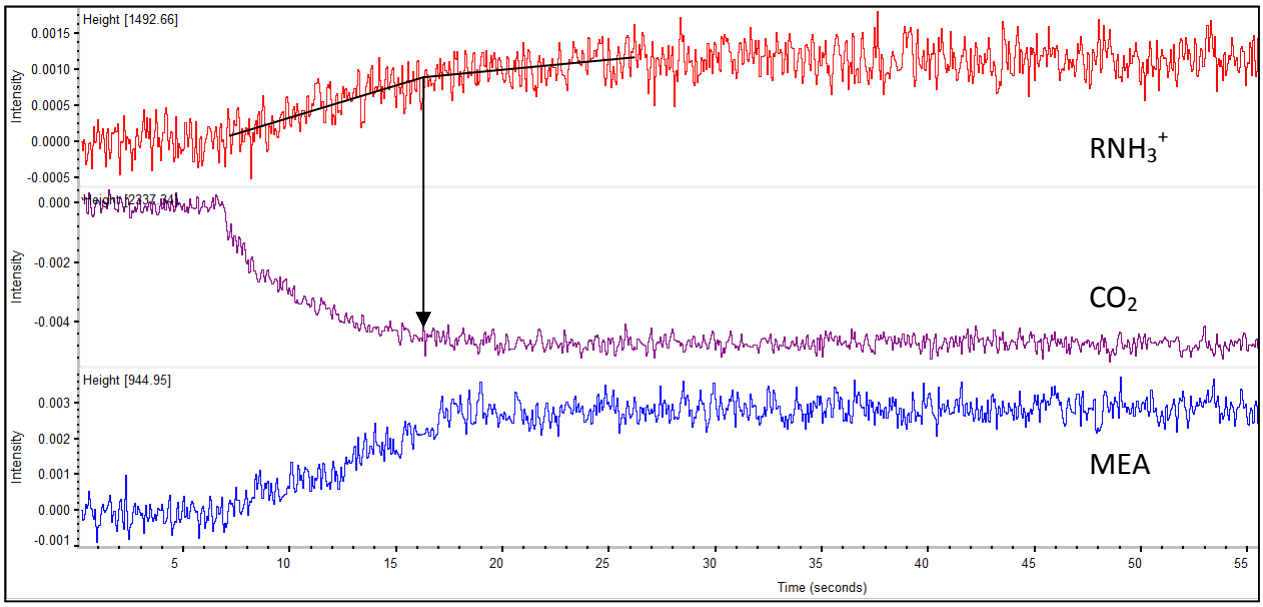

Figure 3.21 Typical Peak Area Profiles of CO_2, MEA and RNH_3^+/MEA Obtained During Data Collection. Reaction Conditions: 35°C, [MEA]:[CO_2] = 10:1 and an MEA molar flow rate of 0.011 mol/s. The x-axis denotes Time in seconds and the y-axis Peak Height (displayed as Intensity).

Figure 3.21 shows that the peak height profiles obtained are in agreement with the reaction mechanism. The peak height of CO_2 decreases sharply as it reacts with the MEA that is being pumped into the reactor at a constant molar flow rate. The peak height of RNH_3^+ increases as expected, since it is a product of the reaction. From the slope lines drawn in **Figure 3.21** it may be noticed that there is a decrease in the slope of the RNH_3^+ profile in the time zone where CO_2 approaches its equilibrium value. This change of slope indicates that the product formation has

slowed down as it also nears equilibrium. The fact that the profile keeps increasing instead of levelling out is only indicative of the MEA effect on the RNH_3^+ peak height (see section 3.5.4).

Applying the calibration factors of **Table 3.2**, **Table 3.4** and **Table 3.5**, a concentration time profile for the three species was obtained. For the purpose of modelling semi-batch reactor data it was beneficial to convert the concentration data into molar amounts. This was achieved by taking the volumetric flow rate of the MEA/alcohol mixture into account.

The initial volume inside the reactor was calculated from the mass of n-Propanol loaded into the reactor and the density of n-Propanol at the experimental temperature. The final volume inside the reactor was calculated from the mass of MEA/n-Propanol injected into the reactor. Since both MEA and n-Propanol was pre-heated before it was loaded into the reactor, minimal thermal expansion occurred. In order to convert molar concentration data to molar amounts, the exact volume at each point in time must be known. It was therefore of utmost importance that both the flow rate of MEA/alcohol and the pump initiation time for each experiment was known. The pump initiation time was determined by examining the peak height profiles. From **Figure 3.21** it may be noticed that there is a point in time in the CO_2 profile where the peak height starts decreasing sharply. This point in time was chosen as the reaction (and pump) initiation time. The volume inside the reactor would increase constantly from this time until the final reactor volume was reached.

All three species that were measured by FTIR could now be converted from concentration to molar amounts. A further advantage of this conversion is the simplification of calculating the concentration of the zwitterion intermediate by means of an elemental carbon mole balance.

3.8.1 Carbon Balance to Calculate the Zwitterion Concentration

Once the MEA correction was made in order to obtain the true RNH_3^+ concentration (see section 3.5.4) all that remains to account for all the species in equation 3.3 was to calculate the concentration of the zwitterion intermediate. The other salt product concentration was assumed to be equal to the concentration of RNH_3^+, since these two compounds will always exist in equal stoichiometric quantities according to the reaction mechanism.

The zwitterion concentration was calculated by means of a carbon balance. In order to simplify the syntax of the equations, equation 3.3 is simplified to:

$$CO_2 + RNH_2 \underset{k_2}{\overset{k_1}{\rightleftharpoons}} Z$$
$$Z + RNH_2 \underset{k_4}{\overset{k_3}{\rightleftharpoons}} 2S \qquad 3.10$$

The carbon balance may be written as:

$$n_{C,\text{in}} = n_{C,\text{out}}$$
$$\therefore n_{CO_2,\text{initially}} = n_{CO_2} + n_Z + n_S$$
$$\therefore n_Z = n_{CO_2,\text{initially}} - n_{CO_2} - n_S$$

The number of moles of zwitterion was easily converted to concentration data by means of the volume profile inside the reactor as described in section 3.8. All species in equation 3.3 were accounted for on both a molar amount and concentration basis.

3.8.2 FTIR Measurement Repeatability Study

FTIR has built up a reputation for being one of the most repeatable methods of analysis available (Sherman Hsu, 1997). The accuracy and sensitivity of the results, however, depends strongly on the quality of the background spectra used. This study revealed the importance of ensuring that the most appropriate purge conditions in a temperature controlled environment are achieved and maintained. The reason for this level of precision in operation lies in both the use of an ATR element as well as the procedure followed in executing the experiments.

As mentioned in section 3.4.1, ATR is known for its high IR attenuation requiring the use of the most sensitive liquid N_2 cooled MCT detector to obtain the greatest sensitivity possible during measurements of especially species of low concentration. The probe mirrors must also be aligned in order to maximize the signal strength of the IR beam returning from the ATR crystal on its way to the detector.

Since CO_2 is one of the target species for analysis, it had to be purged from the reaction atmosphere as thoroughly as possible. It was found that the purge time required for reducing

the amount of atmospheric CO_2 to above 93% removed (user specified quality check in OMNIC®) varied between 2 and 5 hours due to fluctuations in the laboratory atmosphere and the content of CO_2 in the baseline N_2 used as purge gas.

At above 93% CO_2 removed from the spectrometer atmosphere and after purging the instrument for a day before any experimental work were performed, the most repeatable, accurate results were obtained. An ideal operation of the spectrometer would be to have it constantly purged with dry CO_2 free N_2, but this would be a very expensive operation and is therefore not practical. It is, therefore, recommended that as many experiments as possible are carried out once optimum purge conditions are obtained and maintained.

Negative peak heights in the data scatter were encountered for all three species of interest at low concentrations. This may be attributed to a decrease in the signal to noise ratio at these low concentrations. This was one of the reasons for collecting 256 scans per background reference, in order to maximize the signal to noise ratio at low concentrations. The signal to noise ratio decreases as the species concentration decreases causing inaccuracy of the measured peak heights.

The calibration curves obtained for both CO_2 and MEA, however, revealed a linear correlation passing through the origin with an $R^2 = 0.99$ in all cases. It was therefore assumed that at lower concentrations (i.e. lower measured peak heights) the calibration factors were still valid. At lower concentrations of MEA and RNH_3^+, there was inevitably a greater scatter in the data due to a decrease in the signal to noise ratio. ATR is not the ideal technology for measuring low species concentrations (Sherman Hsu, 1997). This is why the data collection was designed to have all peaks increase in height as the reaction progresses. The CO_2 peak is a special case, since its peak height increases negatively as described in section 3.5.5.

The measurement repeatability was firstly confirmed during calibration as described in sections 3.5.2 - 3.5.5 and as expected, the FTIR lived up to its reputation of being a method of analysis with a high degree of repeatability under optimum, steady state purge conditions. The repeatability of the experimental runs was confirmed by performing three experiments at similar experimental conditions for all temperatures and relative concentrations. Similarly,

good repeatability was found for all conditions and so the three runs at 35°C and [MEA]:[CO_2] = 10 will be shown as an example.

The experimental parameters of the three runs are tabulated in **Table 3.7**

Table 3.7 Experimental Parameters for Repeatability Study at 35°C and [MEA]:[CO_2] = 10:1

Experimental Run #	n_{CO2} loaded (mol)	n_{MEA} injected (mol)	F_{MEA} (mol/s)	[RNH_3^+] from Titration (mol/dm^3)
35_10_1	0.0115	0.117	0.0105	0.0202
35_10_2	0.0121	0.121	0.0108	0.0207
35_10_3	0.0126	0.129	0.0112	0.0207

The stoichiometric ratios obtained for the three reaction runs were:

$$35\_10\_1: n_{\text{MEA, reacted}} : n_{CO_2\text{, reacted}} = 2.1$$
$$35\_10\_2: n_{\text{MEA, reacted}} : n_{CO_2\text{, reacted}} = 2.1$$
$$35\_10\_3: n_{\text{MEA, reacted}} : n_{CO_2\text{, reacted}} = 1.9$$

After titration of the samples withdrawn from the reactor, the following was determined:

$$35\_10\_1: n_{RNH_3^+\text{, formed}} : n_{CO_2\text{, loaded}} = 0.9$$
$$35\_10\_2: n_{RNH_3^+\text{, formed}} : n_{CO_2\text{, loaded}} = 0.9$$
$$35\_10\_3: n_{RNH_3^+\text{, formed}} : n_{CO_2\text{, loaded}} = 0.9$$

A visual representation of the repeatability of the CO_2 concentration profiles is illustrated in **Figure 3.22**. The data in **Figure 3.22** proves the repeatability of the method to monitor a reaction accurately under the optimum purge conditions as well as affirming the validity of the conductometric method of analysis for RNH_3^+. Similar quality repeatability of both the MEA and RNH_3^+ concentration profiles were obtained. The repeatability in measurements for the other reaction conditions investigated was similar to the example presented here. The consistency in the stoichiometry achieved, proved that the equilibrium concentration ratio is

only dependent upon the initial concentration ratio and not on the initial molar amounts. This proves the validity of using a dilution series to calibrate for the salt product.

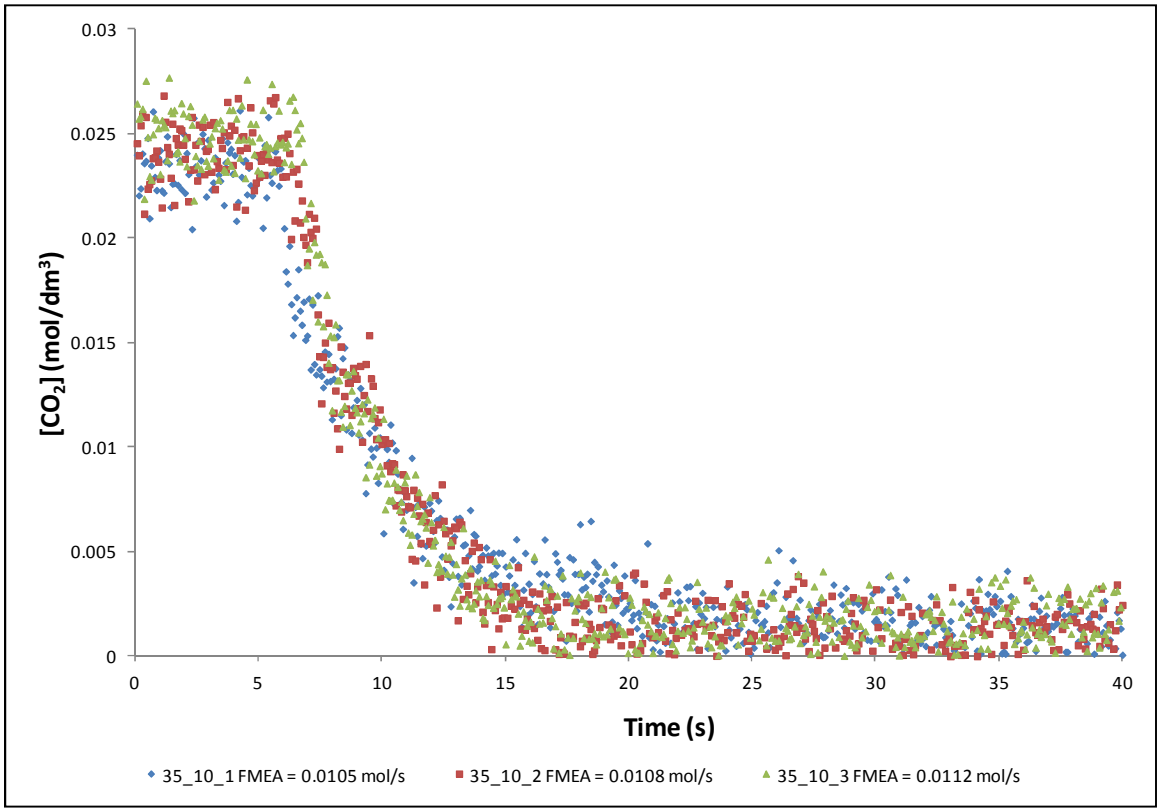

Figure 3.22 Repeatability of CO_2 Concentration Profiles at 35°C and [MEA]:[CO_2] = 10:1

3.8.3 Molar Amount vs. Time Profiles

An illustrative example of the initial stage of the reaction at 35°C, 1 atm, [MEA]:[CO_2] = 10:1 and F_{MEA} = 0.0112 mol/s is shown in **Figure 3.23**. It should firstly be noted from **Figure 3.23** that the profiles are presented on separate axis because of the great excess of MEA in the system. The profiles in **Figure 3.23** were in complete agreement with the zwitterion reaction mechanism. It was even able to capture the initial rise in the number of moles of the zwitterion during the dominance of the first reaction in the mechanism.

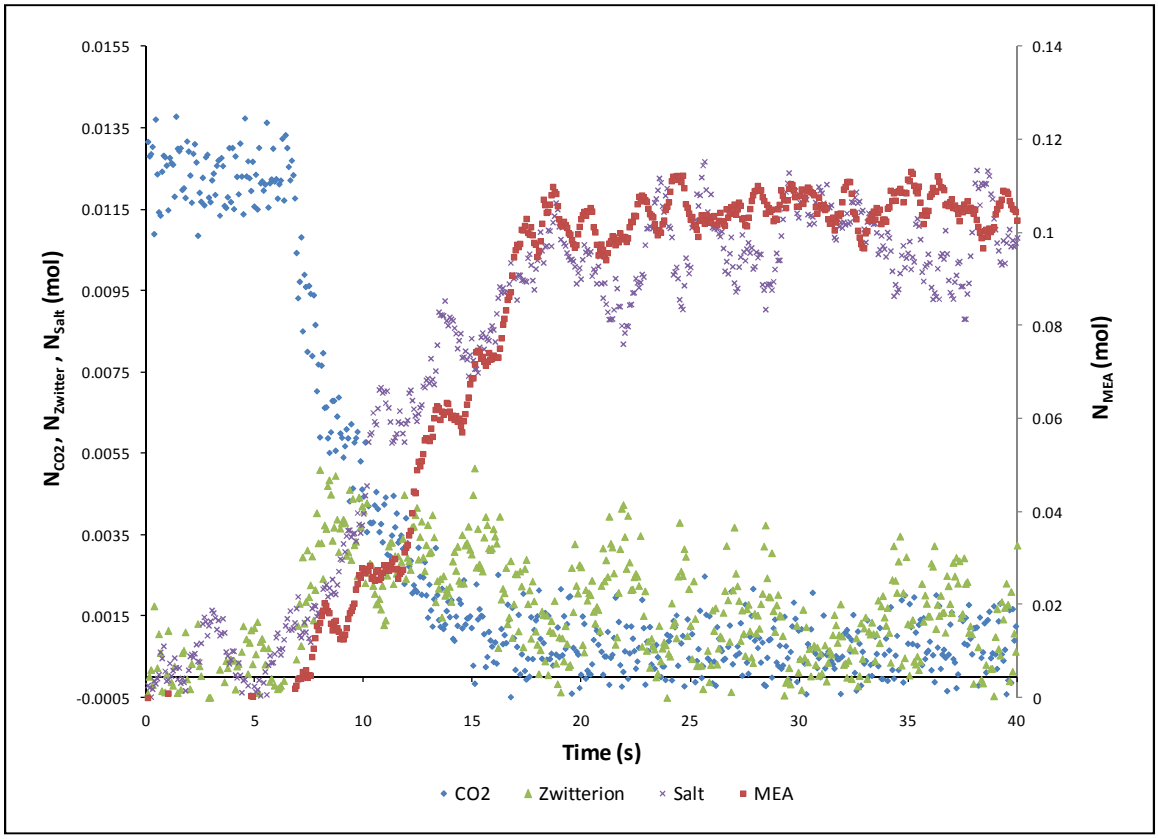

Figure 3.23 Molar amount vs. Time Profiles for the First 40 seconds of Data Collection at 35°C, 1 atm, [MEA]:[CO_2] = 10:1 and F_{MEA} = 0.0112 mol/s

The life time of the zwitterion is short, indicated by its sharp decrease as the deprotonation reaction starts taking place. The lifetime and maximum zwitterion concentration decreases with an increase in relative initial MEA concentration. It indicated that MEA, as the only base present in the reaction mixture, was responsible for deprotonating the zwitterion and as the MEA concentration increases, so does the rate of zwitterion deprotonation.

The visible formation and reaction of the zwitterion in **Figure 3.23** is in support of the zwitterion mechanism and in disagreement with a mechanism such as the termolecular mechanism. The termolecular mechanism assumes that the reaction occurs in one step, without the formation of a reactive intermediate. This will be discussed in further detail in section 4.3.2 once the concentration data has been modelled. The rapid nature of the reaction was noticed in the sharp decrease of both the zwitterion and CO_2 molar amounts and concentrations. This is

agreement with the findings in literature (Versteeg & van Swaaij, 1988; Sada, et al., 1986; Alvarez-Fuster, et al., 1981) and serves to affirm that this reaction is suitable for effective area determination. It may further be noticed that, with the effect of MEA on the salt peak area taken into account, the salt product reaches its equilibrium concentration at approximately the same time as the CO_2 profile. This is in further agreement with the zwitterion reaction mechanism.

One of the considerations made to improve on the data scatter noted in the concentration vs. time profiles was to impose a moving average on the data. It was found that a period of 10 (every data point represents the average the 10 following it) was sufficient for reducing the scatter in the MEA data, a period of 5 for CO_2 and 15 for RNH_3^+. **Figure 3.23** shows MEA with its moving average already imposed. The results of imposing the moving average on CO_2 and RNH_3^+ molar data is illustrated in **Figure 3.24**.

There is conceivably a periodic trend noticeable in the salt and MEA profiles in **Figure 3.24**. The slight periodic trend in the MEA curve could be a result of the rotations of the peristaltic pump not delivering an absolutely constant flow rate when considering very small volume segments. The trend in the salt profile is in fact an amplification of the slight periodic trend of the MEA concentration curve, since the MEA concentration has an influence on the concentration of RNH_3^+ through its peak interference as discussed in section 3.5.4. The effect of imposing a moving average on the data will be further investigated when the data is modelled in Chapter 4.

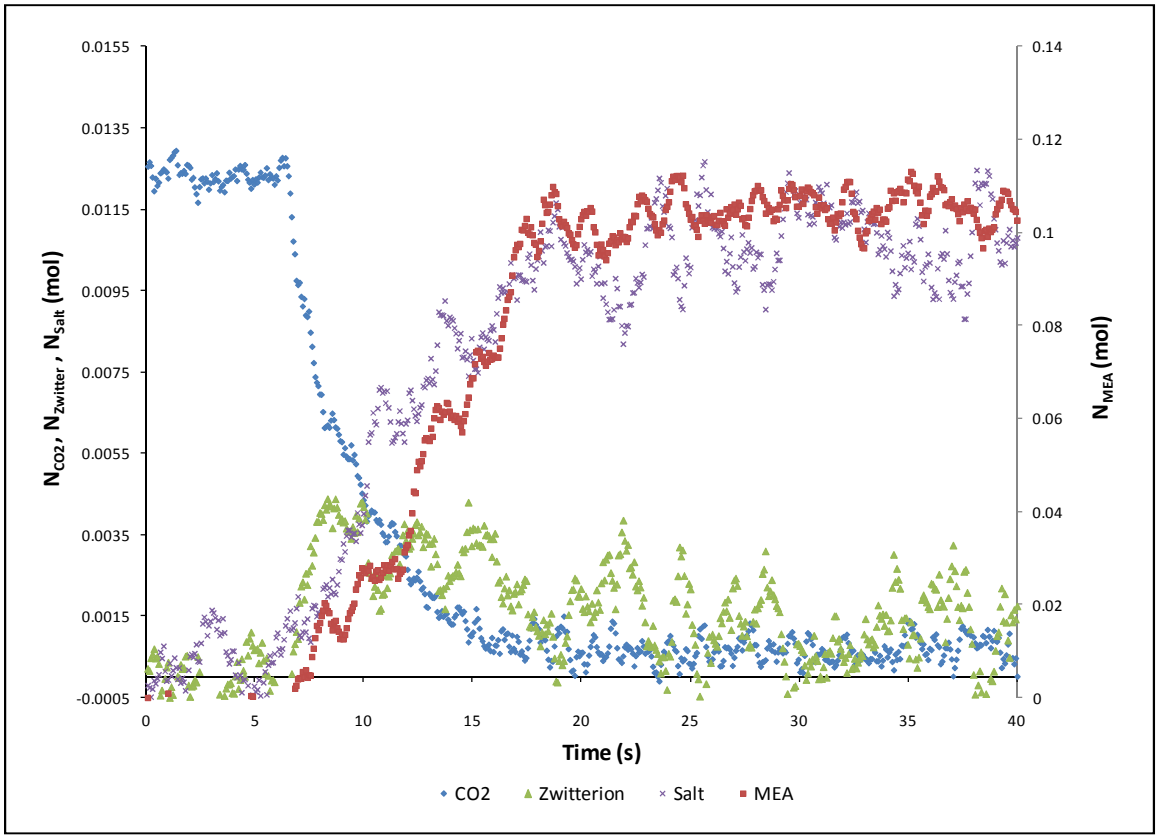

Figure 3.24 Data Scatter Reduction in the Molar Amount profiles. Data Collection at 35°C, 1 atm, [MEA]:[CO_2] = 10:1 and F_{MEA} = 0.0112 mol/s

3.8.4 Effect of MEA Molar Flow Rate

The effect of the molar flow rate of MEA (F_{MEA}) into the reactor will firstly be discussed. The effect of flow rate was investigated to ensure that the data collected was under reaction kinetic control. For fast reactions, reaction equilibrium is also achieved quickly. It is, therefore, of interest to see if the data measured is in fact reaction kinetic data and not just a flow rate of a reagent influencing the reaction equilibrium already achieved. An illustrative example of the effect of F_{MEA} may be seen in comparison of the CO_2 concentration profiles of **Figure 3.25**.

The two profiles represent reaction runs with similar initial concentrations of CO_2 in the reactor. It further represents reaction conditions at [MEA]:[CO_2] = 5:1 and 10:1 with the run at 5:1 having the lower F_{MEA}. At the higher F_{MEA}, more MEA is introduced to the reactor per second, leading to higher concentrations of MEA to react with CO_2. This increase in concentration

increases the rate of reaction (steeper slope in the concentration profile at higher F_{MEA}) which was expected and is supported by the data in **Figure 3.25**.

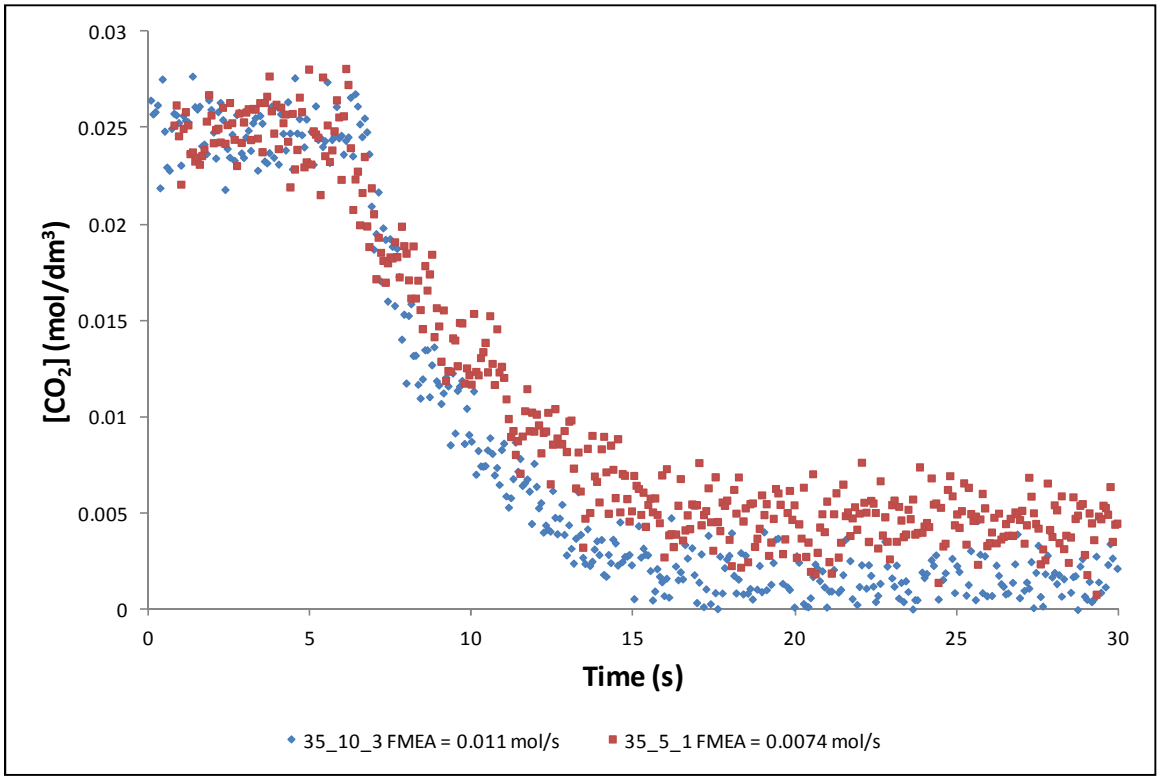

Figure 3.25 Effect of MEA Molar Flow Rate on the CO_2 Concentration vs. Time Profiles. Data Collection at 35°C, 1 atm

The data in **Figure 3.25**, therefore indicates that the reaction was most likely monitored under reaction kinetic control but was not conclusive in this regard. A validation of reaction kinetic control may rather be found when the profiles of **Figure 3.23** and **Figure 3.24** are also considered. The fact that the zwitterion formation and deprotonation is clearly visible from the measured data serves to prove that kinetic control is achieved during the measurements. If the reaction achieved instantaneous equilibrium, the formation and deprotonation of the zwitterion would not be visible. Another possible test is to investigate how the equilibrium constant of the reaction changes with time. This is presented in the next section when an analysis of the equilibrium data is performed

3.8.5 Analysis of Equilibrium Data

A summary of the equilibrium reaction stoichiometry, CO_2 and MEA conversion is tabulated in **Table 3.8**.

Table 3.8 Summary of Reaction Kinetic Data

[MEA]:[CO_2] = 5:1									
Temperature (°C)	**25**			**30**			**35**		
Run #	**25_5_1**	**25_5_2**	**25_5_3**	**30_5_1**	**30_5_2**	**30_5_3**	**35_5_1**	**35_5_2**	**35_5_3**
$N_{MEA,reacted}$:$N_{CO2,reacted}$	2.0	2.0	1.9	2.0	2.0	1.9	2.0	2.1	2.0
$N_{MEA,reacted}$:$N_{Salt,formed}$	1.9	1.9	1.9	1.9	2.0	2.1	2.0	2.0	2.0
$N_{CO2,reacted}$:$N_{salt,formed}$	1.0	1.0	1.0	1.0	1.0	1.1	1.0	0.9	1.0
CO_2 Conversion (%)	87.74	87.08	90.20	87.43	87.69	86.89	80.26	82.59	82.48
Average X_{CO2} (%)		**88.34**			**87.34**			**81.78**	
MEA Conversion (%)	33.20	34.79	33.15	33.77	34.67	33.26	30.64	33.72	34.81
Average X_{MEA} (%)		**33.71**			**33.90**			**33.06**	
[MEA]:[CO_2] = 10:1									
Temperature (°C)	**25**			**30**			**35**		
Run #	**25_10_1**	**25_10_2**	**25_10_3**	**30_10_1**	**30_10_2**	**30_10_3**	**35_10_1**	**35_10_2**	**35_10_3**
$N_{MEA,reacted}$:$N_{CO2,reacted}$	1.9	1.9	1.9	2.0	2.0	1.9	2.1	2.1	1.9
$N_{MEA,reacted}$:$N_{Salt,formed}$	2.1	1.9	2.0	2.1	2.1	2.1	2.1	2.1	2.1
$N_{CO2,reacted}$:$N_{salt,formed}$	1.1	1.0	1.0	1.0	1.0	1.1	1.0	1.0	1.1
CO_2 Conversion (%)	98.12	97.04	97.20	97.06	97.55	97.72	93.27	96.58	94.96
Average X_{CO2} (%)		**97.45**			**97.45**			**94.93**	
MEA Conversion (%)	19.13	18.74	19.41	19.24	19.07	18.27	18.86	20.31	17.59
Average X_{MEA} (%)		**19.09**			**18.86**			**18.92**	

It may firstly be noticed that for all reactions, the equilibrium stoichiometry falls within the range specified in section 3.5.6. These experiments were therefore regarded as successful. The data in **Table 3.8** further illustrate that the reaction may indeed be considered to be reversible, since 100% CO_2 conversion was never achieved. As shown in **Figure 3.25**, the conversion of CO_2 increased for an increase in [MEA]:[CO_2]. This was expected and is confirmed by the equilibrium data in **Table 3.8**. An increase in MEA conversion was noticed with a decrease in [MEA]:[CO_2]. At both the [MEA]:[CO_2] conditions, appreciable interfacial depletion will occur during specific absorption studies, rendering the pseudo first order assumption invalid (Tsai, 2010). According to the objectives of this study, these conditions are of interest, since it was

desirable to study the effect of surface depletion and renewal rates on effective interfacial mass transfer area. This will be discussed further in Chapter 6 and Appendix B.

As mentioned in section 3.5.5 a sensitivity analysis of the CO_2 conversion with respect to the error bars of the CO_2 calibration factor was performed. It was found that for the range of CO_2 calibration factors resulting from the range in data scatter the CO_2 conversion varied by ±2.4% in the worst case. The exothermic nature of the reaction may be confirmed by studying the effect of temperature on CO_2 conversion. It may be noticed from the data in **Table 3.8** that the CO_2 conversion decreases significantly when the temperature increases from 25°C to 35°C, with the sensitivity analysis results taken into consideration. This is consistent with an exothermic reversible reaction and is in agreement with literature (Hikita, et al., 1976; Fogler, 1999).

The same trend was not necessarily noticed for MEA. Since MEA takes part in both reactions in equation 3.3, the influence of temperature on MEA conversion was considered to have a higher degree of complexity. Another factor to consider is that the exact amount of MEA injected into the reactor could never be determined to a high enough degree of accuracy to make any firm conclusions with regard to the effect of temperature on the MEA conversion.

Based on the reaction mechanism of equation 3.3, the equilibrium constant of the reaction was calculated as follows:

$$K_C = \frac{\left[RNH_3^+\right]_{equil}^2}{\left[RNH_2\right]_{equil}^2 \left[CO_2\right]_{equil}} \qquad 3.11$$

The equilibrium constants calculated for the 18 successful data sets collected in this study is tabulated in **Table 3.9**. Since no data on the reaction equilibrium of CO_2 and MEA in n-Propanol could be found in literature, a comparison with published data was not possible.

Table 3.9 Calculated Equilibrium Constants

[MEA]:[CO_2]	**5**		**10**	
Temperature (°C)		**K_C**		**K_C**
25		25.5		30.1
		25.4		22.2
		32.5		24.7
	Average	27.8	Average	25.7
30		25.1		20.2
		23.6		24.6
		20.8		21.7
	Average	23.2	Average	22.1
35		11.2		8.4
		19.7		18.3
		17.5		9.1
	Average	16.1	Average	12.0

From the data it may be seen that there are in some instances a large difference in the calculated equilibrium constant for same reaction conditions. This is most notable at 35°C and [MEA]:[CO_2] = 10:1. When comparing the average K_C values for the sets of three runs, there is good agreement between the [MEA]:[CO_2] = 10:1 and [MEA]:[CO_2] = 5:1. This shows that, although this method is not ideal for studying the reaction equilibrium, the calculated K_C values are independent of relative concentration, which is fundamentally correct. The temperature dependence of the average calculated K_C is illustrated in **Figure 3.26**.

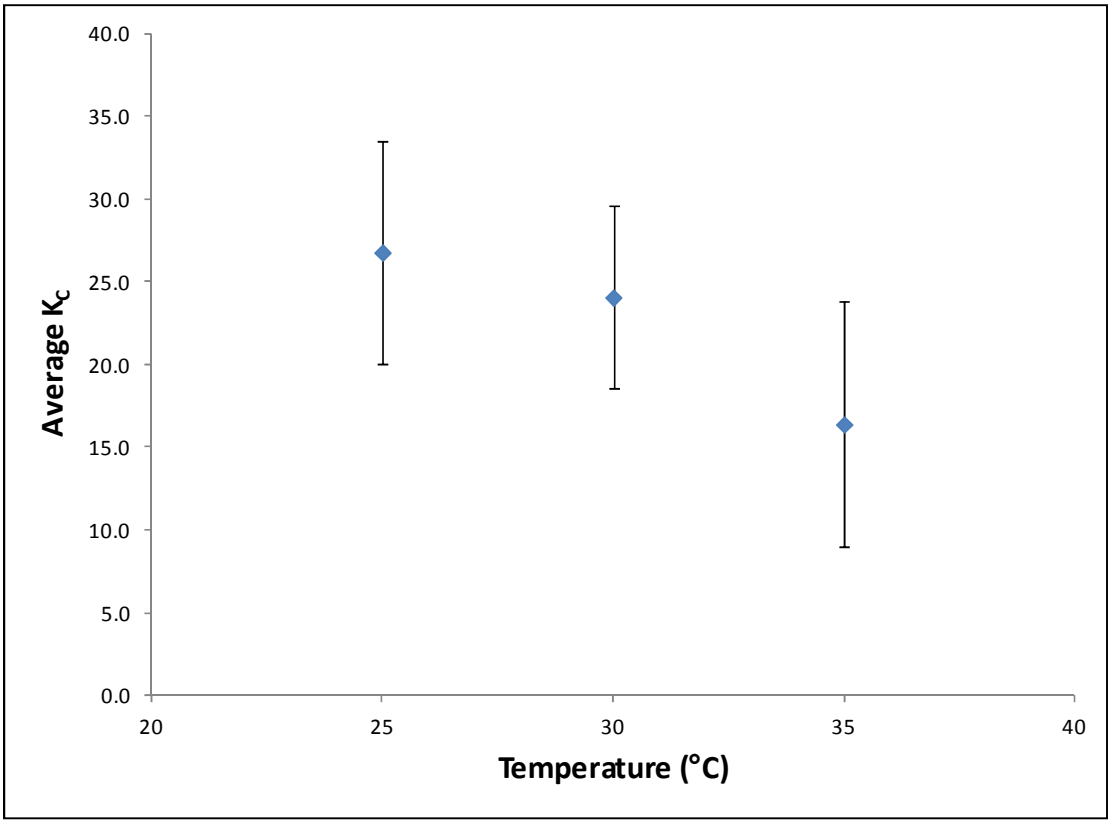

Figure 3.26 Average K_C Values as a Function of Temperature

The data in **Figure 3.26** show that there is a noticeable decrease in K_C for an increase in temperature. This is consistent with an exothermic reaction (Fogler, 1999). The large error bars are firstly a result of the range of K_C values calculated for each of the three experimental data sets that were averaged for the calculated K_C value presented in **Figure 3.26**. The error bars are also representative of a sensitivity analysis performed with regards to the CO_2 calibration factor. The magnitude of the error bars once again shows that the method is not suitable for a truly accurate equilibrium data analysis. Due to this reason, the heat of reaction was not calculated from the equilibrium data, since the accuracy of the heat of reaction result will not be sufficient.

As mentioned in section 3.8.4, an analysis of the change of the equilibrium constant with time will provide further information to whether or not the reaction is indeed under kinetic control. The time dependence of K_C for an experimental run at 25°C and [MEA]:[CO_2] = 5:1 is illustrated in **Figure 3.27**.

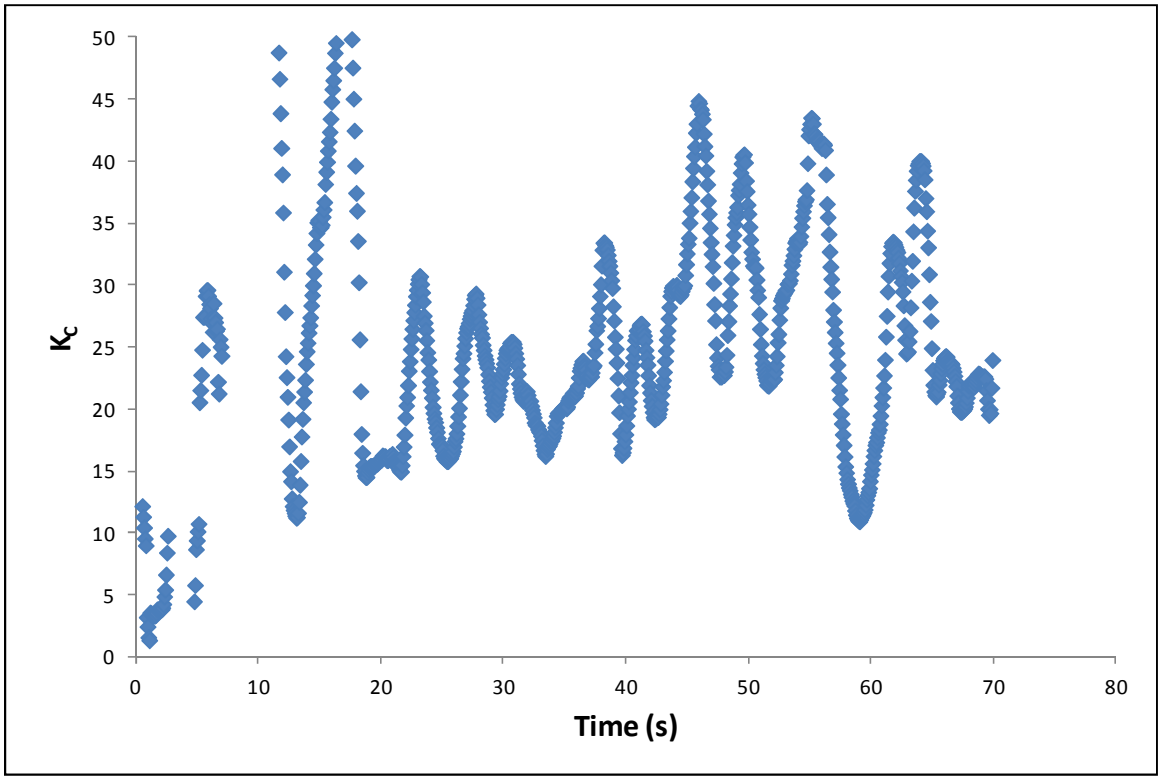

Figure 3.27 Change in K_C with Time for an experimental run at 25°C and [MEA]:[CO_2] = 5:1

The data in **Figure 3.27** is noisy and caution should, therefore, be applied when drawing conclusions from the data. The data do, however, seem to indicate that K_C increases from zero to its average value of approximately 25 from 40 seconds onward. If the reaction was equilibrium controlled, K_C would be at its average value for the entire time period. The increase in K_C during the first 30 seconds of data collection is in further support of the data being under kinetic control when the measurements were made. A similar trend was noticed for all experimental data sets collected in this study.

With 18 successful data sets collected and ear marked for modelling, the process of selecting and evaluating the best representative rate expressions for this reactive system may be presented. This will be presented in Chapter 4.

3.9 Chapter Conclusions

This chapter introduced the zwitterion reaction mechanism for the reaction of CO_2 with the primary amine, MEA in the alcoholic solvent system, n-Propanol. It further discussed a novel, FTIR method developed in this study to collect rapid real time concentration data during the liquid phase reaction time. The reaction was monitored successfully using a semi-batch reactor with a gas tight floating head to maintain a constant pressure of 1atm (abs) as an MEA/alcohol mixture was pumped into the reactor at a constant flow rate to react with the dissolved CO_2. The concentration of the salt product, RNH_3^+ was determined via a conductometric titration method of analysis also developed in this study.

Based on the success of the calibration, validation and experimental procedure studies performed, it may be concluded that the FTIR method is suitable for the reaction kinetic study of CO_2 with MEA in alcoholic solvents. The measured peak height profiles as a function of real time displayed the correct trend with regards to the widely accepted zwitterion reaction mechanism. The zwitterion mechanism describes the reaction of CO_2 with primary amines in non-aqueous solvents where MEA is the only base responsible for deprotonating the zwitterion. An elemental carbon mole balance was performed to calculate the zwitterion concentration profile as a function of time. The zwitterion concentration profile showed a sharp increase in the initial stages of the reaction, followed by a sharp decrease as the excess MEA deprotonated it to form the salt products. Under the optimum purge conditions, 18 successful data sets were collected for the concentration and temperature range of this study and these data sets were selected for the modelling of both existing and newly proposed reaction rate expressions on the experimental data.

Chapter 4 REACTION KINETICS RESULTS AND MODELLING

In Chapter 3 the novel FTIR method of analysis for studying the liquid phase reaction of CO_2 with MEA in the alcoholic solvent, n-Propanol was developed and discussed. All experiments were conducted at a pressure of 1 atm (abs). Refer to Appendix E for the actual amounts of reagents used in each of the 18 data sets chosen for modelling purposes. The actual amounts used in each experiment are linked with the concentration ratio ([MEA]:[CO_2]) investigated in that specific experiment. The data in this chapter will be presented in terms of [MEA]:[CO_2] and the molar flow rate of MEA into the reactor.

The relevant reaction kinetic points of discussion that will be addressed in this section are:

- The best representative rate expressions and the rate parameters associated with them
- A discussion on the applicability of current literature models to describe this important reaction.
- Proposing a fundamental model that best describes this reactive system.

4.1 Modelling of Semi-batch Reaction Kinetic Data

In this section the modelling procedure and results of both the existing and proposed rate expressions for the reaction of CO_2 with MEA in alcoholic solvents are presented. The existing rate expressions, derived mostly from heterogeneous studies under conditions where pseudo first order kinetics were assumed, will firstly be evaluated and discussed, followed by new, fundamentally derived rate expressions. The equations governing semi-batch reactor operation and kinetics were established in this section. These equations form the basis from where the reaction kinetic rate parameters were determined.

4.1.1 Semi-batch Reactor Design Equations

The design equations for a semi-batch reactor are well known and form part of basic theory in courses on reactor design. There are many forms of semi-batch reactor design equations, all in order to interpret different forms of kinetic data. The data presented in this study is of both molar and of concentration format, so the most basic form of semi-batch reactor design equations is called for.

The semi-batch reactor considered in this study is one with a constant molar feed rate of MEA. The starting point for deriving the equations for each of the reaction species is a material balance based on the conservation of mass (Fogler, 1999):

$$[\text{Molar Flow Rate In}]-[\text{Molar Flow Rate Out}]+[\text{Rate of Generation}]=[\text{Rate of Accumulation}]$$

Or in mathematical terms for CO_2:

$$[0]-[0]+\left[r_{CO_2}\cdot V(t)\right]=\left[\frac{dN_{CO_2}}{dt}\right]$$

which may be simplified to:

$$\frac{dN_{CO_2}}{dt}=r_{CO_2}\cdot V(t) \qquad 4.1$$

Similarly for the other species in equation 3.3

$$\frac{dN_{Zwitter}}{dt}=r_{Zwitter}\cdot V(t) \qquad 4.2$$

$$\frac{dN_{RNH_3^+}}{dt}=r_{RNH_3^+}\cdot V(t) \qquad 4.3$$

And for the inflowing MEA:

$$\frac{dN_{RNH_2}}{dt}=r_{RNH_2}\cdot V(t)+F_{RNH_2} \qquad 4.4$$

For a semi-batch reactor, the reactor reaction volume is a function of time (hence $V(t)$ in equations 4.1 - 4.4). For a constant molar feed to the reactor, this time dependence is linear and may be expressed by:

for $0 \le t \le t_{\max}$:

$$V(t) = V(0) + \dot{V} \cdot t \qquad 4.5$$

and for $t > t_{\max}$:

$$V(t) = V(t_{\max}) \qquad 4.6$$

where $\dot{V}$ is the constant volumetric flow rate into the reactor delivered by the peristaltic pump and $t_{\max}$ represents the time elapsed during reagent delivery to the reactor. It was found through experiment that MEA and n-Propanol form an ideal solution. There was, therefore, insignificant volume change with mixing inside the reactor, confirming the validity of using equation 4.5 to calculate the time dependence of the reaction mixture volume as a function of time. The molar flow rate of MEA, F_{RNH_2}, was calculated from the total volumetric flow rate and the concentration of MEA in the syringe reservoir. Equations 4.1 - 4.4 are the representative equations optimized in the modelling algorithm for different forms of the rate expressions, r_j. It is the different forms of the rate expressions that will be investigated in this study.

4.1.2 Modelling Procedure

Mathematically, the CO_2-MEA reaction system may be expressed in terms of a set of coupled ordinary differential equations (equations 4.1 - 4.4), as determined by the choice of reaction rate expression. Each rate expression prescribes a set of linear coefficients (the rate constants) that must be solved to fit the model to the experimental data. Hence, the numeric problem is an optimisation problem with a multi-objective goal. However, there are some complicating factors to consider.

The first challenge in fitting any of the considered models lies with defining the multi-objective goal. It may seem simple at first acquaintance: Define the goal as some error function of the predicted molar amount. But, whereas the experimental data measure molar concentration, the coefficient vector of the model is defined on the set of reaction rate equations. In other words, the integral of the rate equations must be determined in order to define the model optimisation goal. The preferred approach to this challenge is to choose an appropriate ODE solver in combination with a suitable multi-objective goal finder. Alternative approaches that may attempt to numerically differentiate the mole concentration data are hampered by numerical inaccuracies due to the amplification of experimental noise in the data when numerical differentiation is performed.

The multi-objective goal attainment algorithm, the MATLAB R2011a function, *fgoalattain* was used in this study. This algorithm applies sequential quadratic programming (Gembicki, 1974) to attain a multi-object goal, optionally subject to constraints. The ordinary differential equations were solved using a modified Rosenbrock formula of order 2 (Brayton, et al., 1979), for stiff ODE systems with constant mass matrix, the MATLAB R2011a function, ode23s. For a particular model, the maximum sum square error (SSE) of each predicted mole concentration was set as the individual goal, based on an equivalent maximum error of 10% per reaction constituent. The multi-objective function was defined as a vector of the sum squared error of the experimental and model predicted species concentrations:

Multi-Objective Function:

$$\begin{bmatrix} \sum \left(C_{i,\text{exp}} - C_{i,\text{predicted}} \right)^2 \\ \vdots \end{bmatrix} \quad \text{where } i = \text{CO}_2, \text{RNH}_2 \text{ etc.} \tag{4.7}$$

The goal vector in *fgoalattain* was defined as 10% of the sum of squares of the measured species concentrations. In other words, the optimization was aimed at arriving at a predicted value that is less than the sum squared of 10% of the experimental concentration:

$$\text{goal} = \sum \left(0.1 C_i \right)^2 \text{ with } i = \text{CO}_2, \text{RNH}_2 \text{ etc.} \tag{4.8}$$

Since the concentrations to be fitted were of different orders in magnitude, the individual goals were weighted to imply the same relative importance:

$$\text{weight} = \left|\text{goal}\right| \qquad 4.9$$

This nullified the order of magnitude difference in the concentration data with regards to the optimization. The data used for modelling was selected as a subset of the full data set. The subset ranged from reaction initiation (time when CO_2 concentration starts to decrease) to 15 seconds of reaction time that followed. This subset was consistent with the transient region of the reaction and included a few seconds (2-3 seconds) where the reaction has reached equilibrium. One of the reasons for collecting data at a resolution of 32 cm^{-1} was to maximise the number of data point in the transient region of the reaction. This allows the model estimation algorithm to use smaller time steps when fitting the rate equations to the data.

The second challenge was raised by local minima in the optimisation error surface. Due to the model structures under consideration, numerous local minima can be expected which will handicap efforts of finding a global optimal solution for the model coefficient (rate constant) vector. A pragmatic approach to this problem is to configure a sufficient number of optimisation trials, each starting from a different set of scaled random, initial conditions – initial coefficient vectors, in this case. The scale of the initial guesses was obtained from the order of magnitude of published rate constants. The overall best solution was selected at the end of the trial runs and the rate constants resulting from the best solution were used as the optimised initial guesses for subsequent modelling.

The chosen work-flow of the modelling problem is described in the flow diagram of **Figure 4.1**.

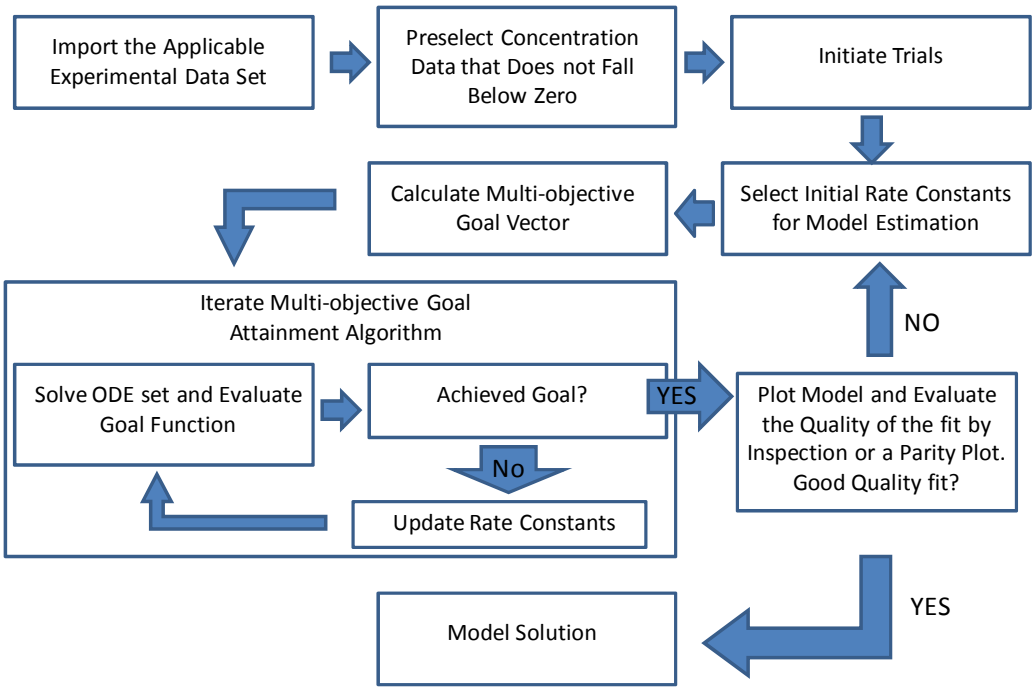

Figure 4.1 Flow Diagram of Modelling Procedure

When using *fgoalattain*, no Jacobian matrix in terms of the model parameters was available for use in determining the confidence intervals of the estimated rate constants. The confidence intervals of the rate constants were estimated via a bootstrap procedure. 20 randomly selected subsets of data containing 90% of the original data set were selected for each of the reaction species in the specific model fit. The optimization algorithm was performed on each subset and the best fit selected based on the lowest attainment factor achieved. The attainment factor is an indication of how well the algorithm attained its goal, with an attainment factor of zero indicating a perfect model fit.

The bootstrap resulted in 20 sets of optimised rate constants. There were, thus, 20 optimised values for each of the rate constants of a particular model. From these sets, the 5 and 95 percentile were calculated to comprise the bracket or maximum estimated confidence interval for each rate constant in the proposed rate expression. It should be noted that the true confidence interval for the rate constants will be smaller than the range given by the 5 and 95 percentile but the larger interval may be used as a more conservative estimate of accuracy.

A possible way to estimate the true confidence interval would be to construct a histogram of the rate constants estimated from the 20 bootstrap trials. From the histogram, the distribution of each estimated rate constant around the mean of the trial set may be found. The confidence interval will be selected as one standard deviation from the mean, for example. This approach was, however abandoned due to the interconnectedness of the rate constants. The best model fit is obtained for a certain combination of rate constants. It could, therefore, happen that a combination of one rate constant near the 5 percentile and one near the 95 percentile produce the best fit. A histogram analysis may not include these values in its narrower estimated confidence interval, meaning the optimum fit is excluded from the confidence interval. This was tested and found to be the case for some of the data sets and it was therefore decided to present the data with the maximum confidence interval instead.

The median of the 20 sets were also determined, along with the best model fit based on the lowest attainment factor. The rate constants which gave the best model fit along with the median, upper bound (95% percentile) and lower bound (5% percentile) will be presented in the sections to follow. The quality of the model fit was determined by plotting the estimated concentration profile along with the experimental data on the same graph.

As mentioned in section 3.8.3 an investigation was made into the effect of smoothing the data before modelling. In order to eliminate the bias brought on by smoothing operations, it was decided to use as little smoothing as possible. CO_2 concentrations were not smoothed. MEA was smoothed using a forward moving average with a period of 10, whilst RNH_3^+ had a period of 15. Smoothing was kept to a minimum, but was considered sufficient to decrease scatter in the data in order to clarify the trend noticed in the data.

4.2 Existing Rate Expressions

The three most popular rate expressions used in literature to attempt to describe the reaction kinetics of CO_2 and MEA in both aqueous and non-aqueous solvent systems are the power rate law, pseudo steady state hypothesis (PSSH) rate law and the pseudo first order rate law. A literature review on the most popular rate expressions was presented in section 3.1.2. In this

section the best model fits obtained on the experimental data for these rate expressions will be presented under the conditions where they are considered to be valid. A discussion on the quality of the model fits and the behaviour of the estimated rate constants will follow.

4.2.1 Power Rate Law Model

One of the simplest rate expressions assumed to be valid for describing the reaction of CO_2 and MEA is the power rate law model (Alvarez-Fuster, et al., 1981; Laddha & Danckwerts, 1981). The rate expression was derived under the assumption that under certain conditions the reaction is practically irreversible and that the deprotonation of the zwitterion is fast enough for it to not have any influence on the overall reaction rate. This situation was discussed in section 3.1.2 and the general power rate law expression may be given as:

$$-r_{CO_2} = k\left[CO_2\right]^m \left[RNH_2\right]^n \qquad 4.10$$

The majority of previous research suggests that the reaction order with respect to MEA and CO_2 is unity for all solvents, but in alcoholic solvents the reaction order with respect to MEA is 2 (Alvarez-Fuster, et al., 1981; Sada, et al., 1986). These are the reaction orders that will be assumed valid for the purpose of modelling the experimental data collected in this study. The power rate law rate expression modelled is thus of the form:

$$-r_{CO_2} = k_1\left[CO_2\right]\left[RNH_2\right]^2 \qquad 3.8$$

Strictly speaking, a true power rate law investigation will estimate the reaction orders as well. That was not done in this study, since the aim was to evaluate the power rate law expression proposed in literature. Estimation of the reaction orders should, however, be investigated in future. For the power rate law, only equations 4.1 and 4.3 were solved and optimised, since only CO_2 and MEA are included in the rate expression. The order of magnitude of the initial guess for the third order rate constant of equation 3.8 was taken from literature (Davis & Sandall, 1993). The order of magnitude was 10^2 and the initial guess was set at 100. The initial guess was varied between 100 and 900, with no significant effect on the resulting estimated rate constant.

It was expected that the power rate law rate expression would not be able to accurately fit the data collected in this study, since it was found in Chapter 3 that the reaction is indeed governed by a reversible reaction mechanism. A model fit at [MEA]:[CO_2] = 10:1 for n-Propanol at 30°C (run#: 30_10_1) is illustrated in **Figure 4.2**.

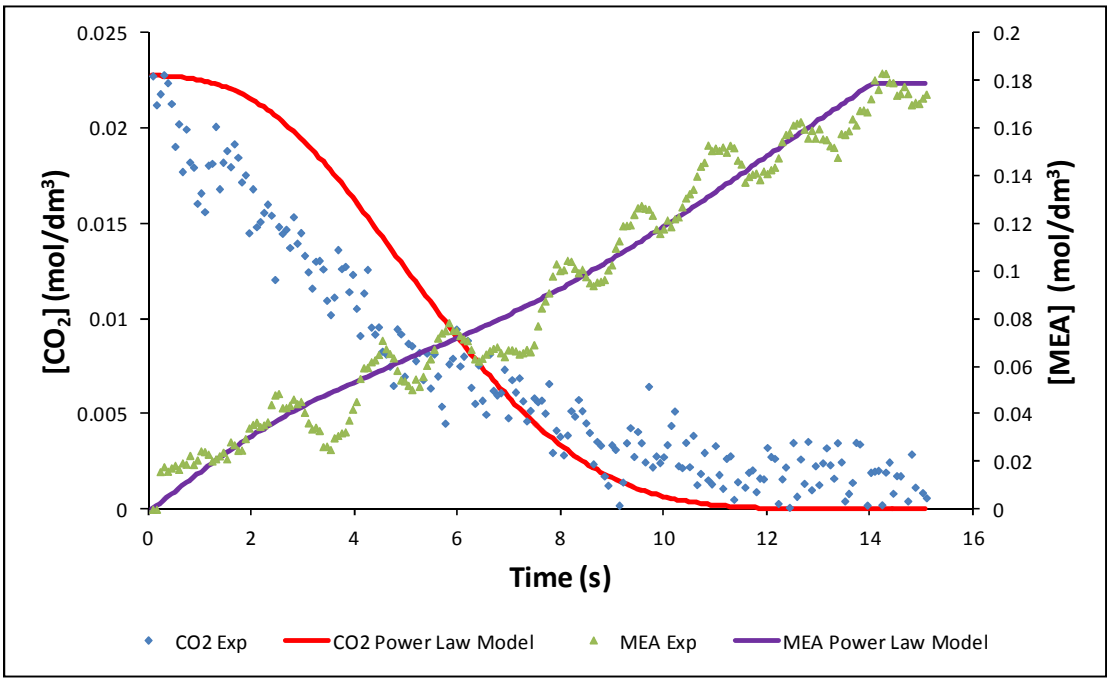

Figure 4.2 Power Rate Law Model Fit for the Reaction of CO_2 with MEA in n-Propanol at 30°C, [MEA]:[CO_2] = 10:1 (run#: 30_10_1)

The model fit illustrated in **Figure 4.2** confirms the expected poor fit. The irreversibility of the model structure is evident from the fact that the predicted CO_2 concentration falls to zero and is maintained throughout the reaction equilibrium. The model also over-predicts the initial CO_2 concentration. The model predicts the MEA concentration profile well, but this may be due to the MEA molar flow rate term of equation 4.4 enforcing a good fit on the data. A similar quality fit was noticed over the entire temperature and concentration range investigated in this study. It is evident that the model does not fit the experimental data well in the region leading up to reaction equilibrium. This is due to the fundamental reversible nature of the reaction as well as the deprotonation of the zwitterion having an effect on the reaction rate in this region.

The reaction rate constants for the power rate law model fit are tabulated in **Table 4.1**.

Table 4.1 Power Rate Law Rate Constant for n-Propanol

[MEA]:[CO_2] = 5:1				
T (°C)		***k*** ***($dm^6.mol^{-2}.s^{-1}$)***	**MSE x 10^6** **Equation 4.1**	**Equation 4.4**
25	Best fit	322	4.28	52.5
	Upper Bound (95%)	437	4.64	45.3
	Median	301	4.02	53.2
	Lower Bound (5%)	129	3.17	85.3
30	Best fit	260	3.35	23.9
	Upper Bound (95%)	272	3.36	23.1
	Median	246	3.35	23.5
	Lower Bound (5%)	216	3.36	24.9
35	Best fit	101	4.46	32.9
	Upper Bound (95%)	162	4.24	22.9
	Median	135	4.22	25.2
	Lower Bound (5%)	99	4.49	33.4
[MEA]:[CO_2] = 10:1				
T (°C)		***k*** ***($dm^6.mol^{-2}.s^{-1}$)***	**MSE x 10^6** **Equation 4.1**	**Equation 4.4**
25	Best fit	494	2.51	190
	Upper Bound (95%)	564	2.53	190
	Median	473	2.50	189
	Lower Bound (5%)	416	2.51	188
30	Best fit	363	2.92	58.6
	Upper Bound (95%)	528	2.72	62.3
	Median	410	2.70	59.2
	Lower Bound (5%)	359	2.80	58.1
35	Best fit	191	3.64	36.8
	Upper Bound (95%)	310	3.58	38.2
	Median	252	3.57	37.7
	Lower Bound (5%)	182	3.65	36.5

The data in **Table 4.1** are arranged to firstly show the estimated rate constant that produced the best fit of the experimental data. The upper bound, median and lower bound give an idea of the range of estimated rate constants obtained from the bootstrap approach described in

section 4.1.2. The data represents the average estimated rate constant for the three runs conducted at the same temperature and [MEA]:[CO_2] relative concentrations. The Mean Squared Error (MSE) values presented in **Table 4.1** respresents the average of the sum of squared errors for each optimised differential equation. The MSE values gives and indication of how closely the predicted concentration values are to the experimental data. A small MSE (10^{-7}-10^{-6}) indicates a close agreement.

As the tabulated data shows, the third order rate constant, k, was found to vary as the concentration range of this study varied. The data shows an increase in k for an increase in [MEA]:[CO_2]. Since a rate expression with a fundamental basis, should have a rate constant independent of concentration (Fogler, 1999) it means that the power rate law has no fundamental basis for describing this reaction. Furthermore, the estimated rate constants show a decrease in value for an increase in temperature, which results in negative activation energy for the reaction. This is fundamentally incorrect and further confirms the conclusion that the power rate law is not suitable for describing the reaction of CO_2 with MEA in alcoholic solvents under conditions where there is appreciable conversion of MEA.

The MSE values indicate that the model fit, although not good, shows the correct trend. The upper bound and lower bound values were all in the order of ±50 - ±80 from the median. It should be noted that the true confidence interval is expected to be smaller than the range given by the upper and lower bound values, since these values represent the extreme. This suggests that the estimated rate constant has a good confidence interval.

Therefore, the power rate law is not rejected as a simplifying rate expression to be used under conditions where an irreversible pseudo $(m,n)^{th}$ order reaction may be assumed valid. It is, however, rejected as a model structure to use under conditions where interfacial depletion of MEA is appreciable and will thus not be used in the method developed in this study to measure effective interfacial mass transfer area under conditions where interfacial depletion exists.

4.2.2 Pseudo Steady State Hypothesis Model

From literature studies concerned with deriving only the reaction kinetics for the reaction of CO_2 with MEA, one of the most popular rate expressions was derived based on the pseudo steady state hypothesis (PSSH) assumption (Versteeg & van Swaaij, 1988). The PSSH assumption assumes that the effective rate of reaction with regards to the zwitterion in equation 3.3 is zero (refer to Appendix E.1 for derivation). This essentially means that the zwitterion is consumed as soon as it is produced. Applying this assumption, along with assuming that both salt products in equation 3.3 always have the same concentration (see section 3.8.1) equation 3.4 results:

$$-r_{CO_2} = \frac{k'''[CO_2][RNH_2]^2 - k_4\left[RNH_3^+\right]^2}{1 + k''[RNH_2]} \qquad 3.4$$

where $k'' = \frac{k_3}{k_2}$ and $k''' = k_1 k''$. Under the PSSH assumption the following holds true:

$$-r_{CO_2} = 0.5\left(-r_{RNH_2}\right) \qquad 4.11$$

$$r_{RNH_3^+} = -r_{RNH_2} - \left(-r_{CO_2}\right) \qquad 4.12$$

which is essential information for the modelling algorithm to solve the set of ordinary differential equations. It may be noticed from equation 3.4 that the rate constants appear as lumped entities, with the individual constants, k_2 and k_3 impossible to determine individually. This is one of the limitations of the PSSH assumption. Being unable to determine these rate constants individually makes a temperature dependence investigation of these constants difficult to perform and interpret.

The order of magnitude for the initial guesses for the rate constants in equation 3.4 were taken from literature (Sada, et al., 1985). The first fit was attempted with all the rate constants having an order of magnitude of 10^3. It was, however found that a better fit could be obtained if the order of magnitude were as follows:

$k''' \rightarrow 10^3$, k'' and $k_4 \rightarrow 10^2$

It was noticed in this study that the PSSH rate expression gave an overall good quality fit on the experimental data. An example of a good quality model fit is illustrated in **Figure 4.3**.

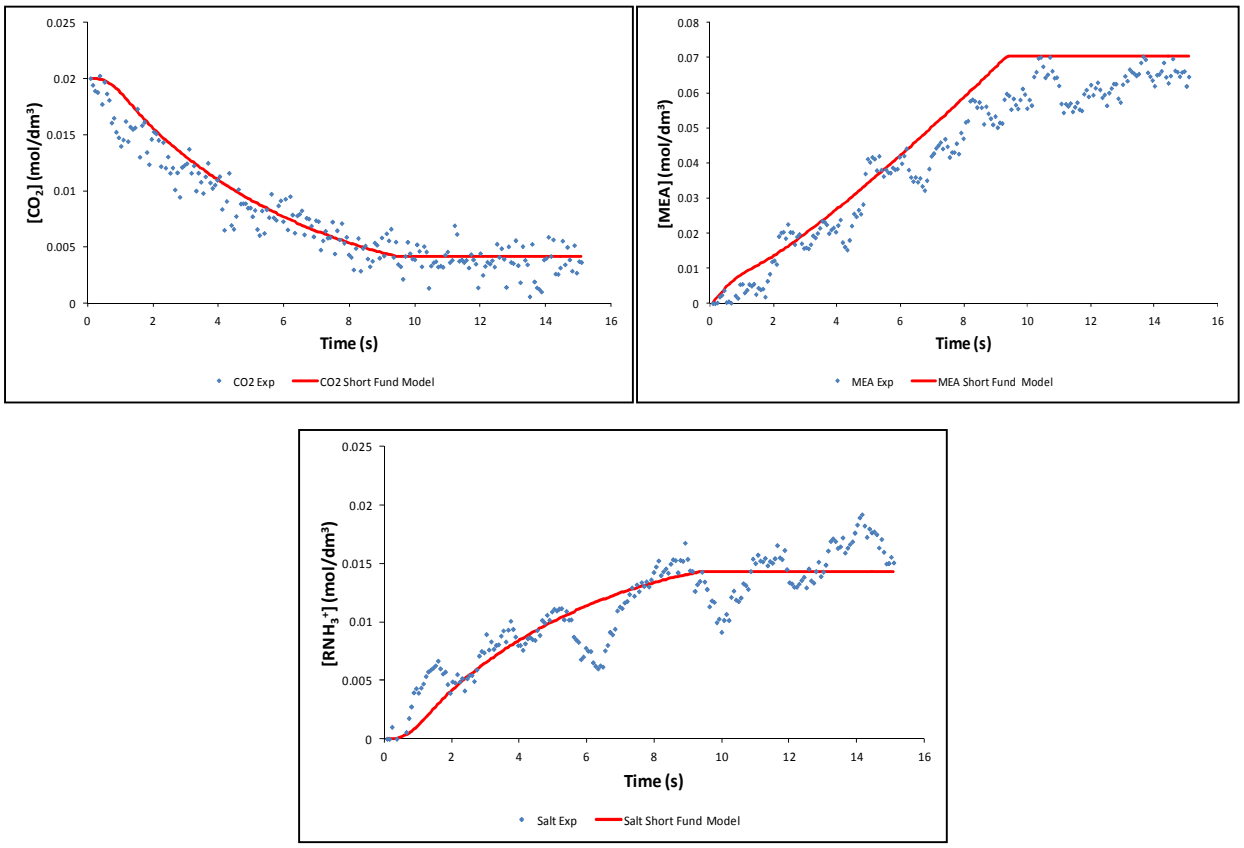

Figure 4.3 PSSH Rate Law Model Fit for the Reaction of CO_2 with MEA in n-Propanol at 35°C, [MEA]:[CO_2] = 5:1 (run# 35_5_2)

The data in **Figure 4.3** showed that the PSSH model was able to follow the correct trend in the data for both the transient and equilibrium stages in the reaction. Not all the fits were of the same good quality as illustrated in **Figure 4.3**. An example of a poor quality model fit is illustrated in **Figure 4.4**.

For the data set of **Figure 4.4**, the PSSH model showed an under prediction for the CO_2 concentrations and an over prediction the MEA and RNH_3^+ concentrations. A possible reason

for this was because the data for this specific experiment was not well behaved at especially low MEA and RNH_3^+ concentrations. Data scatter at the low concentrations may cause the model to have an incorrect starting point relative to the data.

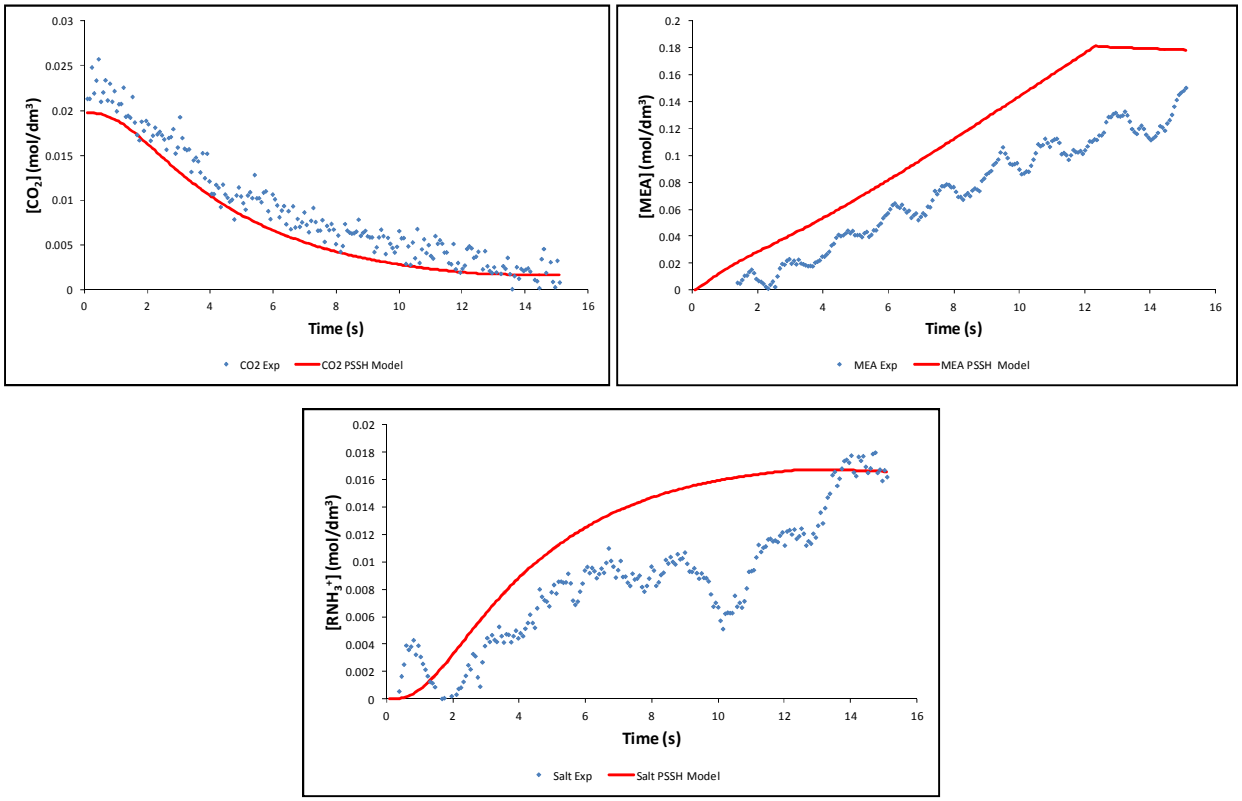

Figure 4.4 PSSH Rate Law Model Fit for the Reaction of CO_2 with MEA in n-Propanol at 25°C, [MEA]:[CO_2] = 10:1 (run# 25_10_2)

The MEA concentration profile of **Figure 4.4** is an example of this. The data scatter caused an incorrect initial decrease in the MEA concentration. The PSSH model was unable to cope with the initial decrease and continued to overestimate the MEA concentration data. This should not be attributed to the inadequacy of the model alone, but should also be interpreted as a limitation in the data collection method at these low concentrations. This was found to be a recurring problem for all the rate expressions investigated in this study. The reaction rate constants that provided the best quality model fit for the PSSH model are tabulated in **Table 4.2**.

Table 4.2 Pseudo Steady State Hypothesis Rate Law Rate Constants for n-Propanol

[MEA]:[CO_2] = 5:1							
Temp (°C)		***k'''*** ***($dm^6.mol^{-2}.s^{-1}$)***	***k''*** ***($dm^3.mol^{-1}.s^{-1}$)***	***k_4*** ***(s^{-1})***	**MSE x 10^6 Equation 4.1**	**Equation 4.4**	**Equation 4.3**
25	Best fit	1072	38	52	3.24	55.7	5.92
	Upper Bound (95%)	1525	153	122	1.48	98.2	2.02
	Median	1005	81	87	1.28	94.5	2.32
	Lower Bound (5%)	987	22	13	4.11	47.3	8.45
30	Best fit	904	119	110	2.50	57.4	3.86
	Upper Bound (95%)	1002	156	155	2.96	62.7	3.58
	Median	962	115	115	2.34	54.3	3.97
	Lower Bound (5%)	812	98	90	2.31	55.0	4.09
35	Best fit	1112	91	72	1.15	29.2	2.15
	Upper Bound (95%)	1112	117	121	1.48	35.9	1.95
	Median	1002	103	97	1.35	34.4	2.07
	Lower Bound (5%)	941	72	65	1.20	28.3	2.23
[MEA]:[CO_2] = 10:1							
Temp (°C)		***k'''*** ***($dm^6.mol^{-2}.s^{-1}$)***	***k''*** ***($dm^3.mol^{-1}.s^{-1}$)***	***k_4*** ***(s^{-1})***	**MSE x 10^6 Equation 4.1**	**Equation 4.4**	**Equation 4.3**
25	Best fit	1024	171	54	1.54	279	2.28
	Upper Bound (95%)	156159	20090	123	1.14	252	4.44
	Median	1000	119	68	1.23	252	4.26
	Lower Bound (5%)	971	78	8	1.10	267	4.35
30	Best fit	994	203	126	2.97	47.8	3.33
	Upper Bound (95%)	2018	391	128	3.02	57.7	3.35
	Median	999	218	35	2.01	55.8	4.71
	Lower Bound (5%)	800	103	0	1.21	53.4	6.88
35	Best fit	1423	199	1	1.17	41.9	2.06
	Upper Bound (95%)	2043	224	43	1.19	41.0	2.18
	Median	1014	120	14	1.27	40.3	2.30
	Lower Bound (5%)	986	79	0	1.38	39.8	3.35

The data in **Table 4.2** once again represents the average best fit, median, upper and lower bound of the three data sets collected at the same conditions. The data of **Table 4.2** show that the PSSH model fitted the data at [MEA]:[CO_2] = 5:1 with smaller confidence intervals. The large confidence intervals at [MEA]:[CO_2] = 10:1 raises some concern about the accuracy of the fitted rate constants for these data sets. A further reason for concern in this regard lies with the expectation that the PSSH model should provide a more accurate fit at higher [MEA]:[CO_2]. At higher MEA concentrations, it is expected that the zwitterion will be more easily and rapidly deprotonated. The PSSH model assumes that the zwitterion will deprotonate instantly, which is why a higher MEA concentration should provide for a more accurate fit. This was not the case in this study.

The data further shows that there is possibly a concentration dependence for k'' and k_4. This shows that the PSSH model is not entirely fundamentally correct, since the rate constants should be independent of concentration. The estimated rate constant further shows no discernable temperature relation that could be used to calculate the activation energies of each of the reactions in the PSSH mechanism. The MSE values indicate that the PSSH model found it most difficult to fit the MEA concentration profile, a similar result when compared with the fits achieved by the power rate law model.

The PSSH model is, however, closer to the fundamental truth of the reaction mechanism compared with the power rate law model and due to some of the good fits achieved it is not completely rejected as a purely reaction kinetic model. However, due to the inconsistency of the rate constants over the concentration range of this study, along with an indeterminate temperature dependence of the highly complex rate constants, the PSSH model is rejected as a kinetic model for a study of effective interfacial mass transfer area.

4.2.3 Pseudo First Order Model

The simplest form of a rate expression considered applicable to a reactive absorption process where there is insignificant depletion of the liquid phase reactant during reaction is the pseudo first order rate expression. One of the current corner stone assumptions in calculating the

interfacial mass transfer area on separation column internals is that the absorption reaction is subject to pseudo-first order kinetics (Tsai, 2010). For the reaction of CO_2 with MEA, the MEA concentration is considered to remain constant and is lumped with the pseudo first order rate constant to obtain:

$$-r_{CO_2} = k'[CO_2] \qquad 4.13$$

The pseudo first order rate expression cannot be applied to reaction kinetic data measured in a semi-batch reactor system where the liquid phase concentration of MEA varies with time. A pseudo first order model assumes the MEA concentration to remain constant. A modelling attempt was, therefore, not done on the experimental data collected in this study.

The pseudo first order rate expression is, however, still considered to be a good approximation of the reaction kinetics of CO_2 with MEA under conditions where the MEA concentration may be considered to be constant. It remains a good approximation under conditions where MEA is in great excess and undergoes insignificant depletion in the liquid film.

4.3 Proposed Rate Expressions

It has now been established in this study that the existing rate expressions are insufficient in describing the reaction kinetics of CO_2 with MEA in alcoholic solvent systems for the concentration ranges where MEA depletion in the liquid film becomes appreciable. The power rate law model and PSSH model fail to describe the kinetics accurately over the range of concentrations and temperatures investigated in this study. The temperature dependence of the estimated rate constants for these models were either incorrect or carried no fundamental meaning. The PSSH model had more of a fundamental basis, but also failed to predict the reaction kinetics accurately at low MEA concentrations. Its lumped rate constants are complex to use and apply and were found to be inconsistent over a wide concentration range with indeterminate temperature dependence.

Two fundamentally derived model structures will be presented in this section. One is representative of the full zwitterion reaction mechanism in equation 3.3, whilst the other is a simplified model structure based on the nett equilibrium form of equation 3.3.

4.3.1 Fundamental Model

In order for the derivation of the proposed fundamental rate expression to be followed more easily, equation 3.3 is reintroduced:

$$\begin{aligned} &1)\ CO_2 + RNH_2 \underset{k_2}{\overset{k_1}{\rightleftarrows}} RNH_2^+COO^- \\ &2)\ RNH_2^+COO^- + RNH_2 \underset{k_4}{\overset{k_3}{\rightleftarrows}} RNHCOO^- + RNH_3^+ \end{aligned} \qquad 3.3$$

It was shown in section 3.8.1 that the mechanism may be presented in simplified syntax as:

$$\begin{aligned} &CO_2 + RNH_2 \underset{k_2}{\overset{k_1}{\rightleftarrows}} Z \\ &Z + RNH_2 \underset{k_4}{\overset{k_3}{\rightleftarrows}} 2S \end{aligned} \qquad 3.9$$

Based on the syntax of equation 3.9 the fundamental rate expressions proposed in this study may be derived and presented as follows:

$$-r_{CO_2} = k_1[CO_2][RNH_2] - k_2[Z] \qquad 4.14$$

$$-r_{RNH_2} = k_1[CO_2][RNH_2] - k_2[Z] + k_3[Z][RNH_2] - k_4[S]^2 \qquad 4.15$$

$$-r_Z = -k_1[CO_2][RNH_2] + k_2[Z] + k_3[Z][RNH_2] - k_4[S]^2 \qquad 4.16$$

$$-r_S = -k_3[Z][RNH_2] + k_4[S]^2 \qquad 4.17$$

From the number of rate constants to be estimated (4) and the degree of complexity of solving equations 4.14 - 4.17, the threat of local minima on the error surface was considered likely. This was one of the reasons why the rate expressions were first modelled with all concentrations having an order of unity. The second order imposed on the salt concentration is due to both salts occurring in equal molar amounts. The correct order of magnitude of the

initial guesses of the rate constants were also of great importance. For guidance in this regard, literature was consulted. One study on non-aqueous systems (ethanol and ethylene glycol) with high MEA concentrations (Alvarez-Fuster, et al., 1981) reported the second order rate constant, k_1, to be in the order of magnitude, 10^3 ($dm^3.mol^{-1}.s^{-1}$) at 20°C. There is no information available in literature regarding the other three rate constants, since the previous methods of analysis employed were unable to measure or deduce the separate values for these rate constants.

Based on the limited information available, the order of magnitude of the remaining three rate constants were estimated from the reaction kinetic data collected in this study. From the conversion data for CO_2 in **Table 3.8** it may be concluded that the equilibrium for the reaction lies far to the product side. This means that $k_1 > k_2$. The initial, order of magnitude estimates for k_2 were, therefore, set at 10. The initial, order of magnitude estimates for k_3 and k_4 were set at 10^2, with the following applicable: $k_3 > k_4$, once again due to the equilibrium of the reaction lying far to the product side.

The optimisation trial model fits obtained showed that the optimum initial guesses were when $k_1 > k_2$ with k_1 of order of magnitude 10^2 and k_2 of order of magnitude 10. It was found that k_3 and k_4 were of order of magnitude 10^2 except for 25°C where k_3 was of order of magnitude 10. It was, however, found that $k_3 < k_4$ gave the best model fits, indicating that the deprotonation rate of the zwitterion is slower than expected. It is known that the deprotonation of the zwitterion is slower in non-aqueous solvents compared to aqueous solvent systems (Sada, et al., 1986). This may be attributed to the weak basisity of MEA in n-Propanol and provides insight into the relative reaction rates of the two reactions in the mechanism.

The initial guesses implemented for the fundamental model area tabulated in **Table 4.3**.

Table 4.3 Initial Guesses for the Fundamental Model Fit

T (°C)	k_1 ($dm^3.mol^{-1}.s^{-1}$)	k_2 (s^{-1})	k_3 ($dm^3.mol^{-1}.s^{-1}$)	k_4 ($dm^3.mol^{-1}.s^{-1}$)
25	330	25	80	140
30	460	70	110	230
35	660	90	160	340

Similar to the PSSH model, the Fundamental model also showed better quality fits on some of the data sets, with less good fits on others. The Fundamental model showed a good quality model fit for more data sets than any other rate expression investigated, which is already evidence that it is the best representative rate expression for the temperature and concentration ranges investigated in this study. An example of a less good quality model fit is illustrated in **Figure 4.5**

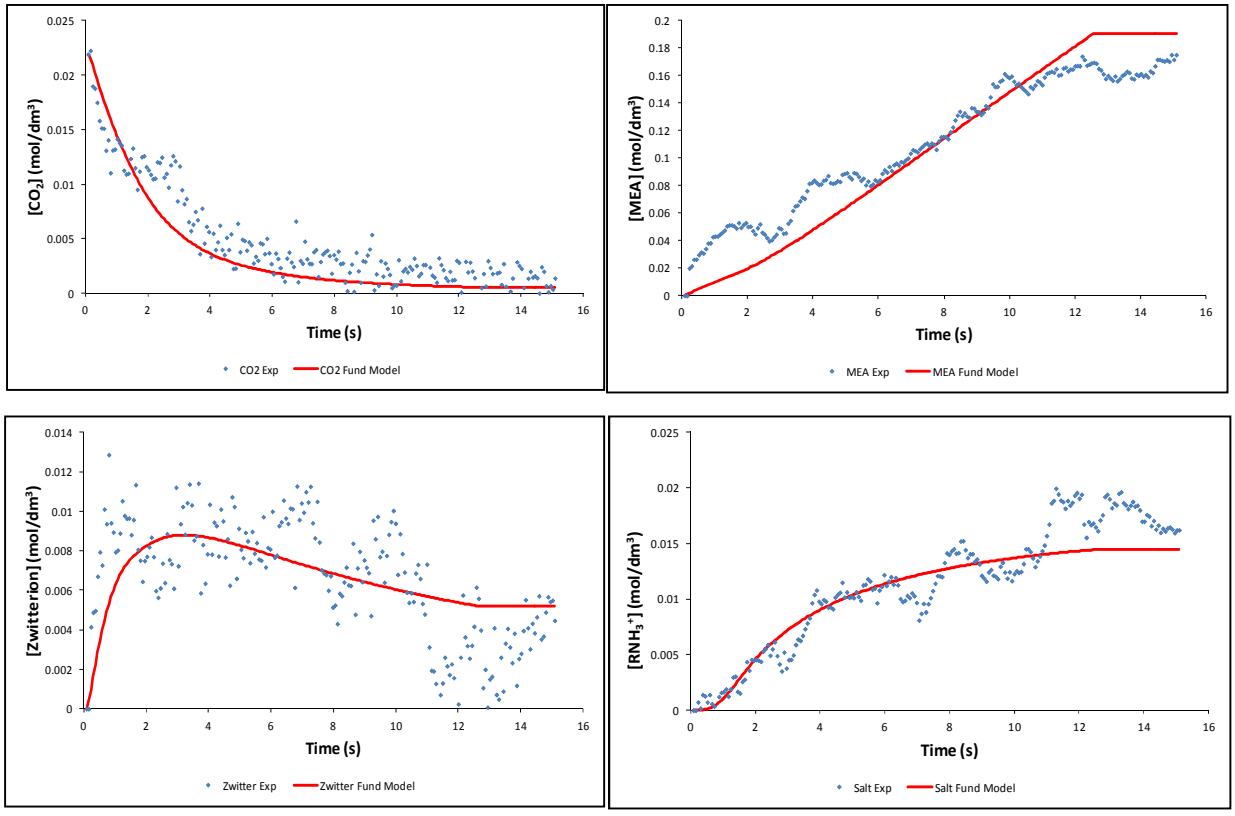

Figure 4.5 Fundamental Rate Model Fit for the Reaction of CO_2 with MEA in n-Propanol at 30°C, [MEA]:[CO_2] = 10:1 (run# 30_10_3)

The data in **Figure 4.5** show that even though this was identified as a less good model fit, a reasonable model fit is obtained for all four species of interest. A similar problem to the PSSH model at low MEA concentrations is once again noticed for the fundamental model fit. The data scatter at low concentrations caused the model to underestimate the MEA concentration in this region, which was the case for all rate expressions fitted on this data set. The model was, however, capable of following the correct trend for all reaction species. The predicted equilibrium concentrations for MEA and RNH_3^+ may be seen to be overestimated and underestimated, respectively. This effect could not be improved through investigation into changing the initial guesses of the model fit.

A possible reason for this deviation may lie in the fit on the zwitterion concentration profile. It was found that the scatter in the zwitterion data caused the model to overestimate its equilibrium concentration, which is expected to be close to zero. The model may, therefore have overestimated the MEA concentration and underestimated the RNH_3^+ concentration to compensate. This is one of the limitations of the data collection method. The data scatter in the zwitterion concentration profile was expected to cause difficulty for the modelling algorithm. The correct trend in the zwitterion concentration profile was, however obtained for all data sets. For data sets with a better behaved zwitterion concentration profile, the correct equilibrium concentrations for MEA and RNH_3^+ were obtained. These trends are illustrated in **Figure 4.6**.

The data in **Figure 4.6** shows a good quality model fit for the fundamental rate expression for all four reaction species. The equilibrium concentration of MEA and RNH_3^+ are more accurately determined due to the zwitterion concentration profile showing an equilibrium concentration closer to zero that that of **Figure 4.5**. The CO_2 concentration is slightly under predicted in the transient region and at equilibrium. This could not be improved with a change in initial guesses. The quality of fit of the fundamental model for all experimental data sets was similar to that shown in **Figure 4.5** and **Figure 4.6**.

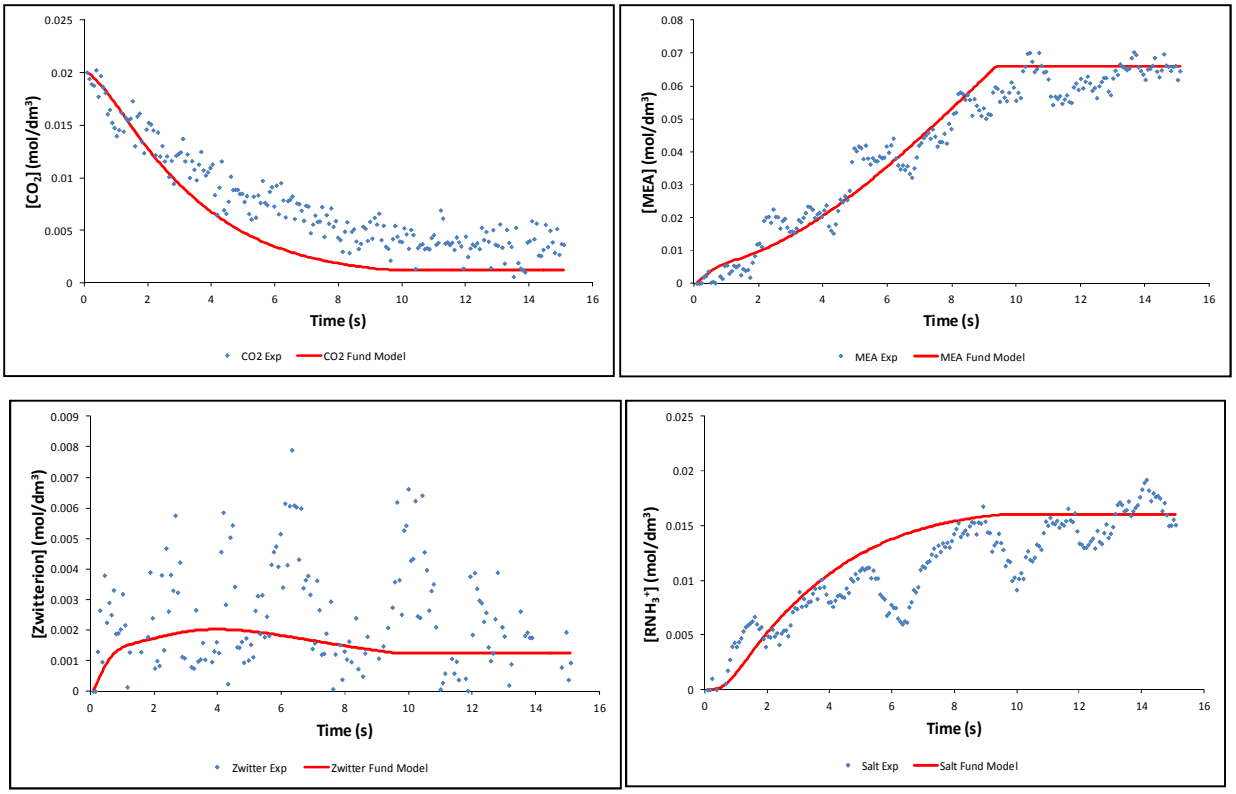

Figure 4.6 Fundamental Rate Model Fit for the Reaction of CO_2 with MEA in n-Propanol at 35°C, [MEA]:[CO_2] = 5:1 (run# 35_5_2)

The estimated rate constants for the fundamental rate expression are tabulated in **Table 4.4**. The data once again represents the average best fit, median, upper and lower bound of the three data sets collected at the same temperature and relative concentrations. The estimated model parameters for each experimental data set are given in Appendix E. The data firstly shows that there is consistency in the estimated rate constants for a change in concentration. This supports the fundamental nature of the rate expression. The largest deviation from consistency is noticed for k_1 at 35°C and k_3 at 25°C. The inconsistency of k_3 at 25°C did raise some concern, but since the other rate constants showed much better consistency, it was still concluded that the model has a sound fundamental basis.

Table 4.4 Fundamental Model Rate Law Rate Constants for n-Propanol

[MEA]:[CO_2] = 5:1									
T (°C)		k_1 ($dm^3.mol^{-1}.s^{-1}$)	k_2 (s^{-1})	k_3 ($dm^3.mol^{-1}.s^{-1}$)	k_4 ($dm^3.mol^{-1}.s^{-1}$)	MSE x 10^6 Eq. 4.1	Eq. 4.2	Eq. 4.4	Eq. 4.3
25	Best fit	322	24	70	112	2.23	96.9	1.51	1.68
	Upper Bound (95%)	409	46	149	183	1.57	111	2.06	3.13
	Median	327	23	92	120	1.90	90.1	1.85	2.09
	Lower Bound (5%)	283	8	53	59	4.40	70.3	1.78	2.43
30	Best fit	448	22	112	229	2.54	58.7	2.77	4.48
	Upper Bound (95%)	802	64	473	598	1.34	57.4	5.22	3.91
	Median	476	19	88	249	2.69	57.5	2.82	4.06
	Lower Bound (5%)	405	9	59	217	4.27	58.3	3.54	5.28
35	Best fit	590	22	314	328	6.42	28.2	2.02	5.93
	Upper Bound (95%)	694	224	408	404	2.61	61.5	2.52	5.39
	Median	648	129	194	316	1.84	60.9	2.56	5.59
	Lower Bound (5%)	473	40	129	142	2.84	33.7	2.33	3.11

Table 4.4 continued.

[MEA]:[CO_2] = 10:1									
T (°C)		k_1 ($dm^3.mol^{-1}.s^{-1}$)	k_2 (s^{-1})	k_3 ($dm^3.mol^{-1}.s^{-1}$)	k_4 ($dm^3.mol^{-1}.s^{-1}$)	MSE x 10^6 Eq. 4.1	Eq. 4.2	Eq. 4.4	Eq. 4.3
25	Best fit	330	15	44	160	1.10	201	1.28	1.53
	Upper Bound (95%)	423	29	65	216	0.73	185	2.39	1.24
	Median	334	17	50	161	1.20	189	1.95	1.41
	Lower Bound (5%)	289	12	28	147	1.64	198	1.29	1.41
30	Best fit	461	25	116	243	1.58	65.9	1.60	1.59
	Upper Bound (95%)	593	73	149	430	1.23	58.8	4.17	1.62
	Median	475	38	75	259	1.31	63.7	2.90	1.57
	Lower Bound (5%)	385	9	36	205	1.94	66.4	1.64	1.56
35	Best fit	639	32	286	328	3.06	48.8	1.53	3.24
	Upper Bound (95%)	758	123	335	353	0.85	48.3	2.01	1.68
	Median	660	65	185	323	0.86	50.5	1.98	1.90
	Lower Bound (5%)	516	23	157	227	2.51	49.6	1.77	2.57

The maximum confidence intervals of the estimated rate constants are of the same order in magnitude as the best fit and median, indicating that the estimated rate constants are of a greater accuracy compared to the PSSH model. As already mentioned, the actual confidence interval is in all likelihood smaller than the range given by the 5 and 95 percentile, which instils further confidence in the accuracy of the estimated rate constants. The MSE values of the model fits indicate once again that the MEA concentration profile was the hardest to fit accurately. This may, however, be due to the higher concentration values of MEA causing the calculated MSE to be higher than that of the lower concentration values of the other reaction species.

A fundamentally consistent rate expression should ideally have rate constants that obey an Arrhenius type expression of the following form:

$$k_i = A_i e^{\left(\frac{-E_a}{RT}\right)} \qquad 4.18$$

Taking the natural logarithm of both sides of equation 4.18, produces the following expression:

$$\ln\left(k_i\right) = \ln A_i + \left(\frac{-E_a}{R}\right)\cdot\frac{1}{T} \qquad 4.19$$

where E_a is the activation energy of the reaction, R the universal gas constant (J.mol^{-1}.K^{-1}) and T the temperature in Kelvin. If the rate expression is fundamentally correct, a plot of $\ln(k_i)$ vs. $1/T$ should reveal a straight line. From the slope and intercept of the plot, the activation energy and constant, A for the reaction may be determined.

The estimated rate constants that provided the best quality model fit at each temperature was subjected to a plot of equation 4.19. The average of the rate constants over the concentration range at a certain temperature was used in the temperature dependence study. The Arrhenius plot obtained for the estimated rate constants for n-Propanol is illustrated in **Figure 4.7**.

The data in **Figure 4.7** show a linear plot for all rate constants was obtained from where the activation energy and Arrhenius constants could be derived. The temperature dependence investigation data are tabulated in **Table 4.5**.

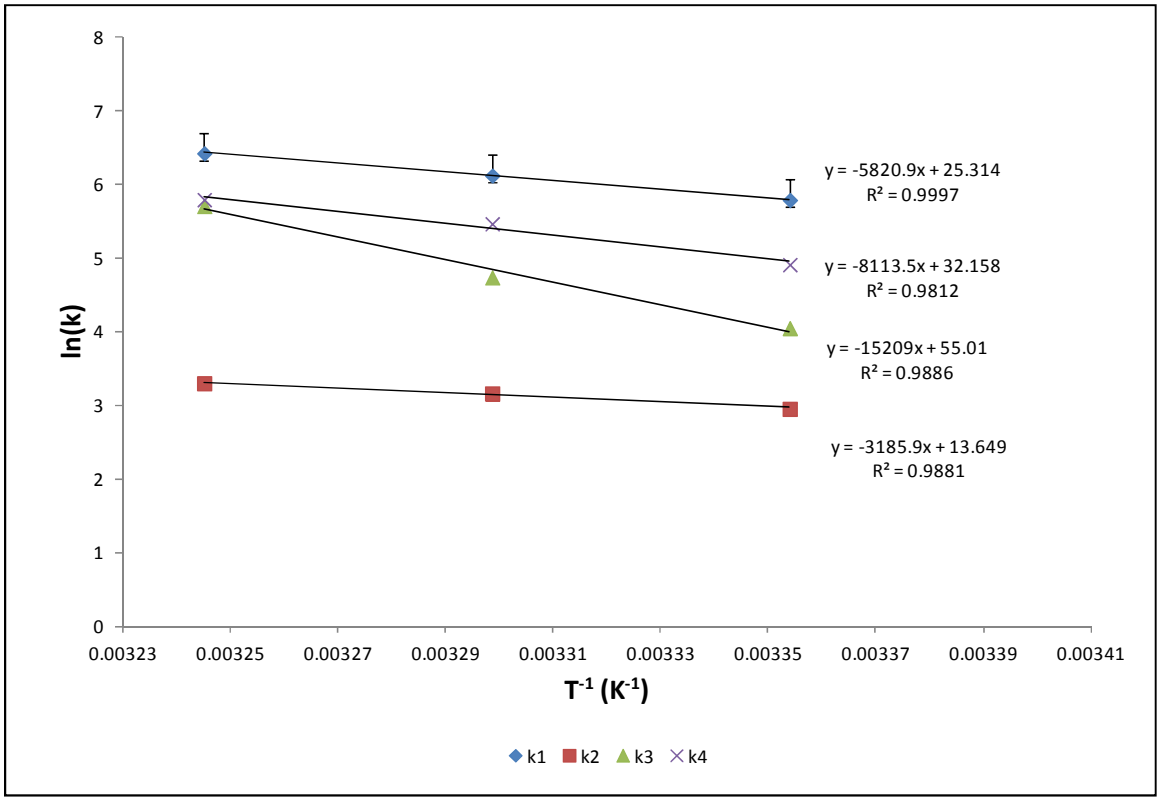

Figure 4.7 Arrhenius Plot of Fundamental Rate Expression for n-Propanol

Table 4.5 Temperature Investigation Data for n-Propanol showing Activation Energies and Arrhenius Constants for the Estimated Rate Constants of the Fundamental Model

Temperature (°C)	k_1 ($dm^3.mol^{-1}.s^{-1}$)	k_2 (s^{-1})	k_3 ($dm^3.mol^{-1}.s^{-1}$)	k_4 ($dm^3.mol^{-1}.s^{-1}$)
25	326	19	57	136
30	455	24	114	236
35	615	27	300	328
E_a (kJ/mol)	48.4	26.5	126.4	67.5
A (same units as k_i)	9.86E+10	8.47E+05	7.77E+23	9.25E+13

The activation energy for the second order rate constant, k_1 obtained in this study is in good agreement with what is reported in literature (Versteeg & van Swaaij, 1988; Patil, et al., 2011). It also agrees with the general rule of thumb that states for a 10°C increase in temperature, the

rate constant should approximately double in magnitude (Fogler, 1999). The low activation energy of k_2 suggests that the zwitterion is unstable and easily decomposes back to CO_2 and MEA. This is in agreement with literature regarding the stability of the zwitterion in non-aqueous solvents (Versteeg & van Swaaij, 1988). The high activation energy of k_3 suggests that the deprotonation of the zwitterion requires the most energy in the reaction mechanism. This may be attributed to the weak basic activity of MEA in non-aqueous solvents. The fact that the activation energy of k_4 is higher than that of k_1 is possible evidence of the overall exothermic nature of the reaction. It is also in agreement with the fact that at high temperatures (80°C - 100°C) the reaction is reversed to strip CO_2 from the mixture. This quality of the solution was utilised in Chapter 6 to regenerate the solvent used in the reactive absorption study.

A final test of the estimated rate constant determined in this study was to compare them with rate constants calculated using only the activation energies and Arrhenius constants (using equation 4.13). A comparison plot of the results for n-Propanol is illustrated in **Figure 4.8**.

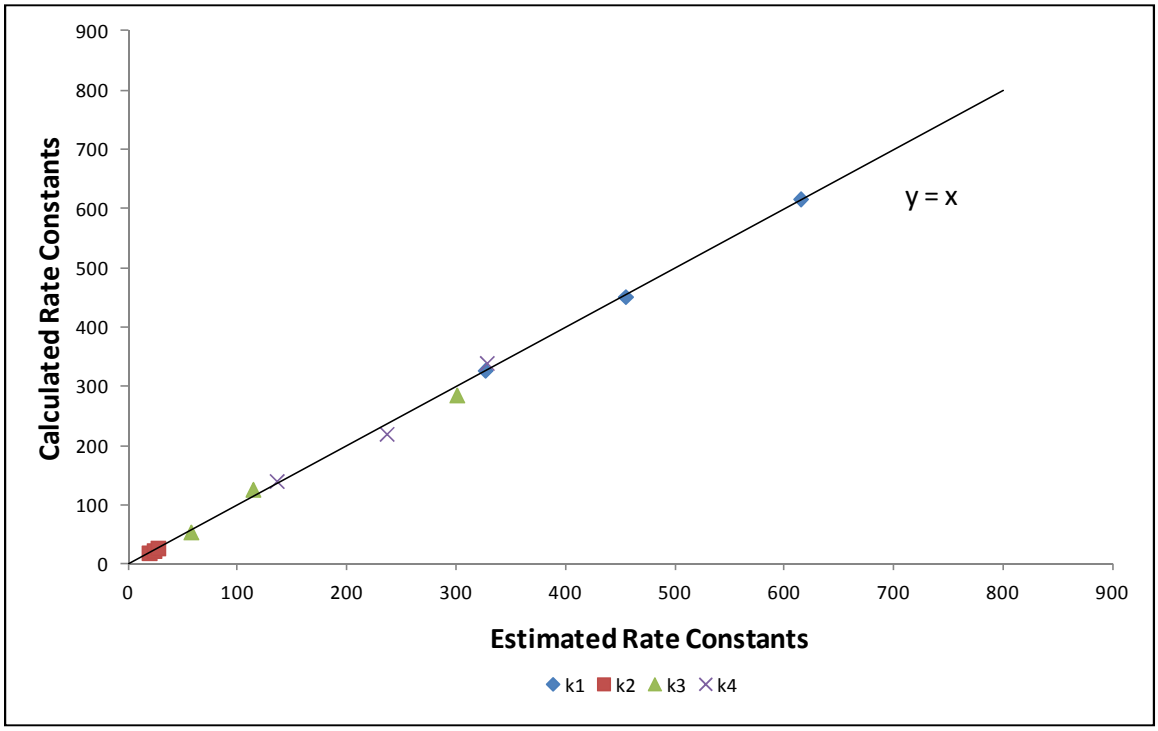

Figure 4.8 Calculated and Estimated Fundamental Rate Expression Constants of n-Propanol

Good agreement between the estimated and calculated rate constants is evident from the data presented in **Figure 4.8**. From the results presented in this section, it may be concluded that the fundamental rate expression proposed in this study (equations 4.14 - 4.17) gave good quality model fits, with rate constants that are independent of concentration and show an Arrhenius type correlation with temperature in the concentration and temperature ranges investigated in this study. Most importantly, the fundamental model provides a good quality model fit under conditions where MEA depletion in the liquid phase is considered appreciable. In order to be able to use the fast reaction of CO_2 with MEA under such conditions, to measure the effective interfacial mass transfer area, the rate expressions of the fundamental model proves to be accurate. It is recommended that this model structure be incorporated into a reactive absorption model designed to measure effective interfacial mass transfer area under conditions where interfacial depletion and surface renewal is significant. This will be discussed in further detail in Chapter 6 and Appendix B.

4.3.2 Shortened Fundamental (Equilibrium) Model

The incorporation of the full fundamental model proposed in this study (equations 4.14 - 4.17) into a reactive absorption model, may present some challenges due to the complexity of the model structure. The reaction rate expressions will be incorporated into partial differential equations which will be solved numerically (see Appendix B). A model structure of high complexity increases the computational time required for convergence in a numerical solution. An investigation into finding a less complex model structure was, therefore, undertaken.

A shortened version of the fundamental rate expression was investigated. It assumed the reaction to reach equilibrium fast (a reasonable assumption with regards to the rapid nature of the reaction) and may be expressed as follows:

$$CO_2 + 2RNH_2 \underset{k_2}{\overset{k_1}{\rightleftarrows}} 2S \qquad 4.20$$

Equation 4.20 is merely the net reaction equation of the zwitterion mechanism at equilibrium. The proposed rate expressions derived from equation 4.20 may be formulated as follows:

$$-r_{CO_2} = k_1[CO_2][RNH_2]^2 - k_2[S]^2 \qquad 4.21$$

$$-r_{RNH_2} = 2\left(-r_{CO_2}\right) \qquad 4.22$$

$$-r_{RNH_3^+} = -\left(-r_{CO_2}\right) \qquad 4.23$$

It may be noticed that now only two rate constants are required to define the reaction kinetics of the system. The rate expressions are of a similar form to the power rate law, but showed an improvement in being able to account for the irreversible nature of the reaction. Since the shortened fundamental model effectively assumes a one-step reaction, it may provide insight into the validity of the termolecular reaction mechanism as well.

A similar approach to the one followed for the full fundamental model was used to determine the order of magnitude for the initial guesses of the two rate constants. A further investigation was made with regards to the equilibrium constants tabulated in **Table 3.9**. If the equilibrium constant as calculated by equation 3.11 is evaluated by incorporating the rate constants, then the following relationship results:

$$K_C = \frac{k_1}{k_2} \qquad 4.24$$

The relationship of equation 4.24 was used to try and constrain the initial guesses used. It was, however found that the best model fits were obtained for initial guesses of the rate constants not adhering to the above ratio. This may serve as further evidence that the equilibrium constants determined in this study is not of sufficient accuracy. As discussed in section 3.8.5, this may be due to the FTIR method of analysis not being able to measure the equilibrium concentrations with sufficient accuracy under the conditions investigated in this study. The optimum initial guesses used for the shortened fundamental model fits are tabulated in **Table 4.6**

Table 4.6 Initial Guesses for the Shortened Fundamental Model Fit

T (°C)	k_1 ($dm^6.mol^{-2}.s^{-1}$)	k_2 ($dm^3.mol^{-1}.s^{-1}$)
25	800	200
30	1100	300
35	1600	500

Similar to the PSSH and fundamental model, the shortened fundamental model provided model fits of varying quality. It was found that the model fits of the shortened fundamental model were of worse quality compared to the PSSH and fundamental model. Examples of model fits with the shortened fundamental model are illustrated in **Figure 4.9** and **Figure 4.10**.

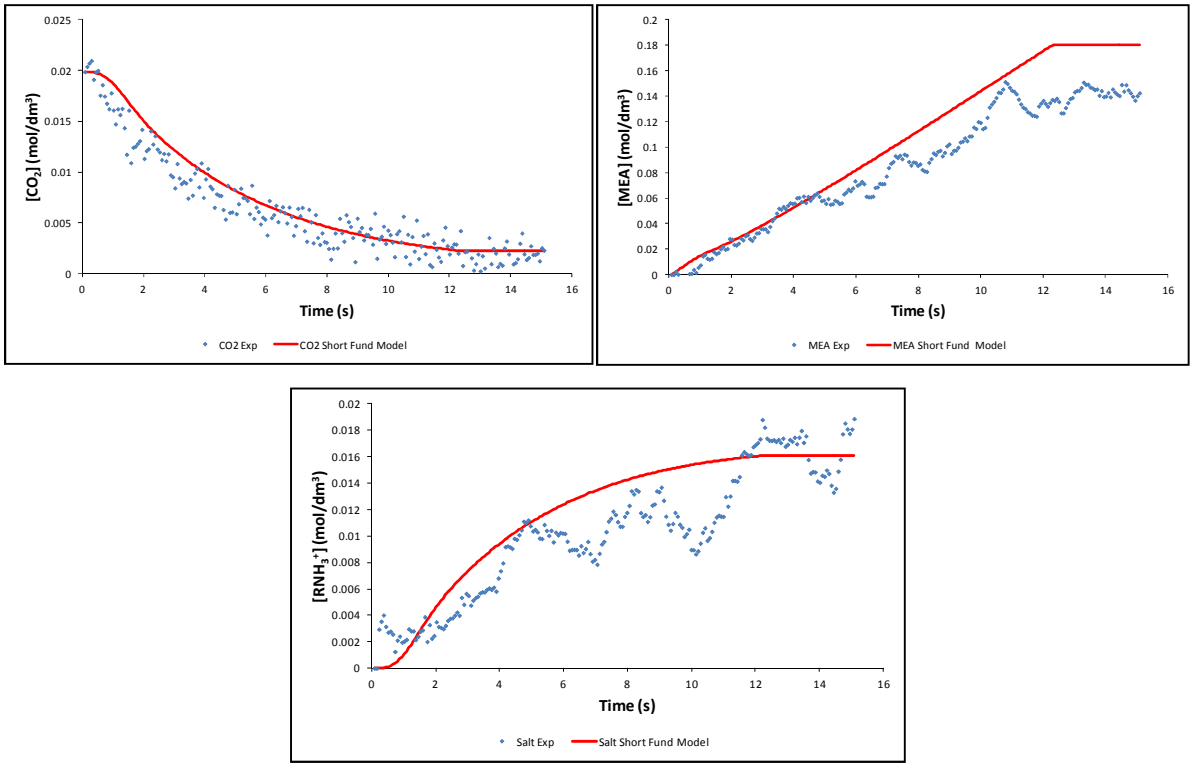

Figure 4.9 Shortened Fundamental Rate Model Fit for the Reaction of CO_2 with MEA in n-Propanol at 25°C, [MEA]:[CO_2] = 10:1 (run# 25_10_3)

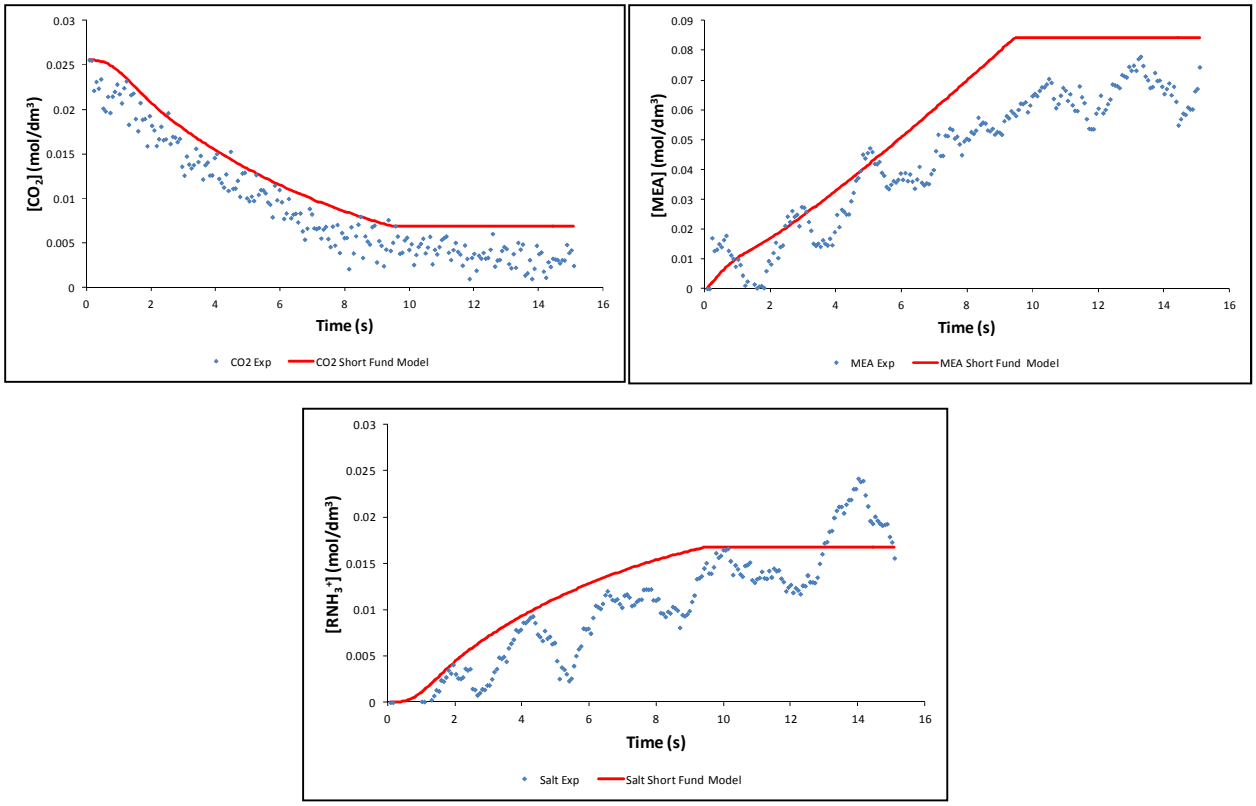

Figure 4.10 Shortened Fundamental Rate Model Fit for the Reaction of CO_2 with MEA in n-Propanol at 30°C, [MEA]:[CO_2] = 5:1 (run# 30_5_1)

The data in **Figure 4.9** and **Figure 4.10** shows that the shortened fundamental model provides the correct trend in the concentration profiles, but overestimates the equilibrium MEA concentration and the concentration of RNH_3^+ in the transient region. The over prediction in the RNH_3^+ concentration may be attributed to the inability of the shortened fundamental model to account for the deprotonation of the zwitterion. This serves to prove that under these conditions, the reaction mechanism is comprised of two reaction steps and, therefore, the zwitterion mechanism is the preferred choice over the one reaction step termolecular mechanism. This serves as evidence that under conditions where there is significant MEA conversion, the termolecular mechanism is an over simplification to the true, governing reaction mechanism.

The estimated rate constants for the shortened fundamental model are tabulated in **Table 4.7**.

Table 4.7 Shortened Fundamental Model Rate Law Rate Constants for n-Propanol

[MEA]:[CO_2] = 5:1						
T (°C)		k_1 ($dm^6.mol^{-2}.s^{-1}$)	k_2 ($dm^3.mol^{-1}.s^{-1}$)	MSE x 10^6 Eq. 4.1	Eq. 4.4	Eq. 4.3
25	Best fit	918	64	2.76	65.9	5.06
	Upper Bound (95%)	1038	200	2.40	120	2.07
	Median	810	167	2.57	127	2.55
	Lower Bound (5%)	771	57	2.64	69.7	4.87
30	Best fit	1142	247	2.59	65.8	4.23
	Upper Bound (95%)	1218	299	3.22	72.0	3.87
	Median	1107	279	3.43	73.9	3.82
	Lower Bound (5%)	1092	230	2.52	64.8	4.26
35	Best fit	1986	317	1.06	37.1	2.21
	Upper Bound (95%)	2238	494	1.81	48.7	2.53
	Median	1630	411	2.18	52.8	2.95
	Lower Bound (5%)	1596	229	1.02	36.4	2.25
[MEA]:[CO_2] = 10:1						
T (°C)		k_1 ($dm^6.mol^{-2}.s^{-1}$)	k_2 ($dm^3.mol^{-1}.s^{-1}$)	MSE x 10^6 Eq. 4.1	Eq. 4.4	Eq. 4.3
25	Best fit	992	248	1.31	187	3.18
	Upper Bound (95%)	6312	818	1.22	193	3.29
	Median	681	214	1.50	190	3.59
	Lower Bound (5%)	652	199	1.51	193	4.04
30	Best fit	1634	323	2.13	57.9	4.14
	Upper Bound (95%)	1804	384	2.18	58.4	4.08
	Median	1102	289	2.13	57.8	4.50
	Lower Bound (5%)	910	228	2.15	58.6	4.91
35	Best fit	2145	361	1.04	42.7	2.10
	Upper Bound (95%)	4526	589	0.96	43.8	2.03
	Median	1750	227	1.01	42.0	2.30
	Lower Bound (5%)	1645	202	1.03	41.6	2.41

The data in **Table 4.7** shows that there is a concentration dependence for especially k_2. This serves as further evidence that the shortened fundamental model is not entirely fundamentally based in its derivation and may be an oversimplification of the true reaction mechanism. The

estimated maximum confidence interval is larger than what was calculated for the fundamental model. This shows that the rate constants determined for the shortened fundamental model is not as accurate as that of the fundamental model. Similar order in magnitude values for the MSE of the model equations to that of the fundamental model is observed.

The concentration dependence noticed in the rate constants of the short fundamental model has already cast doubt to its validity of a representative rate expression under condition where appreciable conversion of MEA occurs. A temperature dependence investigation similar to that of the fundamental model was, nevertheless done. The results of the investigation are tabulated in **Table 4.8** and the Arrhenius plot illustrated in **Figure 4.11**.

Table 4.8 Temperature Dependence of the Short Fundamental Rate Expression Rate Constants for n-Propanol

Temperature (°C)	k_1 ($dm^6.mol^{-2}.s^{-1}$)	k_2 ($dm^3.mol^{-1}.s^{-1}$)
25	955	156
30	1388	285
35	2066	339
E_a (kJ/mol)	58.9	59.4
A (same units as k_i)	2.01E+13	4.22E+12

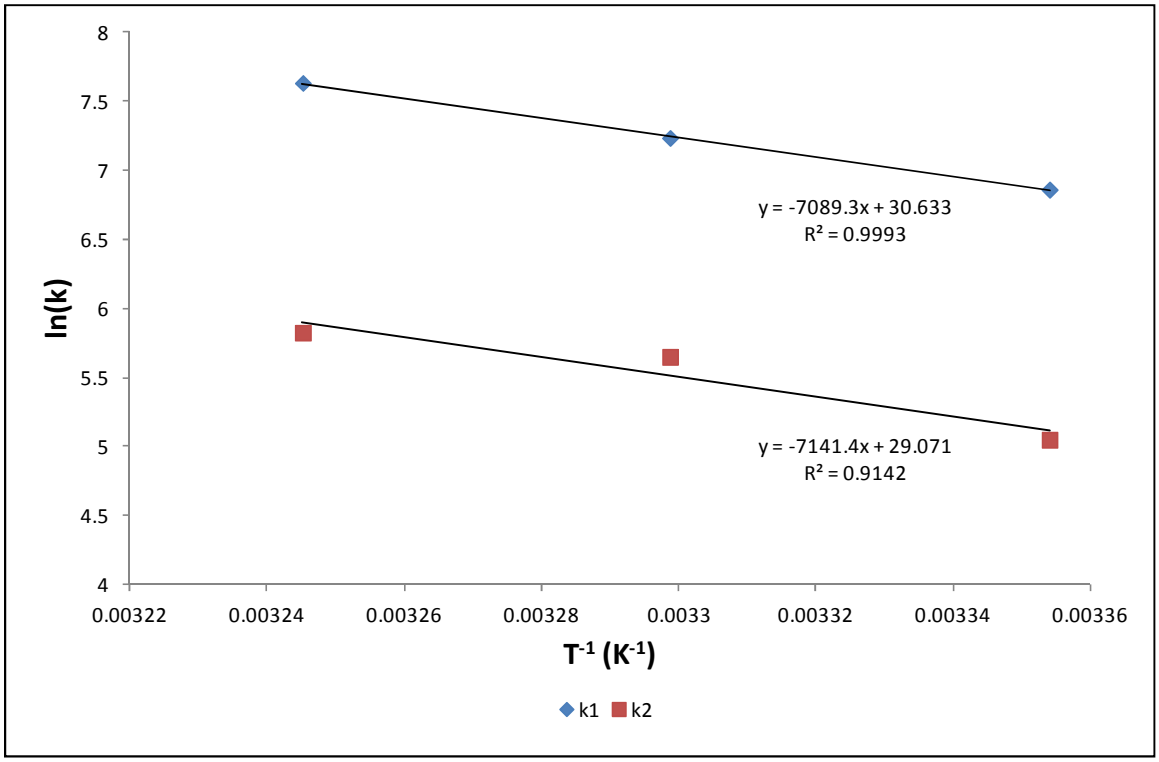

Figure 4.11 Arrhenius Plot of Short Fundamental Rate Expression for n-Propanol

The data shows that a linear correlation with respect to temperature is evident for both rate constants. The forward rate constant, k_1 showed a better linear correlation than the reverse rate constant, k_2. This indicates that the model does not provide a fundamental representation of the reaction mechanism. The activation energies of the estimated rate constants are basically equal, with the reverse reaction having slightly higher activation energy. For an exothermic reaction it is expected that the activation energy of the reverse reaction be higher than that of the forward reaction. This was not clearly evident from the estimated rate constants of the shortened fundamental model.

From the results obtained for the shortened fundamental model it may be concluded that a good quality model fit is obtained. However, an analysis of the estimated rate constants suggest that the model structure is an over simplification of the true reaction mechanism under the conditions investigated in this study. The rate expression was able to account for the irreversibility of the reaction and is of similar model complexity to the power rate law and much

simpler than the PSSH model which provided a similar quality fit of the data. It is, therefore, recommended that the shortened fundamental model be used as a first approximation in a reactive absorption model developed to measure effective interfacial mass transfer area, with the full fundamental model still the most preferred model structure to use. The implementation of both fundamental and shortened fundamental models in the method developed to measure effective interfacial mass transfer area under conditions of appreciable surface depletion and renewal rates is presented in Appendix B.

4.4 Comparison of Model Fits

Throughout sections 4.2.1-4.3.2 mention was made to the difference in the quality of the model fits obtained for the different rate expressions investigated. The comparison of the different quality model fits obtained is best presented graphically and illustrated in **Figure 4.12**.

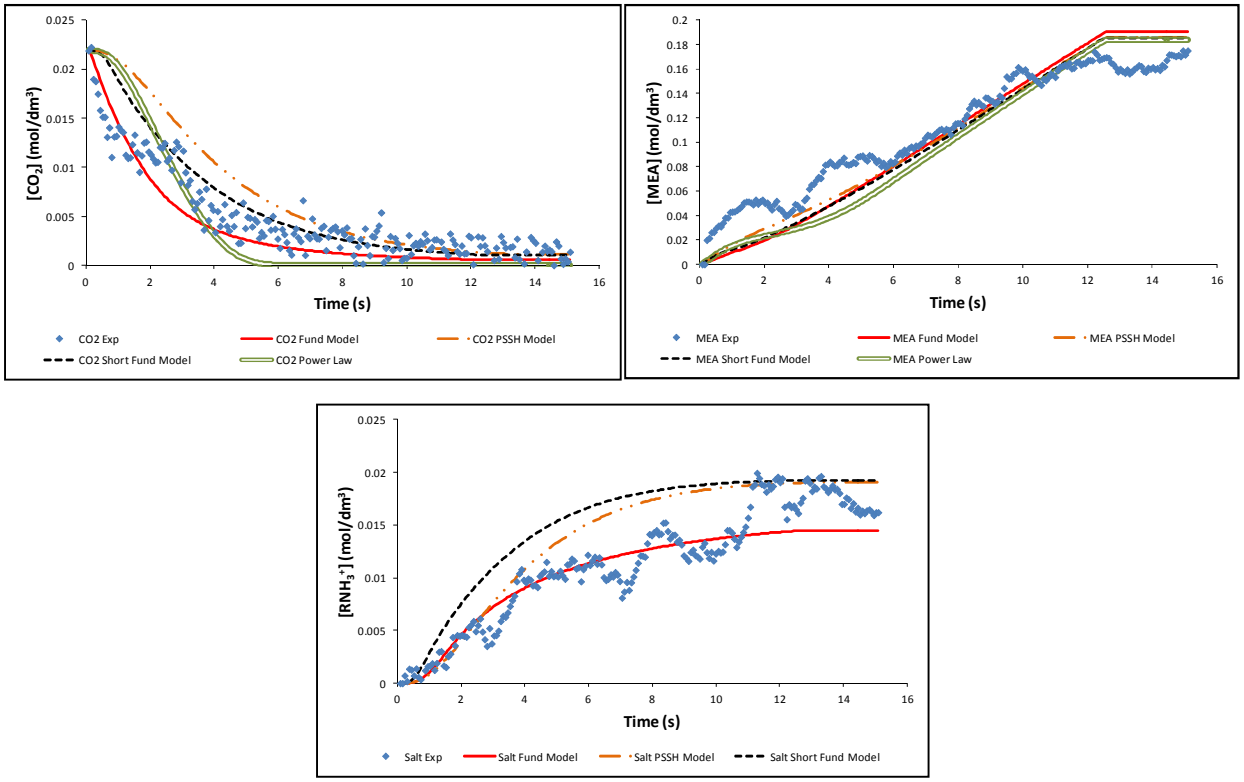

Figure 4.12 Comparison of the Quality of the Model Fits Obtained (run#30_10_3)

The comparison plot of **Figure 4.12** confirms the statement that the fundamental model provides the best quality model fit of the data. This was noticed for all data sets modelled. It further confirms the conclusion that the fundamental model provides to most accurate representation of the reaction kinetics. The comparison of the PSSH model and shortened fundamental model showed that they give similar quality model fits. If the shortened fundamental model fit the CO_2 data better than the PSSH model, then the PSSH model provided a better quality fit on the RNH_3^+ data.

Both the PSSH and shortened fundamental model provided better quality predictions of the RNH_3^+ equilibrium concentration compared with the fundamental model. This is due to the assumption of a fast reaction equilibrium obtained applied in their derivation. The PSSH model provides a better quality model fit in the transient region than the short fundamental model. This study was aimed at finding a rate expression that best fits the data in the transient region of the reaction and thus the fundamental model is the preferred model choice, since it fit the data best for all reaction species in this region.

4.5 Chapter Conclusions

The modelling of existing and proposed reaction rate expressions for the reaction of CO_2 with MEA in nPropanol, on the experimental data sets collected in this study, was presented in this chapter. The modelling procedure firstly consisted of evaluating the proposed rate expression found in literature. It may be concluded that the existing literature models do not describe the liquid side reaction kinetics accurately for the concentration range investigated in this study. The power rate law and PSSH models are not rejected as simple rate expression applicable to conditions where the interfacial depletion of MEA is negligible. The PSSH model is, however, considered to be too complex to use in effective interfacial mass transfer area studies.

A fundamental and shortened fundamental model for describing the liquid side reaction kinetics of CO_2 with MEA in alcoholic solvents was proposed. The rate constants obtained for the fundamental model gave good quality model fits over the entire temperature and concentration range of this study. They were determined to be independent of concentration

and showed an Arrhenius temperature relation. It may, therefore, be recommended that the fundamental model be used in a reactive absorption model for determining the effective area of separation column internals such as structured and random packing under conditions where interfacial depletion of MEA is appreciable. This will allow a study of the effect of surface renewal rate on the effective interfacial mass transfer area achieved by different types of separation column internals.

The shortened fundamental model rate constants showed some inconsistency with a change in concentration. It showed a poorer quality fit on the experimental data compared to both the fundamental and PSSH model. The estimated rate constants did; however, show a correct Arrhnius temperature dependence, but the activation energy of the rate constants were not in convincing agreement with what is expected for an exothermic reaction. Since the shortened fundamental model is a simpler model than the fundamental model, it is recommended that it is used as a first estimate in an effective area model. The results from this first estimate may be used as the initial guesses for when the fundamental model is employed.

Chapter 5 EXISTING MASS TRANSFER AREA THEORY AND CORRELATIONS

One of the most important efficiency parameters for separation columns is the effective interfacial mass transfer area (a_e) provided by the column internals. Many previous researchers have attempted to estimate or measure this important parameter (Tsai, 2010). This chapter will give an account of the existing theories and correlations used to calculate a_e for column internals such as random and structured packing material.

Before this can be done sufficiently, the various definitions of interfacial areas encountered in the derived equations must firstly be presented (Shi & Mersmann, 1985; Erasmus, 2004):

- a_p: Geometrical area of the packing material
- a_i: Actual interfacial area between gas and liquid
- a_w: Interfacial area between packing and liquid (wetted area)
- a_G: Active interfacial area for gas phase mass transfer
- a_L: Active interfacial area for liquid phase mass transfer
- a_v: Active interfacial area for evaporation
- a_c: Active interfacial area for mass transfer with chemical reaction

The effective interfacial mass transfer area (a_e) may therefore be a combination of a_G, a_L, a_v and a_c depending on the process under consideration. The aim of a method to determine a_e should keep this in mind at all times.

Following on the review conducted by Wang et al. on the existing mass transfer correlations for packed columns, it may be concluded that the problem of distinguishing between the three

efficiency parameters of column internals, k_L, k_G and a_e is far from resolved (Wang, et al., 2005). The importance of these parameters is illustrated in the formulation of the equations used to determine the efficiency of column internals. The efficiency of a packed column is measured in terms of its height equivalent to a theoretical plate (HETP) achieved. HETP is related to the height of a mass transfer unit for the gas phase (HTU_G) and for the liquid phase (HTU_L) (Olujic, et al., 1999; Wang, et al., 2005) according to:

$$\mathrm{HETP} = \frac{\ln \lambda}{\lambda - 1}\left(\mathrm{HTU_G} + \lambda \mathrm{HTU_L}\right) \qquad 5.1$$

where

$$\lambda = \frac{m}{L/V} \qquad 5.2$$

with m the local slope of the equilibrium line for the system in question and L/V the slope of the column operating line. Using the definitions of HTU_G and HTU_L in terms of the gas $\left(k_G a_e\right)$ and liquid $\left(k_L a_e\right)$ volumetric mass transfer coefficients, equation 5.1 may be written as:

$$\mathrm{HETP} = \frac{\ln \lambda}{\lambda - 1}\left(\frac{u_G}{k_G a_e} + \lambda \frac{u_L}{k_L a_e}\right) \qquad 5.3$$

It may now be noticed that in order to be able to determine the efficiency of a distillation column internal, the volumetric mass transfer coefficients should at least be known. It would be beneficial to be able to determine the mass transfer coefficients separately from the effective area. This chapter will give an overview of the correlations that has made the most impact in this field. It will firstly introduce correlations derived from geometric and hydraulic considerations (packing dimensions and orientation, liquid distribution, liquid physical properties etc.) followed by correlations derived from measuring the effective are via a reactive absorption process, called the chemical method.

Chapter 5 will conclude with a comparative investigation and discussion of the predictions made by the existing correlations. This comparison is done in section 5.3

5.1 Hydraulic and Geometry Based Correlations

Some of the first attempts at deriving correlations for calculating effective interfacial area were based on the study of liquid flow profiles and distribution patterns. These geometry based models must assume that a_i represents a_e. This is a good first approximation, but the method cannot account for systems where the interface is not constantly refreshed with effective surface elements and will therefore remain as an approximation. Nevertheless, these studies have provided valuable insight and understanding of liquid distribution profiles within random and structured packing and are, therefore, of utmost importance to this study. The correlations presented in this section are focused on those derived for structured packing, unless otherwise stated. Each correlation will be discussed and evaluated individually at first. Comparisons with other correlations will be discussed once all the correlations are introduced. This evaluation is done in section 5.3.

Packed columns are characterised by the volumetric mass transfer coefficients through direct experimental measurements (Olujic, et al., 1999; Wang, et al., 2005). The need exists to determine the constituents (k_L, k_G and a_e) of the volumetric mass transfer coefficient separately. The reason is to be able to distinguish the different effects that solution properties such as viscosity, density and surface tension and packing properties such as type, material, void fraction and geometric design has on these parameters (Shi & Mersmann, 1985). It would also be beneficial to be able to calculate the volumetric mass transfer coefficient for different types of packing material in advance, instead of measuring it every time.

It is important to be able to distinguish between wetted area (a_w) and effective area (a_e), since the latter excludes so called dead zones (wetted area that is mass transfer impotent) and includes liquid droplets and jets not accounted for by the wetted surface area. These droplets and jets do not form part of the current liquid distribution models proposed to determine the wetted area. The type and size of the packing material influences the significance of dead zones and liquid droplets. Despite knowledge of these differences, the wetted area is often assumed to be equal to the effective area.

The variety of different coefficients and exponents used in the existing empirical models derived by various researchers illustrates the need to derive more fundamental methods for determining effective interfacial area, so that a better correlation of a_e with various liquid and packing properties can be derived. This will hopefully eliminate the contradictions found in literature regarding the effect of especially viscosity and surface tension on the effective interfacial area available for mass transfer.

5.1.1 Correlations of Shi and Mersmann

For a geometric model to be used to calculate interfacial mass transfer area, it is first and foremost necessary to obtain an accurate hydrodynamic model for the liquid flowing on the packing material (Shi & Mersmann, 1985). A liquid distribution model, effectively. On the assumption that the liquid flows in uniformly distributed rivulets, with the total volumetric liquid flux distributed evenly between the rivulets, the width of a rivulet is of great importance for calculating a_w. This approach by Shi and Mersmann (1985) was made for determining a_w for random packing elements, but since it assumes evenly distributed liquid rivulet flow, it seems to be ideally suited for structured packing as well.

Assuming constant velocity, laminar flow of a smooth surfaced liquid rivulet down an inclined plate allows for the derivation of expressions to calculate rivulet width and thickness for a dynamic (flow) system through balancing the gravity and viscous forces acting on the flowing liquid. A schematic of a liquid film flowing from a point source over an inclined plate is illustrated in **Figure 5.1**.

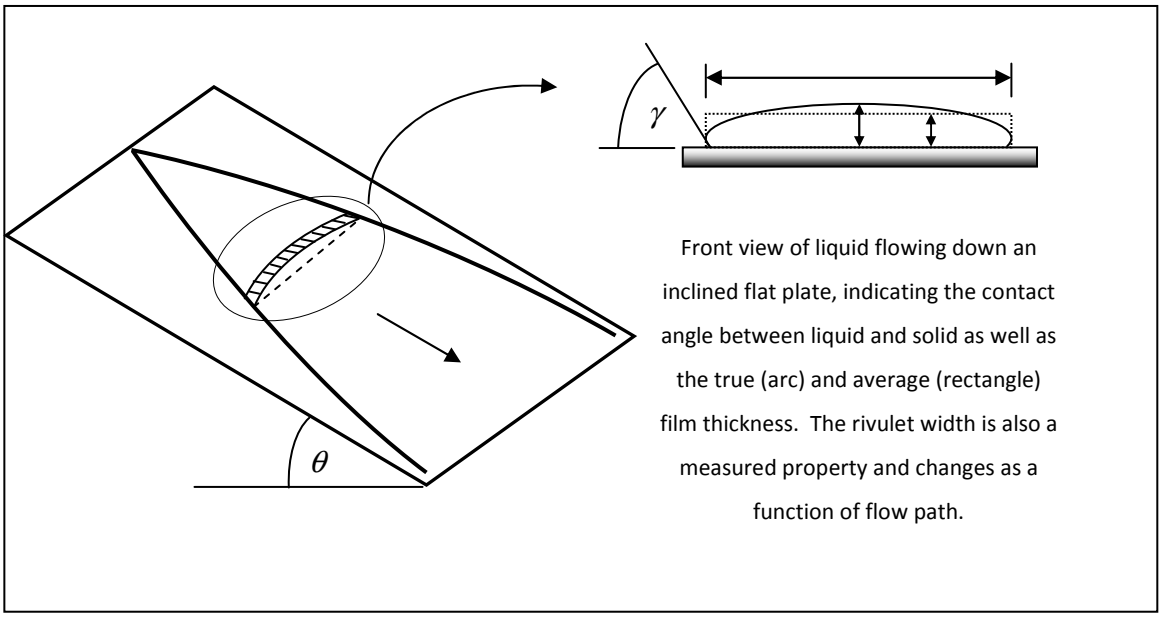

Figure 5.1 Schematic of a Liquid Rivulet Flowing from a Point Source Down an Inclined Flat Plate

The rivulet width and film thickness of static systems was also determined by measuring the liquid-solid contact angle, liquid surface tension and estimating the cohesion pressure of the liquid with the use of geometric models. The measurements were carried out on a 45° inclined surface of seven different materials and ten different solvents. The dimensions of the inclined plate were 400 mm x 210 mm and the viscosity and surface tension of the solvents ranged from 1 – 21 mPa.s and 23 – 73 mN/m respectively.

The measured surface tension and contact angle data did not agree well with the theoretically derived model. Measurement of the rivulet width results in the calculation of the dynamic film thickness. With knowledge of the liquid film thickness an expression for a_w becomes possible, which was one of the first area models proposed in literature derived from fundamental hydraulic principles:

$$\frac{a_w}{a_p} = \frac{0.76 u_L^{0.4} \nu_L^{0.2}}{1 - 0.93\cos\gamma} \left(\frac{\rho_L}{\sigma g} \right)^{0.15} \frac{a_p^{0.2}}{\varepsilon^{0.6}} \qquad 5.4$$

For liquid side mass transfer controlled processes, Higbie's penetration theory was assumed. k_L correlations can be derived from a combination of the liquid film thickness, rivulet width, wetted area and continuity equations. The authors commented that a_e depends on a_W, surface renewal, formation of drops and static liquid hold-up. Surface renewal is affected by the kinetic energy of the flowing liquid, the Marangoni effect and the non-wettability of the solid surface. The Marangoni effect is the phenomenon where liquid elements flow away from a region of low surface tension. These parameters are not easily determined, so the author introduces a correction factor relating to the ratio of $a_e : a_p$:

$$\frac{a_e}{a_p} = \frac{0.76 C_1 d_{PE}^{1.1} u_L^{0.4} v_L^{0.2}}{1 - 0.93\cos\gamma} \left(\frac{\rho_L}{\sigma g}\right)^{0.15} \frac{a_p^{0.2}}{\varepsilon^{0.6}} \qquad 5.5$$

The empirical correction factor mainly revealed that the formation of drops and jets increases with increasing size in the packing elements (d_{PE}).

In conclusion, the models proposed by Shi and Mersmann are of a mechanistic nature and are widely recognised as valid for determing a_e under the assumption that $a_e = a_w$ (Wang, et al., 2005). The approach in deriving the rivulet width and film thickness is sound, but needs to incorporate turbulent flow over a periodic surface. The chemical method, combined with the hydrodynamic model will ultimately shed light on the true a_e of the system.

5.1.2 Studies by Shetty and Cerro

Shetty and Cerro conducted several studies on the liquid flow profiles and distribution patterns on both smooth and periodic surfaces (Shetty & Cerro, 1993; Shetty & Cerro, 1995; Shetty & Cerro, 1997; Shetty & Cerro, 1998). A schematic of the periodic surfaces studied are illustrated in **Figure 5.2**.

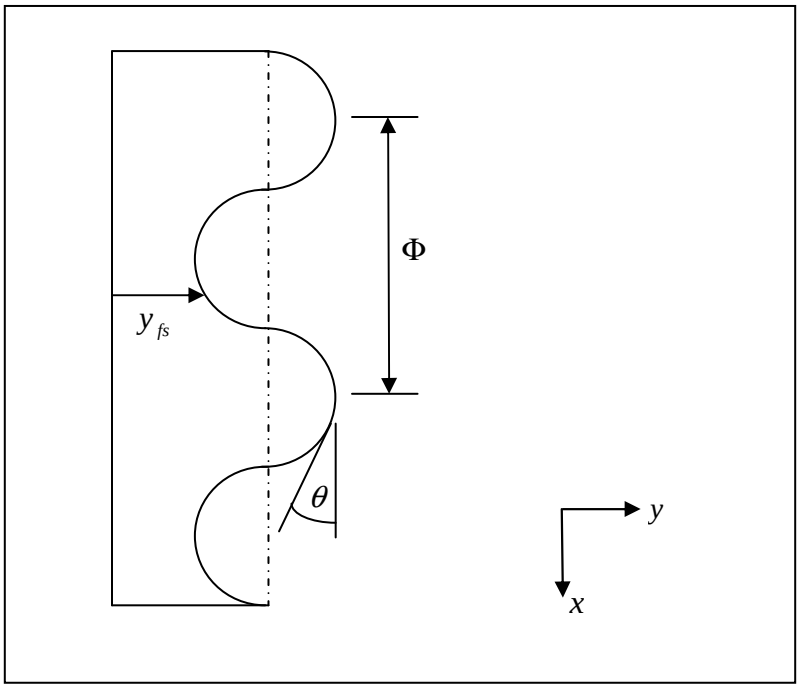

Figure 5.2 Schematic of Periodic Surfaces Studied by Cerro et al. (1997)

They derived several models for heat and mass transfer based on the study of flow patterns and velocity profiles of thin, viscous liquid films over periodic surfaces at different angles (45^o - 90^o) to the entrance liquid flow path. The integration of the velocity profiles revealed expressions for determining liquid hold-up and wetted area. The effect of the size of the structured packing as well as the liquid properties of the system was explored. Penetration theory was used to derive mass transfer correlations. The contact time of a liquid element flowing down one segment of periodic surface was determined by timing the flow of a tracer.

Structured packing has both a macro and microstructure that influences liquid distribution and helps maintain a near complete wetted surface to maximize a_W which should maximize a_e. The main objective of their study was to lay a foundation from where design parameters such as a_e, k_L etc. can be derived from liquid flow patterns. An understanding of liquid flow patterns is the first step in deriving expressions for calculating mass and energy transfer. Parameters such as a_e and liquid hold-up is essential for this purpose which will shed light on the optimum operating conditions for the separation process in question.

Earlier work from these authors includes the study of the spreading of a liquid point source over periodic surfaces (Shetty & Cerro, 1993; Shetty & Cerro, 1998). For liquid flow over the macrostructure of the periodic surface, a simple, yet accurate expression was derived from the complex film evolution equation (Shetty & Cerro, 1993; Shetty & Cerro, 1995) for the dimensionless film thickness. It was observed that two maximums in film thickness were achieved over one period of the solid surface. For flow over the microstructure, the complete film evolution equation had to be solved numerically. As expected, the flow profile was flatter and single periodic in nature. For flow over an inclined macrostructure the same approach was followed and a simple expression was proposed incorporating the angle of the corrugations.

The introduction of the liquid film evolution equation was aimed at providing the necessary platform from which the design parameters such as liquid hold-up and effective area were calculated. The first assumption is on complete and even liquid distribution over the packing surface. This is not realistic, but the authors claim that the model is easily modified to include factors for liquid maldistribution. From the assumption of complete wetting, the dynamic liquid hold-up can be calculated from the film thickness (Shi & Mersmann, 1985). A numerical integration of the film profile was used to calculate the volume of the liquid per unit volume of the packing surface. The liquid film thickness was calculated from the film evolution equation discussed. The liquid hold-up was always over-estimated by this model, since maldistribution of liquid is a reality.

The effective area is calculated from the numerical integration over the packing surface area of the free surface (fs) profiles obtained through the integration of the liquid film evolution equation for a Cartesian coordinate system. The derived equation reads (refer to **Figure 5.2** for symbol definitions):

$$a_e = \frac{4\sum\sqrt{dy_{fs}^2 + dx^2}}{\Phi^2} \qquad 5.6$$

This is done to avoid the large errors made in trying to measure the effective area. It still assumes the wetted area to be equal to the effective area which is unrealistic and further assumes no dead zones and no wave action on the liquid surface.

Studying the movement of a tracer helped the authors in deriving an expression for determining the contact time of each liquid element by integration of the liquid evolution equation. The liquid side mass transfer coefficient could then be derived using penetration theory proposed by Higbie (1935). Although admitting to certain shortcomings, this study laid the foundation for a fundamental approach for determining design parameters such as liquid hold-up, effective area, mass transfer coefficients and HETP.

5.1.3 SRP Model

One of the first studies carried out to try and obtain a comprehensive mass transfer model for structured packing was undertaken at the Separations Research Program (SRP) at the University of Texis. The study (Bravo, et al., 1985) was done on a finely woven gauze packing, Sulzer BX, measuring mass transport data for systems like, *o*/*p*-xylenes and ethylbenzene/styrene under total reflux conditions. The liquid flow profile and pathways followed was modeled as a network of interconnected triangular shaped wetted wall columns. Concepts like effective gas and liquid velocities were introduced and incorporated into correlations for predicting gas and liquid film mass transfer coefficients. This was done to account for the effect that the two phases have on one another as they interact in flow. These correlations are still assumed valid by many researchers.

Since the gauze packing was assumed to be completely wetted under the experimental conditions of the study and the effective area was assumed to be equal to the wetted area, the geometrical area of the packing was used in the calculation of efficiency parameters. In later investigations involving sheet metal packing (Fair & Bravo, 1990) the authors introduced an efficiency factor to account for incomplete wetting of the surface in the pre-loading and loading regions of column operation:

$$a_e = \beta a_p \qquad 5.7$$

The efficiency factor was empirically correlated with the degree of flooding achieved within the column. After 85% flooding was achieved, the efficiency factor assumes the value of unity:

$$\beta = 0.5 + 0.0058(\%\ \text{Flooding}) \qquad 5.8$$

Equation 5.8 is, therefore, valid for a system in the range of 0 – 85% flooding.

Subsequent researchers at the SRP then set to work to better determine a_i for sheet metal structured packing. The work of Rocha et al. (Rocha, et al., 1996) focussed on the importance of taking fractional liquid hold-up (h_L) into account. The fractional area model derived was of similar form to the one proposed by Shi and Mersmann (equations 5.4 and 5.5) with the addition of allowing for variable inclination angles of the packing. The correlation also includes a term, F_{SE}, that accounts for the surface texture of the structured packing:

$$\frac{a_e}{a_p} = F_{SE} \cdot F_t = F_{SE} \frac{29.12 u_L^{0.4} \nu_L^{0.2} S^{0.359}}{(1 - 0.93\cos\gamma)(\sin\theta)^{0.3} \varepsilon^{0.6}} \left(\frac{\rho_L}{\sigma g}\right)^{0.15} \qquad 5.9$$

with S the side dimension of a structured packing channel and θ the angle that the channel makes with regards to the horizontal (mostly 45° and 60° used in industry). The contact angle was given by:

$$\begin{aligned} \cos\gamma &= 5.211 \times 10^{-16.835\sigma} && \text{for } \sigma > 55 \text{ mN/m} \\ \cos\gamma &= 0.9 && \text{for } \sigma < 55 \text{ mN/m} \end{aligned} \qquad 5.10$$

For gas phase mass transfer, the mass transfer coefficient was calculated by a correlation fitted on wetted wall experimental data. The general form of the correlation reads:

$$\text{Sh}_G = C_1 \text{Re}_G^m \text{Sc}_G^n \qquad 5.11$$

which translates to:

$$\frac{k_G S}{D_G} = 0.054 \left(\frac{(u_{G,eff} + u_{L,eff})\rho_G S}{\mu_G}\right)^{m=0.8} \left(\frac{\mu_G \rho_G}{D_G}\right)^{n=0.33} \qquad 5.12$$

when the experimental data is applied and the dimensionless numbers expanded. The exponents, m and n of equation 5.12 do not both agree with the boundary layer theory it was derived from Luo et al. (2012). The exponent, n, is correct, but according to boundary layer theory, m should be 0.5 (Sherwood, et al., 1975; Incropera & De Witt, 2002; Seader & Henley, 1998).

The effective liquid and gas linear velocities were calculated from:

$$u_{G,eff} = \frac{u_G}{\varepsilon\left(1-h_L\right)\sin\theta} \qquad 5.13$$

$$u_{L,eff} = \frac{u_L}{\varepsilon h_L \sin\theta} \qquad 5.14$$

Penetration theory was adopted to calculate the liquid side mass transfer coefficient:

$$k_L = 2\sqrt{\frac{D_L C_E u_{L,eff}}{\pi S}} \qquad 5.15$$

with the factor, C_E introduced to account for liquid regions with low surface renewal rates. Experimental evidence for structured packing suggested a value of 0.9 for this constant. Model validation experiments were conducted on 9 different types of structured packing material (all metal) using six chemical systems over a pressure range of $0.02 - 4.14$ bar. The main conclusion was that the model provided good correlation with experimentally determined data.

5.1.4 Billet and Schultes Model

The work of Billet and Schultes once again emphasized the importance of taking fractional liquid hold-up into account when deriving mass transfer correlations. They proposed a theoretical expression for calculating liquid hold-up (Billet & Schultes, 1993):

$$h_L = \left(12\frac{\mu}{g\rho_L}u_L a_p^2\right)^{1/3} \qquad 5.16$$

Unlike the mass transfer model of the SRP which uses boundary layer theory to calculate the gas phase mass transfer coefficient (Rocha, et al., 1996), the model proposed by Billet and Schultes incorporates penetration theory to calculate both mass transfer coefficients:

$$k_L = 2\sqrt{\frac{D_L u_L}{\pi h_L l_\tau}} \qquad 5.17$$

$$k_G = 2\sqrt{\frac{D_G u_G}{\pi(\varepsilon - h_L) l_\tau}} \qquad 5.18$$

where l_τ is the characteristic flow path length, unique to each type of packing material and equated to the hydraulic diameter:

$$l_\tau = d_h = \frac{4\varepsilon}{a_p} \qquad 5.19$$

Experimental studies of 70 different packing elements (mostly random packing, with some structured packing included) of a variety of materials (metal, ceramic, plastic etc.) were carried out with the use of 30 different chemical systems. The chemical systems were chosen to represent the three modes of mass transfer limitations: gas phase control, liquid phase control and both phases resisting mass transfer significantly.

The data were collected in the form of the volumetric mass transfer coefficients. Effective area was then subsequently calculated after the evaluation of equations 5.17 and 5.18. A dimensional analysis was conducted which revealed the following expression for the fractional mass transfer area:

$$\frac{a_e}{a_p} = 1.5\left(a_P d_h\right)^{-0.5}\left(\frac{u_L d_h}{\nu_L}\right)^{-0.2}\left(\frac{u_L^2 \rho_L d_h}{\sigma}\right)^{0.75}\left(\frac{u_L^2}{g d_h}\right)^{-0.45} \qquad 5.20$$

Equation 5.20 is applicable to systems with a neutral or positive liquid surface tension gradient measured from top to bottom of column liquid flow. For systems with a negative gradient, the Marangoni effect should be accounted for by introducing another term in equation 5.20. This

effect is encapsulated in the Marangoni number which is a ratio of thermal surface tension forces and viscous forces.

The Billet and Schultes model relies heavily on a vast amount of experimental data and since a_e is indirectly calculated from the volumetric transfer coefficient, the validity of equation 5.20 is restricted to the range of properties and thermodynamic conditions of the experimental test systems. A more fundamentally derived area model will alleviate this restriction.

5.1.5 Delft Model

The Delft model for structured packing was derived by studying the hydraulic performance of a thin liquid film of uniform thickness flowing in the corrugations of the packing material (Olujic, et al., 1999). It assumes the gas phase to travel up the column in a zig zag profile through each packing element. For the purpose of deriving the appropriate gas phase mass transfer coefficient, the hydraulic diameter of the gas phase had to be determined. This was achieved by studying the geometry of the packing material as illustrated in **Figure 5.1**.

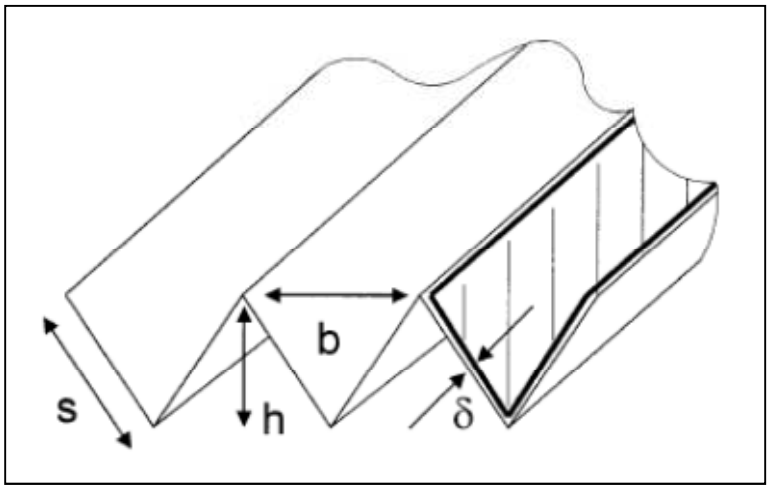

Figure 5.3: Geometry of a Triangular Gas-Liquid Flow Channel (Redrawn with permission from (Olujic, et al., 1999))

Based on the dimensions given in **Figure 5.3**, the hydraulic diameter of the triangular flow channel may be derived to be:

$$d_{h,G} = \frac{\frac{(bh-2\delta S)^2}{bh}}{\left[\left(\frac{bh-2\delta S}{2h}\right)^2 + \left(\frac{bh-2\delta S}{b}\right)^2\right]^{0.5} + \frac{bh-2\delta S}{2h}} \quad 5.21$$

The V-shaped fraction of the liquid film occupying the flow channel may be calculated from:

$$\varphi = \frac{2S}{b+2S} \quad 5.22$$

Similar to the SRP model, the Delft model also incorporates effective gas and liquid velocities in its mass transfer equations. It adopts the same expressions (equations 5.13 and 5.14) with a different definition for the liquid hold-up. The Delft model assumes the liquid to be evenly distributed with a uniform film thickness calculated via the Nusselt formula:

$$\delta = \left(\frac{3\mu_L u_L}{\rho_L g a_p \sin\theta}\right)^{1/3} = \left(\frac{3\mu_L}{\rho_L g \sin\theta}\left(\frac{\dot{V}_L}{L_P}\right)\right)^{1/3} \quad 5.23$$

Where

$$a_p = \frac{L_P}{A_{\text{column}}} = \frac{4S}{bh} \quad 5.24$$

which leads the equation approximating the liquid hold-up under pre-loading operating conditions when liquid entrainment is considered to be at a minimum:

$$h_L = \delta a_p \quad 5.25$$

The Delft model further assumes that under typical industrial operating conditions, the gas phase is in a pseudo turbulent state. This state is brought about by entrance effects as the gas flows from one sheet to the next, causing turbulence. It therefore assumes the overall gas phase mass transfer coefficient to be the average of a laminar and turbulent coefficient:

$$k_G = \sqrt{k_{G,\text{lam}}^2 + k_{G,\text{turb}}^2} \quad 5.26$$

The coefficients are calculated from their respective Sherwood numbers:

$$\frac{k_{G,\text{lam}}d_{h,G}}{D_G} = \text{Sh}_{G,\text{lam}} = 0.664 \cdot \text{Sc}_G^{0.33}\sqrt{\text{Re}_{G,\text{rv}}\frac{d_{h,G}}{l_{G,\text{pe}}}} \qquad 5.27$$

$$\frac{k_{G,\text{turb}}d_{h,G}}{D_G} = \text{Sh}_{G,\text{turb}} = \frac{\text{Re}_{G,\text{rv}}\text{Sc}_G\frac{\xi_{G-L}\varphi}{8}}{1+12.7\sqrt{\frac{\xi_{G-L}\varphi}{8}}\left(\text{Sc}_G^{2/3}-1\right)}\left[1+\left(\frac{d_{h,G}}{l_{G,\text{pe}}}\right)^{2/3}\right] \qquad 5.28$$

where $\left(d_{h,G}/l_{G,\text{pe}}\right)$ is the ratio of hydraulic diameter to the length of a gas flow channel within the packing element. The Reynolds and Schmidt numbers are of the same form as in equation 5.12 with the side dimension length, S replaced by the hydraulic diameter of equation 5.21:

$$\text{Re}_{G\text{rv}} = \frac{\rho_G\left(u_{G,eff}+u_{L,eff}\right)d_{h,G}}{\mu_G} \qquad 5.29$$

Equation 5.28 incorporates the gas-liquid friction factor for liquid flow in channels. It is best calculated with an accurate explicit expression proposed by Colebrook and White and refined by Olujic (Olujic, 1981):

$$\xi_{G-L} = \left\{-2\log\left[\frac{\left(\frac{\delta}{d_{h,G}}\right)}{3.7}-\frac{5.02}{\text{Re}_{G\text{rv}}}\log\left[\frac{\left(\frac{\delta}{d_{h,G}}\right)}{3.7}-\frac{14.5}{\text{Re}_{G\text{rv}}}\right]\right]\right\}^{-2} \qquad 5.30$$

The liquid phase mass transfer coefficient is calculated via the penetration theory. The Delft model once again uses the same expression as the SRP model (equation 5.15), with two modifications. S is replaced with the hydraulic diameter and the constant C_E now appears in the denominator. The latter difference may be due to a difference in the definition of exposure time by the two models. The Delft model expression for the liquid phase mass transfer coefficient reads:

$$k_L = 2\sqrt{\frac{D_L u_{L,eff}}{0.9 \cdot \pi d_{h,G}}} \qquad 5.31$$

The third parameter in the Delft model is an expression for the effective interfacial mass transfer area. Although the authors admit that not all packing materials provide even and complete liquid distribution, they had to assume this in order to derive their expression for a_e:

$$a_e = a_p \frac{1-\Omega}{1+\frac{A}{u_L^B}} \qquad 5.32$$

where Ω represents the packing surface void fraction (in the order of 0.1 for most packings) and A and B are constants unique to each packing type and size. The Delft model was later updated to include and expression proposed by Onda et al. (1968) for random packing (Olujic, et al., 2001; Olujic, et al., 2004; Wang, et al., 2005):

$$\frac{a_e}{a_p} = (1-\Omega)\left(\frac{a_e}{a_p}\right)_{\text{Onda}} \left(\frac{\sin 45}{\sin \alpha_L}\right)^n \qquad 5.33$$

where α_L is the effective liquid flow angle. Equation 5.33 is a compact form of a large expression. The exponent n is represented by:

$$n = \left(1-\frac{a_p}{250}\right)\left(1-\frac{\alpha_L}{45}\right) + \ln\left(\frac{a_{e,\text{Onda}}}{250}\right) + \left(0.49-\sqrt{\frac{760}{P}}\right)\left(1.2-\frac{\alpha_L}{45}\right) \qquad 5.34$$

With the operating pressure, P, expressed in units of torr. The expression proposed by Onda for calculating the fractional area is defined as:

$$\frac{a_e}{a_p} = 1-\exp\left[-1.45\left(\frac{\sigma_c}{\sigma_L}\right)^{0.75} \text{Re}_L^{0.1}\,\text{Fr}_L^{-0.05}\text{We}_L^{0.2}\right] \quad , \quad 0.3 < \frac{\sigma_c}{\sigma_L} < 2 \qquad 5.35$$

The dimensionless numbers of equation 5.35 are defined as:

$$\mathrm{Re}_L = \frac{\rho_L u_L}{a_p \mu_L} \qquad 0.04 < \mathrm{Re}_L < 500 \qquad 5.36$$

$$\mathrm{Fr}_L = \frac{u_L^2 a_p}{g} \qquad 5\times10^{-9} < \mathrm{Fr}_L < 1.8 \qquad 5.37$$

$$\mathrm{We}_L = \frac{\rho_L u_L^2}{a_p \sigma_L} \qquad 1.2\times10^{-8} < \mathrm{We}_L < 0.272 \qquad 5.38$$

and the term σ_c is defined as the critical surface tension, specific to each material. For steel packing it assumes a value of 75 mN/m (Tsai, 2010).

In assuming complete and even liquid distribution on the packing material, the Delft model is incapable of accounting for mass transfer inactive zones in the liquid film. The effect of liquid turbulence on mass transfer rate and effective area generation is also not accounted for. These limitations cause it to mostly under predict the effective interfacial mass transfer area measured via the chemical method (see section 5.2) (Tsai, 2010).

5.1.6 Correlations Proposed by Del Carlo et al.

The model proposed by Del Carlo et al (Del Carlo, et al., 2006) is another attempt at deriving the governing equations for mass transfer on structured packing based on purely geometric considerations. They aimed at producing a model that is independent of any empirical tuning parameters. The main aim of their work was to obtain correlations for the prediction of the efficiency parameters of equation 5.3 to a higher degree of accuracy compared to previous geometrically based correlations. Their model was validated on 17 types of packing material (mostly Mellapak™ and Montz-B1 packing) using 4 types of test systems (mostly chlorobenzene/ethylbenzene and cyclohexane/n-heptane) over a pressure range of 0.1 – 27.2 bar.

In the introduction of their paper, they especially discuss the need for deriving more applicable and accurate models for calculating a_e under actual separation column operating conditions. Similar to the SRP model, they also believe that fractional liquid hold-up is at the centre of the

interfacial area problem. They adopted the correlation proposed by Suess and Spiegel for calculating h_L (Suess & Spiegel, 1992):

$$h_L(\%) = c_1 a_p^{0.83} (3600 u_L)^{c_2} \left(\frac{\mu_L}{\mu_{H_2O@20^\circ C}} \right)^{0.25} \quad 5.39$$

where

$$\left.\begin{matrix} c_1 = 0.0169 \\ c_2 = 0.37 \end{matrix}\right\} u_L < 0.011 \text{ m/s} \quad \text{and} \quad \left.\begin{matrix} c_1 = 0.0075 \\ c_2 = 0.59 \end{matrix}\right\} u_L > 0.011 \text{ m/s}$$

The fractional liquid hold-up was then incorporated into a correlation for calculating the fractional wetted area as proposed by Brunazzi et al. (1995):

$$\frac{a_e}{a_p} = \left(\frac{d_h}{4\varepsilon} \right) \left(\frac{h_L}{\varepsilon} \right)^{1.5} \left(\frac{\varepsilon \rho_L g \sin^2 \theta}{3 \mu_L u_L} \right)^{0.5} \quad 5.40$$

The hydraulic diameter has the same definition as in the Billet & Shultes model (equation 5.19).

The gas phase mass transfer coefficient was calculated using the same expression used by the SRP model (equation 5.12). The liquid phase mass transfer coefficient was once again based on correlations proposed in a later paper by Brunazzi & Paglianti (1997). In this model it was assumed that the mass transfer resistance in the liquid phase is more significant than other models (such as the Delft model) presume it to be. Due to this assumption, the liquid phase mass transfer coefficient was not simply calculated using penetration theory, but was correlated using dimensionless numbers:

$$\text{Sh}_L = 16.43 \frac{\text{Gz}^{0.915}}{\text{Ka}^{0.09}} \quad 5.41$$

$$\text{Ka} = \frac{\sigma^3 \rho_L}{\mu_L^4 g} \quad 5.42$$

$$\text{Gz} = \text{Re}_L \, \text{Sc}_L \frac{\delta \sin \varpi}{h_{PE}} \quad 5.43$$

where h_{PE} is the height of a packing element and ϖ the effective liquid flow angle. The effective liquid flow angel is a function of the corrugation angle of the packing material and was determined to be 60° for 45° packing and 69° for 60° packing (Brunazzi & Paglianti, 1997). Under conditions where the shear stress between vapor and liquid is negligible (low pressures), the liquid film thickness may be calculated from:

$$\delta = \sqrt{\frac{3\mu_L}{\rho_L g \sin\varpi} \cdot \frac{u_L}{h_L \sin\varpi}} \qquad 5.44$$

The model was derived under the assumption that the liquid flow follows the behaviour of a falling film. This limits the application of this model to the pre-loading and loading regions of distillation operation. Under these conditions the liquid flows as a stratified film. Furthermore, the accuracy of the model is strongly dependent on the accuracy of the fractional liquid hold-up correlation. It is therefore of utmost importance that this parameter is evaluated to a high degree of precision and certainty. Judging by the step function nature of equation 5.39, this is not always easy to obtain.

5.1.7 CFD and X-Ray CT Approach

Computational Fluid Dynamics (CFD) is a computer based method that solves a system of mass and momentum balance equations numerically. It is able to predict flow patterns of gas and liquid phase flow as well as the interaction between the phases given the appropriate boundary conditions. CFD has been applied to the two phase flow of structured packing in several studies (Mahr & Mewes, 2007; Haroun, et al., 2010; Shojaee, et al., 2011; Haroun, et al., 2012). Previous studies were mainly concerned with visualizing liquid distribution (Mahr & Mewes, 2007) or determining dynamic liquid hold-up of the packing material. Incorporating mass transfer correlations into the governing model equations allowed for the estimation of the mass transfer performance of the packing material (Haroun, et al., 2012).

In a study aimed at approximating the interfacial area achieved on structured packing with CFD, a volume of fluid (VOF) multiphase-flow model was developed (Shojaee, et al., 2011). This model assumes that the interface of two immiscible phases may be determined with the

knowledge of the volume fractions of each phase within a computational cell. Mass and momentum balance equations are solved to determine the volume of each phase within a cell. The liquid film thickness is also taken into account along with the calculated liquid hold-up.

The results of the CFD simulation to determine the interfacial area were compared with models in literature (Delft model, SRP model etc.). The comparison did not warrant any decisive conclusion on the accuracy of the model, since the literature models themselves are in disagreement with one another. The CFD model did show an increase in interfacial area with an increase in both liquid and vapour velocities. The former has been shown by previous researchers to be true, whilst the latter was explained with the formation of ripples and droplets. As the vapour flow rate at the gas-liquid interface increases, an increase in liquid ripples and droplet formation may be noticed. These effects mark an increase in interfacial area.

One of the main concerns with CFD results is validation. Since CFD provides visual flow field results, an argument could be made that the validation of the results rely on optical measurements such as particle image velocimetry or particle tracking velocimetry (Owens, et al., 2009). These methods have the disadvantage of having their view obscured by the packing elements. X-ray computed tomography (CT) may be a feasible method to overcome the limitations of an obstructed field of view, since X-rays can pass through the column walls and detect the liquid flowing on the packing elements (Green, et al., 2007). It is theoretically possible to distinguish between certain contacting phases due to the difference in the attenuation of the X-ray energy by each phase (Green, et al., 2007; Owens, et al., 2009).

The degree of attenuation may be distributed on a grey scale ranging in values of 0 (black) for total attenuation and 255 (white) for zero attenuation. It is expected that more dense material will attenuate more X-ray energy than less dense material. The attenuation calibration of the sheet metal structured packing material was achieved from X-ray scans of a dry packed bed. The geometric area of the packing obtained from the reconstructed images agreed well with the area calculated by taking all void fractions inside the column as well as the area of the wall

wipers into account (Aferka, et al., 2010). Two grey scale values were obtained and allocated to both air and steel.

When water was introduced to the system, the properties of the air in the system started fluctuating, making it difficult to distinguish between the grey scale values of air and water at the interface (Green, et al., 2007). A blurry interface means that the results of the X-ray scans may only be interpreted on a qualitative basis. The trends noticed in the liquid hold-up measurements were correct and some of the interfacial area estimation values agreed with the values obtained using a chemical method. Higher energy X-rays with increased phase boundary resolution will be required to improve the accuracy of this technique. Improvements of this technique are in progress and it will, no doubt, be a feasible method for CFD validation in the near future.

A detailed comparison of the most widely used hydraulic and geometry based effective area correlations will be presented in section 5.3. Furthermore, in section 5.3 a comparison between the predictions of the hydraulic and geometry based correlations and the predictions of the correlations derived using the chemical method, will also be presented. The chemical method is discussed in section 5.2.

5.2 The Chemical Method

A method that has been widely accepted as providing the best approximation of the interfacial area achieved by a separation column internal relies on a fast chemical reaction (Astarita, 1967; Danckwerts, 1970; Charpentier, 1981; Erasmus, 2004; Tsai, et al., 2008). The chemical method involves the reactive absorption of a gas into a liquid. The gas then undergoes a fast reaction in the liquid film, which controls the rate of absorption. The absorption therefore becomes independent of the physical liquid side mass transfer coefficient (k_L) and only depends on the available effective interfacial area between the gas and liquid.

This, seemingly simple, method has produced surprisingly variable interfacial area predictions and correlations from different studies (Tsai, 2010). This section will present the different theories derived from the fast reactive absorption method along with the correlations obtained

for calculating interfacial area. It will present the most popular chemical systems used along with the assumptions made regarding the conditions under which the reactive absorption experiments were carried out. The most popular equipment used in the experiments will be discussed and the latest interfacial mass transfer area correlations derived from the chemical method will be presented.

5.2.1 Pseudo First Order Conditions

In section 2.2.1 reactive absorption with an assumed irreversible reaction in the liquid film was discussed. Equation 2.16 is used as a representative reaction once again. Under certain experimental conditions, it may be assumed that the reagent (*B*) in the liquid film undergoes insignificant depletion due to its reaction with the reactively absorbing gas (*A*). Under these conditions pseudo mth order reaction kinetics may be assumed:

$$-r_A = k_{m,n} C_A^m C_B^n \approx k_{m,0} C_A^m \qquad 2.34$$

The chemical methods used by previous researchers to determine interfacial area all used a system where pseudo mth order kinetics was assumed (Danckwerts, 1970; Puranik & Sharma, 1970; Sridharan & Sharma, 1976; Neelakantan & Gehlawat, 1982; de Brito, et al., 1994; Erasmus, 2004; Tsai, et al., 2008). Further, the systems chosen by these researchers were assumed to be pseudo first order with respect to the reacting gas, which simplifies the mathematics even more. The reason for selecting pseudo mth order conditions was twofold:

1. Under pseudo mth order conditions there is no interfacial depletion of the liquid phase reagent, causing the entire interface to be effective for mass transfer given insignificant gas phase resistance to mass transfer.
2. The insignificant depletion of the liquid side reagent effectively means that the liquid surface renewal rate is infinite. The absorption rate is, therefore, independent of contact time which serves as a positive test for pseudo mth order reaction conditions (Charpentier, 1981; Erasmus, 2004)

The criteria required for reactive absorption to take place under the fast pseudo mth order conditions are presented in section 2.2.1, but will be revisited here. Whenever absorption is accompanied with a chemical reaction it is convenient to employ an enhancement factor (equation 2.24) to account for the change in absorption rate due to the presence of a chemical reaction. The absorption rate may then be calculated from:

$$\left(N_A\right)_x \cdot a_e = n_A = Ek_L a_e \left(C_{A,i} - C_{A,L}\right) \qquad 2.25$$

A dimensionless number, the Hatta number, is a convenient way in which to evaluate the effect of the chemical reaction on the absorption rate. It is expressed as the ratio of the reaction kinetics to the physical absorption kinetics. An example of the Hatta number for an m,nth order irreversible reaction is:

$$\mathrm{Ha} = \frac{\sqrt{\left(\frac{2}{m+1}\right)\left(k_{m,n} D_A C_{A,i}^{m-1} C_{B,L}^{n}\right)}}{k_L} \qquad 2.27$$

If the Hatta number is large $\mathrm{Ha}^2 >> 1$ (Tsai, et al., 2008), it may be assumed that the reaction kinetics dominates the absorption rate and physical mass transfer becomes insignificant. There are of course limitations to how fast the reaction may be. If the reaction kinetics is fast enough to indicate an instantaneous reaction rate $\mathrm{Ha} > 10E_i$ (Charpentier, 1981), then physical mass transfer effects such as the diffusion of the liquid side reagent to the reaction zone in the liquid film starts controlling the absorption rate. The range of Hatta numbers indicating a fast pseudo first order $\left(m = 1\right)$ reaction to occur in the liquid phase with absorption independent of the liquid side mass transfer coefficient is (Danckwerts, 1970; Charpentier, 1981):

$$3 < \mathrm{Ha} < 0.5E_i \qquad 2.30$$

where E_i is the enhancement factor relating to an instantaneous reaction:

$$E_i = 1 + \left(\frac{a \cdot D_B}{b \cdot D_A}\right)\left(\frac{C_{B,L}}{C_{A,i}}\right) \qquad 2.28$$

Under the assumption of pseudo first order conditions, equation 2.15 is solved assuming the concentration of CO_2 in the liquid phase to be zero. For this solution the Hatta number and enhancement factors are approximately equal (Charpentier, 1981; Erasmus, 2004; Tsai, 2010) and the absorption rate may be calculated from:

$$\left(N_A\right)_x = \frac{n_A}{a_e} = k_G\left(P_{A,0} - P_{A,i}\right) = \mathrm{Ha}\cdot k_L\left(C_{A,i} - C_{A,L}\right) = \frac{\mathrm{Ha}\cdot k_L}{H_A}\left(P_{A,i} - P_{A,L}\right) \qquad 2.31$$

For a pseudo first order irreversible reaction $\left(m=1,\, n=0,\, P_{A,L}=0\right)$, the absorption rate simplifies to (Tsai, 2010):

$$\left(N_A\right)_x = \frac{n_A}{a_{\text{contact device}}} = \frac{\sqrt{k_{1,0}D_A}}{H_A}P_{A,i} \qquad 5.45$$

Two different approaches to relate equation 5.45 to the interfacial mass transfer area of separation column internals were followed by previous researchers. These approaches will be discussed separately.

5.2.2 Specific Absorption Rate Approach

The first approach assumed it unnecessary to determine the transport $\left(D_{A,L},\, H_A\right)$ and reaction kinetic $\left(k_{1,0}\right)$ parameters separately (Charpentier, 1981; de Brito, et al., 1994; Erasmus, 2004). These studies assumed that if the reaction is determined to be suitable (absorption rate independent of contact time) then an absorption rate correlation derived from reactively absorbing a gas into a known interfacial surface area of liquid could be used to determine the interfacial area of separation column internals. Absorption rate per area is known as the specific absorption rate. The specific absorption rate correlation is expressed in terms of the gas phase partial pressure and liquid phase reagent concentration (Erasmus, 2004):

$$N_A = kP_{A,i}^{\mathrm{A}}C_{B,b}^{\mathrm{B}} \qquad 5.46$$

For this approach to be feasible, insignificant gas phase mass transfer resistance may exist and the partial pressure driving force in the separation column experiments must be equal to the

partial pressure driving force used in the known interfacial surface area contacting device (Astarita, 1967). It may then be assumed that the absorption rate per area in the known area contacting device is equal to the absorption rate per area in the separation column. The most popular contacting devices with known interfacial areas used in specific absorption studies are discussed in section 5.2.5.

A material balance of the reactively absorbing gas over a differential height (dz) of separation column internal yields the following expression (Erasmus, 2004):

$$\dot{V}_G dy_A = a_i N_A A_{\text{column}} dz \qquad 5.47$$

where $\dot{V}_G$ is the volumetric flow rate of the gas phase, y_A is the mole fraction of the reacting gas in the gas phase and A_{column} is the cross sectional area of the separation column internal. Integration of equation 5.47 for a certain column internal height, h, yields the following expression for calculating a_i from the measured molar absorption rate, n_A:

$$a_i = \frac{n_A}{A_{\text{column}} \int_0^h N_A dz} \qquad 5.48$$

In order to be able to evaluate the integral in equation 5.48, the specific absorption rate of the gas as a function of column height must be known. This is not an easy functionality to determine, since both the partial pressure of the gas and the interfacial concentration of the liquid reagent vary indeterminately with column height. Linear concentration profiles for both gas and liquid reagents were assumed (Erasmus, 2004), which is incorrect based on the concentration profiles obtained in the reaction kinetic data collected in this study. The reaction kinetics and physical absorption parameters may in fact be crucial information required to determine the specific absorption rate as a function of column height.

5.2.3 Series Resistance Approach

The second approach to calculating interfacial mass transfer, more recently used (Tsai, et al., 2008; Shabani, et al., 2010), involves modelling the overall gas absorption rate as a series of resistances:

$$\frac{1}{K_G} = \frac{1}{k_G} + \frac{H_A}{k_L} \qquad 2.2$$

If it is assumed that the gas phase resistance in the separation column is negligible, then the overall mass transfer coefficient is equal to a modified liquid side mass transfer coefficient (Tsai, 2010):

$$K_G = k_L' \qquad 5.49$$

The reason for calling it a modified liquid side mass transfer coefficient is because it is used in conjunction with the partial pressure driving force of the reacting gas and not, as for the traditional coefficient, with the liquid phase concentration difference in the liquid film. For an irreversible pseudo first order reaction system (equation 5.45), the modified liquid side mass transfer coefficient may be determined to be (de Brito, et al., 1994; Tsai, et al., 2008):

$$k_L' = \frac{\sqrt{k_{1,0} D_{A,L}}}{H_A} = \frac{\sqrt{k_{m,n} C_B^n D_{A,L}}}{H_A} \qquad 5.50$$

From equation 5.50 it is evident that in order to be able to calculate the overall mass transfer coefficient, knowledge of the transport and kinetic parameters becomes essential. As mentioned in section 2.2.1, the pseudo first order rate constant may be determined directly from the rate of absorption into a known interfacial area of liquid, provided that the physical mass transfer parameters are known.

A differential material balance for a short section of column internal may also be expressed as (Tsai, 2010):

$$u_G \frac{dy_A}{dz} = \left(K_G a_i\right)\left(RT\right)\left(y_{A,L} - y_A\right) \qquad 5.51$$

Assuming the gas velocity $\left(u_G\right)$ and volumetric mass transfer coefficient $\left(K_G a_i\right)$ to be independent of column height and the liquid phase mole fraction of the gas $\left(y_{A,L}\right)$ to be zero due to the irreversible nature of the pseudo first order reaction conditions, equation 5.51 may be expressed as:

$$\int_{y_{A,out}}^{y_{A,in}} \frac{dy}{y} = \frac{(K_G a_i)(RT)}{u_G} \int_0^h dz \qquad 5.52$$

Integration of equation 5.52 and rearranging yield the following expression for calculating interfacial area under pseudo first order reaction conditions:

$$a_i = \frac{u_G \ln\left(\frac{y_{A,in}}{y_{A,out}}\right)}{hK_G RT} \approx \frac{u_G \ln\left(\frac{y_{A,in}}{y_{A,out}}\right)}{hk_L' RT} = \frac{u_G \ln\left(\frac{y_{A,in}}{y_{A,out}}\right)}{hRT} \cdot \frac{H_A}{\sqrt{k_{m,n} C_B D_{A,L}}} \qquad 5.53$$

Both the reaction kinetics and physical absorption parameters are now included in the expression to calculate interfacial mass transfer area under pseudo first order reaction conditions. The series resistance approach may therefore be concluded to be more accurate than the specific absorption rate approach.

5.2.4 Most Popular Absorption Systems Used for Calculating Interfacial Area

The most popular absorption system employed for determining interfacial mass transfer area with the use of the chemical method is the reactive absorption of CO_2 into aqueous solutions of sodium hydroxide (NaOH) (Danckwerts, 1970; Charpentier, 1981; de Brito, et al., 1994; Tsai, et al., 2008). The liquid phase reaction is considered to fall in the fast reaction regime with the mechanism given by (Tsai, et al., 2008; Tsai, 2010):

$$\begin{aligned} CO_2 + OH^- &\underset{k_2}{\overset{k_1}{\rightleftharpoons}} HCO_3^- \\ HCO_3^- + OH^- &\underset{k_4}{\overset{k_3}{\rightleftharpoons}} CO_3^{2-} + H_2O \end{aligned} \qquad 5.54$$

This reaction mechanism is analogous with the mechanism of the reaction of CO_2 with MEA in alcoholic solvents (equation 3.3). If irreversible pseudo first order reaction conditions with respect to CO_2 are assumed to be valid, then the rate expression used for determining a_i with the chemical method is assumed to be:

$$-r_{CO_2} = k_{OH^-}[CO_2][OH^-] = k_{1,0}[CO_2] \qquad 5.55$$

Equation 5.45 may now be expressed as:

$$\left(N_{CO_2}\right)_x = \frac{n_{CO_2}}{a_{\text{contact device}}} = \frac{\sqrt{k_{1,0}D_{CO_2}}}{He_{CO_2}} P_{CO_2,i} = \frac{\sqrt{k_{OH^-}\left[OH^-\right]D_{CO_2}}}{He_{CO_2}} P_{CO_2,i} \qquad 5.56$$

And the interfacial mass transfer area based on the CO_2/NaOH system may be calculated from:

$$a_i = \frac{u_G \ln\left(\frac{y_{CO_2,\text{in}}}{y_{CO_2,\text{out}}}\right)}{hRT} \cdot \frac{H_{CO_2}}{\sqrt{k_{OH^-}\left[OH^-\right]D_{CO_2,L}}} \qquad 5.57$$

The rate constant and the physical absorption parameters are calculated from expressions derived from a study to determine these parameters from specific absorption data (Pohorecki & Moniuk, 1988; Tsai, 2010)

The disadvantage of the CO_2/NaOH system is that it may only be used in aqueous systems due to solubility issues related with organic solvents. Aqueous systems are notorious for not providing adequate liquid distribution on the separation column internal due to the high surface tension of water (Erasmus, 2004; Shi & Mersmann, 1985; Tsai, 2010). This has sparked an investigation into finding suitable systems for the lower surface tension organic solvents as well. The most widely used system is the reactive absorption of CO_2 into non-aqueous solutions of amines (Sridharan & Sharma, 1976; Charpentier, 1981). The CO_2/MEA/alcohol system under investigation in this study is an example of such a suitable system.

Although the aqueous CO_2/NaOH and aqueous - and non-aqueous CO_2/amine systems are the most popular to use in the pseudo first order chemical method, other systems have also been used. These systems are summarized in literature (Sridharan & Sharma, 1976; Charpentier, 1981; de Brito, et al., 1994).

5.2.5 Equipment used in Specific Absorption Rate Studies

In order to be able to collect specific absorption rate data, the gas liquid contacting device used to conduct the experiments on should have an accurately measureable interfacial area. Specific absorption studies may also be subject to the influence of the physical transport parameters

and the gas-liquid contact time. There are a number of contact devices available for specific absorption rate studies of which the most popular are tabulated in **Table 5.1**.

Table 5.1 Summary of Absorption Equipment Used to Conduct Kinetic Studies (Charpentier, 1981)

Type	Laminar Jet	Cylindrical Wetted Wall	Spherical Wetted Wall	String of Discs	Rotating Drum	Stirred Vessel
k_L (cm/s)	0.016 – 0.16	3.6×10^{-3} – 0.016	5×10^{-3} – 0.016	3.6×10^{-3} – 0.016	0.016 – 0.36	1.6×10^{-3} – 0.02
Contact Times (s)	10^{-3} – 10^{-1}	0.1 - 2	0.1 - 1	0.1 - 2	2×10^{-4} - 10	0.06 - 10
Interfacial Area	0.3 – 10cm^2 High Precision	10 – 100cm^2 High Precision	10 – 40cm^2 High Precision	30 – 360cm^2 Moderate Precision	Diameter 10cm, Length 12cm High Precision	0.3 – 10cm^2 Good Precision

For the purpose of determining the pseudo first order rate constants for the CO_2/NaOH and CO_2/amine systems, the most popular contacting devices used by previous researchers are:

- Laminar Jet Absorber (Pohorecki & Moniuk, 1988; Aboudheir, et al., 2003)
- Cylindrical Wetted Wall Column (Lamourelle & Sandall, 1972; Alvarez-Fuster, et al., 1980; Alvarez-Fuster, et al., 1981; Aboudheir, et al., 2003; Zhi & Kai, 2009; Luo, et al., 2012)
- Stirred Vessel (Laddha & Danckwerts, 1981; Sada, et al., 1985; Versteeg & van Swaaij, 1988; Patil, et al., 2011)

The laminar jet absorber has simple hydrodynamics to consider (Astarita, 1967) and contact times that are much lower than the other two devices. It makes up for the low contact times by

having a higher physical mass transfer coefficient, which relates to similar absorption rates compared to the wetted wall and stirred vessel. The stirred vessel is a popular device to use for pseudo first order reaction kinetic studies, because the stirring of the liquid phase is assumed to rapidly renew the liquid surface with reagent. Under pseudo first order conditions, this becomes irrelevant, since the surface undergoes insignificant depletion and is therefore in no need of forced surface renewal.

In a study conducted on the physical absorption rate of CO_2 into a stirred vessel containing organic solvents (short chain alcohols), interesting observations were made with regards to the location of the stirring blades (Littel, et al., 1991). The stirring rod of the vessel was fitted with six blades. Depending on the volume of liquid inside the vessel, the blades were at different submerged depths. The conclusion of the study was that if the stirrer blade was shallower submerged, the absorption rate increased, which is not surprising since it meant that the rate of liquid surface renewal was increased. This effect was not noticed for aqueous solutions, since the submerged depth of the stirrer had no influence on the physical absorption rate of N_2O. The effect of surface tension on the surface renewal rate (Marangoni effect) was provided as a possible explanation for this observation.

Another interesting finding from the stirrer position study was that the absorption rate in 1-octanol was higher than in 1-butanol under the same conditions. This defies absorption theory, since diffusion rates in 1-butanol should be higher than that in 1-octanol based on the higher viscosity of 1-octanol (Reid & Sherwood, 1966). It further defies the surface tension explanation, since 1-octanol has a significantly higher surface tension than 1-butanol. The validity of the results was checked by making sure the equipment measured the correct absorption rate for aqueous systems. It was found that the equipment measurement and model predictions for aqueous absorption rates agreed well. The absorption rates of CO_2 into alcoholic solvents were higher than that predicted by the models. This study seems to indicate that surface renewal rate is a vital liquid film characteristic for modelling absorption rates. It may in fact be central to the problem of determining effective interfacial mass transfer area,

since the area available for mass transfer on the gas liquid interface is directly linked to the surface renewal rate achieved by the liquid film.

The surface renewal rate phenomena noticed in stirred vessels may be present in the liquid film flowing down a wetted wall column as well. The wetted wall column provides the best correlating conditions with that found in separation column internals. In most, but not all applications, both set-ups have the liquid film flowing under gravitational force, contacting the gas phase counter-currently. This is probably why the cylindrical wetted wall is a popular contacting device used for specific absorption studies with the aim of calculating interfacial area (Tsai, et al., 2008). As the liquid flow path on both a wetted wall and separation column internal increases, so does the Reynolds number causing an increase in liquid phase turbulence. This turbulence manifests as surface ripples or waves and enhances mass transfer rates (Danckwerts, 1970). These ripples are in fact increasing the rate of surface renewal in the liquid film, which results in an increase in effective interfacial area. The effect of the surface ripples on effective interfacial area will be discussed in Chapter 6.

5.2.6 Correlations Resulting from the Chemical Method

Absorption rate data collected for a known height of separation column internal is used to calculate interfacial area using the theories discussed in sections 5.2.2 and 5.2.3. The absorption runs may be conducted at different liquid and gas flow rates and also for different liquid phase physical properties (Tsai, 2010). The interfacial mass transfer area may then be correlated as a function of these parameters. The first correlation presented is the correlation derived by de Brito et al (de Brito, et al., 1994):

$$\frac{a_e}{a_p} = 0.465\,\mathrm{Re}_L^{0.3} = 0.465\left(\frac{\rho_L u_L}{\mu_L a_p}\right)^{0.3} \qquad 5.58$$

Equation 5.58 was derived from the reactive absorption data of CO_2 into fairly concentrated aqueous NaOH solutions (1.6 – 2 M) on Mellapak^{TM} 125Y, 250Y and 500Y structured packing. The specific absorption data was collected using cylindrical wetted wall. The liquid loads in the separation column were varied between 12.3 and 71.5 m^3/m^2h with the gas flow velocity

ranging from 0.75 – 3 m/s. The density and viscosity of the liquid phase was never altered, yet these parameters were incorporated in the correlation. The correlation predicts fractional areas of above unity at low liquid loads and at higher liquid loads the predictions exceed a value of 2. These results were deemed suspect by later researchers (Tsai, 2010).

Another correlation in the same form as equation 5.58 was developed by Dragan et al (2000):

$$\frac{a_e}{a_p} = 0.1245\,\mathrm{Re}_L^{0.4} = 0.1245\left(\frac{6(1-\varepsilon)\rho_L u_L}{a_p \mu_L}\right)^{0.4} \qquad 5.59$$

Equation 5.59 was also developed from absorption data of diluted CO_2 (5 – 10 vol%) into aqueous NaOH solutions (0.5 and 1 M) on MellapakTM 750Y. The liquid loads were varied between 12.3 and 30.8 m^3/m^2h with the gas velocities ranging between 0.1 and 0.35 m/s. The resulting correlation (equation 5.59) predicts fractional areas in the range of 0.12 to 0.2. These predictions are far removed for the predictions of equation 5.58 for the same liquid loads and the same absorption system. One or both of these correlations may therefore be subject to a fundamental error.

A recent study conducted at the SRP (Tsai, 2010) intended to shed light on the effect of liquid properties such as viscosity and surface tension on the fractional area. Once again, the absorption rate data of diluted CO_2 into aqueous solutions of NaOH (0.1 M) were used. The specific absorption data was collected using a cylindrical wetted wall and the interfacial area was calculated using the series resistance approach.

The liquid properties were altered in this study. The liquid surface tension ranged from 30 to 72 mN/m and the liquid viscosity was varied between 1 and 15 mPa.s. The liquid load varied between 2.5 and 75 $m^3/m^2.h$ and the gas velocity between 0.6 and 2.3 m/s. The geometric area of the structured packing investigated varied in the range of 125 to 500 m^2/m^3.

The surface texture of the packing material was also altered to investigate the effect of surface texture on interfacial area. The experimental database of absorption data was correlated with

the use of two dimensionless numbers, the Weber $\left(\mathrm{We}_L\right)$ and Foude $\left(\mathrm{Fr}_L\right)$ numbers defined as:

$$\mathrm{We}_L = \frac{\rho_L u_L^2 \delta}{\sigma} = \frac{1}{\sigma}\left[\frac{\rho_L^4 g\left(\sin\theta\right)}{3\mu_L}\left(\frac{\dot{V}_L}{L_P}\right)^5\right]^{1/3} \qquad 5.60$$

$$\mathrm{Fr}_L = \frac{u_L^2}{g\delta} = \frac{\rho_L \sin\theta}{3\mu_L}\left(\frac{\dot{V}_L}{L_p}\right) \qquad 5.61$$

The global model resulting from regression analysis of the form:

$$\ln\left(\frac{a_e}{a_p}\right) = C_1 \ln\left(\mathrm{We}_L\right) + C_2 \ln\left(\mathrm{Fr}_L\right) + C_3 \qquad 5.62$$

was determined to be:

$$\left(\frac{a_e}{a_p}\right) = 1.34\left[\left(\mathrm{We}_L\right)\left(\mathrm{Fr}\right)^{-1/3}\right]^{0.116} = 1.34\left[\left(\frac{\rho_L}{\sigma}\right) g^{1/3}\left(\frac{\dot{V}_L}{L_P}\right)^{4/3}\right]^{0.116} \qquad 5.63$$

The interfacial area predictions of equation 5.63 did not agree well with the other existing correlations presented in this chapter, including the geometry based correlations. For the most part, it predicts larger interfacial areas than the geometry based correlations (see section 5.3). This may be attributed to the geometry based correlations' inadequacy to account for the increase in interfacial area due to droplet formation and a wavy liquid surface. Equation 5.63 predicts interfacial areas that seem realistic and up to date it is probably the best interfacial area correlation available for structured packing. The study found that interfacial area is mainly dependent upon packing geometric area, liquid flow rate and surface tension. It found it to be independent of liquid viscosity and packing material surface texture. The latter could be due to the fact that pseudo first order conditions were used to determine interfacial area. If the liquid phase surface renewal rate is infinite, then the diffusion of reagent to the surface is also infinite and the viscosity effect of the liquid will go undetected, since viscosity has a strong influence on the rate of species diffusion (Reid & Sherwood, 1966).

Although CO_2/amine systems are popular for measuring specific absorption data and using it to measure interfacial area, no regression fit on the separation column data to derive an interfacial mass transfer are model is available in literature (to the knowledge of the author). The only correlation found was based on the specific absorption rate approach (Erasmus, 2004). Absorption runs of diluted CO_2 into alcoholic solutions of MEA were performed in a separation column containing Flexipac 350Y for liquid loads in the range of 5 to 25 m^3/m^2hr and three gas flow factors, 1.1, 1.5 and 2 $(m/s)(kg/m^3)^{0.5}$. The interfacial area correlation was regressed in terms of liquid flow rate only and may be presented as:

$$\frac{a_e}{a_p} = 0.331 \cdot \ln\left(u_L + 10^{-3}\right) + 2.29 \qquad 5.64$$

Equation 5.64 shows no correlation of interfacial area with liquid or packing type properties and it is therefore considered to be a packing specific correlation. Its prediction of interfacial area is also in poor agreement with the other correlations presented in this chapter. It predicts interfacial areas in the order of 50 – 70% lower than the geometry based correlations presented in this chapter. Although it shows a similar increase in interfacial area prediction with an increase in liquid load, it predicts a lower interfacial area than equation 5.63 as well. A direct comparison is not possible, because equation 5.63 was not correlated on Flexipac 350Y. The nearest structured packing geometry for the use of comparison is M250Y packing. Equation 5.64 predicts interfacial areas in the region of 30% lower than equation 5.63 based on this comparison. A detailed comparison of the correlations derived from the chemical method with one another and the geometry based correlations is presented in section 5.3.

5.3 Comparison of Existing Effective Area Correlations

In this section a comparison of the effective area correlations presented in this chapter will be provided. The correlations used for comparison are tabulated in **Table 5.2** and the types of packing along with their properties used in the comparison are tabulated in **Table 5.3**.

Table 5.2 Summary of Some of the Effective Area Correlations Presented in Chapter 5

Source	Correlation	Packing Type
Rocha et al.	$\frac{a_e}{a_p} = F_{SE} \cdot F_t = F_{SE} \frac{29.12 u_L^{0.4} \nu_L^{0.2} S^{0.359}}{(1-0.93\cos\gamma)(\sin\theta)^{0.3} \varepsilon^{0.6}} \left(\frac{\rho_L}{\sigma g}\right)^{0.15}$ $\cos\gamma = 5.211\times10^{-16.835\sigma}$ for $\sigma > 55$ mN/m $\cos\gamma = 0.9$ for $\sigma < 55$ mN/m	Structured
Billet & Schultes	$\frac{a_e}{a_p} = 1.5(a_P d_h)^{-0.5} \left(\frac{u_L d_h}{\nu_L}\right)^{-0.2} \left(\frac{u_L^2 \rho_L d_h}{\sigma}\right)^{0.75} \left(\frac{u_L^2}{g d_h}\right)^{-0.45}$	Random and Structured
Onda et al.	$\frac{a_e}{a_p} = 1 - \exp\left[-1.45\left(\frac{\sigma_c}{\sigma_L}\right)^{0.75} \mathrm{Re}_L^{0.1} \mathrm{Fr}_L^{-0.05} \mathrm{We}_L^{0.2}\right]$, $0.3 < \frac{\sigma_c}{\sigma_L} < 2$ $\mathrm{Re}_L = \frac{\rho_L u_L}{a_p \mu_L}$ $0.04 < \mathrm{Re}_L < 500$ $\mathrm{Fr}_L = \frac{u_L^2 a_p}{g}$ $5\times10^{-9} < \mathrm{Fr}_L < 1.8$ $\mathrm{We}_L = \frac{\rho_L u_L^2}{a_p \sigma_L}$ $1.2\times10^{-8} < \mathrm{We}_L < 0.272$	Random

Brunazzi et al.	$\frac{a_e}{a_p}=\left(\frac{d_h}{4\varepsilon}\right)\left(\frac{h_L}{\varepsilon}\right)^{1.5}\left(\frac{\varepsilon\rho_L g\sin^2\theta}{3\mu_L u_L}\right)^{0.5}$ $h_L(\%)=c_1 a_p^{0.83}\left(3600u_L\right)^{c_2}\left(\frac{\mu_L}{\mu_{H_2O@20\,^\circ\mathrm{C}}}\right)^{0.25}$ $\left.\begin{matrix}c_1=0.0169\\c_2=0.37\end{matrix}\right\}\ u_L<0.011\ \mathrm{m/s}$ and $\left.\begin{matrix}c_1=0.0075\\c_2=0.59\end{matrix}\right\}\ u_L>0.011\ \mathrm{m/s}$	Structured
de Brito et al.	$\frac{a_e}{a_p}=0.465\,\mathrm{Re}_L^{0.3}=0.465\left(\frac{\rho_L u_L}{\mu_L a_p}\right)^{0.3}$	Structured
Dragan et al.	$\frac{a_e}{a_p}=0.1245\,\mathrm{Re}_L^{0.4}=0.1245\left(\frac{6(1-\varepsilon)\rho_L u_L}{a_p\mu_L}\right)^{0.4}$	Structured
Tsai	$\frac{a_e}{a_p}=1.34\left[\left(\mathrm{We}_L\right)\left(\mathrm{Fr}\right)^{-1/3}\right]^{0.116}=1.34\left[\left(\frac{\rho_L}{\sigma}\right)g^{1/3}\left(\frac{\dot{V}_L}{L_P}\right)^{4/3}\right]^{0.116}$	Structured
Erasmus	$\frac{a_e}{a_p}=0.331\cdot\ln\left(u_L+10^{-3}\right)+2.29$	Structured

Table 5.3 Packing Type and Properties Used for Effective Area Correlations Comparison

Packing	Specific Area, a_p (m^2/m^3)	Corrugation Angle, Θ (°)	Channel Side, S (m)	Channel Base, b (m)	Crimp Height, h (m)	L_P/A (m/m^2)	Void Fraction, ε
Mellapak™ 125Y	125	45	0.037	0.055	0.0248	109	0.99
Mellapak™ 250Y	250	45	0.017	0.0241	0.0119	237	0.95
Mellapak™ 500Y	500	45	0.0081	0.0096	0.00653	517	0.92

The first comparative investigation was to evaluate the prediction of the effective area correlations in **Table 5.2** for the same type of structured packing (Mellapak^{TM}) but for different packing specific areas. The correlation predictions for Mellapak^{TM} 125Y, Mellapak^{TM} 250Y and Mellapak^{TM} 500Y are illustrated in **Figure 5.4**, **Figure 5.5** and **Figure 5.6** respectively. The figures are presented in terms of predicted fractional area (ratio of effective area to packing specific area) as a function of liquid load in the column. Liquid load is the volumetric liquid flow rate per cross sectional area of the column.

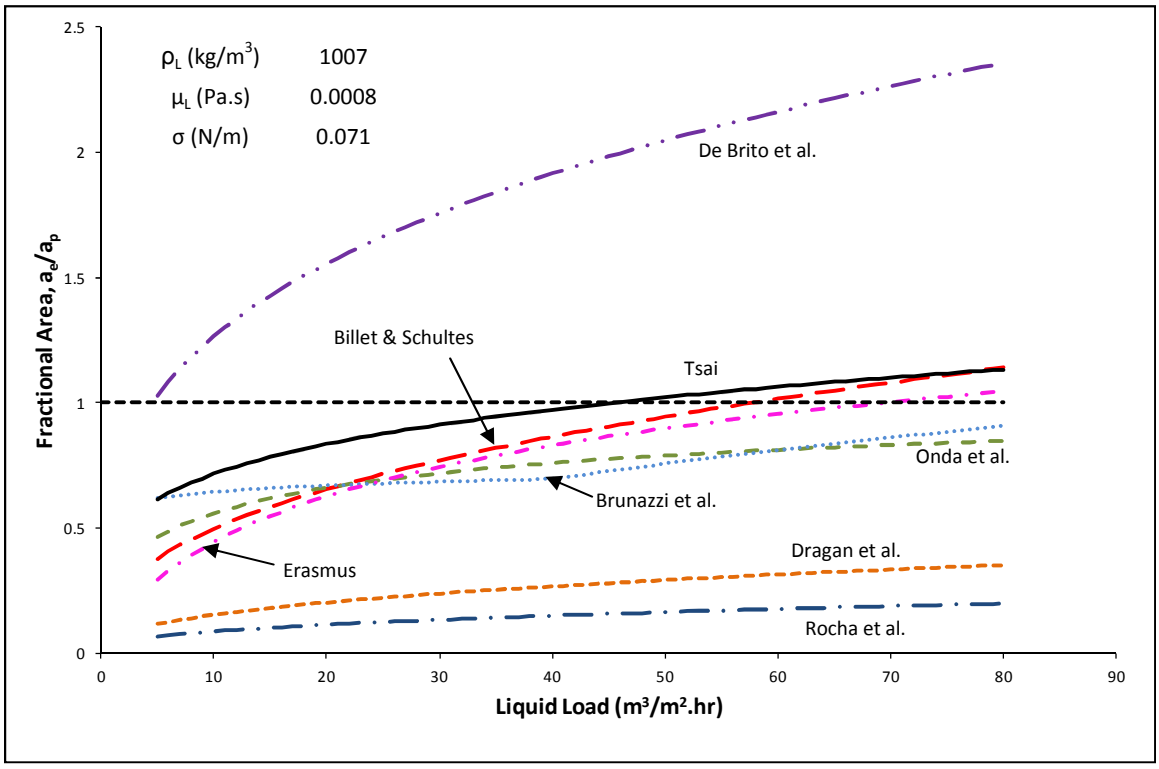

Figure 5.4 Comparison of Effective Area Correlations for Mellapak^{TM} 125Y Structured Packing

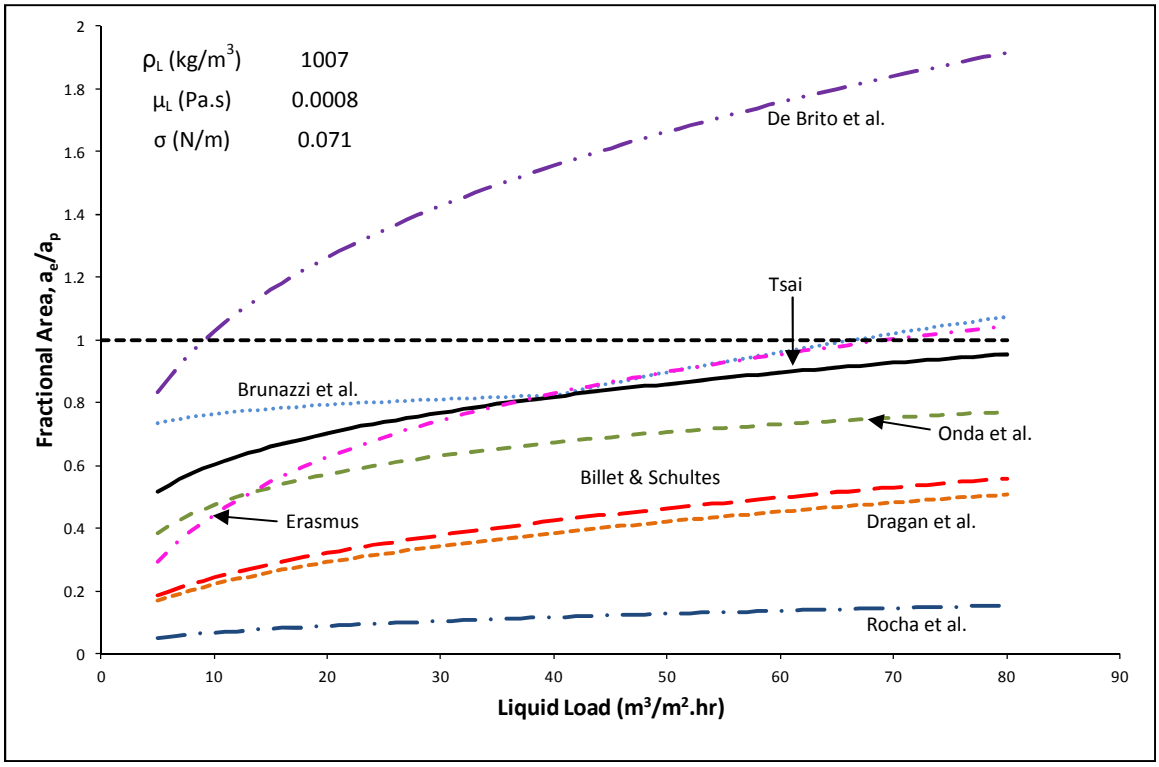

Figure 5.5 Comparison of Effective Area Correlations for Mellapak^{TM} 250Y Structured Packing

From the comparative illustrations in **Figure 5.4**, **Figure 5.5** and **Figure 5.6** the large difference in fractional area predictions of the existing effective area correlations are obvious. All the correlations predict an increase in fractional area with an increase in liquid load, which is expected, since an increase in liquid load causes an increase in the wetting of structured packing material up to the point where the packing achieves its optimum liquid capacity (Olujic, et al., 1999). The increase in liquid distribution causes an increase in the wetted area of the packing, which increased the gas-liquid interfacial area.

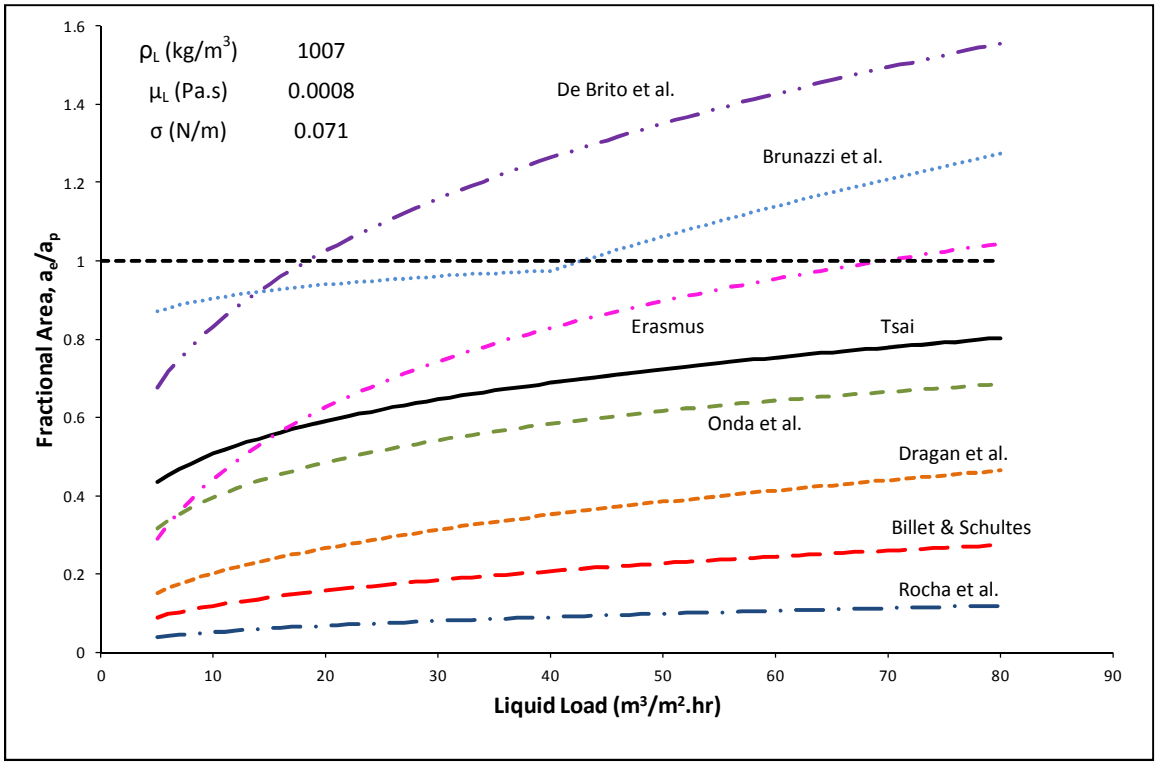

Figure 5.6 Comparison of Effective Area Correlations for Mellapak^{TM} 500Y Structured Packing

The correlation by Rocha et al. consistently predicts fractional areas well below that of the other correlations. It was derived from the correlation proposed by Shi and Mersmann (1985) which was effectively a liquid distribution model. The reason for the under prediction in fractional area may be due to it predicting the liquid distribution of water (physical properties used in this comparative study) on stainless steel. Water is known to show poor liquid distribution on stainless steel surfaces (Shi & Mersmann, 1985). The correlation by de Brito et al. predicts fractional areas far greater than the other correlations. It consistently predicts fractional areas greater than 1 and goes up to 2.5 for Mellapak^{TM} 125Y. The authors claim that this over prediction is partly due to liquid turbulence causing an increase in absorption rates due to an increase in effective area and partly due to droplet formation at higher liquid flow rates (de Brito, et al., 1994). Their correlation has, however, been termed suspect by other researchers, because of its high fractional area predictions (Tsai, 2010).

The correlation by Erasmus is independent of packing properties and so, as expected, its fractional area prediction stays constant for each of the three types of packing. The correlation

by Erasmus is only dependent upon liquid load and was actually derived for a different type of structured packing all together, Flexipac 350Y, which has a packing specific area of 350 m^2/m^3. The reason why it was included in this comparative study is because it is a simple correlation that agrees reasonably well with the correlation of Tsai for all three types of packing investigated here. It will, however, not form part of any of the discussion to follow, since it can strictly only be used for Flexipac 350Y structured packing.

The correlation by Tsai is the most recently derived correlation in this comparative study and since it was derived from a databank of 9 different types of packing materials $\left(a_p = 125-500\ \mathrm{m^2/m^3}\right)$, a range of surface tension $\left(30-72\ \mathrm{mN/m}\right)$, viscosity $\left(1-15\ \mathrm{mP.s}\right)$ and liquid loads $\left(2.5-75\ \mathrm{m^3/m^2.hr}\right)$, it is considered to be to most accurate correlation in the comparative study. It shows that there is a decrease in fractional area for an increase in specific packing area. All the other correlations share this trend except for the correlations by Brunazzi et al. and Dragan et al. The correlation by Brunazzi et al. shows a direct proportionality between fractional area and liquid hold-up, whilst the percentage liquid hold-up increases with an increase in packing specific area according to their correlation. This causes their correlation to predict the opposite trend compared with the correlation by Tsai.

The correlation by Dragan et al. has the indirect proportionality of fractional area and specific area, but it also includes the void fraction of the packing. According to **Table 5.3**, the void fraction of Mellapak™ packing decreases as its specific area increases. The term, $1-\varepsilon$, will thus increase with an increase in packing specific area. The overall effect is that the correlation by Dragan et al. predicts an increase in fractional area from Mellapak™ 125Y to Mellapak™ 250Y, a decrease in fractional area from Mellapak™ 250Y to Mellapak™ 500Y with an overall increase in fractional area from Mellapak™ 125Y to Mellapak™ 500Y.

The correlation by Onda et al. probably compares best with the correlation by Tsai. This is a surprising finding, since the correlation by Onda et al. was derived for random and not structured packing. Both of the correlations were derived from the Weber and Froude numbers which takes surface tension, inertia and gravity forces of the liquid phase into

account. The correlation by Onda et al includes viscous forces through its use of the Reynolds number, which is where the biggest difference between the two correlations lies. Tsai found an insignificant effect of liquid viscosity on the fractional area and, therefore, effective area available for mass transfer. As already discussed, the effect of viscosity may not be fully accounted for under conditions where a pseudo first order reaction is assumed valid. The infinite surface renewal rate in the liquid phase may, under higher viscosity conditions, cause an over prediction in effective area.

In the correlation by Onda et al. an increase in liquid viscosity causes a decrease in fractional area, which may be attributed to a decrease in liquid distribution with an increase in viscosity. An increase in liquid viscosity may also cause a decrease in effective area, since surface renewal rates is decreased. The correlation by Onda et al. may, therefore, show the overall correct relationship between viscosity and effective area. The effect of a change in liquid properties such as density, viscosity and surface tension also formed part of this comparative study. The correlations chosen for this comparison are that of Tsai, Onda et al., Rocha et al. and Billet & Schultes. The reason for this selection is that these correlations were derived and tested on systems with different liquid properties. The comparison was done between a water type system and an alcohol type system, similar to the MEA/n-Propanol system used in the reactive absorption study (see Chapter 6). The results of this comparison are illustrated in **Figure 5.7**, **Figure 5.8** and **Figure 5.9**.

All four correlations show an increase in the predicted fractional area for the alcohol solvent systems compared with water solvent systems. The increase in the prediction by Tsai may be attributed to the decrease in the surface tension of alcohol. The decrease in both surface tension and viscosity of the alcohol solvent system is responsible for the increase in the predictions of the other three correlations.

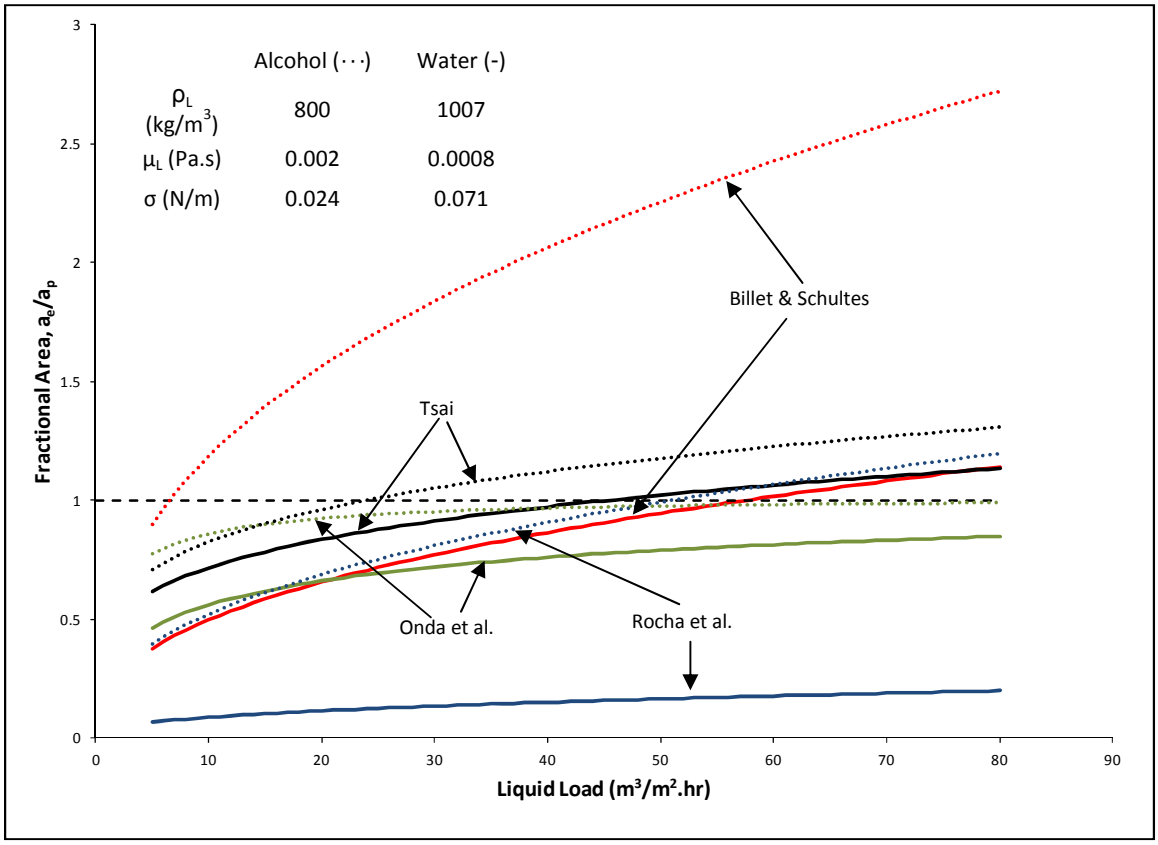

Figure 5.7 Comparison of Effective Area Correlations for Water and Alcohol (n-Propanol) Type Liquid Properties for Mellapak^{TM} 125Y Structured Packing

The correlations by Rocha et al., Onda et al. and Billet and Schultes show a greater difference between their predictions for the two systems, than the correlation by Tsai. This greater difference may be attributed to the fact that both surface tension and viscosity are influential in the correlations by Rocha et al., Onda et al. and Billet and Schultes, whilst the correlation by Tsai is only influenced by a change in surface tension.

The effect of viscosity on the effective mass transfer area of structured packing may, therefore, be more significant than what the correlation by Tsai suggests. As mentioned, a pseudo first order system could be incapable of accounting for all the influences that viscosity has on the available effective mass transfer area.

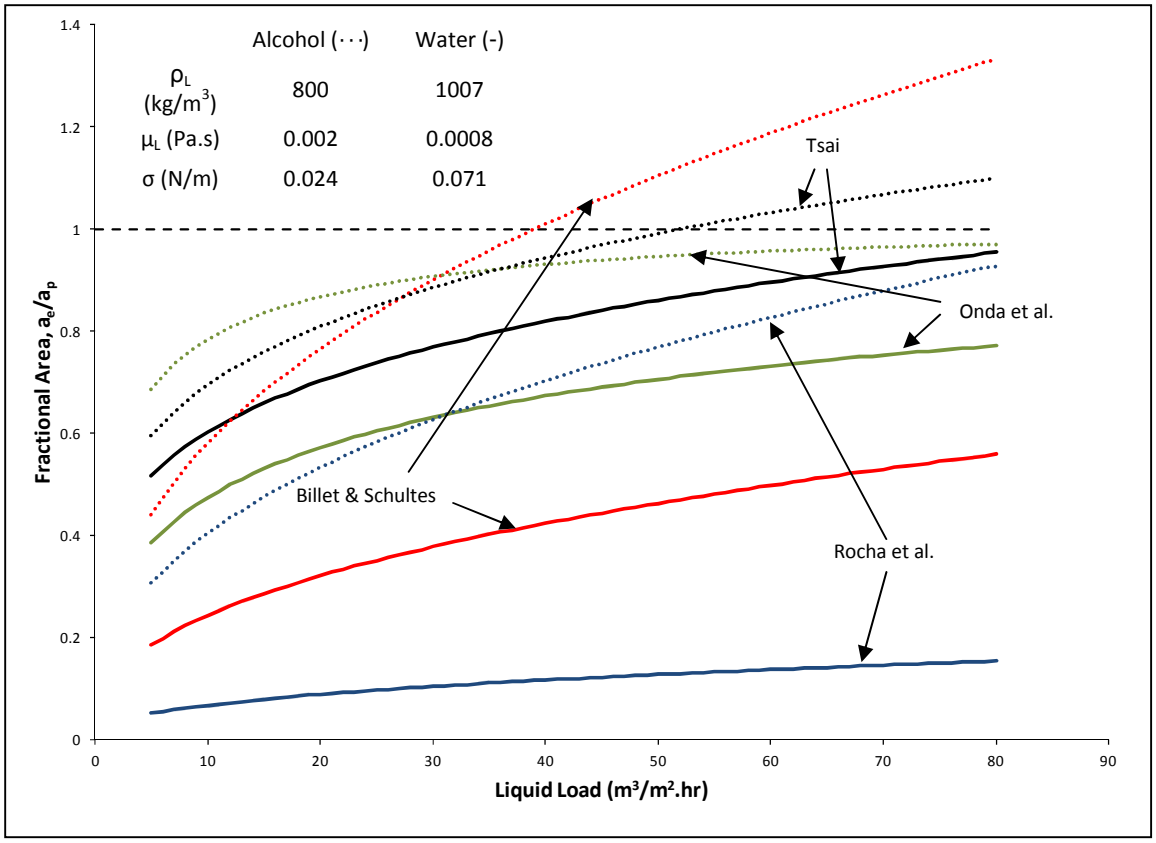

Figure 5.8 Comparison of Effective Area Correlations for Water and Alcohol (n-Propanol) Type Liquid Properties for Mellapak^{TM} 250Y Structured Packing

A reactive absorption system utilising a fast reaction in the liquid film with appreciable surface depletion of the liquid phase reactant will have the advantage of including the effect of surface depletion and renewal rates in its absorption measurements. Under these conditions a better account of the liquid viscosity effect on effective mass transfer area is possible. The reactive absorption of CO_2 into alcoholic solutions of a primary amine, such as MEA has great potential to be a system suitable for this purpose.

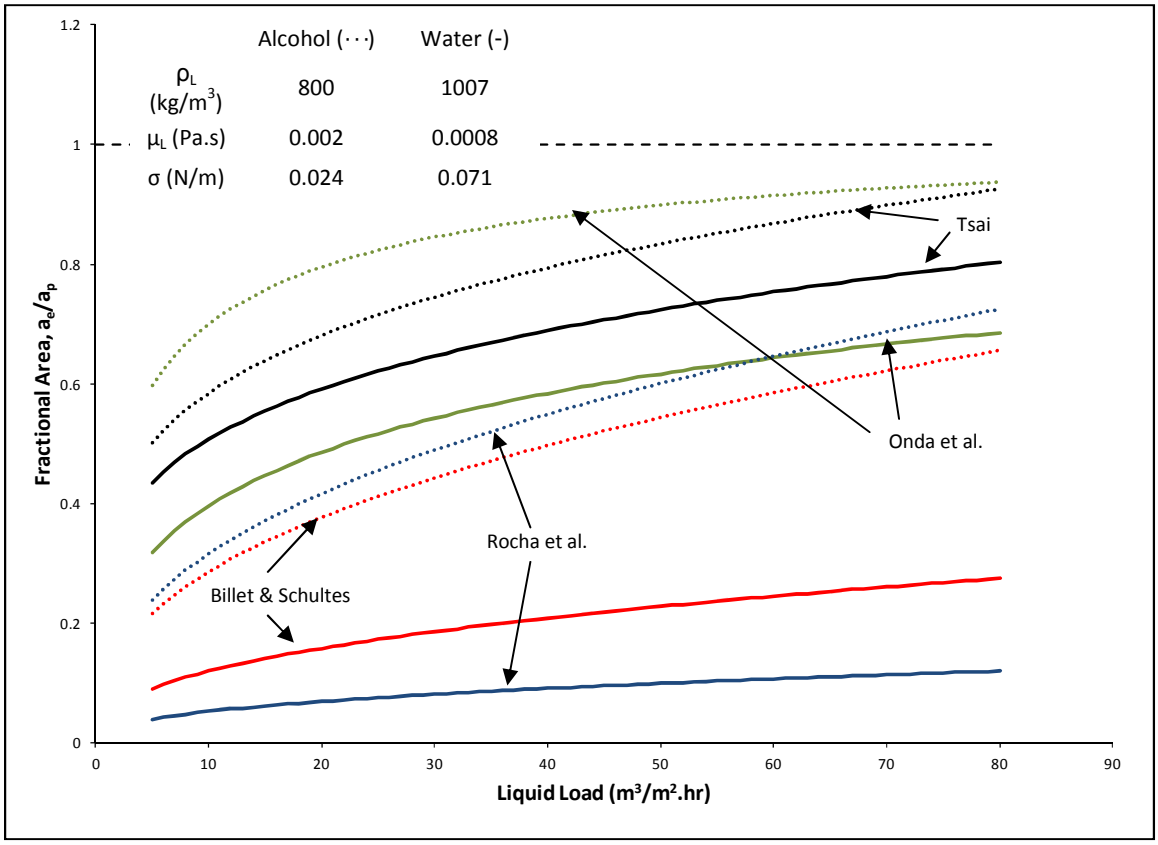

Figure 5.9 Comparison of Effective Area Correlations for Water and Alcohol (n-Propanol) Type Liquid Properties for Mellapak^{TM} 500Y Structured Packing

5.4 Chapter Conclusions

From the literature review conducted it may firstly be concluded that there are several correlations available for the prediction of interfacial mass transfer area. These correlations do not, however, show good agreement in their predictions, which raises concern about the accuracy of the correlations derived. The geometry based correlations rely on liquid distribution and hold-up data to estimate the interfacial area provided by a column internal. It is, however, known that the interfacial area is not necessarily representative of the effective interfacial area, since liquid dead zones may be established under steady state conditions inside the separation column. The geometry based models can also not account for liquid droplets, which also contribute to mass transfer and therefore increase the effective mass transfer area.

The chemical method can account for liquid droplets and even liquid dead zones at steady state, since the effective area available for mass transfer is measured via a mass transfer process. Currently, the chemical method relies on pseudo first order reaction conditions, which implies that there is no surface depletion of the liquid side reagent during reactive absorption measurements. A state of infinite surface renewal exists and thus, the method is not capable of measuring the effective area under conditions where surface depletion and renewal rates are significant. Effective area is a function of surface renewal rate (Shi & Mersmann, 1985) and a method that can measure effective area under conditions where the surface renewal rate of the type of packing material is tested will provide new knowledge in the field of separation efficiency. A chemical method is called for in this regard. This should be a method that utilizes a fast reaction under conditions where surface depletion and renewal rates are considered significant. Under, these conditions, pseudo first order reaction kinetics is no longer valid and the fundamental and shortened fundamental models developed in Chapter 4, must be employed.

Chapter 6 REACTIVE ABSORPTION STUDY

In Chapter 3 and Chapter 4 the liquid phase reaction kinetics of CO_2 and mono-ethanolamine (MEA) in n-Propanol were determined. The main conclusion from the reaction kinetics study was that the current rate expressions are insufficient to describe the reaction kinetics for conditions where there is appreciable conversion of MEA. The expressions proposed in literature may only serve as an approximation under conditions where MEA is in such great excess that its conversion is negligible.

As mentioned in Chapter 5, the reactive absorption of CO_2 with MEA is a suitable system to determine the gas-liquid interfacial area via the chemical method. This chapter will begin by describing the wetted wall experimental set-up specifically built for the specialized absorption measurements undertaken in this study. The set-up will then be validated by performing absorption runs similar to previous research. After the set-up validation is in place, the results obtained in this study will be presented. Along with the specific absorption rate results a preliminary image analysis of the gas-liquid interface will be presented.

6.1 The Wetted Wall Experimental Set-up

As mentioned in section 5.2.5 the cylindrical wetted wall column is a popular contacting device used for measuring specific absorption rates. The wetted wall column design used in this study was based on the works of previous researchers (Danckwerts, 1970; Erasmus, 2004). In this section, the design considerations of the full experimental set-up supporting the wetted wall column will be discussed. The set-up was constructed to additionally facilitate the measurement of the liquid film thickness of the free falling film flowing down the column, as well as capturing the interfacial surface profile of the film using an endoscopic camera. This will give unique insight into the shape and nature of the gas-liquid interface during gas absorption into an assumed known interfacial area.

6.1.1 The Wetted Wall Column

The wetted wall column used in this study is a thick walled (3 mm) stainless steel (416) pipe with an outer surface precision machined to an outer diameter of 26.4 mm and polished to obtain a smooth finish. The wetted wall fits inside a dome. The fully assembled dome set-up is illustrated in **Figure 6.1** and **Figure 6.2**. The dome was designed to be fully submerged in a temperature controlled water bath to ensure that isothermal conditions were achieved during the specific absorption rate experiments. The PVC dome encapsulating the wetted wall column was fitted in place by bolting it to the base plate of the reactor using a flange. The set-up is then bolted into place inside the water bath and positioned so that the wetted wall column is vertically orientated.

The liquid enters at the bottom of the column and fills the inside of the wetted wall column. It then exits through the 24 evenly spaced 1 mm holes all along the circumference of the wall. This is to ensure that even liquid distribution is achieved on the outer wall. To further aid in even liquid distribution, a distributor cap is fitted to the top of the wetted wall column. The cap fits with an annular gap of 1.3 mm and covers the top 22 mm of the column to ensure that the liquid freely gravitating down the outer surface of the wall is fully distributed over the circumference of the wetted wall, once it emerges from under the distributor cap and comes into contact with the gas phase. Fully annotated mechanical drawings of the wetted wall are given in Appendix C.

The loaded, freely gravitating liquid exits the dome through an exit collar at the base of the wetted wall column. The exit collar is illustrated in **Figure 6.3**. The collar fits snugly around the column to ensure the column is orientated at 90° with respect to the horizontal. It was designed to allow for some liquid hold-up at the base of the column. This film of liquid effectively seals off the liquid in the exit chamber from the gas phase in the dome. The liquid level is controlled with a needle valve placed in the exiting liquid line. The outer surface of the collar is fitted with grooves to draw some of the liquid off the base section of the column. These grooves help to eliminate the stagnant liquid bulge that forms at the base of the column as the liquid exits through the narrow collar. This stagnant zone has been known to cause an

unwanted decrease in the absorption rate in the bottom section of the column (Danckwerts, 1970).

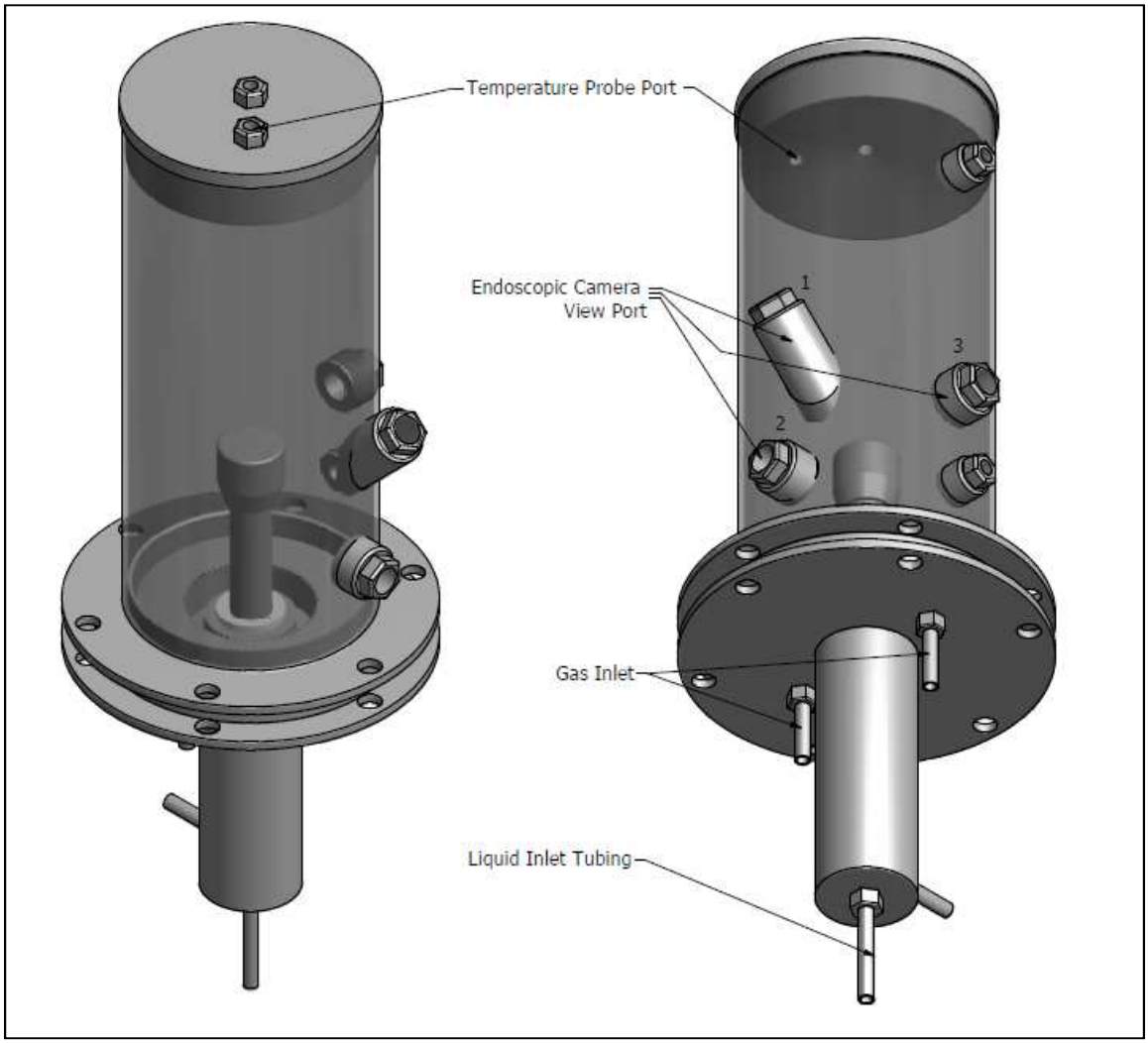

Figure 6.1 Fully Assembled Wetted Wall Column Set-up

Another problem encountered with wetted wall columns is the formation of surface ripples or waves in the bottom section of the column (Danckwerts, 1970). These waves are due to the onset of turbulent liquid flow and cause the interfacial area to become unknown. Absorption rates into turbulent liquids are known to be higher than those measured for laminar flowing liquids (Yu, et al., 2006) which cause further uncertainty in the specific absorption rate data. In order to limit the effect of surface ripples on the absorption rate, either surfactants or short

column heights must be used (Danckwerts, 1970). Due to the unknown effect that surfactants may have on the absorption kinetics, it was decided to resort to short column heights (60 and 90 mm) in this study. The complementary image analysis of the gas-liquid interface of the wetted wall will shed light on the degree of surface turbulence noticed for the column heights used in this study.

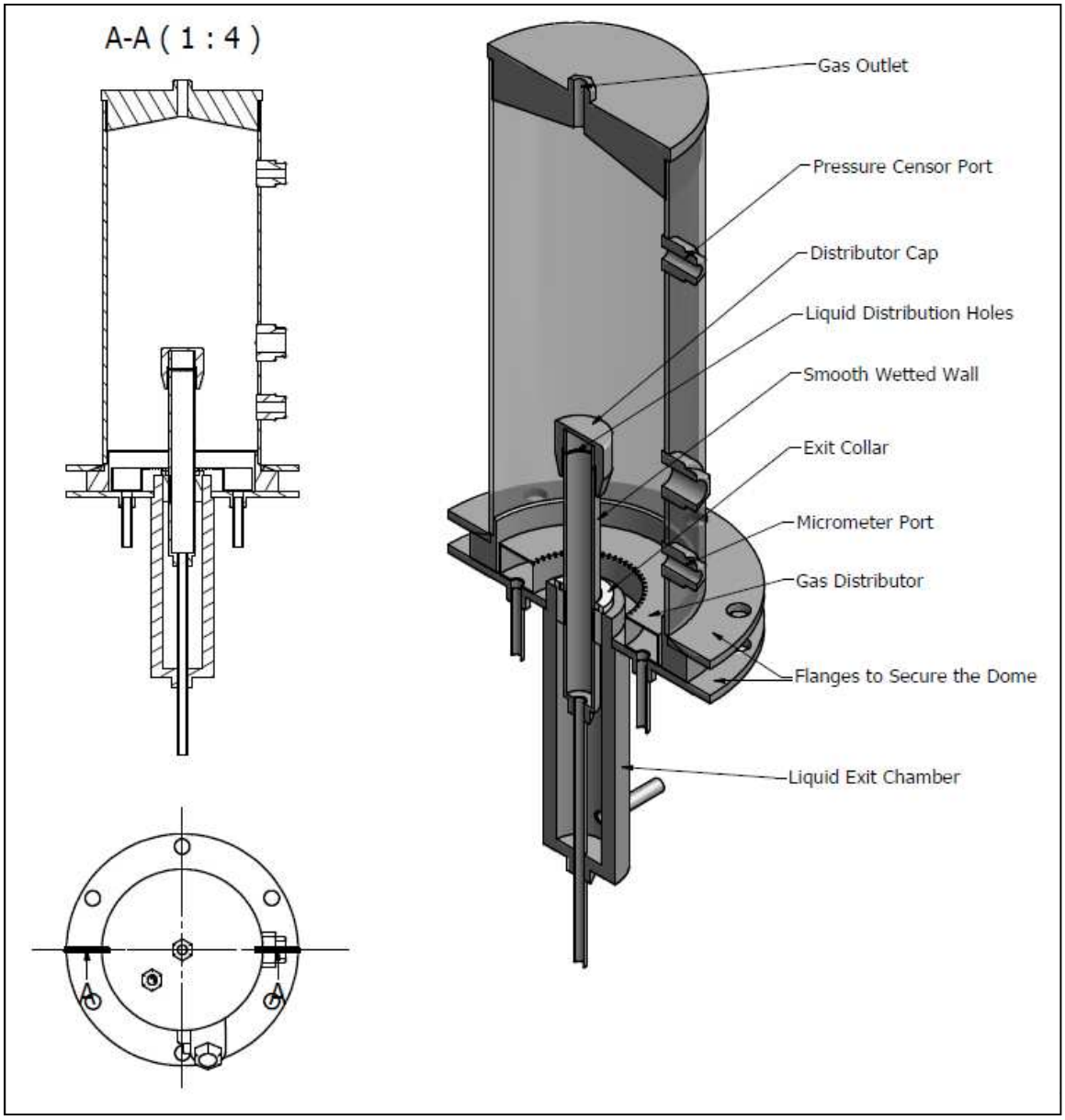

Figure 6.2 Sectioned Drawing of the Fully Assembled Wetted Wall Reactor

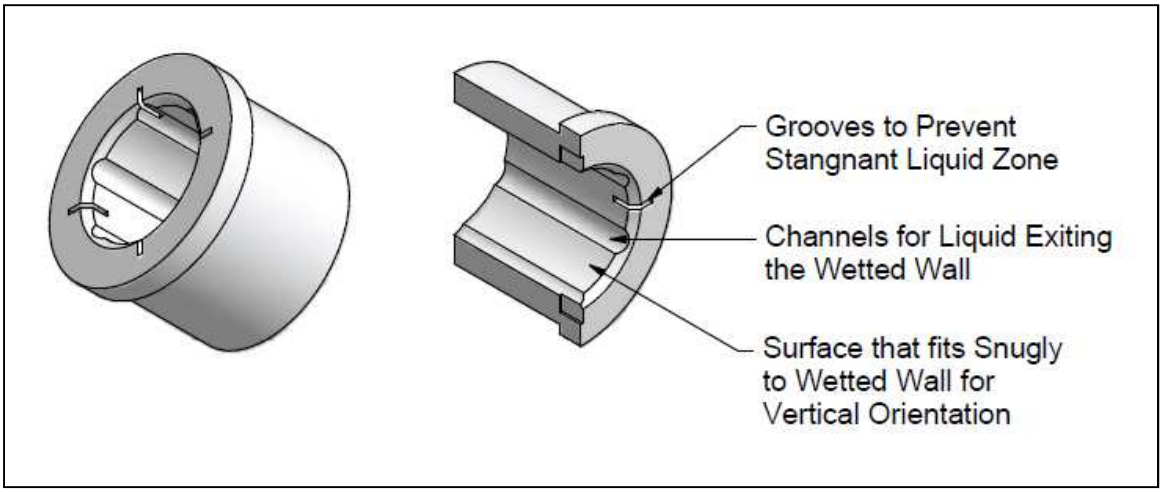

Figure 6.3 Wetted Wall Exit Collar

One of the additional aims of this study is to film the profile of the gas-liquid interface to attempt to derive the interfacial area in the presence of ripple or wave action. This was achieved by recording video data of the gas-liquid interface during absorption and processing the images using an image analysis algorithm in Matlab® (see section 6.1.3). This information, along with the higher absorption rates measured in the presence of surface waves, may shed light on the true effective interfacial area in the turbulent region. The turbulence of the liquid phase increases the surface renewal rate which increases the effective interfacial area. This is valuable information with regards to the turbulent liquid flow encountered on separation column internals such as structured packing.

In order to be able to measure specific absorption rates at different gas-liquid contact times and interfacial areas, the wetted wall column height must be adjustable. The experimental set-up was designed to facilitate the adjustment of the wetted wall without removing it from the water bath. The inlet pipe to the wetted wall was fitted to a lever that can adjust the wall height at any time. The wetted wall extends and collapses into the exit chamber whilst the inlet piping is sealed with a Teflon® ferule to ensure mobility during column height adjustments. This modification saves on experimental time, since different column heights may now be investigated during the same experimental run.

The gas was introduced to the reactor dome through a donut shaped gas distributor surrounding the wall at the base of the column. The distributor has evenly spaced perforations on the inside perimeter of the donut in order for the gas to be introduced as near as possible to the gas-liquid interface and travel counter currently with respect to the down flowing liquid. This 'direct injection' of the gas phase was done to try and maximize the linear velocity of the gas phase near the gas-liquid interface without decreasing the diameter of the dome, but by effectively decreasing the hydraulic diameter of the gas phase. A greater linear velocity near the interface will aid in minimizing the gas phase resistance to mass transfer. This is further discussed in section 6.2.3. The short wetted wall column lengths used in this study supports this hypothesis by keeping the flow path of the gas phase along the gas-liquid interface to a minimum.

In order to ensure that the gas is evenly distributed in the donut shell, two entry points on the bottom of the distributor on opposite sides were fitted to the shell. A test was done to confirm even distribution in the shell. The test consisted of holding a light piece of paper in the gas flow at different locations along the perforated inner perimeter of the distributor, at the same height above the distributor. It was found that the paper was bent at equal angles by the up flowing gas all around the distributor, indicating evenly distributed gas flow.

6.1.2 Piping and Instrumentation of the Wetted Wall Experimental Set-up

A P&ID of the wetted wall experimental set-up is illustrated in **Figure 6.4**. Thermal equilibrium throughout the experimental set-up was achieved with the combination of temperature controlled water baths and insulated heat tracing fitted to the gas lines. Both the gas and liquid lines were coiled through a pre-heater water bath set at the desired temperature. The liquid was circulated to the reservoir until it achieved the desired operating temperature. The accuracy of the temperature control was ±0.5 °C. The gas was bubbled through a saturator unit containing random packing (15 mm diameter pall rings) and n-Propanol. The saturator unit was submerged in its own temperature controlled water bath, kept at a controller setting of 0.5 °C lower than the desired operating temperature. This was done to prevent possible condensation of the solvent in the gas lines.

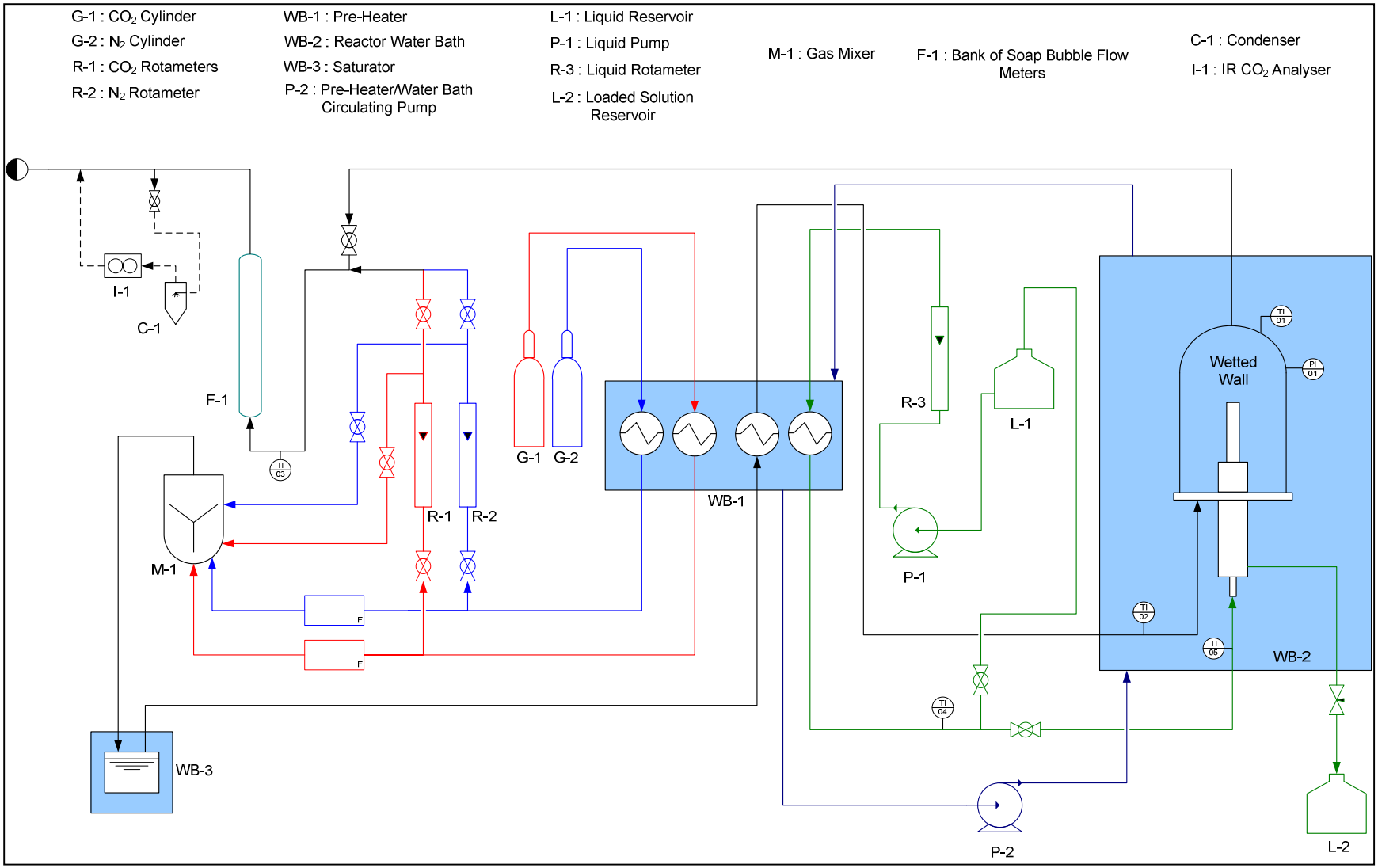

Figure 6.4 P&ID of the Wetted Wall Experimental Set-up

The pressure inside the reactor dome was measured with an Endress and Hauser® Cerebar S Pressure sensor (accuracy: 0.075% of reading value), the same type of sensor used in the reaction kinetics study. All temperatures in the set-up were measured with PT-100 temperature sensors (accuracy = ±0.5°C).The liquid was pumped using a centrifugal pump and the liquid flow rate was controlled with a rotameter calibrated with a measuring cylinder and stopwatch. The gas flow rate was regulated with 4 gas rotameters. The rotameters have different operating flow rate ranges to allow the set-up to be able to handle a large range of gas flow rates. The four rotameters used may be summarised as follows (Nitrogen used as carrier gas in this study; all flow rates in cm^3/min):

- N_2 Rotameter: Flow Rate Range (air): 351 – 7825 cm^3/min
- CO_2 Rotameter: Flow Rate Range (air): 4.8 – 92.7 cm^3/min
- CO_2 Rotameter: Flow Rate Range (air): 70 – 844 cm^3/min
- CO_2 Rotameter: Flow Rate Range (air): 351 – 7825 cm^3/min

These four rotameters were selected to cover the flow rate ranges of interest to this study as well as allowing for other flow rates to be investigated in future research. The gas flow rate in the system was measured using a bank of glass, soap bubble flow meters of varying diameter. The soap bubble flow meters used may be summarised as follows:

- Low flow: Diameter = 16 mm
- Medium flow: Diameter = 35 mm
- High flow: Diameter = 3 x 40 mm (parallel)

The medium flow soap bubble meter was mostly used in this study, along with the low flow meter to measure the CO_2 flow rate. The reason for using three soap bubble flow meters in parallel for the high gas flow rate was because the diameter required for one glass column would not support the soap bubble. It was, therefore, decided to design three smaller diameter flow meters fitted in parallel with the assumption that the sum of the three flow rates represents the total gas flow rate. The high flow soap bubble flow meters were not used in this

study but were included in the design for future research. The volume segments marked off on the soap bubble flow meters were determined using known volumes of water.

The soap bubble flow meters were not submerged in the temperature controlled water bath. The gas lines of both the entry and exit ports of the soap film meters were fitted with heat tracing and the gas temperature at the inlet was measured and found to be equal to the system temperature for all experiments in this study. This means that the temperature difference over the soap bubble flow meter had to be small. A sensitivity analysis on the effect of a temperature difference over the soap bubble flow meter was done. Assuming ideal gas behaviour, a temperature difference of ±5°C will translate into a ±1.65% change in volumetric flow rate, hardly significant and within experimental error. The temperature difference of 5°C was chosen as a worst case. It was therefore decided that it is not necessary to submerge the soap bubble flow meters in a temperature controlled water bath.

6.1.3 Measuring Liquid Film Thickness and Capturing the Interfacial Profile on Video

One of the complimentary aims of this research was the construction of a specific absorption experimental set-up that can capture the profile of the gas-liquid interface under conditions of reactive absorption as well as measure the liquid film thickness flowing down the smooth wetted wall. In order to be able to achieve these aims, some interesting modifications to the reactor dome and water bath windows were required.

The wetted wall reactor dome and water bath windows were fitted with custom designed and machined fittings to facilitate the measurement of the liquid film thickness on the wetted wall as well as allowing the gas-liquid interface profile to be video recorded during gas absorption. The fittings fitted to the dome are illustrated in **Figure 6.1** and **Figure 6.2** labelled Endoscopic Camera View Ports. The view ports for the Stryker® 1188 HD endoscopic camera (see Appendix D for equipment specifications) are numbered in **Figure 6.1**. View port 2 was used to capture the interfacial profile as well as ensuring the most accurate use of the Mitutoyo® series 128 depth micrometer (see Appendix D for equipment specifications) to measure the liquid film thickness.

The micrometer was fitted with a needle that extends from the micrometer body fitted to the outside wall of the water bath, to the smooth wetted wall column inside the submerged dome. The surface of the smooth wetted wall was the zero calibration point for the micrometer needle. The liquid film thickness was measured by retracting the needle until it breaks free from the liquid surface and then adjusting the needle tip until it touches the liquid surface. The reading is then recorded (±0.01 mm accuracy) and the measurement repeated. The average of 5 readings was used as the representative measurement.

All three view ports were fitted with glass tubes sealed off at one end with a disc of optic glass. The end with the optic window was situated inside the dome allowing for the endoscopic camera to rest inside the glass tube with the camera lens against the optic window. The open end of the glass tube was situated outside the water bath, therefore creating a view port for the endoscopic camera inside the submerged dome. View port 2 was fitted with a direct view of the gas-liquid interface and aligned to have a full view of the micrometer needle tip at 90° with respect to the micrometer. The video data was recorded with the use of a Hauppauge Colossus recording card at a resolution of 720p. The output signal of the endoscopic camera had to be converted to a 720p signal using a PC/HD to HDMi converter (see Appendix D for equipment specifications). The image analysis procedure and results are discussed in section 6.4.

6.1.4 Solvent Regeneration

Due to the reversible nature of the CO_2/MEA reaction, it is possible to regenerate the solvent used in the reactive absorption study. The loaded solvent is heated under total reflux to a temperature of 60°C whilst stirred. The reaction is reversed and the CO_2 in the solvent is driven off. The solvent is checked for CO_2 content via a GC method of analysis (see section 6.2.2).

The regenerated solvent is left to cool under a blanket of N_2 and is re-used. The regenerated solvent was shown to provide the same absorption rates compared to the measured rates of a freshly prepared solvent, indicating that the MEA in the solvent is still fully active.

6.1.5 Experimental Procedure

The experimental procedure followed during the specific absorption rate study may be summarized as follows (refer to **Figure 6.4** for equipment referencing):

- The wetted wall reactor is assembled and fitted in place inside the water bath, checking that the wall is orientated exactly vertically. The water bath and pre-heater is filled with water and the temperature set-point set to the desired experimental temperature. The heat tracing on the gas lines is switched on and set to the experimental temperature. The pre-heater stirrer is switched on as well as the water circulation pump, circulating the water between the water bath and pre-heater.
- The endoscopic camera and computer is fitted into place and switched on. The signal converter converting the signal from the camera to the recording card is checked to provide a 720p output. The micrometer needle is calibrated to zero on the wetted wall column surface. The wetted wall column height is adjusted to the desired experimental height.
- The liquid mixture is prepared on a mass basis to the desired MEA concentration and poured into the nitrogen purged liquid reservoir. A sample is withdrawn for GC analysis (see section 6.2.2) to check that the liquid phase is free from CO_2. The liquid pump is switched on and the liquid is allowed to circulate to the reservoir until it reaches the experimental temperature. The desired liquid flow rate is controlled by the liquid rotameter.
- The saturator is filled with alcohol solvent and fitted in its water bath controlled to 0.5°C lower than the experimental temperature. The gas flow is opened once the system has reached the experimental temperature. The gas flow is firstly set to bypass the reactor dome and the total gas flow rate is measured with the medium flow soap bubble flow meter. The flow rate of CO_2 is adjusted until the desired inlet CO_2 concentration is reached on the Infra red CO_2 analyser (see section 6.2.1). The flow is then directed to the dome and the inlet CO_2 concentration is double checked.

- Once a stable CO_2 reading is obtained in the dome, the liquid flow is directed to the dome at the desired volumetric flow rate. The liquid level at the base of the column is regulated with a needle valve at the liquid exit. The liquid level is such that it seals off the liquid in the exit chamber from the gas in the dome. Enough time (approximately 5 – 7 min) is allowed for the IR analyser reading to stabilize after which it is recorded.
- The liquid flow is once again set to circulate to the reservoir. The gas flow is set to bypass the dome and the next CO_2 concentration is set. If needed, the wetted wall column height may be adjusted and the experimental procedure is repeated.

6.2 Reactive Absorption Study Experimental Design and Methods of Analysis

This section will discuss the considerations made with regards to the experimental design of the specific absorption rate study. The methods of analysis used in the specific absorption rate study will also be presented.

6.2.1 Gas Phase Method of Analysis

Due to inaccuracies encountered during liquid phase analysis of reactive absorption measurements (de Brito, et al., 1994; Erasmus, 2004; Tsai, 2010), most researchers opt to rely on gas phase measurements to determine absorption rates. This study will do the same. As mentioned in section 6.1.5, the CO_2 vol% is recorded before and after absorption, with the difference in readings used to calculate the absorption rate of CO_2.

The Dräger® PIR 7200 CO_2 analyser used in this study was used previously in a CO_2 capture study conducted on an absorber/stripper unit containing structured packing material (Kritzinger, 2013). It has a measuring range of 0 – 20 vol% CO_2 and is accurate to within 1.5% of the measured value. The absolute accuracy of the CO_2 analyser was not of great concern, since the molar absorption rate was calculated from the difference in vol% readings. The resolution of the analyser (0.01 vol%) and the repeatability of the readings were, therefore, of greater importance. The absorption rate experiments conducted in this study fell within the measuring range of the analyser.

The absorption rate of CO_2 was calculated with the knowledge of the volumetric gas flow rate, the pressure inside the reactor dome, the gas phase temperature and the CO_2 vol%. Assuming ideal gas behaviour, the molar flow rate may be calculated from:

$$\dot{n}_{CO_2} = \frac{P_{\text{dome}}\dot{V}_G}{RT} \cdot \left(\text{vol\% } CO_2\right) \qquad 6.1$$

The steady state difference in CO_2 molar flow rate before and after absorption is the absorption rate of CO_2 into the liquid film. Due to the small amount of CO_2 absorbed in an experimental run (most absorbed in any experiment was 0.6% of total molar gas flow, average absorption around 0.1%), it was assumed that the volumetric gas flow rate remains constant for a specific experimental run. This was checked and confirmed with the soap bubble flow meter. The change in flow rate could not be detected. Accordingly, the pressure inside the dome remained practically unaffected by the amount of CO_2 absorbed and thus equation 6.1 is valid to use for calculating the inlet and outlet molar flow rates of CO_2.

6.2.2 GC Method of Analysis

One of the original aims of both the reaction kinetic and reactive absorption study was to analyse the liquid phase of each study via Gas Chromatography (GC) to determine both MEA and CO_2 concentrations. A method was developed using a 1/8" Tenax® 80/100 TA column followed by a Ni catalysed methaniser to convert CO_2, via its reaction with H_2 at 380°C, to CH_4. A schematic of the GC arrangement is illustrated in **Figure 6.5**.

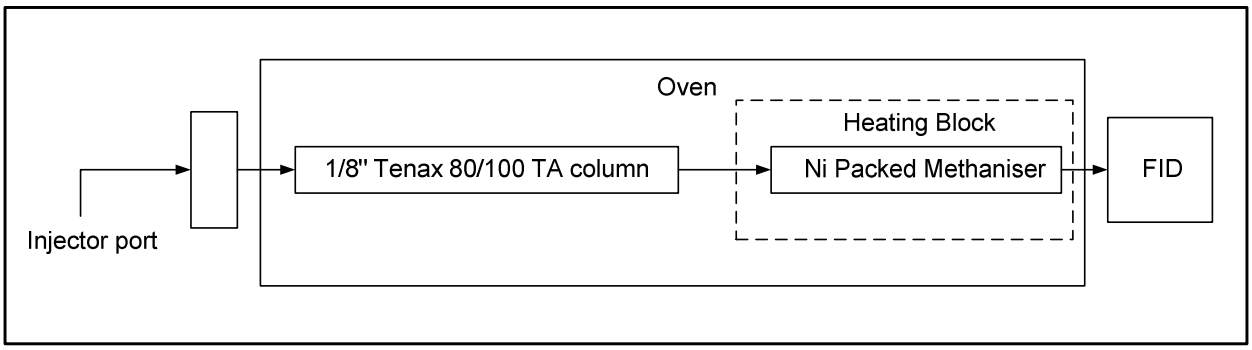

Figure 6.5 GC arrangement for analyzing liquid phase MEA and CO_2

The use of the methaniser improved the sensitivity of the CO_2 detection greatly and eliminated the need for the TCD detector. Good separation of the three components in the mixture could be achieved under certain operating conditions. As expected, however, the high temperatures of the injector port (270°C) decomposed the reaction products and the analysis revealed the original amounts of MEA and CO_2 loaded. The GC analysis was therefore only used as a qualitative measure to determine whether the regenerated solvent is free from CO_2. A typical chromatogram illustrating the three components along with the internal standard, n – Octanol, is illustrated in **Figure 6.6**.

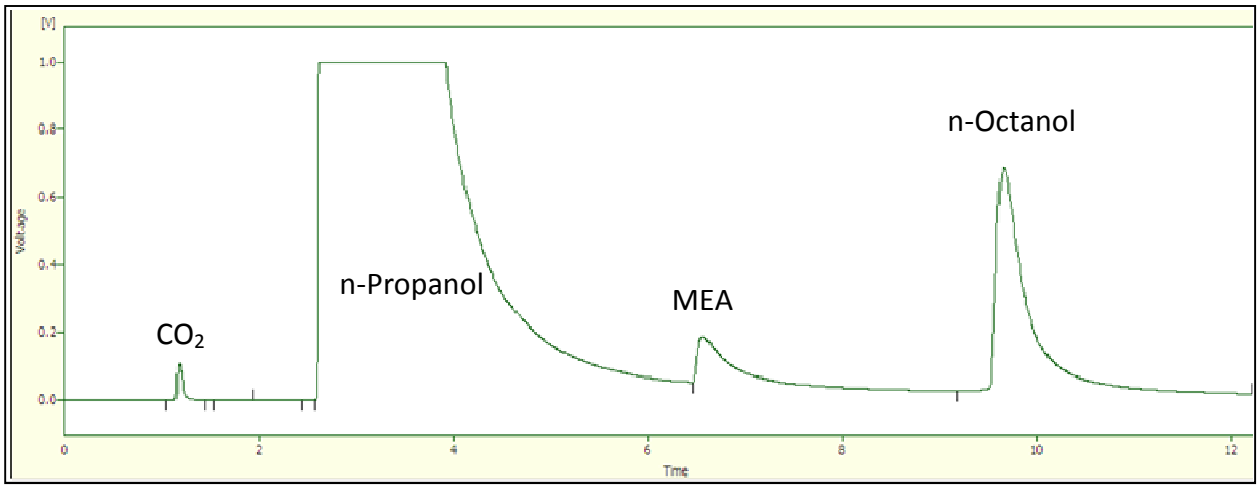

Figure 6.6 GC Chromatogram Indicating the Presence of CO_2 in the Sample

The internal standard is present in the chromatogram because it was originally thought that a method for measuring the MEA concentration in the liquid phase could be achieved. The repeatability of especially the MEA analysis was found to be insufficient for accurate analysis.

The development of a more accurate GC method of analysis should be investigated in future, since this method may have great potential for analysing samples withdrawn from different positions on the wetted wall, which may reveal the concentration profile of MEA and possibly CO_2 and the salt products as a function of column height.

6.2.3 Specific Absorption Rates Experimental Design

The experimental design for the specific absorption rate of CO_2 in solutions of MEA/n-Propanol is presented in this section. The choice of alcohol solvent rested on the availability of validation data from a previous study on a similar experimental set-up (Erasmus, 2004) and to be consistent with the solvent used in the reaction kinetic study. The experimental runs earmarked for validation purposed are tabulated in **Table 6.1**. The results of the validation study are presented in section 6.3.1.

Table 6.1 Validation Study Experimental Design (Erasmus, 2004)

[MEA] (mol/dm^3)	h_{column} (mm)	T_L (°C)	T_G (°C)	V_L (cm^3/s)	V_G (cm^3/s)	CO_2 in (vol %)	CO_2 out (vol%)	P_{dome} (kPa)
0.2	90	30	30	0.99	43.7	1.24	1.08	100.23
						0.8	0.69	
						0.61	0.52	

The design of experiments for the reactive absorption study had two main goals in mind. These goals may be summarized as follows:

1. To study the effect of liquid Reynolds number on the reactive absorption rate, experiments would have to be conducted at different column heights and liquid flow rates. The goal is to attempt to study the effect of turbulence on the absorption rate, which enables a discussion of the liquid phase surface renewal rate and how it may affect the effective interfacial mass transfer area.
2. To study the effect of surface depletion in the liquid phase by conducting reactive absorption experiments at relatively high CO_2 partial pressures. The different absorption rates will be discussed in terms of the degree of surface depletion during absorption and how this effect influences the effective interfacial mass transfer area.

Surface depletion of MEA in the liquid film will be most prominent when the liquid phase [MEA]:[CO_2] is low. The liquid phase concentration of MEA was known from the solvent preparation on a mass basis. The liquid phase concentration of CO_2 at reaction initiation must be calculated from its solubility data. The solubility of CO_2 in solvents containing MEA must be

estimated with the use of the N_2O analogy (Laddha, et al., 1980; Sada, et al., 1986; Oyevaar, et al., 1989; Li & Lai, 1995; Xu, et al., 2013), which is discussed in further detail in Appendix B, section 7.1.2. From the N_2O analogy, the Henry's law coefficient for CO_2 in solvents containing various concentrations of MEA, may be calculated (refer to Appendix B.3). The concentration of CO_2 in the liquid phase may be calculated from its partial pressure and the estimated Henry's law coefficient according to:

$$C_{CO_2,i,[\mathrm{MEA}]} = \frac{P_{CO_2}}{H_{CO_2,[\mathrm{MEA}]}} \qquad 6.2$$

The Henry's law coefficients for CO_2 applicable to the solvents used in this study are tabulated in **Table B 5** in Appendix B.4. Another consideration is to ensure that the conditions for the liquid phase reaction to fall within the fast reaction category are met. These conditions are given in section 2.2.1. The condition for a fast reaction in liquid film with a degree of depletion of MEA in the liquid film relies on the following relationship (Charpentier, 1981):

$$0.3 < \mathrm{Ha} < 3 \qquad 2.29$$

where

$$\mathrm{Ha} = \frac{\sqrt{\left(\frac{2}{m+1}\right)\left(k_{m,n} D_A C_{A,i}^{m-1} C_{B,L}^{n}\right)}}{k_L} \qquad 2.27$$

and

$$E_i = 1 + \left(\frac{a \cdot D_B}{b \cdot D_A}\right)\left(\frac{C_{B,L}}{C_{A,i}}\right) \qquad 2.28$$

In accordance with the reaction stoichiometry determined in Chapter 4, a stoichiometric ratio $a/b = 0.5$ was used. The reaction orders were taken to be $m = 1$ and $n = 2$, which is in agreement with literature (Alvarez-Fuster, et al., 1981) and the reaction rate orders assumed valid in this study. The third order reaction rate constant $\left(k_{m,n}\right)$ used was of similar magnitude

to the rate constants determined for the power rate law model fit in section 4.2.1 and in agreement with values reported in literature (Davis & Sandall, 1993). The liquid side mass transfer coefficient (k_L) was calculated from penetration theory (equation 2.10). The diffusivity and solubility data used in the calculations is tabulated in **Table B 4** and **Table B 5** in Appendix B.4. The results of the confirmation of a fast reaction system are tabulated in **Table 6.2**.

Table 6.2 Results Validating the Fast Reaction Regime for the Reactive Absorption Experimental Conditions

Temperature (°C)	[MEA] (mol/dm^3)	P_{CO2} (kPa)	Hatta Number	E_i	$0.5E_i$	$10E_i$
25	0.08	2.25	0.97	12.70	6.35	127
		4.45		6.57	3.28	66
		20		2.23	1.12	22
	0.2	5.6	2.42	12.28	6.14	123
		11		6.98	3.49	70
		20		4.15	2.07	41.5
30	0.08	2.25	1.03	12.39	6.19	124
		4.5		6.69	3.35	67
		20		2.28	1.14	23
	0.2	5.6	2.57	12.55	6.27	125
		11.2		6.83	3.42	68
		20.12		4.26	2.13	43

The condition for a fast reaction occurring in the liquid film (equation 2.29) with appreciable surface depletion of MEA was comfortably met at all CO_2 partial pressures identified for investigation in this study. In all cases the Hatta number was greater than 1 but less than 3, indicating that the reaction fell well within the fast reaction regime (Charpentier, 1981). At the higher CO_2 partial pressures (19 - 20 kPa) the Hatta number came closest to 3, which would have meant that the reaction falls within the fast pseudo first order regime according to equation 2.30 (Charpentier, 1981; Tsai, et al., 2008):

$$3 < \mathrm{Ha} < 0.5E_i \qquad 2.30$$

Equation 2.30 is only an indication that the reaction may be considered to be pseudo first order. In order to confirm pseudo first order conditions the conversion of MEA in the liquid film during reactive absorption must be evaluated. Only if insignificant surface depletion of MEA occurred, can pseudo first order conditions be confirmed. This will be discussed in section 6.3.3.

Whenever a fast reaction in the liquid film is obtained, care must be taken to ensure that the Hatta number is not large enough to satisfy the following criteria:

$$\mathrm{Ha} \geq 10E_i \qquad 6.3$$

Equation 6.3 indicates conditions for which the reaction may be considered to occur instantaneously within the liquid film (Danckwerts, 1970; Charpentier, 1981). Under these conditions both liquid and gas side resistances to mass transfer occur. As shown in **Table 6.2**, the Hatta number was always well below $10E_i$ for all systems investigated in this study.

Based on the above mentioned considerations, the experimental design followed in this study is presented in **Table 6.3**

Table 6.3 Experimental Design

[MEA] (mol/dm^3)	h_{column} (mm)	T_L (°C)	T_G (°C)	V_L (cm^3/s)	V_G (cm^3/s)	[MEA]:[CO_2]	CO_2 in (vol %)	P_{dome} (kPa)
0.08	60	25, 30	25, 30	1.016, 1.345	80	5, 20, 45	19, 10.5, 5.5	104 - 105
	90	25, 30	25, 30	0.874, 1.345				
0.2	60	25, 30	25, 30	1.016, 1.345	80	10, 20, 40	19, 4.5, 2.15	104 - 105
	90	25, 30	25, 30	0.874, 1.345				

The lower [MEA]:[CO_2] corresponds with the higher CO_2 vol% in **Table 6.3**. The experiments were designed to achieve a range of $5 \leq [MEA]:[CO_2] \leq 45$ in order for the effects of surface depletion and renewal rates of MEA to have varying degrees of significance on the measured absorption rates. In the reaction kinetic study, the percentage conversion of MEA for the two [MEA]:[CO_2] relative concentrations (5:1 and 10:1) were determined. These conversions are

tabulated in **Table 3.8**. Absorption experiments were intentionally conducted at these low relative concentrations to investigate the effect of surface depletion of MEA (higher reaction conversion of MEA) on especially the specific absorption rate of CO_2.

Knowledge of both surface renewal rate and degree of surface depletion could be used to shed more light on the true effective area achieved on separation column internals at various liquid flow rates. The absorption data may then be used to solve the diffusion equation (equation 2.15), subject to certain boundary conditions and incorporating the reaction kinetic parameters derived in sections 4.4.1 and 4.4.2. The details of this new approach to determine effective interfacial mass transfer area will be discussed in Appendix B.

6.2.4 Gas Phase Mass Transfer Resistance Considerations

As can be seen in the comparison of **Table 6.1** and **Table 6.3**, the experimental runs in this study was conducted at much higher CO_2 partial pressures and a higher gas flow rate (almost double) than the validation study. The former was chosen to achieve a degree of liquid phase surface depletion and to conduct absorption experiments at similar relative concentrations as the reaction kinetic study. The latter was to try and ensure that gas-phase resistance to mass transfer was kept at a minimum. It may be argued that at higher CO_2 driving forces (higher CO_2 partial pressures) the gas film resistance will increase due to a faster depletion rate of CO_2 in the gas film (Luo, et al., 2012). A similar argument could be made for high reagent concentrations in the liquid film. The driving force effect is difficult to determine since gas side resistance is calculated from the gas side mass transfer coefficient, which is in turn calculated from correlations independent of the partial pressure of the absorbing gas or the concentration of the liquid film reagent (Tsai, et al., 2008; Luo, et al., 2012). The gas side mass transfer coefficient may be estimated from the Sherwood correlation derived from boundary layer theory. The following form of the correlation is applicable to a wetted wall set-up similar to the one used in this study (Luo, et al., 2012):

$$\frac{k_G d_h}{D_{CO_2,N_2}} = 0.665 \cdot \left(\frac{\mu_G}{\rho_G D_{CO_2,N_2}} \right)^{1/3} \cdot \left(\frac{\rho_G u_G d_h}{\mu_G} \right)^{1/2} \qquad 6.4$$

From equation 6.4 it may be seen that the gas side mass transfer coefficient is strongly dependent upon the linear velocity of the gas phase. The linear velocity is calculated from the volumetric flow rate and the hydraulic diameter, d_h:

$$u_G = \frac{\dot{V}}{A_h} = \frac{4\dot{V}}{\pi d_h^2} \qquad 6.5$$

This study incorporated the same gas system (CO_2 diluted with N_2), so it is reasonable to assume that all the physical properties in equation 6.4 are equal to that used by Luo, et al (2012). If the physical properties are, therefore, lumped as a proportionality constant, then the gas side mass transfer coefficient has the following proportionality with respect to the linear velocity and the hydraulic diameter:

$$k_G \propto \left(\frac{u_G}{d_h}\right)^{1/2} \qquad 6.6$$

The linear velocity near the gas-liquid interface on the wetted wall was maximized with the use of the donut shaped gas distributor illustrated in **Figure 6.2**. This 'direct injection' method is also thought to decrease the effective hydraulic diameter of gas flow. Both these effects will increase the gas side mass transfer coefficient according to the proportionality of equation 6.6, which in turn decreases gas film resistance. Quantification of this effect is difficult, which is why the gas film resistance encountered in this study will be estimated both from boundary layer theory and by comparison with other studies. The criteria considered for comparison are:

- linear velocity
- hydraulic diameter
- partial pressure driving force
- liquid reagent (MEA) concentration.

If it is assumed that the hydraulic diameter of the gas flowing next to the liquid film of the wetted wall in this study, is in the order of 0.03 m (this is the horizontal distance from the wall surface to the inner edge of the donut distributor) then the linear velocity of the gas phase is in the order of 0.11 m/s. This is of similar order in magnitude to the low gas flow rates used by

Luo et al. in their wetted wall set-up (Luo, et al., 2012). They reported gas phase resistances for their wetted wall column absorber in the order of 12 - 52 %. Under similar conditions on another type of absorber unit (a string of discs column) they found the gas phase resistance to be in the order of 5 – 20 %, a significant decrease. When they compared their absorption rate results obtained on the two units, they found that these relatively high gas phase resistances to mass transfer were in fact negligible, since similar overall mass transfer coefficients were obtained. They conducted experiments at relatively high MEA concentrations (1M and 5M). With such high liquid phase concentrations, gas side mass transfer resistance is expected to be significant (Tsai, et al., 2008), but they found it not to be.

Gas phase resistance was considered negligible under the validation study conditions (Erasmus, 2004). Gas phase mass transfer resistance may, thus, have occurred under the high CO_2 partial pressure experiments, causing a decrease in the absorption rate, but based on the finding of Luo et al. (2012), the gas phase resistance could very well also be negligible. A boundary layer analysis of the gas phase flowing counter current with respect to the liquid phase on the wetted wall was done in order to estimate the gas side mass transfer coefficient. The calculation is presented in Appendix A.3. The results of the calculation revealed that the gas phase resistance was in the order of 2.13 – 8.81 % of the total resistance to mass transfer. This is a lower gas phase resistance than that encountered by Luo et al. (2012) and Tsai et al. (2008). It could not be concluded that an increase in CO_2 partial pressure alone, caused an increase in gas phase resistance. The gas phase resistance was found to be dependent upon the ratio of MEA to CO_2 at the interface. The highest gas phase resistance was encountered at the lower [MEA]:[CO_2].

From boundary layer theory it would seem to indicate that gas film resistance may be considered to have a small influence on the absorption rate measurements made in this study. This will be kept in mind during the discussion of the wetted wall absorption rate results. Considering column internal (structured packing) geometry, the greatly reduced gas phase hydraulic diameter of structured packing causes an increase in the linear gas velocity leading to gas phase resistance falling to around 1.5% (Tsai, et al., 2008). This means that the conditions for studying the effective interfacial mass transfer area with appreciable interfacial depletion of

MEA (one of the main aims of this research) can easily be obtained during column absorption experiments without significant gas phase resistance.

Ideally, the gas side mass transfer coefficient for each absorption unit should be determined experimentally. This, for example, may be achieved by absorbing SO_2 into a dilute aqueous solution (0.1 M) of NaOH (a gas film controlled process) to determine the gas side mass transfer coefficient of the system (Tsai, 2010). The gas side mass transfer resistance is the reciprocal of the mass transfer coefficient. The coefficient was not directly measured in this study, but should be completed in future work.

6.2.5 Gas-Liquid Contact Time

The liquid volumetric flow rates and column heights were chosen on the basis of their influence on the degree of turbulence of the liquid film. Higher liquid flow rates over longer flow paths increases the degree of turbulence in the liquid film (Telles & Dukler, 1970). Relatively short column heights were chosen to keep the wave formation within the capillary wave region as far as possible, since it is the easiest wave structure to analyse due to its close resemblance to sine waves (Yu, et al., 2006). The wave structure of the gas-liquid interface will further be discussed in section 6.4.

The column height and volumetric liquid flow rate also determines the gas-liquid contact time achieved in the reactor. The contact time is calculated using falling film theory (Danckwerts, 1970):

$$t_c = \frac{h}{u_L} = \frac{2h}{3}\left(\frac{3\mu_L}{\rho_L g}\right)^{1/3}\left(\frac{\pi d}{V_L}\right)^{2/3} \qquad 6.7$$

The liquid viscosity was measured for each experimental solution for the temperature range of interest. The liquid mixture density at each temperature was calculated by assuming an ideal liquid mixture:

$$\frac{1}{\rho_L} = \frac{x_{\text{MEA}}}{\rho_{\text{MEA}}} + \frac{x_{\text{n-Prop}}}{\rho_{\text{n-Prop}}} \qquad 6.8$$

where x_i is the mass fraction of substance i. A test was done to validate the assumption of an ideal mixture. Two known volumes of n-Propanol and MEA were mixed in the MEA concentration range of this study and it was found that the total volume was equal to the sum of the individual volumes. Negligible volume change with mixing may therefore be assumed and thus equation 6.8 is valid. Refer to Appendix A.1 for the pure species liquid properties.

6.3 Reactive Absorption Rate Results and Discussion

In this section the validation and experimental results will be presented and discussed. The discussion of the results will focus mainly on the differences in absolute and specific absorption rates as a function of CO_2 partial pressure driving force, interfacial depletion and surface renewal rate.

6.3.1 Equipment Validation Results

The first consideration in validating the reactive absorption equipment was to ensure that the gas phase in the dome was properly mixed under the experimental conditions. This meant conducting a Residence Time Distribution (RTD) experiment for the gas side of the system. The experiment was started by eliminating all CO_2 from the system, by only allowing N_2 to flow through the system at 80 cm^3/min. Approximately 10 cm^3 of CO_2 was rapidly introduced to the system. The response time of the CO_2 analyser was found to be ±65 seconds. The CO_2 vol% reading was logged with time. Assuming ideal gas behaviour, the CO_2 vol% readings were converted to concentration (mol/m^3) data and the residence time distribution function was calculated as follows (Fogler, 1999):

$$E(t) = \frac{C(t)}{\int_0^\infty C(t)\,dt} = \frac{C(t)}{\sum_0^\infty C(t)\,\Delta t} \qquad 6.9$$

The curve obtained from this residence time distribution function plotted with time is illustrated in **Figure 6.7**.

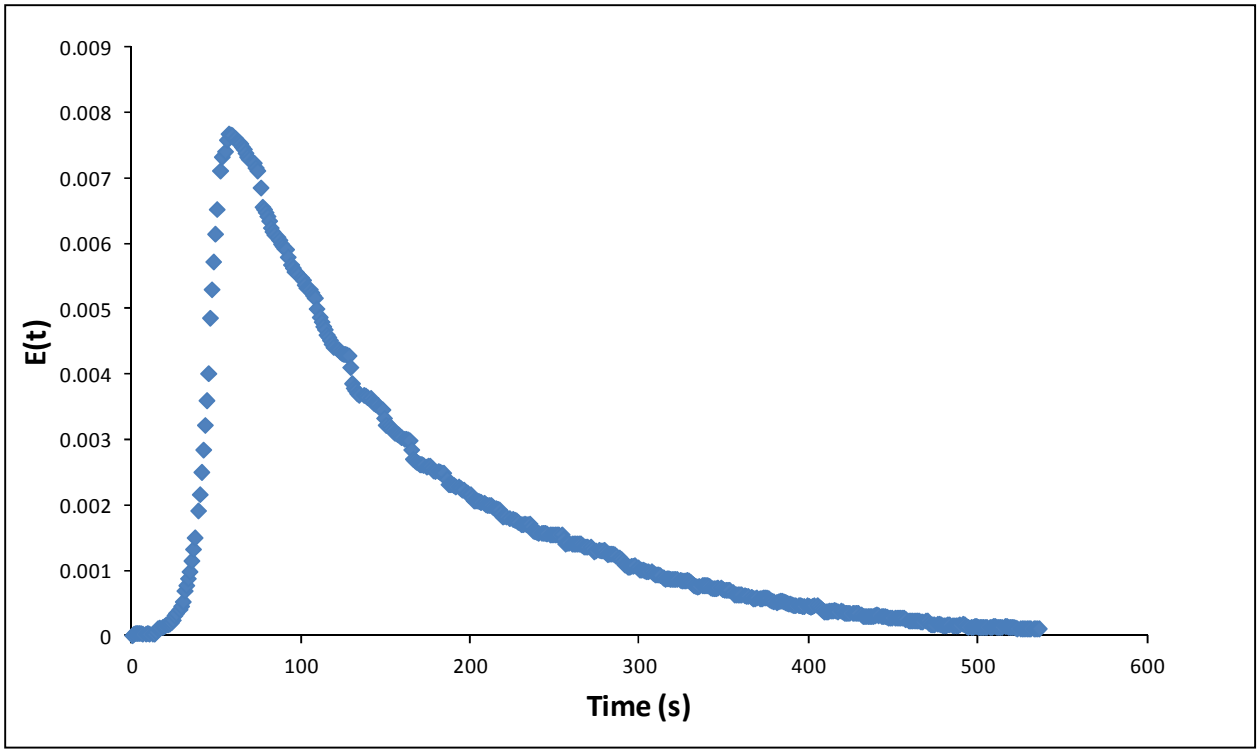

Figure 6.7 Gas Phase Residence Time Distribution Curve of the Wetted Wall Dome Set-up

The shape of the RTD curve in **Figure 6.7** closely resembles that of a series of continuously stirred tank reactors (CSTR) (Fogler, 1999). The number of tanks in series was calculated to be 2.3. This was an expected result, since the gas passes through both a mixing unit and the saturating unit (see **Figure 6.4**) before entering the dome. The results of the RTD study indicate that the gas phase of the system is well mixed when it enters the wetted wall dome under the conditions specified in the experimental design of **Table 6.3**. The CO_2 vol% reading obtained in the experiments may, therefore, be concluded to be representative of the CO_2 vol% inside the dome. Since an average of only 0.1% of the CO_2 was absorbed during an experimental run, it was assumed that the gas phase leaving the dome after absorption remained well mixed and the vol% reading was representative of the gas phase in the dome. It may further be noticed that it takes approximately 8.33 min for the system to return to the original CO_2 free steady state and approximately 6.67 min to reach 98% of the original CO_2 free conditions and 7.8 min to reach 99% of the original CO_2 free conditions. This supports the finding that a steady state vol% reading was obtained after 7 - 8 minutes during an experimental run.

The validation of the experimental set-up was completed by performing the experimental runs tabulated in **Table 6.1**. The results obtained are illustrated in **Figure 6.8**.

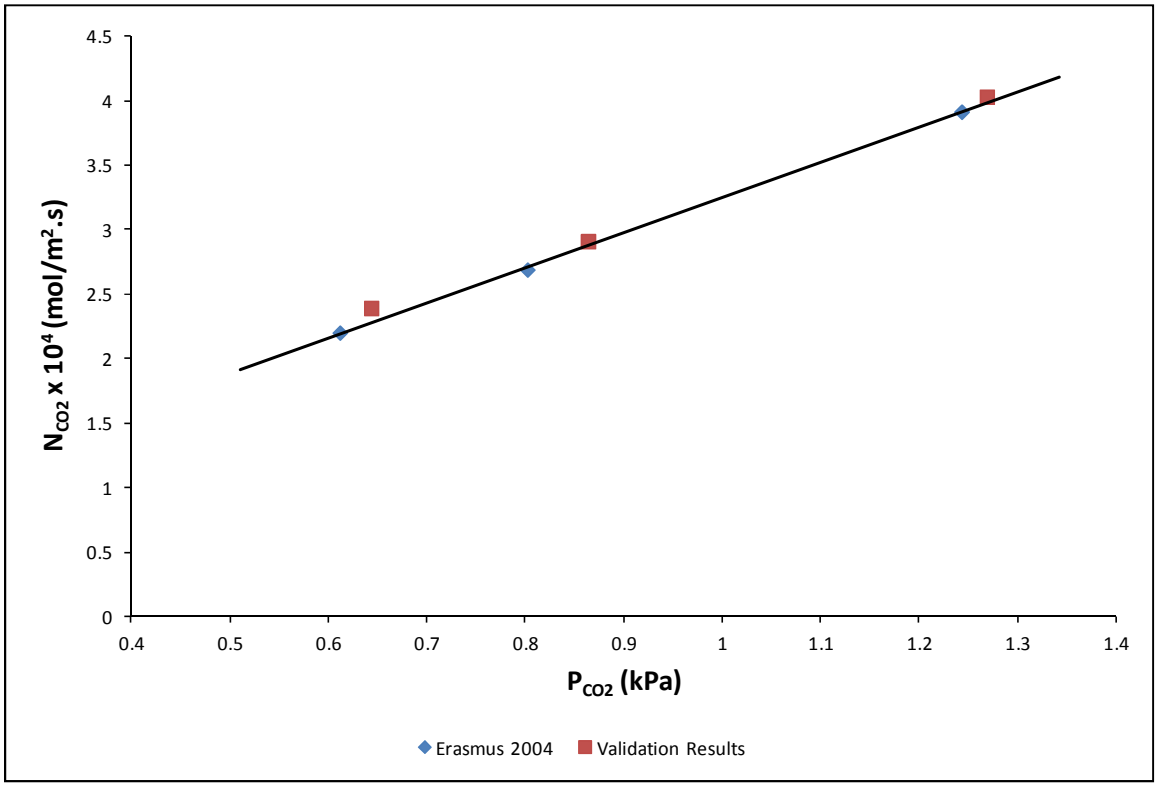

Figure 6.8 Validation Results of Wetted Wall Experimental Set-up

The slightly higher absorption rates obtained in this study may be attributed to the slightly higher dome pressure (102 kPa compared with 100 kPa) encountered as well as a slightly higher liquid flow rate (1.016 cm^3/s compared with 0.98 cm^3/s) causing a more turbulent liquid phase. The close agreement between the measured specific absorption rates in this study and that of Erasmus (2004) was considered to be evidence that the wetted wall experimental set-up was sufficiently validated.

6.3.2 Total Absorption Rate Results

The total absorption rate $\left(n_{CO_2}\right)$ of each experiment was calculated as described in section 6.2.1 by assuming ideal gas behaviour. The total reactive absorption rates as a function of CO_2

partial pressure for the 0.2 M and 0.08 M solutions is illustrated in **Figure 6.9** and **Figure 6.10** respectively.

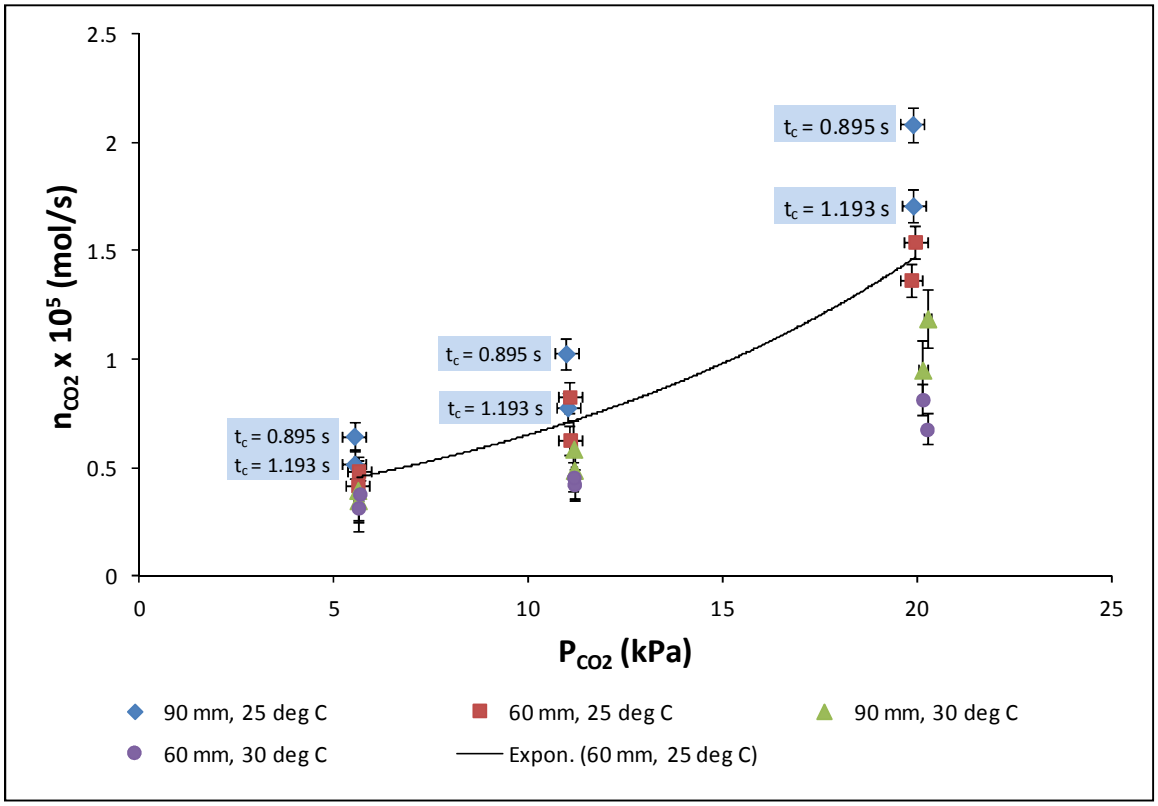

Figure 6.9 Total Reactive Absorption Rates into 0.2 M MEA in n-Propanol as a Function of CO_2 Partial Pressure

The repeatability of the measurements was determined by repeating an absorption experiment 3 times by changing the column height and CO_2 concentration back from another setting. Repeatability studies were conducted at each CO_2 partial pressure of interest. The repeatability absorption measurements fell within 0.01vol% of the average of the three readings. The vertical error bars in **Figure 6.9** and **Figure 6.10** allow for a ±0.01 vol% uncertainty due to the resolution of the CO_2 analyzer as well as the 0.01 vol% range in repeatability. A sample calculation to determine the error bars in **Figure 6.9** and **Figure 6.10** is given in Appendix A.2 The horizontal error bars allow for the slight fluctuation in the dome pressure reading (±0.5 kPa) noticed during the experimental runs.

In **Figure 6.9** the absorption rates at 25°C and a column height of 90 mm are labelled with the gas-liquid contact times calculated for each measurement. A higher absorption rate was measured for a shorter contact time for nearly all absorption measurements. The difference in absorption rate was less pronounced at lower CO_2 partial pressures. At very low CO_2 partial pressures the depletion of MEA in the liquid film, due to its reaction with CO_2, is lower due to the lower concentration of CO_2 absorbing under the reduced partial pressure driving force in the gas phase. Whenever absorption rates are independent of contact time, the concentration of MEA is not depleted to a great extent in the liquid film (Charpentier, 1981). At the lower CO_2 partial pressures there is also some overlap in the error bars of some of the readings, making a definitive conclusion of a higher absorption rate at shorter contact times not possible. The measured absorption rates nevertheless were consistently indicating a higher absorption rate at shorter contact times.

In **Figure 6.10** there is less of a difference between the absorption rates of CO_2 for the different column heights investigated compared with **Figure 6.9**. This is due to the lower MEA concentration in the liquid film experiencing a higher degree of surface depletion. There is, however, still a higher CO_2 absorption rate for shorter contact times (higher liquid flow rate), indicating that the increase in liquid turbulence increases surface renewal rate, which provides more effective interfacial area for reactive absorption. Higher absorption rates at the lower contact times were especially evident at higher CO_2 partial pressures. The higher degree of turbulence in the liquid phase causing an increase in absorption rate is consistent with previous research (Yu, et al., 2006). This will be discussed in further detail with respect to surface depletion and renewal rates of MEA in section 6.3.3.

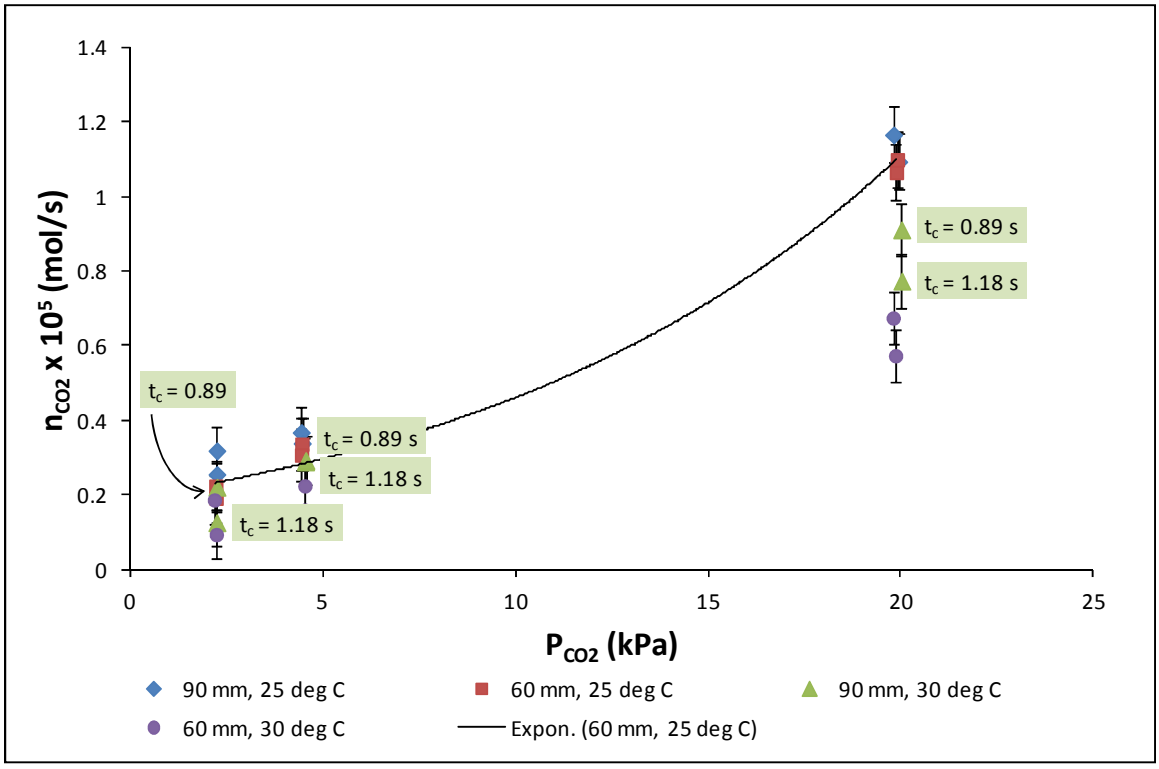

Figure 6.10 Total Reactive Absorption Rates into 0.08 M MEA in n-Propanol as a Function of CO_2 partial pressure

From **Figure 6.9** and **Figure 6.10** an exponential increase in absorption rate with an increase in CO_2 partial pressure is evident for both systems. This is an expected result, since a higher CO_2 partial pressure results in a higher driving force for mass transfer due to the steeper CO_2 concentration gradient at the interface. The absorption rate into the 0.2 M MEA solutions is higher than that of the 0.08 M solutions, which was once again an expected result due to the increase in the liquid phase reaction rate with an increase in MEA concentration. A comparison between the absorption rates for a 2.5 factor increase in MEA concentration is only possible at the same CO_2 partial pressure. The comparison drawn at CO_2 partial pressures of 19 – 20 kPa revealed a 1.5 factor increase in absorption rate at 25°C and a 1.25 factor increase at 30°C.

A decrease in absorption rate was noticed for an increase in temperature. This was in agreement with previous research (Erasmus, 2004; Patil, et al., 2011). The effect of temperature on the reactive absorption rate involves the consideration of both CO_2 solubility and the rate of the liquid phase reaction. The solubility of CO_2 in n-Propanol, decreases with an

increase in temperature (Tokunaga, 1975). When considering the solubility of CO_2 in pure n-Propanol, its molar solubility decreases by 4.73% with an increase in temperature from 25°C to 30°C (Tokunaga, 1975). This does not account for the average of 38.4% decrease in total absorption rate for the 0.2 M MEA solutions or 32.6% decrease for the 0.08 M MEA solutions. A possible explanation for this difference may be found when considering the exothermic nature of the reaction and the effect of temperature on the equilibrium of the reaction.

An increase in temperature causes an increase in both the forward and the reverse reactions of a reversible reaction system. As discussed in Chapter 3, the reaction of CO_2 with MEA obeys reversible reaction kinetics and the reaction was found to be exothermic as determined in Chapter 4. According to Le Chatelier's principle, an increase in temperature will cause a shift in the reaction equilibrium towards the reactants for an exothermic reaction (Fogler, 1999). This shift causes a decrease in the concentration difference of CO_2 between the gas and liquid phases, which decreases the driving force for absorption. The shift in reaction equilibrium may, therefore, be responsible for the decrease in CO_2 absorption rate with an increase in temperature.

6.3.3 Specific Absorption Rate Results

The specific absorption rate $\left(N_{CO_2}\right)$ or CO_2 absorption rate per area or CO_2 flux was calculated by dividing the total absorption rate by the estimated gas-liquid interfacial area. An analysis of the specific absorption rate provides insight into the effective interfacial area available for mass transfer. The estimated interfacial area was calculated by taking the measured film thickness into account and assuming the liquid interface to be smooth. The smoothness assumption of the interface is not exactly valid, since the image analysis done on the interface revealed wave motion for all liquid flow rates investigated (see section 6.4). Since only one gas flow rate was investigated in this study, the liquid film thickness was found to be dependent on the volumetric liquid flow rate only and the results of the film thickness measurements with the depth micrometer are summarized in **Table 6.4**.

Table 6.4 Liquid Film Thickness Measurements

Column Height (mm)	V_L (cm^3/s)	Film Thickness (mm)	Interfacial Area x 10^3 (m^2)
60	1.016	1.04	5.172
	1.345	1.10	5.183
90	0.874	1.00	7.746
	1.345	1.10	7.774

Taking the film thickness for each volumetric flow rate into account, the estimated interfacial area for each column height and liquid flow rate was calculated as the product of the liquid film circumference and the column height. The results are also tabulated in **Table 6.4**. The specific absorption rate results as a function of CO_2 partial pressure are illustrated in **Figure 6.11** and **Figure 6.12**. The data points once again represent absorption rates at different contact times with a predominantly higher specific absorption rate noticed at shorter contact times. This indicates that there is a degree of depletion of MEA in the liquid film at the interface and that the degree of depletion increases with an increase in contact time. From the measured specific absorption rate it is possible to discuss the results from both an interfacial depletion and interfacial renewal rate perspective. Interfacial renewal can only happen if there is interfacial depletion and so these effects are always linked. The discussion that follows will show that both effects may be noticed, but distinguishing between which of the two dominates under certain circumstances is often subject to the perspective of the discussion.

Since the reactive absorption of CO_2 in alcoholic solutions of MEA fall into the fast reaction category, the absorption is independent of the liquid side mass transfer coefficient and is thus only dependent upon the effective area available for absorption (Danckwerts, 1970). The effective area is decreased when surface depletion rates are higher than surface renewal rates. When surface renewal rates are such that it exceeds or balances surface depletion rates, then the effective area increases. Under pseudo first order reaction conditions, the effect of surface depletion on the available effective area is not taken into account, since the liquid side reagent is unaffected by the reaction. Without surface depletion, the effect of surface renewal rate on the available effective area can also not be taken into account.

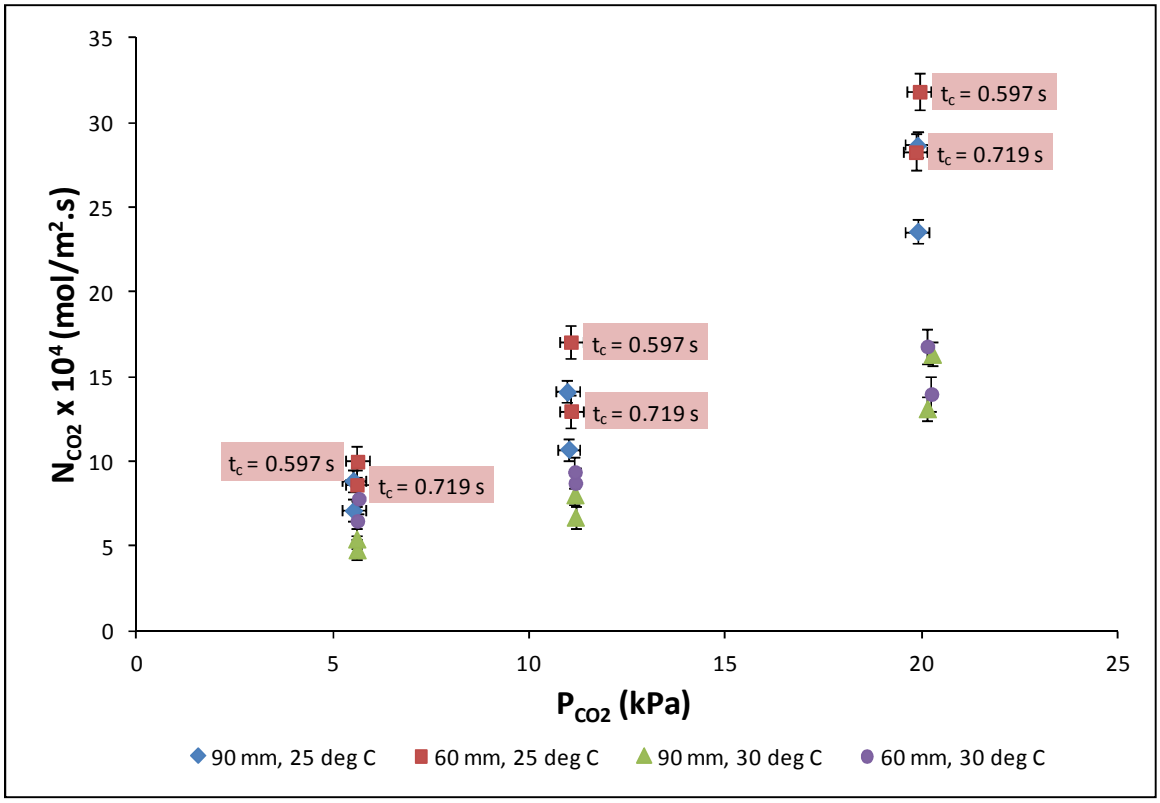

Figure 6.11 Specific Reactive Absorption Rates into 0.2 M MEA in n-Propanol as a Function of CO_2 partial pressure

At higher CO_2 partial pressures there will be a higher surface depletion rate due to the higher driving force for absorption and the faster reaction kinetics in the liquid film at the higher reagent concentrations. This may explain why the specific absorption rate at shorter column heights is higher than that for longer column heights. The higher degree of surface depletion for longer column heights decreases the effective area available for absorption. An estimation of the extent of surface depletion was done, based on a calculation method used by previous researchers to validate their assumption of pseudo first order reaction conditions (Tsai, 2010).

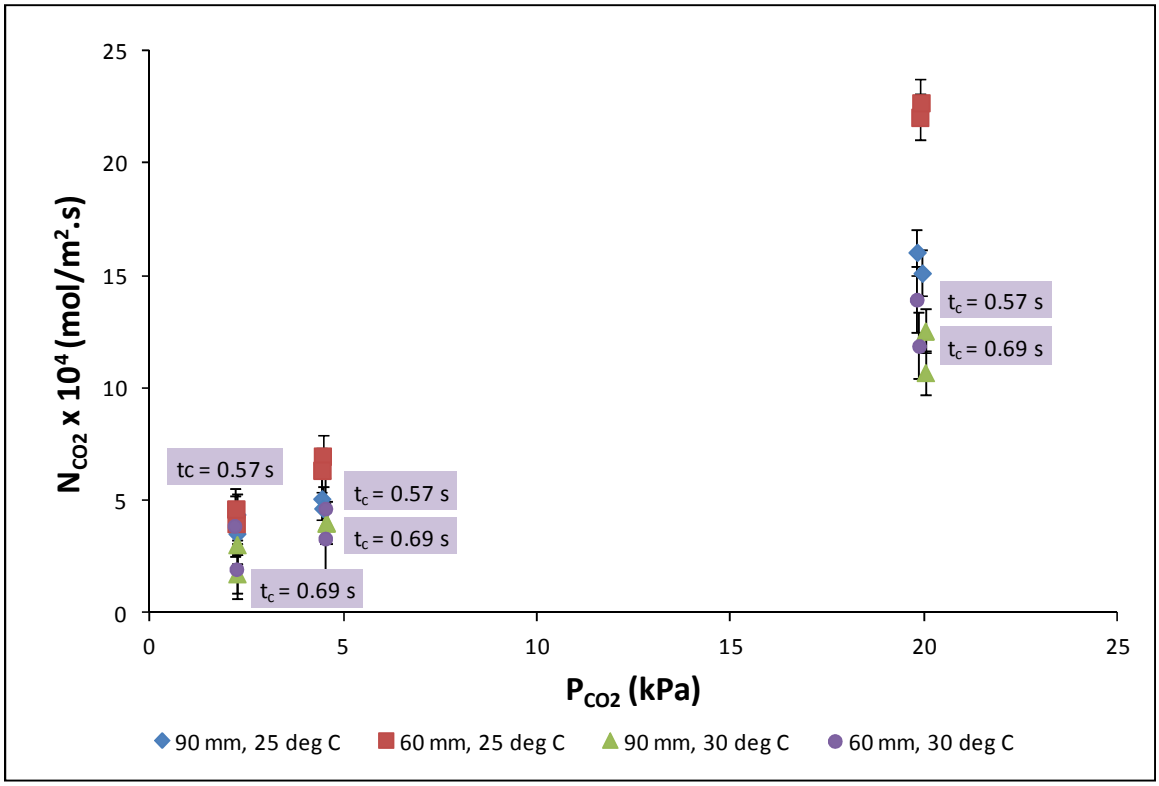

Figure 6.12 Specific Reactive Absorption Rates into 0.08 M MEA in n-Propanol as a Function of CO_2 partial pressure

The calculation is based on the reaction stoichiometry which equates the flux of MEA and CO_2 as follows:

$$N_{MEA} = 2N_{CO_2} \qquad 6.10$$

The flux of MEA to the surface may be defined as:

$$N_{MEA} = k_L \left(C_{MEA,L} - C_{MEA,i} \right) \qquad 6.11$$

where $C_{MEA,L}$ is the bulk liquid concentration of MEA, equal to either 0.2 M or 0.08 M in this case. The flux of CO_2 may be calculated from:

$$N_{CO_2} = K_G \left(P_{CO_2} - P_{CO_2,L} \right)_{LMPD} \qquad 6.12$$

where $\left(P_{CO_2} - P_{CO_2,L} \right)_{LMPD}$ is the log mean partial pressure difference of CO_2 as defined in equation A 2 in Appendix A.3. Combining equations 6.11 and 6.12 and rearranging reveals:

$$C_{MEA,i} = \frac{-2K_G\left(P_{CO_2} - P_{CO_2,L}\right)_{LMPD}}{k_L} + C_{MEA,L} \qquad 6.13$$

The liquid phase mass transfer coefficient for MEA in n-Propanol was calculated from penetration theory (equation 2.10) to be in the order of 0.0035 – 0.0045 cm/s. The diffusivity of MEA in n-Propanol was calculated from equations B 34 and B 35 as described in Appendix B.3. The results of the calculation revealed that the interfacial concentration decreased by between 18.4% and 154.8% relative to the bulk liquid concentration.

The results seem to indicate an unrealistically high surface depletion (more than 100%) which may be due to the inaccuracy in the prediction of the correlation for calculating the diffusivity of MEA in n-Propanol (25% inaccuracy (Charpentier, 1981)). The surface depletion estimation mostly indicates that there is a higher surface depletion of MEA at longer column heights, which was an expected result. It also revealed that there is a higher percentage of MEA that reacts at shorter contact times (higher liquid flow rates). This finding was confirmed in a calculation of the number of moles of MEA that reacted in the liquid film. The number of moles of MEA available for reaction in the liquid film was calculated from the MEA concentration and the volume of liquid in the film. From the molar amount of CO_2 absorbed into the liquid film at steady state and the reaction stoichiometry, the number of moles of MEA that could possibly react, was calculated. The calculation showed that the range of percentage of MEA that could possibly react for all experimental runs performed was 0.43% - 4.36% of the MEA available in the film. This is, however, not an indication of low surface depletion of MEA, but it shows that the results of the interfacial depletion calculation above does indeed overestimate the degree of interfacial depletion considerably. The calculation shows that that more than 95% of the MEA in the liquid film remains unreacted and so interfacial renewal of MEA is always possible.

From the mole balance calculation it was found that for the same column height, there was a larger number of moles of MEA that reacted per second for all experimental runs performed. This finding can be interpreted in support of both interfacial depletion and surface renewal occurring simultaneously. At higher liquid flow rates there is a higher percentage of MEA that reacts per second due to a higher liquid turbulence increasing the surface renewal rate and

contributing to the higher driving force for CO_2 absorption. This could be an explanation for the higher CO_2 absorption rate noticed at shorter contact times.

For the same CO_2 partial pressure, column height and liquid flow rate, there was a larger percentage MEA that reacted per second for the 0.08 M MEA solution, than the 0.2 M solution. Under these conditions, equal surface renewal rates on a basis of the volumetric rate of liquid carried to the surface due to turbulence may be assumed. There will thus be a lower molar amount of MEA reaching the interface per second for the 0.08 M solution. A similar partial pressure driving force for CO_2 will thus cause a greater percentage of MEA molecules to react per second, leading to a higher surface depletion of MEA for the 0.08 M solution compared with the 0.2 M solution. Both interfacial depletion and interfacial renewal may thus be assumed to occur.

On the other hand, the surface depletion rate of MEA per area is dependent upon the specific absorption rate of CO_2 and, therefore, the data indicates that there is a higher surface depletion rate at higher CO_2 partial pressures for shorter column lengths. This is an expected result, since the average absorption driving force (partial pressure gradient) is larger for a shorter column height due to less total CO_2 absorption.

At lower CO_2 partial pressures, the effect of surface depletion is less pronounced, since the reaction proceeds slower due to a lower CO_2 partial pressure driving force. The difference between specific absorption rates at different contact times become less pronounced. The difference in specific absorption rate at the same column height, but different liquid flow rates is smaller at the lower MEA concentration (0.08 M). This may be due to a balance achieved between surface depletion rates and surface renewal rates. At the same CO_2 partial pressure driving force, it is expected that the 0.08 M MEA solution will be subject to a higher degree of surface depletion due to a higher conversion of MEA at the gas-liquid interface. The 0.08 M solutions does, however, have a lower viscosity (2.2% lower at 25°C) than the 0.2 M solution, which will aid the surface renewal rate of this solution due to the faster diffusion rate of MEA in this lower viscosity solution.

A study was done for a final year project at the University of Stellenbosch using the wetted wall experimental set-up developed in this study to investigate the effect of liquid viscosity on the specific absorption rate of CO_2. The study used propylene glycol as additive to 2-Propanol to increase the viscosity of the liquid. The concentrations of MEA investigated were 0.08 M and 0.2 M also at 25°C and 30°C for column heights of 60 mm and 90 mm. Only one liquid flow rate (0.8 cm^3/s) was investigated. The study was conducted under CO_2 partial pressure driving forces leading to interfacial depletion of MEA. The study found that there was an increase in specific absorption rate of CO_2 for a decrease in liquid viscosity for all experimental runs performed. As expected, the degree of liquid turbulence was at its highest for the lower viscosity solution, indicating an increase in interfacial renewal rate, causing an increase in the effective area of the wetted wall column. This may indicate that there is a stronger effect of viscosity on the effective interfacial area than what equation 5.63 (the correlation by Tsai) suggests. The viscosity effect on effective interfacial area cannot be detected by a method based on pseudo first order reaction conditions, since the surface renewal rate for such a solution is infinite, due to no interfacial depletion.

Another, entirely different, possibility to consider would be the effect of possible gas phase resistance at the higher CO_2 partial pressures. For the longer column lengths investigated, the gas flow path in contact with the liquid film was also longer. Greater dispersion of the gas phase is expected to occur as the flow path length increases. This will decrease the effective linear velocity of the gas phase in this region, which will give rise to a greater possibility of significant gas phase resistance. However, as discussed in section 6.2.3, the influence of gas phase resistance may not be significant (Luo, et al., 2012). The boundary layer study of the gas phase shown in Appendix A.3 also indicated that the gas phase resistance to absorption on the wetter wall is low, ranging between 2 – 9 % of the overall resistance. The predominant resistance to mass transfer was thus encountered in the liquid phase, where the absorption rate is controlled by the reaction kinetics under the fast reaction regime.

The effect of the degree of liquid turbulence on the specific absorption rate was investigated by plotting the specific absorption rate of CO_2 as a function of the liquid phase Reynolds number:

$$\mathrm{Re}_L = \frac{\rho_L u_L h_{\mathrm{column}}}{\mu_L}$$

Since the liquid is accelerating under the influence of gravity, the liquid phase velocity was calculated from the height of the column and the contact time and thus represents an average velocity. The plots are illustrated in **Figure 6.13** and **Figure 6.14**.

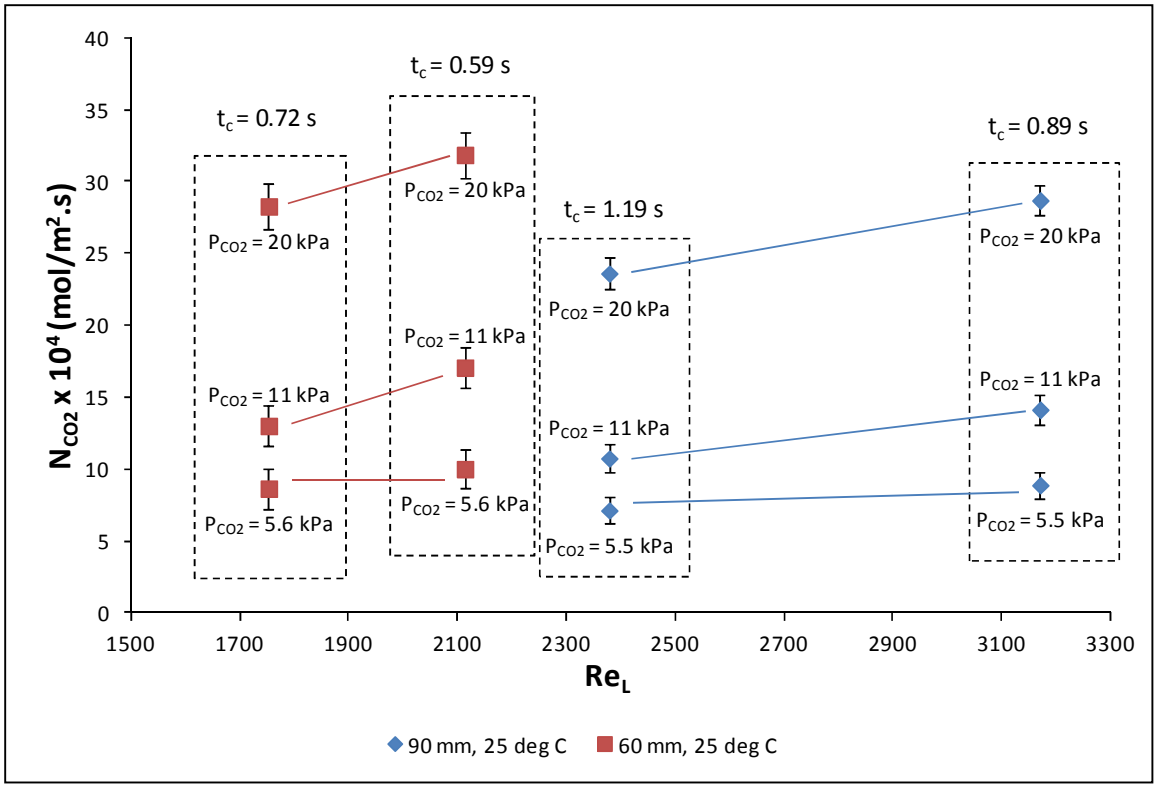

Figure 6.13 Specific Reactive Absorption Rates into 0.2 M MEA in n-Propanol as a Function of Liquid Reynolds Number

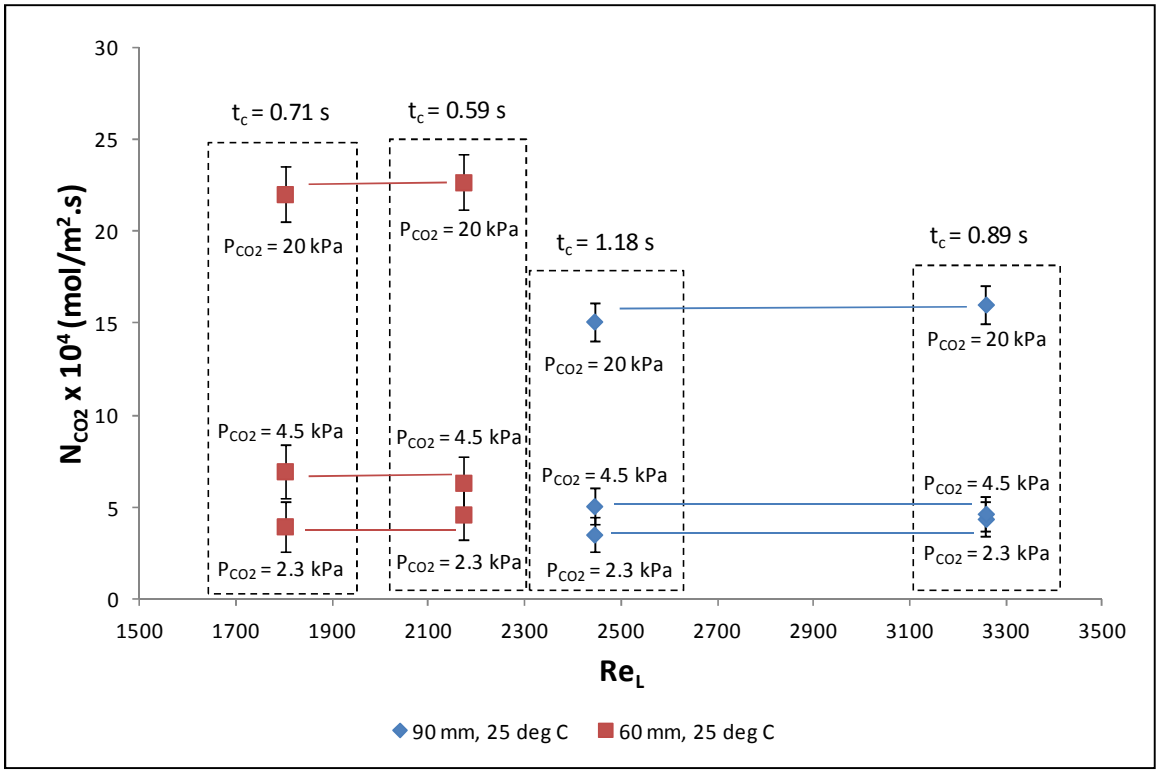

Figure 6.14 Specific Reactive Absorption Rates into 0.08 M MEA in n-Propanol as a Function of Liquid Reynolds Number

The higher specific absorption rates of CO_2 in **Figure 6.13** and **Figure 6.14** corresponds to the higher CO_2 partial pressures (as indicated by the data labels). As mentioned, the higher specific absorption rate is due to the higher partial pressure driving force of CO_2. From **Figure 6.13** it is evident that at the higher MEA concentration (0.2 M) and higher CO_2 partial pressures, an increase in liquid turbulence (higher Reynolds numbers) increased the specific absorption rate for the same column height. This may once again be discussed in terms of both interfacial depletion and renewal rates.

At the higher Reynolds number for the same column height, there is a higher surface renewal rate of MEA per volume of liquid transferred to the interface for the 0.2 M solution compared with the 0.08 M. At longer column heights, there was a decrease in specific absorption rate due to surface depletion even though a higher degree of liquid turbulence was obtained. This may be attributed to the higher number of moles of MEA reacting at longer contact times.

Both these effects were less obvious for the 0.08 M MEA solutions, especially at lower CO_2 partial pressures. A constant specific absorption rate for each column height, at the different liquid flow rates (or contact times) is illustrated in **Figure 6.14**. This may indicate that there is a balance between the interfacial renewal rate of MEA and reaction rate depleting the interface.

For both sovents, the specific absorption rate of CO_2 at low partial pressures may be considered to be independent of contact time. This is especially evident for the 0.08 M solution. Under these conditions the interfacial depletion of MEA is less significant and the reaction kinetics strives toward pseudo first order conditions. Evidence of the comparable pseudo first order conditions is illustrated in **Figure 6.15**.

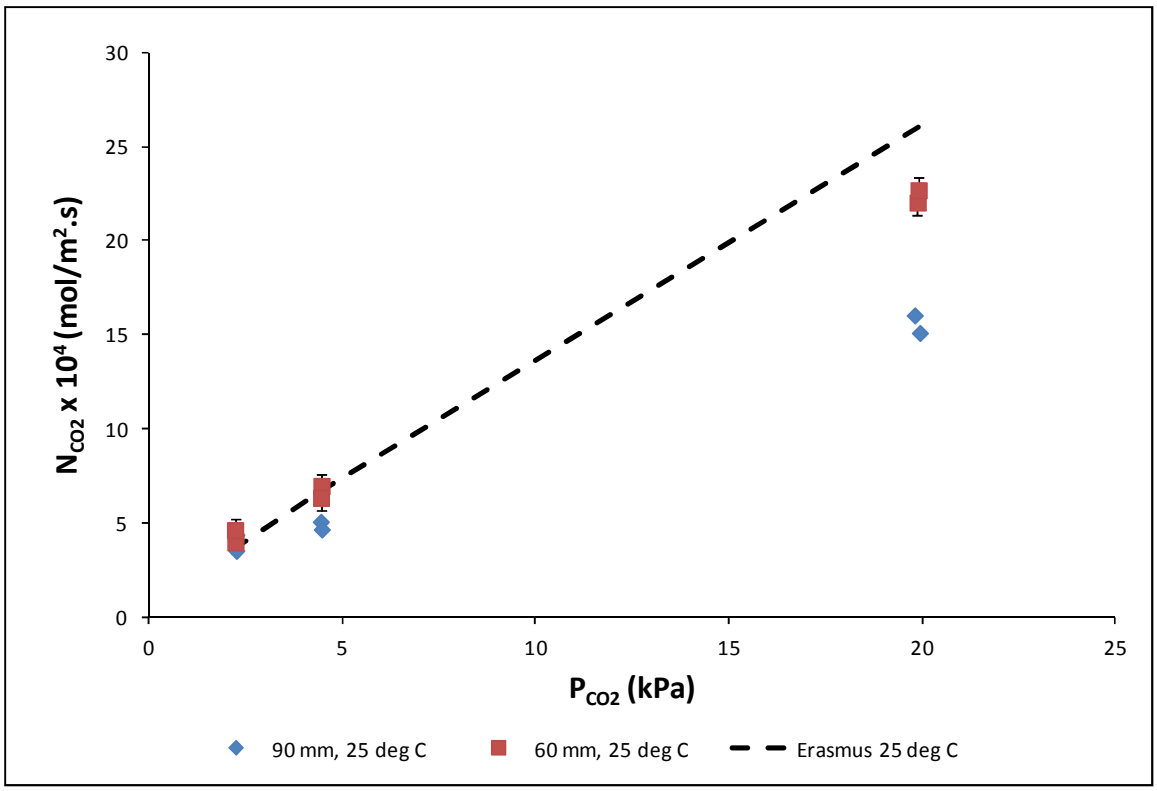

Figure 6.15 Erasmus Correlation (Equation 6.15) fitted on Specific Reactive Absorption Rates into 0.08 M MEA in n-Propanol

The correlation fitted on the specific absorption data of the 0.08 M MEA solution was developed by Erasmus using a similar wetted wall set-up to the one used in this study, also using n-Propanol as solvent (Erasmus, 2004). The correlation is of the form:

$$N_{CO_2} = kP_{CO_2}^{0.9} C_{MEA}^{0.93} \qquad 6.14$$

where the rate constant is temperature dependent according to the following expression:

$$k = -3.818\times10^{-6} \cdot T + 2.985\times10^{-3} \qquad 6.15$$

Equation 6.14 was derived under conditions where a pseudo first order reaction may be assumed to be valid (Alvarez-Fuster, et al., 1980) and it is evident from **Figure 6.15** that there is good agreement between the data and the correlation at the low CO_2 partial pressures. The over estimation of the correlation at higher CO_2 partial pressures may be due to its inability to account for interfacial depletion under conditions of higher MEA conversion, or it may simply be attributed to the fact that it is applied outside the concentration range of its derivation. It is interesting to note that equation 6.14 over estimates the specific absorption rate data at 4.5kPa CO_2 partial pressure and a 90 mm column height. A longer column length suggests more interfacial depletion, which will cause a greater deviation from pseudo first order conditions, causing equation 6.14 to overestimate the specific absorption rate.

An attempt was made to incorporate the effect of liquid turbulence in a correlation for calculating specific absorption rate. The effect of liquid turbulence on both physical and reactive absorption processes has been investigated previously (Lamourelle & Sandall, 1972; Riazi, 1996). In these investigations, the eddy diffusivity model was assumed to describe the absorption rate (see section 2.1.4). The eddy diffusivity is a measure of surface renewal rate of the liquid film by assuming concentration convection currents in the form of eddies renewing the surface. Lamourelle and Sandall (1972) derived a correlation for surface renewal rate as a function of liquid Reynolds number, based on the eddy diffusivity theory:

$$s = 0.115 \cdot \mathrm{Re}_L^{1.678} \qquad 2.12$$

A similar correlation to calculate the eddy diffusivity of a reactive absorption system was used by Riazi (1996):

$$e_d = 0.284\,\mathrm{Re}_L^{1.678}\left(\delta - y\right)^2 \qquad 6.16$$

where δ is the liquid film thickness and y the distance from the top of the wetted wall column. The correlation fitted on the specific absorption data in this study, thus, also included the Reynolds number in an attempt to account for surface renewal rate in the liquid film. The correlation is of the form:

$$N_A = kP_{A,i}^{\mathrm{A}} C_{B,b}^{\mathrm{B}} \mathrm{Re}_L^{\mathrm{X}} \qquad 6.17$$

The best fit of all the specific absorption data was obtained with a sum squared error of 0.73. This indicates a poor model fit since the sum squared error is much greater than zero. The resulting correlation is given by:

$$N_{CO_2} = k \frac{P_{CO_2}^{0.76} \cdot C_{MEA,L}^{0.22}}{\mathrm{Re}_L^{0.23}} \qquad 6.18$$

with

$$k = -1.4674 \cdot T + 458.13 \quad (T \text{ in K}) \qquad 6.19$$

A parity plot of the correlation is given in **Figure 6.16**.

The error margin in **Figure 6.16** is 35%, which is high and would, therefore, seem to indicate that equation 6.18 does not account for all the contributing factors concerning the specific absorption rate of CO_2 into solutions of MEA where surface depletion and renewal rates are significant. A better fit of the correlation could not be achieved by forcing the order of the Reynolds number to be equal to 1.678 as it is in equations 2.12 and 6.17. Equation 6.18 mostly under predicts the specific absorption rate. The under prediction is most prominent at both low and high specific absorption rates. Equation 6.18 was fitted on the experimental data of Erasmus (2004). The parity plot of the model fit is illustrated in **Figure 6.17**.

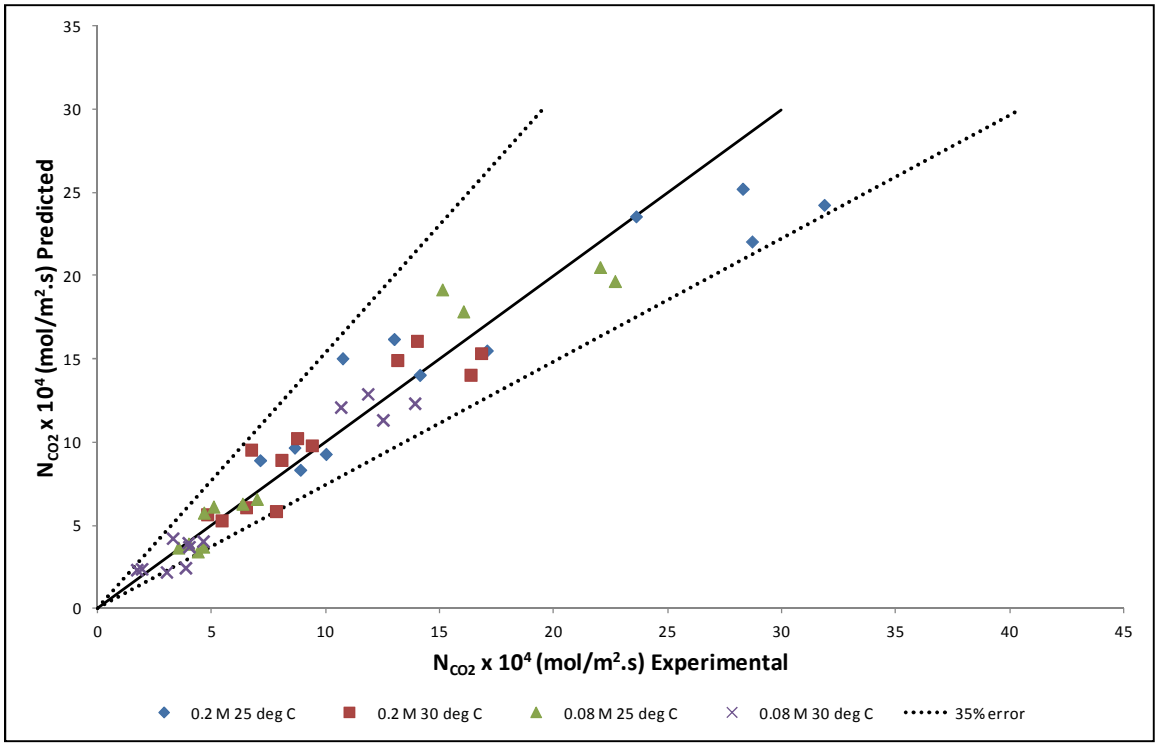

Figure 6.16 Parity Plot of Equation 6.18

The under prediction of equation 6.19 for the low specific absorption rate data of Erasmus (2004) shows an overcompensation to the over prediction of equation 6.14 (see **Figure 6.15**). This seems to indicate that correlations of these forms simply do not have the capability to account for all the significant effects on the specific absorption rate. A numerical solution strategy based on a transient diffusivity model to account for interfacial depletion and renewal rates, also incorporating the fundamental liquid phase reaction kinetics has the potential to be able to account for all the effects significantly influencing the specific absorption rate of CO_2 into alcoholic solutions of MEA. This is why Riazi (1996) incorporated his Reynolds number dependent eddy diffusivity in a mathematical model based a reactive absorption diffusion equation of similar form to equation 2.15.

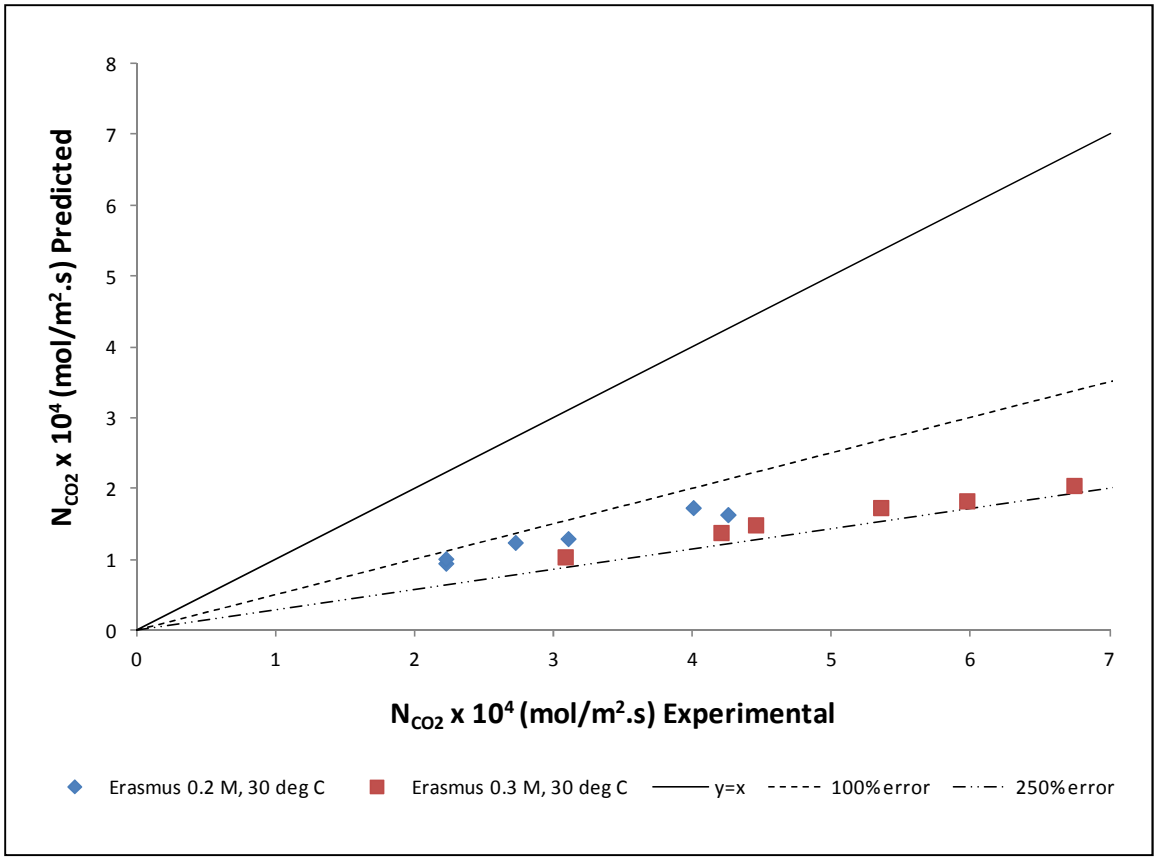

Figure 6.17 Parity Plot of Equation 6.19 Fitted on the Experimental Data of Erasmus (2004)

The specific absorption rate data gathered in this study has made it clear that effective interfacial mass transfer area is strongly dependent upon the rate of surface depletion and how fast surface renewal of the active agent in the liquid solution is achieved. The degree of liquid turbulence does contribute to the surface renewal rate, but it is not the only factor to consider.

Under separation column operation where there is a high partial pressure diving force in the gas phase, care must be taken to ensure that either the liquid phase concentration is high enough to decrease the surface depletion rate or the degree of turbulence is high enough to increase the surface renewal rate. Both of these effects will increase the effective area available for mass transfer.

A general analytical solution for the correct liquid phase concentration or optimum liquid flow rate to achieve the optimum effective mass transfer area is impossible to formulate. Numerical solutions based on the concentration diffusion equation (equation 2.15) will be necessary to

estimate the effective interfacial area available for mass transfer under conditions where surface depletion is appreciable. The effect of liquid properties, such as surface tension and viscosity, on the effective interfacial area under conditions where surface depletion and surface renewal rates are significant, will have to be investigated numerically. Under these conditions, a pseudo first order reaction expression is no longer appropriate for describing the liquid phase reaction kinetics and the fundamental reaction rate expressions developed in Chapter 4 of this study are called for. Such a numerical method is proposed and a possible solution strategy using Matlab® is described in Appendix B.

6.4 Image Analysis of the Gas-Liquid Interface

In section 6.3.3 the effect of liquid turbulence on the measured specific absorption rate is discussed. It was found that an increase in turbulence enhances the specific reactive absorption rate of CO_2 into an alcoholic solution of MEA. The enhanced mass transfer may be attributed to the simultaneous increase in interfacial area due to surface waves (Portalski & Clegg, 1971) and surface renewal rate caused by the turbulent motion within the liquid (Yu, et al., 2006). An increase in surface renewal rate translates to an increase in effective mass transfer area.

In this section, the preliminary study of the gas liquid interfacial profile of a falling film on a cylindrical wetted wall will be presented. The profile will be treated as a two dimensional wave from which the amplitude and wave length may be estimated. A brief literature survey on the effect of wave formation on interfacial area and mass transfer rates will be presented, followed by the preliminary results of an image analysis technique used to study the gas-liquid interfacial profile.

6.4.1 Waves on Falling Liquid Films

In a study on wave formation and amplification in a flowing liquid film revealed that waves in a falling film amplify exponentially as a function of flowing distance (Portalski & Clegg, 1972). This means that surface ripples will always occur on the surface of any flowing liquid. The size

and shape of these ripples affect both the interfacial area of the liquid and the rate of mass transfer across the interface.

A number of theoretical and statistical analyses on the wave motion of falling liquid films are available in literature (Telles & Dukler, 1970; Salazar & Marschall, 1978; Pierson & Whitaker, 1977; Yu, et al., 2006). Both analytical and numerical techniques have been used to find solutions to the proposed wave functions for falling liquid films (Kil, et al., 2001; Dandapat & Mukhopadhyay, 2003; Alekseenko, et al., 2009; Oron, et al., 2009). The mathematical formulation has its roots in the Navier-Stokes equations for viscous flow with the addition of the Orr-Sommerfeld equation to determine the degree of hydrodynamic instability (Pierson & Whitaker, 1977).

The degree of instability is linked with the liquid Reynolds number, which in turn determines the flow regime of the liquid film. Film flow can broadly be classified into three regimes (Yu, et al., 2006):

1. **Smooth Laminar** $\left(\mathrm{Re}_L\right) \leq 20$: Although surface waves are present, they are not visible and the liquid surface appears smooth. Under these conditions, both the penetration theory and surface renewal models for mass transfer provide good agreement with the experimental data (Banerjee, et al., 1967; Yu, et al., 2006). These conditions are seldom encountered in industry.
2. **Partially Laminar and Partially Turbulent** $\left(20 \leq \mathrm{Re}_L \leq 4000\right)$ Surface waves become visible and the nature of the waves may vary from an ordered nature to mild disorder. The waves most often encountered in this region are illustrated in **Figure 6.18**. At lower Reynolds numbers the most abundant waves are capillary waves. These waves are sinusoidal in nature and obey relatively simple mathematics. At higher Reynolds numbers the amplitude of the waves increase to a point where the effect of gravity on the liquid in the wave crest become significant. Under these conditions, the wave crest is compressed as if the wave is on the verge of breaking. These Roll waves obey more complicated mathematics, but numerical solutions based on statistical analyses are

available (Telles & Dukler, 1970). The waves encountered in this study all fell within this flow regime, making it possible to determine the surface profile from image analysis.

3. **Fully Turbulent Flow** $\left(\mathrm{Re}_L \geq 4000\right)$**:** Under fully turbulent conditions, the wave motion is highly irregular and near impossible to express in analytical terms. Mass transfer rates are poorly described by the penetration theory due to the higher rate of surface renewal caused by the turbulence within the liquid. A more representative mass transfer model is needed. The surface renewal and eddy diffusivity models have shown to provide better mass transfer predictions than the penetration or film theory under these conditions (Banerjee, et al., 1967; Lamourelle & Sandall, 1972).

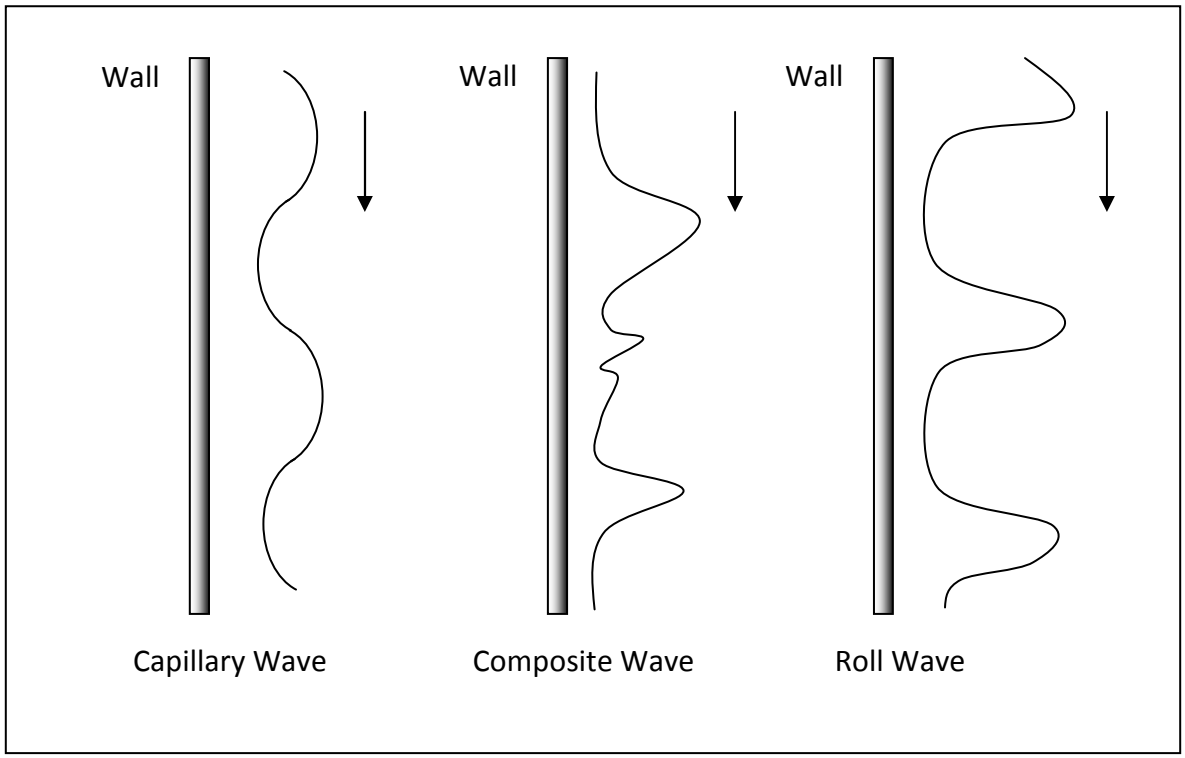

Figure 6.18 Schematic Diagram of Waves in a Falling Film (Redrawn from (Yu, et al., 2006))

The effect of surface waves of a falling liquid film on the gas-liquid interfacial area has also been investigated (Portalski & Clegg, 1971). A finite element theory was developed where the liquid surface area was estimated as the sum of a grid of small rectangles. The theory was tested with experimental measurements using the study of light refraction to determine the variation in

liquid film thickness which may subsequently be used to estimate the surface profile. Since the light scatters in three dimensions, a three dimensional surface profile could be obtained. It was found that a two dimensional representations of this three dimensional image provided satisfactory results. This method required the use of a flat, glass wetted wall and may therefore not be directly applicable to a stainless steel cylindrical wetted wall.

It was found that the surface waves caused an increase in both film thickness and interfacial area. The increase in area is proportional to the wave amplitude and indirectly proportional to the surface tension of the liquid. The indirect proportionality of interfacial area and surface tension was applied by previous researchers in their fractional area correlations (see section 5.3) It was furthermore interesting to find that regular wave motion has a higher interfacial area than larger, irregular waves.

Correlations for the percentage increase in interfacial area for liquid films in the fully developed rippling regime were derived. The following empirical equation was derived:

$$\%\Delta A = 374\left(\frac{\nu^2 \,\mathrm{Re}_L}{\lambda^{4/3} g}\right)^{2/3} \qquad 6.20$$

where $\%\Delta A$ is the percentage area increase, ν the kinematic viscosity of the liquid and λ the measured wavelength. The interfacial area increase of four liquids was determined. Amongst these liquids were both water and 2-Propanol. Their correlations may be summarized as follows:

Water: $\%\Delta A = 0.00814 \cdot \mathrm{Re}_L^{2/3}$ 6.21

2-Propanol: $\%\Delta A = 0.0208 \cdot \mathrm{Re}_L^{2/3}$ 6.22

Equations 6.21 and 6.22 fit the experimental data well. It may therefore be concluded that under similar flow conditions, the lower surface tension of 2-Propanol causes it to have a 2.5 times larger interfacial area than water. An increase in interfacial area may, however, only account for 10% of the observed increase in mass transfer rate (Banerjee, et al., 1967). The rest

is attributed to the increase in effective area due to turbulence increasing the surface renewal rate of the liquid film.

The effect of turbulent (wavy) motion in the liquid film has been found to dramatically increase mass transfer rates (Banerjee, et al., 1967; Lamourelle & Sandall, 1972; Littel, et al., 1991; Yu, et al., 2006). The effect of counter-current gas flow was also investigated and it was found that it decreased the liquid velocity close to the liquid surface. The velocity profile within the liquid film is parabolic in the direction of flow. The counter current gas flow creates a steeper velocity gradient between the higher velocity centre of the liquid film and its interface with the gas phase. These steeper gradients contribute to the turbulence just inside the liquid interfacial region which enhances convective mass and heat transfer in this region (Yu, et al., 2006).

It may be concluded that under turbulent conditions, the penetration theory under predicts the absorption mass transfer rate and that a surface renewal model provides a better prediction of mass transfer rates under these conditions (Banerjee, et al., 1967; Lamourelle & Sandall, 1972; Yu, et al., 2006). It is, therefore, important to know what both the interfacial area and degree of turbulence within the liquid film is, in order to shed light on the effective area available for mass transfer. Image analysis of the gas-liquid interface on a cylindrical wetted wall will aid in calculating the true interfacial area in order to compare the calculated interfacial area with the measured effective area using the chemical method and assuming a surface renewal model for mass transfer.

6.4.2 Image Analysis Procedure

Image analysis was used to detect the profile of the gas-liquid boundary as the liquid flowed down the wetted wall column. Image acquisition comprised of the capturing of videos using an endoscopic camera and further conversion to an acceptable format. It is important to take computational requirements into account when performing image analysis. The correct frame rate and resolution settings can be found that reduces computational cost, but without too much loss of accuracy in the results. The software used for video conversion was Any Video Converter®. The software allows the selection of the video frame rate, resolution, size and

time, making it a very useful pre-processing tool. The video images were converted to a resolution of 1920 x 1080, 30 frames per second, wmv1 codec and .avi format.

Once the video has been converted to the correct format, it is ready for analysis in Matlab. The following actions were carried out in the image analysis algorithm:

Image Inversion: In order to be able to better identify the gas-liquid interface, the image contrast was inverted to the negative. This was done, since a black background was purposefully used in the wetted wall experiments. An example of such an inverted image is illustrated in **Figure 6.19**. The angle of the image can also be adjusted to compensate for any angle deviations of the camera during image capturing

User selections: For image processing to be performed, some user selections are required. These selections are only performed using one image from the video, after which it is applied to each image in the video in the processing algorithm.

Region selection: A region of interest is selected for processing. This enables better image processing through the removal of unnecessary background artefacts. This also has the additional advantage of improving the processing time. The selected region for image analysis is illustrated in **Figure 6.19**.

Contrast enhancement: The minimum and maximum pixel values in the image often does not comprise of the entire intensity range available, which is 0 (white) to 256 (black) for negative resolution images. Adjusting the contrast so that the minimum and maximum is stretched to include these limits enables better boundary detection.

Threshold selection: The contrast enhanced image is inspected for the selection of the boundary threshold. Matlab®'s Image Processing Toolbox has a tool for image pixel inspection, as shown in **Figure 6.20**. To make sure that the selection is suitable, a preliminary result is shown and the option is provided to make another selection if the results were not satisfactory.

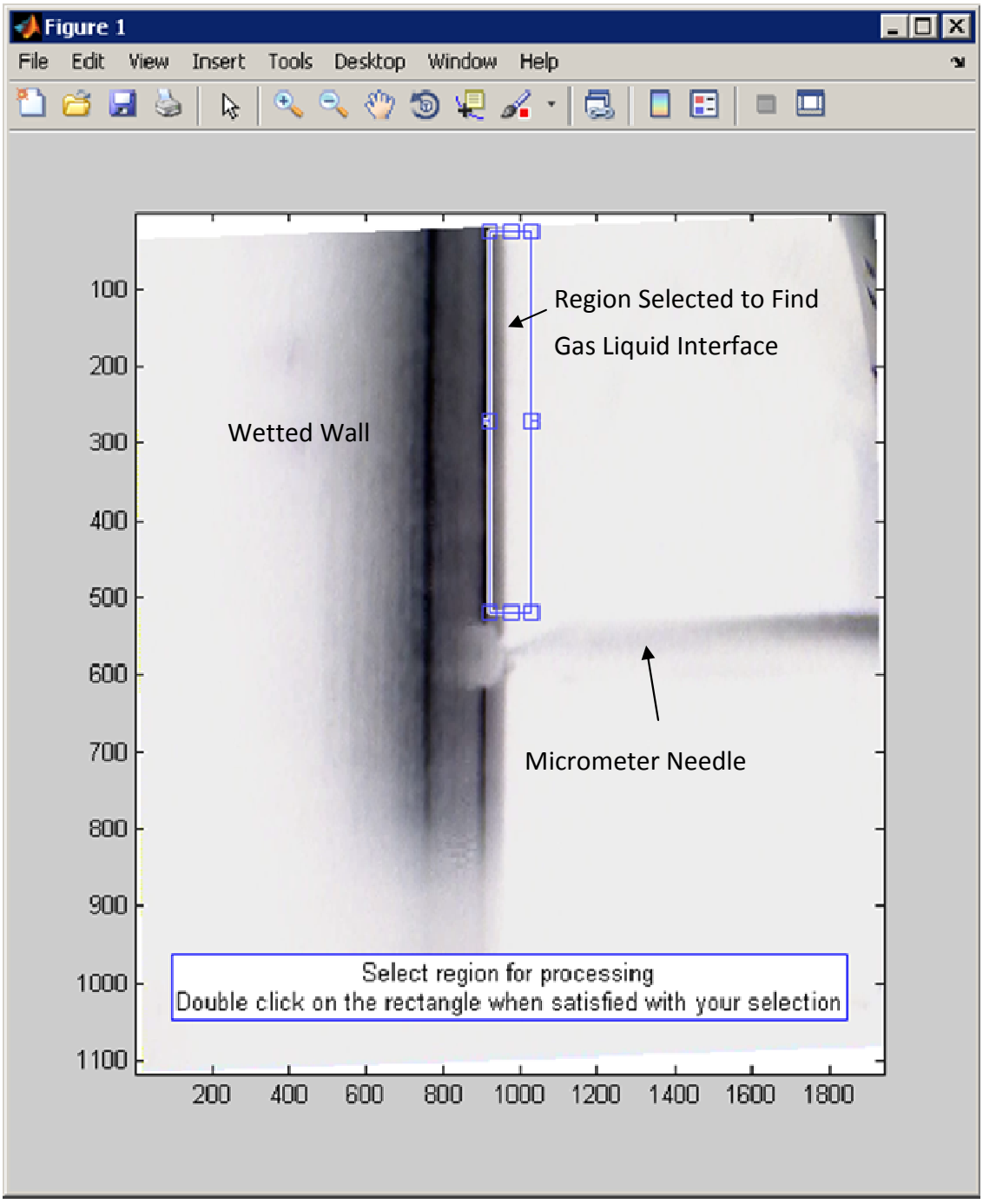

Figure 6.19 User Selection Screen where the Region for Image Analysis of the Gas-Liquid Interface may be selected

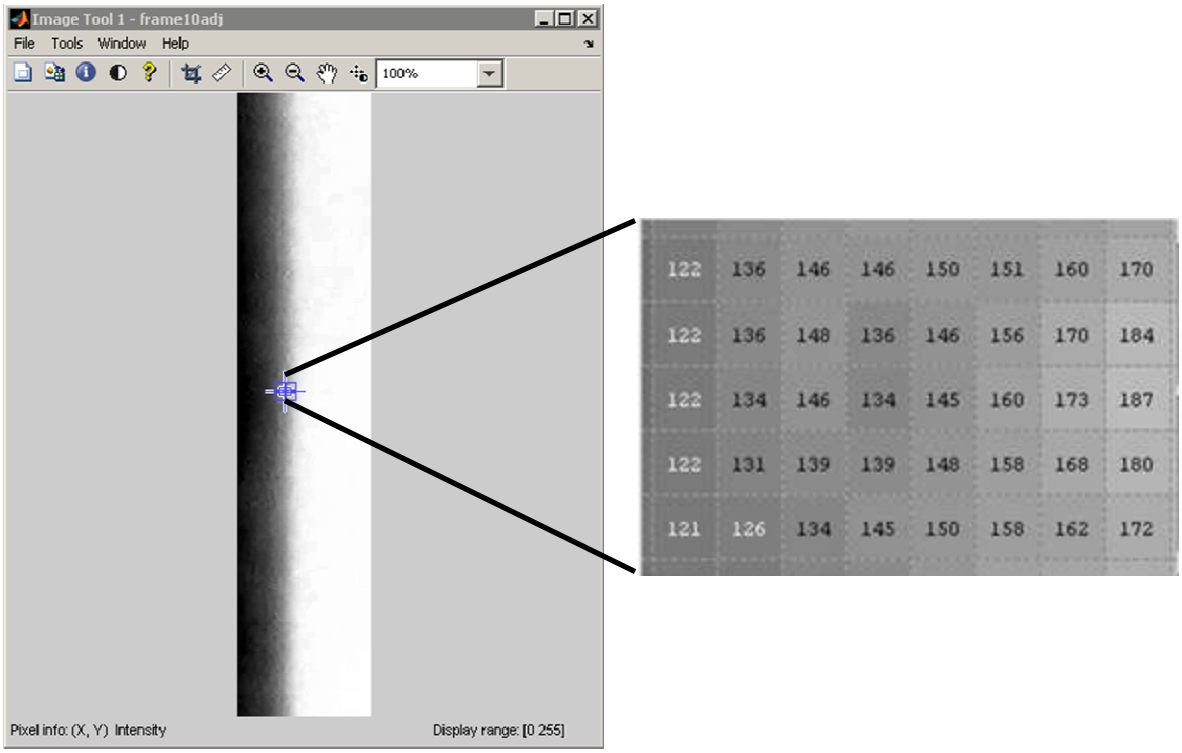

Figure 6.20 Image Pixel Inspection to Find the Contrast of the Gas-liquid Boundary

A typical profile of a selected boundary contrast threshold is illustrated in **Figure 6.21**.

Image processing: Each image in the video is processed in the following way:

- Crop the image according to region selection settings
- Enhance the contrast of the selected region
- Find the boundary location for each row in the image using the predetermined threshold value. The boundary location in a row is the first instance where the pixel value in the row exceeds the threshold value.
- Return the boundary profile

Filtering: The resulting boundary profiles are often rather noisy; therefore, in order to better investigate the underlying signal, some noise needs to be removed. This was done using a moving average filter, in which the user is able to select the window size of the moving average. In this study a window of 15 was selected, which means that every threshold value is the average of the 15 preceding threshold values. The first window values (15 in this case) in the

image were removed in the profile display, since these values were not properly filtered due to the window size.

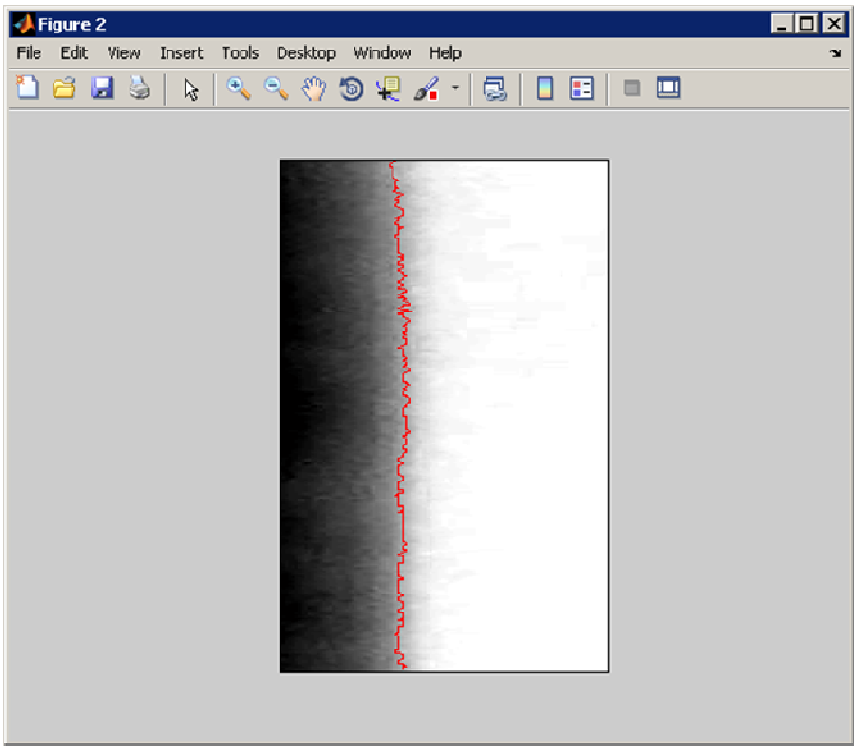

Figure 6.21 Preview of a Selected Gas-liquid Boundary at a Threshold Value of 160

6.4.3 Image Analysis Results

Video footage of the gas-liquid profile was captured under conditions similar to the absorption rate experiment of **Table 6.3**. Only N_2 was used as gas phase and the gas flow rate was set to 80 cm^3/s. Image analysis was captured at three liquid flow rates, 0.874 cm^3/s, 1.016 cm^3/s, 1.345 cm^3/s at a temperature of 25°C in order to qualitatively evaluate the effect of increased liquid phase turbulence on the profile of the gas-liquid interface.

The video footage was processed as described in section 6.4.2 and the results re-recorded into videos with the same resolution, but a rate of 10 frames per second. The gas-liquid interface was best determined at a pixel threshold of 160 (as captioned in **Figure 6.21**). The slower frame rate enables better identification of the wave structure on the liquid surface as it evolves with

time elapsed. The video footage was taken at steady state conditions, so the results are representative of the gas-liquid interface during the reactive absorption experiments.

An in depth analysis of the wave structure of the liquid surface was not done in this study, since, based on the complicated analyses found in literature, it is not a simple task. The aim of this section is to illustrate that the tools enabling image analysis of the gas-liquid interface have been developed, which has laid the foundation for future research. The image analysis results will be discussed in qualitative terms only and where applicable, the suggested course for future investigation will be provided.

A screen shot of a typical re-recoding of an image analysis result for a liquid flow rate of 1.345 cm^3/s is illustrated in **Figure 6.22**. From the filtered threshold data, the wave motion of the gas-liquid interface is clearly visible. When comparing the wave structures of the processed image with that of the typical wave structures encountered on falling liquid films (**Figure 6.18**), all three types of waves may be identified. It is further evident that the wave types are region specific. In the entrance region of the liquid film, capillary waves are most common and as the flow length increases, composite and roll waves start to appear. This is in agreement with literature (Yu, et al., 2006). It is also in agreement with the increase in liquid turbulence predicted for an increase in column height according to the liquid Reynolds number.

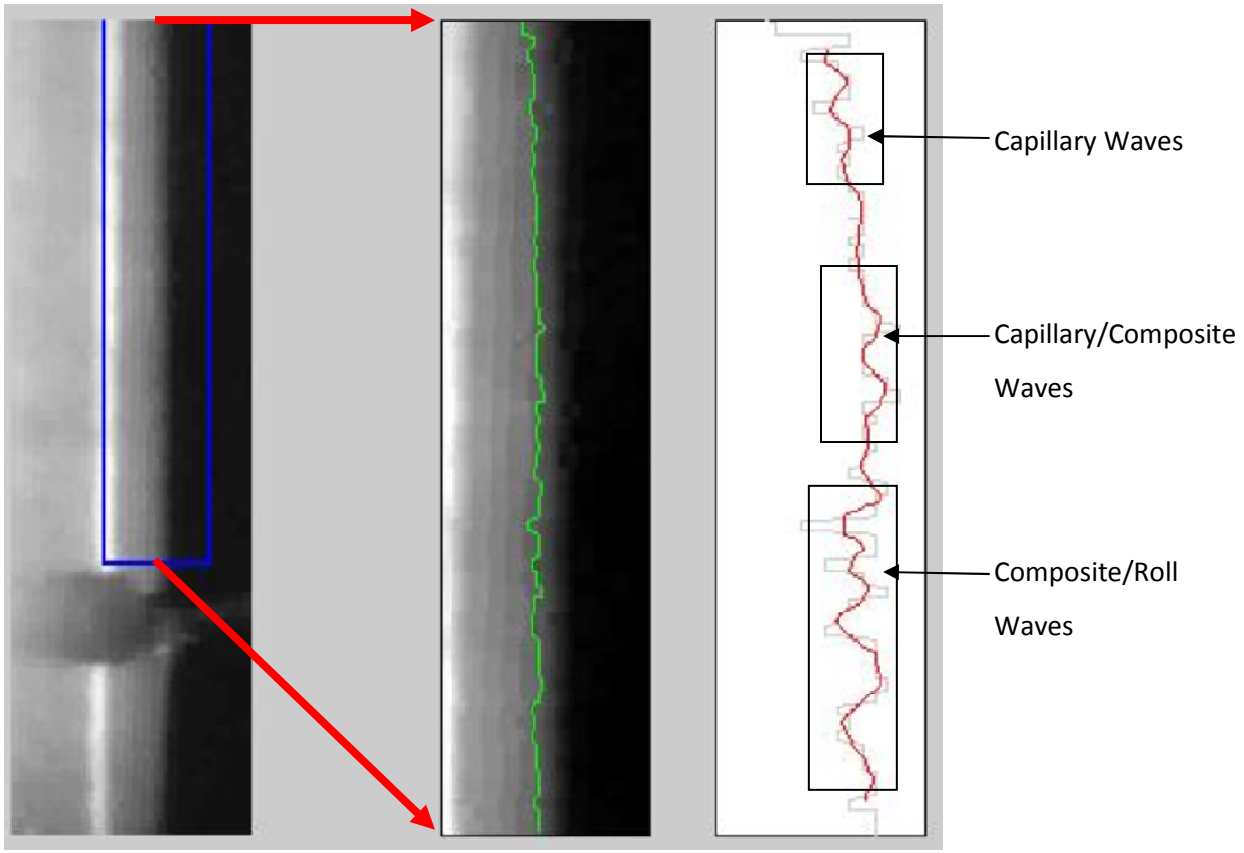

Figure 6.22 Typical Re-recording of the Processed Image Analysis at a Flow Rate of 1.345 cm^3/s Indicating the Three types of Waves Found in Falling Liquid Films

The results of all three liquid flow rates investigated are presented as a series of images for each liquid flow rate, approximately 60 frames apart to illustrate the wave motion on the gas-liquid interface. These images are illustrated in **Figure 6.23** to **Figure 6.25**.

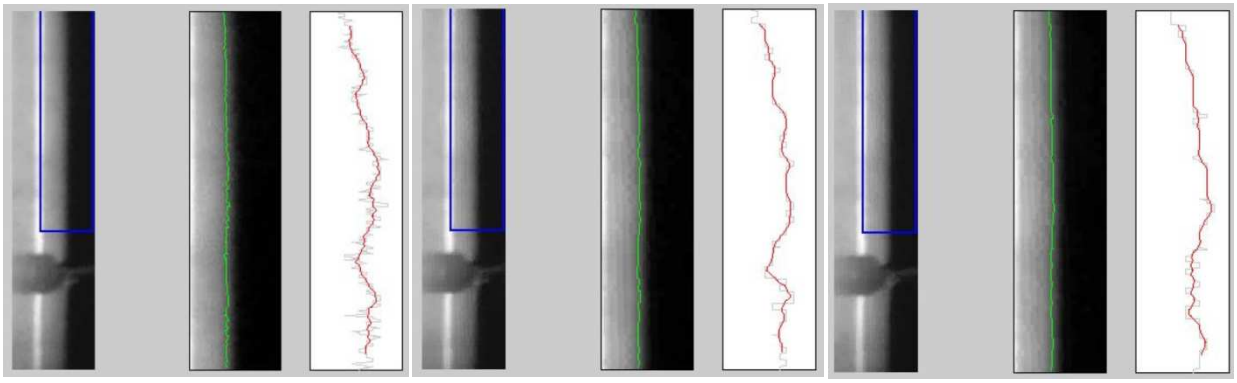

Figure 6.23 Image Analysis of the Gas-liquid Interfacial Profile of n-Propanol Flowing Down a Cylindrical Wetted Wall at 0.874 cm^3/s

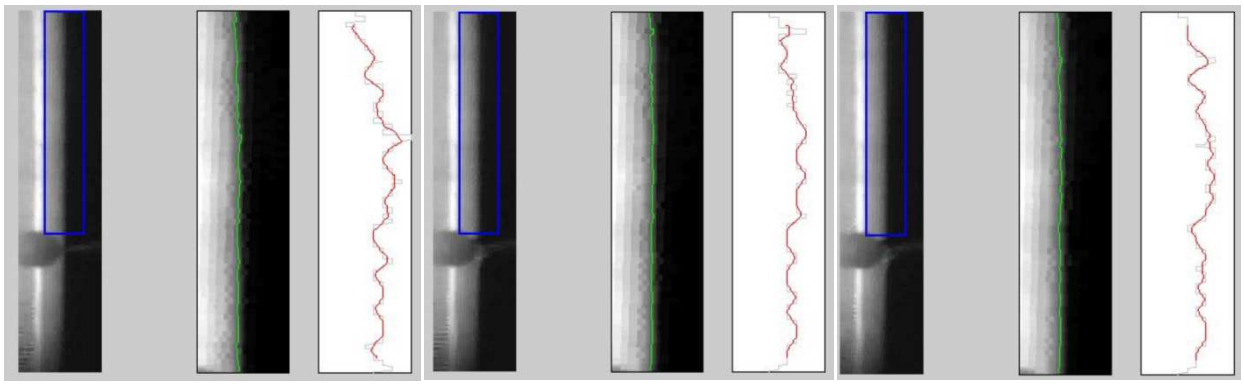

Figure 6.24 Image Analysis of the Gas-liquid Interfacial Profile of n-Propanol Flowing Down a Cylindrical Wetted Wall at 1.016 cm^3/s

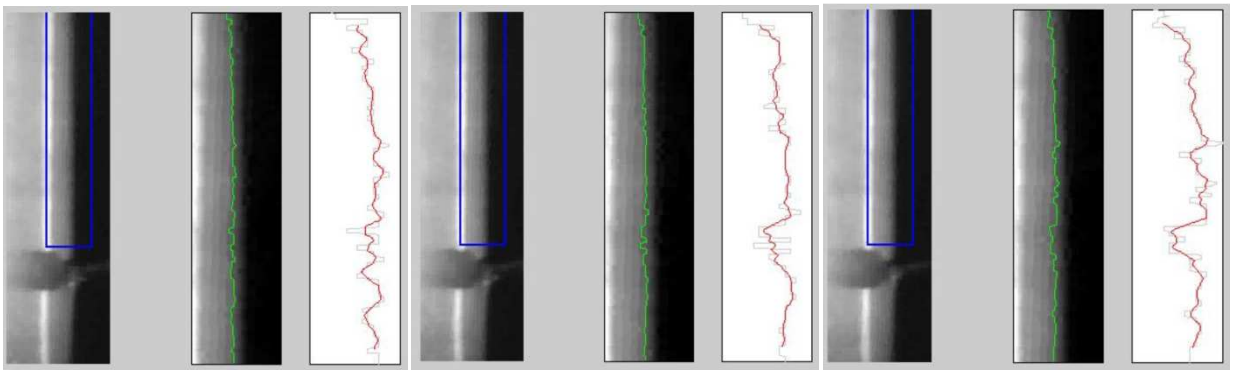

Figure 6.25 Image Analysis of the Gas-liquid Interfacial Profile of n-Propanol Flowing Down a Cylindrical Wetted Wall at 1.345 cm^3/s

From the image analysis results it may firstly be concluded that the assumption of a smooth gas-liquid interface for the liquid flow rates used in this study is an over-simplification. This raises some concern about the smooth interfacial profile assumption made by previous researchers operating at similar and higher liquid flow rates than the flow rates of this study (Alvarez-Fuster, et al., 1981; Erasmus, 2004; Tsai, et al., 2008; Luo, et al., 2012). It may be seen that the ripples on the liquid surface increase in frequency as the liquid flow rate increases. This increase in ripple frequency is caused by the increase in liquid turbulence.

There is furthermore a definite macro and micro structure to the wave motion. A macro-wave has a larger wave length and in the images presented in **Figure 6.23** to **Figure 6.25** there are $1\frac{1}{2}$ macro-waves visible. At 0.874 cm^3/s, the macro waves are of a capillary nature, whilst at

1.345 cm^3/s, roll waves may be identified. The appearance of roll waves was caused by an increase in film thickness as measured with the depth micrometer and tabulated in **Table 6.4**. An increase in liquid film thickness allows gravity to influence the greater mass in the crest of the wave to a higher degree, causing the wave to lean over into the shape of the roll wave. At the lowest flow rate the mico-waves are smaller in amplitude and the longer period macro waves dominate the surface profile. As the liquid flow rate increase, the increase in turbulence gives rise to the micro-waves of shorter period. Image analysis is, therefore, capable of capturing the effect of liquid turbulence on the interfacial area and it may be seen that due to the increase in the number of surface ripples, the area is increased. This partially accounts for the increase in specific absorption rate noticed for an increase in liquid flow rate, as reported in section 6.2.3. Increased surface renewal rates also play a role in increasing the specific absorption rate (Yu, et al., 2006).

In order to be able to determine the exact amplitude, wave length and frequency of the surface ripples, the image will have to be dimensioned with the use of a grid. This was not done in this study, since only a qualitative image analysis was the main aim. After a grid is assigned to the image and the wave properties determined, a more in-depth analysis of the true gas-liquid interfacial profile may be completed. The Orr-Sommerfeld equation may be applied to statistically determine the degree of surface instability (Pierson & Whitaker, 1977). Once the two dimensional interfacial profile is determined the interfacial area may be more accurately estimated by integrating the profile equation around the circumference of the cylindrical wetted wall, using cylindrical coordinates. This investigation will form part of future research.

6.5 Chapter Conclusions

The reactive absorption of CO_2 into solutions of MEA/n-Propanol was investigated using a cylindrical wetted wall experimental set-up. Absorption rates were measured for two MEA concentrations, two temperatures, two column heights and three different liquid flow rates. The experiments were designed in order to study the reactive absorption of CO_2 into these MEA solutions under conditions where the MEA at the liquid surface undergoes appreciable interfacial depletion. The liquid flow rates were varied to study the effect of liquid turbulence

on the absorption rate, in order to get an idea of the effect of liquid turbulence on the surface renewal rate of MEA. The gas phase mass transfer resistance was calculated using boundary layer theory. The calculation revealed that the gas phase resistance was low relative to the overall mass transfer resistance, indicating that the predominant resistance to mass transfer was in the liquid phase. The experiments were conducted in the fast reaction regime, meaning that the absorption rate is independent of the liquid side mass transfer coefficient and only dependent upon the available effective interfacial mass transfer area provided by the presence of MEA at the gas-liquid interface. This study was, thus, conducted under conditions where the effective mass transfer area achieved on the wetted wall column was influenced by surface depletion and renewal rates of MEA.

It may be concluded that specific absorption rate is a function of temperature, CO_2 partial pressure, degree of surface depletions and the degree of liquid turbulence. Specific absorption decreases for an increase in temperature. This is partly due to the decrease in solubility of CO_2 with an increase in temperature. At longer column heights, the specific absorption rate of CO_2 decreases. This may be attributed to a degree of depletion of MEA in the liquid film for the longer liquid flow path, causing a decrease in the available effective area for absorption. At higher liquid flow rates, the increased turbulence causes an increase in the surface renewal rate, which increases the effective area available for absorption.

Image analysis of the gas-liquid interface revealed the wave motion noticed on the falling liquid film surface. All three types of waves commonly occurring on falling liquid films were identified, making image analysis a feasible method for estimating the interfacial area between the gas and liquid phase inside the wetted wall dome. The increase in liquid phase turbulence with and increase in liquid flow rate and flow path length was noticed from the wave motion on the liquid surface changing from capillary waves (lower turbulence) to composite and roll waves (higher turbulence). Image analysis may, therefore also be used to study the degree of liquid turbulence on the wetted wall column.

Chapter 7 CONCLUSIONS AND RECOMMENDED FUTURE WORK

The main conclusions of this study will be summarized in this chapter. It will comprise of the conclusions made at the end of each of the preceding chapters, which forms the basis for the recommended future work identified after completing this study.

7.1 Conclusions from the Reaction Kinetic Study

The homogeneous liquid phase reaction kinetics of CO_2 with MEA in n-Propanol as alcoholic solvent was investigated in this study. A novel, *in-situ* FTIR method of analysis was developed to study the reaction progress in real time. A conductometric titration method of analysis was developed to determine the equilibrium concentration of one of the product species, RNH_3^+, of the reaction. Concentration profiles of CO_2, MEA and RNH_3^+ were determined based on the measure peak area change of the series of FTIR spectra collected in real time. From the measured data, it may be concluded that the zwitterion reactive intermediate mechanism describes the reaction of CO_2 with MEA in alcoholic solvents, sufficiently. This was in agreement with the proposed reaction mechanism for this system, found in literature.

The feasibility of the existing reaction rate expressions were evaluated by modelling the measured concentration profiles on the proposed rate expressions. It may be concluded that the power rate law does not describe the reaction kinetics sufficiently under conditions where appreciable conversion of MEA occurs. The Pseudo Steady State Hypothesis (PSSH) gave reasonable model fits to the experimental data. The rate constants of the existing rate expression showed no consistency over a wide concentration range and also no Arrhenius type temperature dependence. The existing rate expressions are not rejected as representative rate expressions applicable to conditions where the interfacial depletion of MEA is negligible. The

PSSH model is, however, considered to be too complex to use in effective interfacial mass transfer area studies.

A fundamentally derived rate expression was modelled on the data and it may be concluded that the model fit was of good quality over the entire temperature, solvent and concentration range investigated in this study. The fundamental model further showed an Arrhenius type temperature dependence. The fundamental model is therefore valid over a wide concentration range including the range where MEA conversion is significant.

The fundamental model is, however, more complex than the existing rate expressions and will therefore require greater computational time in reaching model convergence if it is used in a rate based model of differential equations, such as the method proposed in Appendix B. A less complex, shortened fundamental model was therefore derived, based on a simplifying assumption of fast reaction equilibrium obtained in the liquid film. Given the rapid rate of the reaction, this was considered a reasonable assumption. The shortened model also provided a good quality model fit on the experimental data. Its rate constants were, however found to show a possible dependence on concentration, which places doubt on the applicability of the model. The estimated rate constants showed an Arrhenius temperature dependence, but the reaverse reaction rate constant only showed a weak linear correlation with temperature. The shortened fundamental model may be used as an initial estimate in the newly proposed method to calculate effective interfacial mass transfer area under conditions where surface depletion and renewal rates become significant. The fundamental model may then be solved using the results of the shortened fundamental model as initial guesses for the model optimization.

7.2 Conclusions from the Reactive Absorption Study

The reactive absorption of CO_2 into solutions of MEA/n-Propanol was investigated using a cylindrical wetted wall experimental set-up. Absorption rates were measured for two MEA concentrations (0.08M and 0.2M), two temperatures (25°C and 30°C), two column heights (60 mm and 90 mm) and three different liquid flow rates. The experiments were designed in order to study the reactive absorption of CO_2 into these MEA solutions under conditions where there is a degree of depletion of MEA in the liquid film. The liquid flow rates were varied to study the effect of liquid turbulence on the absorption rate, in order to get an idea of the effect of liquid turbulence on the surface renewal rate of MEA. The experiments were conducted in the fast reaction regime, meaning that the absorption rate is independent of the liquid side mass transfer coefficient and only dependent upon the available effective interfacial mass transfer area provided by the presence of MEA at the gas-liquid interface. A boundary layer theory investigation was done to estimate the gas phase resistance to mass transfer. The calculation revealed that there was a gas phase resistance of between 2 and 9% of the overall resistance. This study was, thus, conducted under conditions where the effective mass transfer area achieved on the wetted wall column was influenced by surface depletion and renewal rates of MEA. Both these effects occur simultaneously and it is difficult to distinguish between them.

It may be concluded that specific absorption rate is a function of temperature, CO_2 partial pressure, degree of surface depletion and the degree of liquid turbulence. Specific absorption decreases for an increase in temperature. This is partly due to the decrease in solubility of CO_2 with an increase in temperature. At longer column heights, the specific absorption rate of CO_2 decreases. This may be attributed to a degree of depletion of MEA in the liquid film for the longer liquid flow path, causing a decrease in the available effective area for absorption. At higher liquid flow rates, the increase in liquid turbulence causes an increase in interfacial renewal rate. This was especially noticeable for the higher MEA concentration investigated. It may be concluded that for a higher MEA concentration there is more MEA carried to the interface per volume during interfacial renewal, which contributes to the higher absorption rate

of CO_2. This may be attributed to the increase in effective area brought on by an increase in surface renewal rate.

An attempt was made to correlate the specific absorption rate of CO_2 into solutions of MEA/n-Porpanol with CO_2 partial pressure, MEA bulk liquid concentration and the liquid Reynolds number. The liquid Reynolds number was included in the correlation to account for surface renewal rates of MEA due to liquid turbulence. The correlation fitted the experimental data to within 35%, but mostly under predicted the data. It may be concluded that such a simple correlation cannot account for all the factors influencing the specific absorption rate during reactive absorption. A numerical solution strategy based on a concentration diffusion model incorporating fundamentally derived reaction kinetics is recommended. This model can account for both interfacial depletion and renewal of the liquid phase.

Image analysis of the gas-liquid interface revealed the wave motion noticed on the surface of the falling liquid film. All three types of waves commonly occurring on falling liquid films were identified, making image analysis a feasible method for estimating the interfacial area between the gas and liquid phase inside the wetted wall dome.

7.3 Novel Contributions

The novel contributions of this study may be summarised as follows:

1. A novel *in-situ* FTIR method was developed to study the homogeneous liquid phase reaction kinetics of CO_2 with the primary amine, mono-ethanolamine (MEA) in n-Propanol as alcoholic solvent. This method eliminates mass transfer influences when conducting reaction kinetic investigations for a reaction between gaseous CO_2 and the liquid phase primary amine. The semi-batch reactor set-up used in this study provides the means for controlling the rate of this fast reaction by controlling the feed rate of the amine to the reactor. The reaction progress from initiation to equilibrium can be monitored in real time by collecting concentration data of three of the reaction species (CO_2, MEA and one of the salt products) as a function of time. The reaction intermediate (zwitterion) is then calculated with a material balance.

2. A Matlab® based modelling algorithm was developed in this study to model the real time concentration data collected from the *in-situ* FTIR method. The real time concentration data collected with the FTIR method was firstly modelled on existing rate expressions. These expressions include power rate law kinetics and pseudo steady state hypothesis kinetics. These expressions are not rejected for use under conditions where MEA is in great excess. Two fundamentally derived rate expressions based on the zwitterion intermediate reaction mechanism provided good quality model fits of the experimental data. The rate constants of the fundamentally derived rate expression were found to be independent of concentration and showed an Arrhenius temperature relationship, which speaks to the fundamental correctness of the derived expression.
3. Reactive absorption rates of CO_2 into solutions of MEA/n-Propanol were measured on a wetted wall experimental set-up constructed in this study. The absorption rates were measured under conditions where a fast reaction in the liquid film may be assumed to occur. Under these conditions (with insignificant gas phase mass transfer resistance) the absorption rate is controlled by the reaction kinetics in the liquid phase and since a fast reaction regime is applicable, the absorption rate is only dependent upon the effective area available for mass transfer. Absorption experiments were performed under conditions where surface depletion of MEA occurs. The absorption data, therefore, represents data that may be used to study the effect of surface renewal rate in the liquid film on the effective area available for mass transfer. In order to be able to interpret the surface renewal rate data correctly, the fundamental rate expression derived in this study may be used in a numerically based technique to calculate the effective area of the wetted wall.
4. An image analysis method was developed in this study to monitor the wave action on the surface of the liquid film flowing down the wetted wall column. From the surface profiles obtained, the true gas-liquid interfacial area may be estimated more accurately. This will shed light on the ratio of interfacial area to effective interfacial area available under conditions where surface depletion and renewal rates are significant.

7.4 Recommended Future Work

Based on the conclusion drawn from this study, possible future work was identified. Regarding the reaction kinetic study, FTIR may be used to derive the reaction kinetics of CO_2 with other primary amines in solvents (including aqueous solvents) of varying liquid properties. This is important, since effective interfacial mass transfer area is a function of liquid properties and the newly proposed method requires the reaction kinetics to be known. Based on the comparative study on the existing effective area correlations (see section 5.3) the effect of liquid viscosity on effective area should be investigated first. This will be best achieved under conditions where surface depletion and renewal rates are significant. The fundamentally derived reaction rate expressions will have to be used in a numerical method to calculate effective area.

The foundation for such a numerical method for the calculation of the effective interfacial mass transfer area of both random and structured packing has been laid in this body of work. The solution strategy using Matlab® is described in detail in Appendix B. One of the disadvantages of using Matlab® is that the optimization of the solution mesh is complicated to perform. This is why a numerical solution was not yet obtained at the conclusion of this body of work. Other software packages such as openFOAM™ has built-in mesh optimisation tools. At the conclusion of this body of work, openFOAM™ was not yet taken into consideration, but since it has the advantage of mesh optimisation, it will be used in future work to obtain a numerical solution for effective area from absorption data. The method must be validated using a pseudo first order reaction system as reference data. The physiochemical properties required for the initial and boundary condition values of the new method may be obtained from the N_2O analogy by performing N_2O absorption experiments using the wetted wall column set-up.

The specific absorption rates of CO_2 into solvents of different physical properties should be measured using the wetted wall column developed in this study. The effect of surface depletion and renewal rates should be further investigated by varying the CO_2 partial pressures, amine concentrations, liquid flow rates and liquid properties such as density, surface tension and especially viscosity. The gas phase resistance encountered in the wetted wall experimental

set-up should also be measured with the use of an absorption method that is controlled by the gas film. A reactive absorption process under infinitely fast reaction conditions in the liquid film will be suitable.

The image analysis of the gas-liquid interface should be investigated further. From the wave profiles on the liquid surface, a closer approximation of the actual gas-liquid interface may be derived. This will aid in understanding the effect that liquid turbulence has on the absorption rate and the increased effective interfacial area created by it. The effect of gas flow rate on the interfacial waves must also be investigated.

It is finally recommended that the newly proposed method be used to calculate the effective area of separation column internals such as random and structured packing based on reactive absorption rates measured over short packed bed heights. The absorption experiments should be designed to encapsulate both a system where no interfacial depletion is noticed and a system of appreciable interfacial depletion. These systems can both be solved using the fundamental or shortened fundamental rate expressions derived in this study, but for model simplicity, the pseudo first order rate expression may be used under conditions of no interfacial depletion. The liquid properties of the test systems should be varied to be able to derive a correlation between the liquid properties, the degree of surface depletion and the effective interfacial mass transfer area made available by the column internal under these conditions.

References

Aboudheir, A., Tontiwachwuthikul, P., Chakma, A. & Idem, R., 2003. Kinetics of the Reactive Absorption of Carbon Dioxide in High CO2-loaded, Concentrated Aqueous Monoethanolamine Solutions. *Chemical Engineering Science,* Volume 58, pp. 5195 - 5210.

Aboudheir, A., Tontiwachwuthikul, P., Chakma, A. & Idem, R., 2003. On the Numerical Modeling of Gas Absorption into Reactive Liquids in a Laminar Jet Absorber. *Can. Jour. Chem. Eng.,* Volume 81, pp. 604 - 612.

Aferka, S., Marchot, P., Crine, M. & Toye, D., 2010. Interfacial Area Measurement in a Catalytic Distillation Packing Using High Energy X-ray CT. *Chem. Eng. Sci.,* Volume 65, pp. 511 - 516.

Alekseenko, S. et al., 2009. Primary Instabilities of Liquid Film Flow Sheared by Turbulent Gas Stream. *Int. Journ. Multiphase Flow,* Volume 35, pp. 617 - 627.

Alvarez-Fuster, C., Midoux, N., Laurent, A. & Charpentier, J., 1980. Chemical Kinetics of the Reaction of Carbon Dioxide with Amines in Pseudo m-nth order Conditions in Aqueous and Organic Solutions. *Chem. Eng. Sci.,* Volume 35, pp. 1717 - 1723.

Alvarez-Fuster, C., Midoux, N., Laurent, A. & Charpentier, J. C., 1981. Chemical Kinetics of the Reaction of CO2 with Amines in Pseudo m-nth order Conditions in Polar and Viscous Organic Solutions. *Chemical Engineering Science,* Volume 9, pp. 1513-1518.

Aruldhas, G., 2007. *Molecular Structure and Spectroscopy.* 2nd ed. India: Prentice Hall .

Astarita, G., 1967. *Mass Transfer with Chemical Reaction.* Amsterdam: Elsevier.

Axiom, A., 2010. *Instruction Manual DPR-207 ATR Immersion Probes,* Tustin, CA USA: Axiom Analytical Inc..

Banerjee, S., Rhodes, E. & Scott, D., 1967. Mass Transfer to Falling Wavy Liquid Films at Low Reynolds Numbers. *Chem. Eng. Sci.,* Volume 22, pp. 43 - 48.

Barakat, H. & Clark, J., 1966. On the Solution of the Diffusion Equation by Numerical Methods. *J. Heat Transfer, Trans. ASME,* Volume 88, pp. 421 - 427.

Barth, D., Tondre, C. & Delpuech, J., 1984. Kinetics and Mechanisms of the Reactions of Carbon Dioxide with Alkanolamies: A Discussion Concerning the Cases of MDEA and DEA. *Chemical Engineering Science,* Volume 12, pp. 1753-1757.

Bellamy, L., 1976. *The Infra-Red Spectra of Complex Molecules: Volume 1.* 3rd ed. s.l.:Wiley.

Billet, R., 1995. *Packed Towers in Processing and Environmental Technology.* Weinheim: VCH.

Billet, R. & Schultes, M., 1993. Predicting Mass Transfer in Packed Columns. *Chem. Eng. Technol.,* Volume 16, pp. 1 - 9.

Bird, R., Stewart, W. & Lightfoot, E., 2002. *Transport Phenomena.* 2nd ed. New York: J. Wiley.

Bosch, H., Versteeg, G. & van Swaaij, W., 1989. Gas-Liquid Mass Transfer with Parallel Reversible Reactions-I. Absorption of CO2 into Solutions of Sterically Hindered Amines. *Chem. Eng. Sci.,* Volume 44, pp. 2723-2734.

Bravo, J., Rocha, J. & Fair, J., 1985. Mass Transfer in Gauze Packings. *Hydrocarbon Process,* Volume 64, pp. 91 - 95.

Brayton, R., Director, S., Hachtel, G. & Vidigal, L., 1979. A New Algorithm for Statistical Circuit Design BAsed on Quasi-Newton Methods and Function Splitting. *IEEE Transactions on Circuits and Systems,* Volume 26, pp. 784 - 794.

Brinkmann, M., Schafer, M., Warnecke, H.-J. & Pruss, J., 1998. Modelling Reactive Absorption Processes via Film-renewal Theory: Numerical Scheme and Simulation Results. *Computers Chem. Engng,* Volume 22, pp. 515-524.

Brunazzi, E., Nardini, G., Paglianti, A. & Petarca, L., 1995. Interfacial Area of Mellapak Packing: Absorption of 1,1,1-trichloroethane by Gensorb 300. *Chem. Eng. Technol.,* Volume 18, pp. 248 - 255.

Brunazzi, E. & Paglianti, A., 1997. Liquid-film Mass Transfer Coefficient in a Column Equipped with Structured Packing. *Ind. Eng. Chem. Res.,* Volume 36, p. 3792.

Caplow, M., 1968. Kinetics of Carbamate Formation and Breakdown. *Journal of the American Chemical Society,* Volume 90, pp. 6795 - 6803.

Carter, C. et al., 2010. ReactIR Flow Cell: A New Analytical Tool for Continuous Flow Chemical Processing. *Organic Process Research & Development,* Volume 14, p. 393.

Charpentier, J. C., 1981. Mass Transfer Rates in Gas-Liquid Absorbers. In: T. B. Drew, ed. *Advances in Chemical Engineering.* New York: Elsevier, pp. 2-133.

Chen, S., Lei, Q. & Fang, W., 2005. Viscosities and Densities for Binary Mixtures of N-methylpiperazine with Methanol, Ethanol, n-Propanol, iso-Propanol, n-Butanol and iso-Butanol at 293.15, 298.15 and 303.15 K. *Fluid Phase Equil.,* Volume 234, pp. 22 - 33.

Crooks, J. & Donnellan, J., 1989. Kinetics and Mechanism of the Reaction between Carbon Dioxide and Amines in Aqueous Solution. *Journal of Chemical Society of Perkin Transactions ,* Volume II, pp. 331 - 333.

Cummings, A. et al., 1990. An Analytical Method for Determining Bound and Free Alkanolamines in Heat Stable Salt Contaminated Solutions. *AICHE Summer National Meeting Symposium on Gas Processing.*

Danckwerts, P., 1979. The Reaction of CO2 with Ethanolamines. *Chemical Engineering Science,* Volume 34, pp. 443-446.

Danckwerts, P., Kennedy, A. & Roberts, D., 1963. Kinetics of CO2 Absorption in Alkaline Solutions - II Absorption in a Packed Column and Tests of Surface-renewal Models. *Chem. Eng. Sci.,* Volume 18, pp. 63-72.

Danckwerts, P. V., 1951. Significance of Liquid-Film Coefficients in Gas Absorption. *Industrial Engineering Chemistry,* Volume 43, pp. 1460-1467.

Danckwerts, P. V., 1970. *Gas-Liquid Reactions.* New York: McGraw-Hill.

Danckwerts, P. V., 1979. The Reaction of CO2 with Ethanolamines. *Chemical Engineering Science,* Volume 34, pp. 443-446.

Dandapat, B. & Mukhopadhyay, A., 2003. Waves on the Surface of a Falling Power-law Fluid Film. *Int. Journ. Non-Linear Mech.,* Volume 38, pp. 21 - 38.

Davis, R. & Sandall, O., 1993. Kinetics of the Reaction of Carbon Dioxide with Secondary Amines in Polyethalene Glycol. *Chemical Engineering Science,* Volume 48, pp. 3187-3193.

de Brito, M. et al., 1994. Effective Mass-Transfer Area in a Pilot Plant Column Equipped with Structured Packings and with Ceramic Rings. *Ind. Eng. Chem. Res.,* Volume 33, pp. 647 - 656.

DeCoursey, W., 1982. Enhancement Factors for Gas Absorption with Reversible Reaction. *Chem. Eng. Sci,* Volume 37, pp. 1483-1489.

Del Carlo, L., Olujic, Z. & Paglianti, A., 2006. Comprehensive Mass Transfer Model for Distillation Columns Equipped with Structured Packings. *Ind. Eng. Chem. Res.,* Volume 45, pp. 7967 - 7976.

Derks, P. et al., 2011. Determination of the Liquid-Phase Speciation in the MDEA-H2O-CO2 System. *Energy Procedia,* Volume 4, pp. 599 - 605.

Dodd, J. a. D. L., 2002. Curve-fitting: Modeling Spectra. In: *Spectral Enhancement and Band Resolution Techniques.* NY: John Wiley & Sons Ltd, pp. 2215 - 2223.

Dragan, M., Dragan, S. & Siminiceanu, I., 2000. Characterisation of Mellapak 750Y Structured Packing Determining the Effective Mass Transfer Area. *Studia Universitatis Babs-Bolyai, Chemia,* Volume 45, pp. 11 - 22.

Du Preez, L., Schwarz, C. & Knoetze, J., 2009. *Evaluating Reaction Rate Expressions for CO2 and MEA in 2-Propanol.* Presentation at the 8th World Congress of Chemical Engineering, Montreal, Canada, s.n.

Erasmus, A., 2004. *Mass Transfer in Structured Packing,* Stellenbosch: PhD Dissertation: University Stellenbosch.

Fair, J. & Bravo, J., 1990. Distillation Columns Containing Structured Packing. *Chem. Eng. Prog,* Volume 86, pp. 19 - 29.

Fogler, H., 1999. *Elements of Chemical Reaction Engineering.* 3rd ed. U.S.A: Prentice Hall.

Gembicki, F., 1974. *Vector Optimization for Control Performance and Parameter Sensitivity Indices,* Cleveland, Ohio: PhD Dissertation: Case Western Reserve University.

Green, W. et al., 2007. Novel Application of X-ray Computed Tomography: Determination of Gas/Liquid Contact Area and Liquid Holdup in Structured Packing. *Ind. Eng. Chem. Res.,* Volume 46, pp. 5734 - 5753.

Grffiths, P., 2002. Beer's Law. In: *Quantitive Analysis.* s.l.:Wiley & Sons Ltd, pp. 2225 - 2231.

Haroun, Y., Legendre, D. & Raynal, L., 2010. Direct Numerical Simulation of REactive Absorption in Gas-Liquid Flow on Structured Packing Using Interface Capturing Method. *Chem. Eng. Sci,* Volume 65, pp. 351 - 356.

Haroun, Y., Raynal, L. & Legendre, D., 2012. Mass Transfer and Liquid Hold-up Determination in Structured Packing by CFD. *Chem. Eng. Sci.,* Volume 75, pp. 342 - 348.

Higbie, R., 1935. The Rate of Absorption of A Pure Gas in A Still Liquid During Short Periods of Exposure. *Transactions of the American Institute of Chemical Engineers,* Volume 31, pp. 365-389.

Hikita, H., Asai, S., Ishikawa, H. & Honda, M., 1976. The Kinetics of Reaction of Carbon Dioxide with Monoethanolamine, Diethanolamine and Triethanolamine by a Rapid Mixing Method. *The Chemical Engineering Journal,* Volume 13, pp. 7-12.

Incropera, F. & De Witt, D., 2002. *Fundamentals of Heat and Mass Transfer.* 5th ed. Hoboken, NJ: John Wiley & Sons.

Jackson, P., Robinson, K., Puxty, G. & Attalla, M., 2009. In situ Fourier Transform-Infrared (FT-IR) Analysis of Carbon Dioxide Absorption and Desorption in Amine Solutions. *Energy Procedia,* Volume 1, pp. 985 - 994.

Johnson, T., Simon, A., Weil, J. & Harris, G., 1993. Applications of Time-Resolved Step-Scan and Rapid-Scan FT-IR Spectroscopy: Dynamics from Ten Seconds to Ten Nanoseconds. *Applied Spectroscopy,* 47(9), pp. 1376 - 1381.

Joosten, G. H. & Danckwerts, P., 1973. Chemical reaction and effective interfacial areas in gas absorption. *Chemical Engineering Science,* Volume 28, pp. 453-461.

Kapadi, U., Hundiwale, D., Patil, N. & Lande, M., 2002. Viscosities, Excess Molar Volume of Binary Mixtures of Ethanolamine with Water at 303.15, 308.15, 313.15 and 318.15 K. *Fluid Phase Equil.,* Volume 201, pp. 335 - 341.

Kil, S., Kim, S. & Lee, S., 2001. Wave Characteristics of Falling Liquid Film on a Vertical Circular Tube. *Int. Jour. Refrigeration,* Volume 24, pp. 500 - 509.

King, C. J., 1966. Turbulent Liquid Phase Mass Transfer at a Free Gas-Liquid Interface. *Industrial Engineering Chemical Fundamentals,* Volume 5, pp. 1-8.

Kister, H., 1992. *Distillation Design.* New York: McGraw-Hill.

Krishnan, M. & Flanagan, D., 2000. FTIR-ATR spectroscopy for Monitoring Polyanhydride/anhydride-amine Reactions. *Journal of Controlled Release,* Volume 69, pp. 273 - 281.

Kritzinger, L., 2013. *Establishing a Pilot Plant Facility for Post Combustion Carbon Dioxide Capture Studies,* Stellenbosch: MSc Dissertation: University Stellenbosch.

Laddha, S. & Danckwerts, P., 1981. Reaction of CO2 with Ethanolamines: Kinetics from Gas Absorption. *Chem. Eng. Sci.,* Volume 36, pp. 479 - 482.

Laddha, S., Diaz, J. & Danckwerts, P., 1980. The N2O Analogy: The solubility of CO2 and N2O in Aqueous Solutions of Organic Compounds. *Chem. Eng. Sci.,* Volume 36, pp. 228 - 229.

Lamourelle, A. & Sandall, O., 1972. Gas Absorption into a Turbulent Liquid. *Chem. Eng. Sci.,* Volume 27, pp. 1035 - 1043.

Lamprecht, S., 2010. *Establishing a Facility to Measure Packed Column Hydrodynamics,* Stellenbosch: MSc Dissertation: University Stellenbosch.

Lewis, W. K. & Whitman, W. G., 1924. Principles of Gas Absorption. *Industrial Engineering Chemistry,* Volume 16, pp. 1215-1220.

Li, M.-H. & Lai, M.-D., 1995. Solubility of N2O and CO2 in (Monoethanolamine + N-Methyldiethanolamine + Water) and (Monoethanolamine + 2-Amino-2-methyl-1-propanol + Water). *J. Chem. Eng. Data,* Volume 40, pp. 486-492.

Littel, R., Versteeg, G. & van Swaaij, W., 1991. Physical Absorption in Non-aqueous Solutions in a Stirred Cell Reactor. *Chem. Eng. Sci.,* Volume 46, pp. 3308 - 3313.

Littel, R., Versteeg, G. & van Swaaij, W., 1992(a). Kinetics of CO2 with Primary and Secondary Amines in Aqueous Solutions - I. Zwitterion Deprotonation Kinetics for DEA and DIPA in Aqueous Blends of Alkanolamines. *Chemical Engineering Science,* Volume 8, pp. 2027 - 2035.

Littel, R., Versteeg, G. & van Swaaij, W., 1992(b). Kinetics of CO2 with Primary and Secondary Amines in Aquous Solutions - II. Influence of Temperature on Zwitterion Formation and Deprotonation Rates. *Chemical Engineering Science,* Volume 47, pp. 2037 - 2045.

Lockett, M., 1986. *Distillation Tray Fundamentals.* Cambridge: Cambridge University Press.

Luo, X., Hartono, A. & Svendsen, H., 2012. Comparative Kinetics of Carbon Dioxide Absorption in Unloaded Aqueous Monoethanolamine Solutions Using Wetted Wall and String of Discs Columns. *Chem. Eng. Sci,* Volume 82, pp. 31 - 43.

Mahr, B. & Mewes, D., 2007. CFD Modelling and Calculation of Dynamic Two-phase Flow in Columns Equipped with Structured Packing. *Chem. Eng. Res. Des.,* Volume 85, pp. 1112 - 1122.

McMurry, J., 2004. *Organic Chemistry.* 6th ed. Belmont, U.S.A.: Brooks/Cole.

Meldon, J., Olawoyin, O. & Bonanno, D., 2007. Analysis of Mass Transfer with Reversible Chemical Reaction. *Ind. Eng. Chem. Res.,* Volume 46, pp. 6140-6146.

Motin, M., Hafiz Mia, M. & Nasimul Islam, A., 2012. Thermodynamic Properties of Sodium Dodecyl Sulfate Aqueous Solutions with Methanol, Ethanol, n-Propanol and iso-Propanol at Different Temperatures. *Journ. Saudi Chem So.,* p. Article in Press.

Neelakantan, K. & Gehlawat, J., 1982. New Chemical Systems for the Determination of Liquid-Side Mass Transfer Coefficient and Effective Interfacial Area in Gas-Liquid Contactors. *Chem. Eng. Jour.,* Volume 24, pp. 1-6.

Neelakantan, K. & Gehlawat, J., 1982. New Chemical Systems for the Determination of Liquid-Side Mass Transfer Coefficient and Effective Interfacial Area in Gas-Liquid Contactors. *Chem. Eng. Jour.,* Volume 24, pp. 1 - 6.

Olujic, Z., 1981. Compute Friction Factors Fast for Flow in Pipes. *Chem. Eng.,* Volume 88, pp. 91 - 93.

Olujic, Z., Behrens, M., Colli, L. & Paglianti, A., 2004. Predicting the Efficiency of Corrugated Sheet Structured Packings with Large Specific Surface Area. *Chem. Biochem. Eng. Q.,* Volume 18, pp. 89 - 96.

Olujic, Z. et al., 2001. Stretching the Capacity of Structured Packings. *Ind. Eng. Chem. Res.,* Volume 40, pp. 6172 - 6180.

Olujic, Z., Kamerbeek, A. B. & de Graaw, J., 1999. A corrugation geometry based model for efficiency of structured ditillation packing. *Chemical Engineering and Processing,* Volume 38, pp. 683-695.

Onda, K., Sada, E., Kobayashi, T. & Fujine, M., 1972. Gas Absorption Accompanied by Complex Chemical Reactions-IV Unsteady State. *Chem. Eng. Sci.,* Volume 27, pp. 247-255.

Onda, K., Takeuchi, H. & Okumoto, Y., 1968. Mass Transfer Coefficients Between Gas and Liquid Phases in Packed Columns. *J. Chem. Eng. Jpn.,* Volume 1, pp. 56 - 62.

Oron, A., Gottlieb, O. & Novbari, E., 2009. Numerical Analysis of a Weighted-residual Integral Boundary-layer Model for Nonlinear Dynamics of Falling Liquid Films. *Eur. Journ. Mech. B/Fluids,* Volume 28, pp. 1 - 36.

Owens, S., Kossmann, A., Farone, J. & Eldridge, R., 2009. Flow Field Visualization in Structured Packing Using Real Time X-ray Radiography. *Ind. Eng. Chem. Res.,* Volume 48, pp. 3606 - 3618.

Oyevaar, M., Morssinkhof, R. & Westerterp, K., 1989. Density, Viscosity, Solubility and Diffusivity of CO2 and N2O in Solutions of Diethanolamine in Aqueous Ethylene Glycol at 298 K. *J. Chem. Eng. Data,* Volume 34, pp. 77 - 82.

Pandita, S. et al., 2012. Simultaneous DCS-FTIR Spectroscopy: Comparison of Cross-linking Kinetics of an Epoxy/Amine Resin System. *Therm. Acta,* Volume 543, pp. 9 -17.

Parikh, S., Lafferty, B. & Sparks, D., 2008. An ATR-FTIR spectroscopic Approach for Measuring Rapid Kinetics at the Mineral/Water Interface. *Journal of Colloid and Interf. Sci.,* Volume 320, pp. 177 - 185.

Patil, G., Vaidya, P. & Kenig, E., 2011. Reaction Kinetics of CO2 in Aqueous Methyl- and Dimethylmonoethanolamine Solutions. *Ind. Eng. Chem. Res.,* Volume 51, pp. 1592 - 1600.

Pierson, F. & Whitaker, S., 1977. Some Theoretical and Experimental Observations of the Wave Structure of Falling Liquid Films. *Ind. Eng. Chem. Fundam.,* Volume 16, pp. 401 - 408.

PIKE, 2013. *ATR Crystal Selection.* [Online] Available at: http://www.piketech.com/ATR-Crystal-Selection.html [Accessed 1 August 2013].

Pohorecki, R. & Moniuk, W., 1988. Kinetics of Reaction between Carbon Dioxide and Hydroxyl Ions in Aqueous Electrolyte Solutions. *Chem. Eng. Sci.,* Volume 43, pp. 1677 - 1684.

Portalski, S. & Clegg, A., 1971. Interfacial Area Increase in Rippled Film Flow on Wetted Wall Columns. *Chem. Eng. Sci.,* Volume 26, pp. 773 - 784.

Portalski, S. & Clegg, A., 1972. An experimental Study of Wave Inception on Falling Liquid Films. *Chem. Eng. Sci.,* Volume 27, pp. 1257 - 1265.

Puranik, S. & Sharma, M., 1970. Effective Interfacial Area in Packed Liquid Extraction Columns. *Chem. Eng. Sci.,* Volume 25, pp. 257 - 266.

Reid, C. & Sherwood, T., 1966. *The Properties of Gases and Liquids - Their Estimation and Correlation.* 2nd ed. New York San Francisco Toronto London Sydney: McGraw-Hill Book Company.

Riazi, M., 1996. Modeling of Gas Absorption into Turbulent Films with Chemical Reaction. *Gas. Sep. Purif.,* Volume 10, pp. 41 - 46.

Richner, G. & Puxty, G., 2012. Assessing the Chemical Speciation during CO2 Absorption by Aqueous Amines Using in situ FTIR. *Ind. Eng. Chem. Res.,* Volume 51, pp. 14317 - 14324.

Rocha, J., Bravo, J. & Fair, J., 1996. Distillation Columns Containing Structured Packings: A Comprehensive Model for Their Performance. 2. Mass Transfer Model. *Ind. Eng. Chem. Res.,* Volume 35, pp. 1660 - 1667.

Sada, E., Kumazawa, H. & Han, Z. Q., 1985. Kinetics of Reaction Between Carbon Dioxide and Ethylenediamine in Non-aqueous Solvents. *The Chemical Engineering Journal,* Volume 31, pp. 109-115.

Sada, E. et al., 1986. Reaction Kinetics of Carbon Dioxide with Amines in Non-aqueous Solvents. *The Chemical Engineering Journal,* Volume 33, pp. 87 - 95.

Salazar, R. & Marschall, E., 1978. Three-Dimensional Surface Characteristics of a Falling Liquid Film. *Int. J. Multiphase Flow,* Volume 4, pp. 487 - 496.

Scherzer, T. & Decker, U., 1999. Real-time FTIR-ATR Spectroscopy to Study the Kinetics of Ultrafast Photopolymerisation Reactions Induced by Monochromatic UV Light. *Vibrational Spectroscopy,* Volume 19, pp. 385 - 398.

Schultes, M., Chambers, S. & Fleming, B., 2010. *Commercial Scale Test Validation of Modern High Performance Random and Structured Packings for CO2 Capture Ranking.* de Haan, D&A Conference.

Schwarz, C. & Nieuwoudt, I., 2003. Phase Equilibrium of Propane and Alkanes Part I. Experimental Procedures, Dotriacontane Equilibrium and EOS Modelling. *J. of Supercritical Fluids,* Volume 27, pp. 133 - 144.

Seader, J. & Henley, E., 1998. *Separation Process Principles.* 10 ed. New Jersey: John Wiley & Sons, Inc.

Shabani, A., Asl, S. & Shahkraki, B., 2010. Calculation of Effective Interfacial Area in a Turbulent Contact Absorber. *Int. Jour. Chem Eng. App.,* Volume 1, pp. 117 - 122.

Sherman Hsu, C., 1997. Chapter 15 Infrared Spectroscopy. In: *Handbook for Instrumental Techniques for Analytical Chemistry.* U.S.A: Prentice Hall PTR.

Sherwood, T., Pigford, R. & Wilke, C., 1975. *Mass Transfer.* New York: McGraw-Hill.

Shetty, S. & Cerro, R., 1993. Flow of a Thin Film Over a Periodic Surface. *Int. J. Multiphase Flow,* Volume 19, pp. 1013 - 1027.

Shetty, S. & Cerro, R., 1995. Spreading of a Liquid Point Source over Inclined Solid Surfaces. *Ind. Eng. Chem. Res.,* Volume 34, pp. 4078 - 4086.

Shetty, S. & Cerro, R., 1997. Fundamental Liquid Flow Correlations for the Computation of Design Parameters for Ordered Packings. *Industrial Engineering Chemistry Research,* Volume 36, pp. 771 - 783.

Shetty, S. & Cerro, R., 1998. Spreading of a Liquid Point Source over a Complex Surface. *Ind. Eng. Chem. Res.,* Volume 37, pp. 626 - 635.

Shi, M. G. & Mersmann, A., 1985. Effective Interfacial Area in Packed Columns. *German Chemical Engineering,* Volume 8, pp. 87-96.

Shojaee, S., Hosseini, S., Rafati, A. & Ahmadi, G., 2011. Prediction of the Effective Area in Structured Packings by Computanional Fluid Dynamics. *Ind. Eng. Chem. Res.,* Volume 50, pp. 10833 - 10842.

Shultes, M., 2010. *Research on Mass Transfer Columns "Old Hat or Still Relevant?".* Eindhoven, Distillation Absorption Conference.

Silverstein, R. & Bassler, G., 1967. *Spectrometric Identification of Organic Compounds.* 2nd ed. s.l.:Wiley.

Sridharan, K. & Sharma, M. M., 1976. New Systems and Methods for the Measurement of Effective Interfacial Area and Mass Transfer Coefficients in Gas-Liquid Contactors. *Chemical Engineering Science,* Volume 31, pp. 767-774.

Suess, P. & Spiegel, L., 1992. Holdup of Mellapak Structured Packings. *Chem. Eng. Process.,* Volume 32, pp. 119 - 124.

Telles, A. & Dukler, A., 1970. Statistical Characteristics of Thin, Vertical, Wavy, Liquid Films. *Ind. Eng. Chem. Fundam.,* Volume 9, pp. 412 - 421.

Tokunaga, J., 1975. Solubilities of Oxygen, Nitrogen and Carbon Dioxide in Aqueous Alcohol Solutions. *Jour. Chem. Eng. Data,* Volume 20, pp. 41 - 46.

Tsai, R., 2010. *Mass Transfer Area of Structured Packing,* PhD Dissertation, Austin: University of Texas.

Tsai, R. et al., 2008. Influence of Surface Tension on Effective Packing Area. *Industrial Engineering Chemistry Research,* Volume 47, pp. 1253-1260.

Valtz, A., Teodorescu, M., Wichterle, I. & Richon, D., 2004. Liquid Densities and Excess Molar Volumes for Water+Diethylene Glycolamine, and Water, Methanol, Ethanol, 1-Propanol+Triethylene Glycol Binary Systems at Atmospheric Pressure and Temperature in the Range of 283.15 - 363.15 K. *Fluid Phase Equilibria,* Volume 215, pp. 129 - 142.

Van Meurs, N. & Dahmen, E., 1959. Conductometric and Potentiometric Titrations of Nitrogen Bases in Non-aqueous Solvents. *Analytica Chimica Acta,* Volume 21, p. 193.

Van Swaaij, W. & Versteeg, G., 1992. Mass Transfer Accompanied with Complex Reversible Chemical REactions in Gas-Liquid Systems: An Overview. *Chem. Eng. Sci,* Volume 47, pp. 3181-3195.

Vas Bhat, R., Kuipers, J. & Versteeg, G., 2000. Mass Transfer with Complex Chemical Reactions in Gas-liquid Systems: Two-step Reversible Reactions with Unit Stoichiometric and Kinetic Orders. *Chem. Eng. Jour.,* Volume 76, pp. 127-152.

Vas Bhat, R. et al., 1997. Non-isothermal Gas Absorption with Reversible Chemical Reaction. *Chem. Eng. Sci.,* Volume 52, pp. 4079-4094.

Versteeg, G. F. & van Swaaij, W. M., 1988. On the Kinetics Between CO2 and Alkanolamines Both in Aqueous and Non-aqueous Solutions - I. Primary and Secondary Amines. *Chemical Engineering Science,* Volume 43, pp. 573-585.

Versteeg, G., Kuipers, J., Van Beckum, F. & van Swaaij, W., 1990. Mass Transfer with Complex Reversible Chemical Reactions - II Parallel Reversible Chemical Reactions. *Chem. Eng. Sci.,* Volume 45, pp. 183 - 197.

Versteeg, G. & van Swaaij, P., 1988(b). On the Kinetics between CO2 and Alkanolamines both in Aqueous and Non-aqueous solutions - II. Tertiary Amines. *Chemical Engineering Science,* Volume 43, pp. 573 - 585.

Wang, G. Q., Yuan, X. G. & Yu, K. T., 2005. Review of Mass-Transfer Correlations for Packed Columns. *Industrial Engineering Chemistry Research,* Volume 44, pp. 8715 - 8729.

Wang, Y., Xu, S., Otto, F. & Mather, A., 1992. Solubility of N2O in Alkanolamines and in Mixed Solvents. *Chem. Eng. Jour.,* Volume 48, pp. 31 - 40.

Xu, Z., Wang, S. & Chen, C., 2013. Solubility of N2O in and Density and Viscosity of Aqueous Solutions of 1,4-Butanediamine, 2-(Diethylamino)-ethanol, and Their Mixtures From (298.15 to 333.15) K. *J. Chem. Eng. Data,* Volume 58, pp. 1633 - 1640.

Yu, L.-M., Zeng, A.-W. & Yu, K., 2006. Effect of Interfacial Velocity Fluctuations on the Enhancement of the Mass-Transfer Process in Falling-Film Flow. *Ind. Eng. Chem. Res.,* Volume 45, pp. 1201 - 1210.

Zhi, Q. & Kai, G., 2009. Modeling and Kinetic Study on Absorption of CO2 by Aqueous Solutions of N-methyldiethanolamine in a Modified Wetted Wall Column. *Chi. Jour. Chem. Eng.,* Volume 17, pp. 571 - 579.

Appendix

Table of Contents

Appendix A Property Data and Sample Calculations 265

Appendix B Basis for a New Effective Area Theory and Numerical Method of Calculation 273

Appendix C Mechanical Drawings and Schematics of the Equipment Used 290

Appendix D Equipment Specifications 294

Appendix E Data of the Reaction Kinetic Study 304

Appendix F Data of The Reactive Absorption Study 310

List of Figures

Figure A 1 Gas Phase Boundary Layer Profile 270

Figure B 1 Expected Concentration Profiles based on a Solution using the Shortened Fundamental Model 283

Figure C 1 Dimensioned Mechanical Drawing of Semi-batch Reactor 291

Figure C 2 Dimensioned Mechanical Drawing of Wetted Wall 292

Figure C 3 Dimensioned Mechanical Drawing of Wetted Wall Exit Collar 293

List of Tables

Table A 1 Pure Species Properties of MEA (Wang, et al., 1992; Kapadi, et al., 2002) 265

Table A 2 Pure Species Properties of n-Propanol (Motin, et al., 2012; Chen, et al., 2005; Valtz, et al., 2004) 265

Table A 3 Properties of MEA/n-Propanol Solutions 266

Table A 6 Gas Phase Physical Properties Used in Boundary Layer Calculations (Reid & Sherwood, 1966) 269

Table A 7 Gas Phase Resistance from Boundary Layer Theory for the Absorption of CO_2 into 0.2 M MEA solutions at 25°C on the Wetted Wall 272

Table B 1 Diffusivities Used in the Partial Differential Equations of Section B.1.1 278

Table B 2 Solubility Data Used in the Partial Differential Equations of Section B.1.1 279

Table B 3 Molal Volumes 287

Table B 4 Calculated Diffusivities 287

Table B 5 Solubility Data for CO_2 and N_2O 288

Table B 6 Diffusivity and Solubility Data to be used as Initial and Boundary Condition Values 288

Table B 7 Bulk Liquid Concentrations to be used as Initial and Boundary Condition Values 289

Table E 1 Experimental Parameters for n-Propanol 305

Table E 2 Fundamental Model Estimated Rate Constants for Experimental Run# 25_5_1 306

Table E 3 Fundamental Model Estimated Rate Constants for Experimental Run# 25_5_2 306

Table E 4 Fundamental Model Estimated Rate Constants for Experimental Run# 25_5_3 306

Table E 5 Fundamental Model Estimated Rate Constants for Experimental Run# 25_10_1 306

Table E 6 Fundamental Model Estimated Rate Constants for Experimental Run# 25_10_2 307

Table E 7 Fundamental Model Estimated Rate Constants for Experimental Run# 25_10_3 307

Table E 8 Fundamental Model Estimated Rate Constants for Experimental Run# 30_5_1 307

Table E 9 Fundamental Model Estimated Rate Constants for Experimental Run# 30_5_2 307

Table E 10 Fundamental Model Estimated Rate Constants for Experimental Run# 30_5_3 307

Table E 11 Fundamental Model Estimated Rate Constants for Experimental Run# 30_10_1 .. 308

Table E 12 Fundamental Model Estimated Rate Constants for Experimental Run# 30_10_2 .. 308

Table E 13 Fundamental Model Estimated Rate Constants for Experimental Run# 30_10_3 .. 308

Table E 14 Fundamental Model Estimated Rate Constants for Experimental Run# 35_5_1 308

Table E 15 Fundamental Model Estimated Rate Constants for Experimental Run# 35_5_2 308

Table E 16 Fundamental Model Estimated Rate Constants for Experimental Run# 35_5_3.... 309

Table E 17 Fundamental Model Estimated Rate Constants for Experimental Run# 35_10_1.. 309

Table E 18 Fundamental Model Estimated Rate Constants for Experimental Run# 35_10_2.. 309

Table E 19 Fundamental Model Estimated Rate Constants for Experimental Run# 35_10_3.. 309

Table F 1 Reactive Absorption Data for [MEA] = 0.2 mol/dm^3, T = 25°C, P = 104 kPa..... 310

Table F 2 Reactive Absorption Data for [MEA] = 0.2 mol/dm^3, T = 30°C, P = 104 kPa..... 310

Table F 3 Reactive Absorption Data for [MEA] = 0.08 mol/dm^3, T = 25°C, P = 104 kPa..... 311

Table F 4 Reactive Absorption Data for [MEA] = 0.08 mol/dm^3, T = 30°C, P = 104 kPa..... 311

Appendix A PROPERTY DATA AND SAMPLE CALCULATIONS

A.1 Species Properties

The pure species properties of the liquids used in this study are tabulated in **Table A 1** – **Table A 2** Pure Species Properties of n-Propanol (Motin, et al., 2012; Chen, et al., 2005).

Table A 1 Pure Species Properties of MEA (Wang, et al., 1992; Kapadi, et al., 2002)

Mono-ethanolamine (MEA)			
Molecular Weight (g/mol)	61.08		
Temperature (°C)	25	30	35
Density (kg/m^3)	1013	1008	1004
Viscosity (mPa.s)	19.37	15.20	11.97
Boiling Point @ P = 1 atm (°C)	171		

Table A 2 Pure Species Properties of n-Propanol (Motin, et al., 2012; Chen, et al., 2005; Valtz, et al., 2004)

n-Propanol			
Molecular Weight (g/mol)	60.1		
Temperature (°C)	25	30	35
Density (kg/m^3)	799	796	788
Viscosity (mPa.s)	1.66	1.53	1.32
Boiling Point @ P = 1 atm (°C)	97		

The liquid properties of the MEA/n-Propanol solutions used in the reactive absorption study are tabulated in **Table A 3**. The viscosity data was measured experimentally and the density data calculated from equation 6.8.

$$\frac{1}{\rho_L} = \frac{x_{\text{MEA}}}{\rho_{\text{MEA}}} + \frac{x_{\text{n-Prop}}}{\rho_{\text{n-Prop}}} \qquad 6.8$$

Table A 3 Properties of MEA/n-Propanol Solutions

Density (kg/m^3)		
[MEA] (mol/dm^3)	Temperature (°C)	
	25	30
0.08	801	797
0.2	802	798
Viscosity (mPa.s)		
[MEA] (mol/dm^3)	Temperature (°C)	
	25	30
0.08	2.24	2.04
0.2	2.29	2.09

A.2 Calculating Wetted Wall Absorption Rate Measurement Error Range

The error margin for the reactive absorption measurements performed on the wetted wall experimental set-up was calculated from the resolution of the CO_2 analyser and the range of the repeatability measurements. The analyser had a resolution of 0.01 vol% and the repeatability range was also 0.01vol%. The error margin in the absorption data was calculated by adding 0.02 vol% to the steady state CO_2 vol% reading before absorption and subtracting 0.02 vol% to the steady state CO_2 vol% reading after absorption. This provided the error range in CO_2 vol% measurements.

An example of such an error margin calculation will be shown for an experiment conducted at 25°C for a CO_2 partial pressure of 19.88 kPa reactively absorbing into a 0.2M MEA in n-Propanol solution for a wetted wall column height of 90 mm:

CO_2 vol% reading before absorption: 19.21%

CO_2 vol% reading after absorption: 18.71%

Absorption rate of CO_2 (mol/s): 1.708×10^{-5}

Specific absorption rate of CO_2 (mol/m^2.s): 23.604×10^{-4}

CO_2 vol% reading before absorption with error margin added: 19.23%

CO_2 vol% reading after absorption with error margin subtracted: 18.69%

Absorption rate of CO_2 including vol% error margin (mol/s): 1.853×10^{-5}

Specific absorption rate of CO_2 including vol% error margin (mol/m^2.s): 25.616×10^{-4}

Error range in absorption rate (mol/s): $1.853 \times 10^{-5} - 1.708 \times 10^{-5} =$ **0.146×10^{-5}**

Error range in specific absorption rate (mol/m^2.s): $25.616 \times 10^{-4} - 23.604 \times 10^{-4} =$ **2.011×10^{-4}**

A.3 Evaluating the Gas side Mass Transfer Coefficient and Gas Phase Mass Transfer Resistance of the Wetted Wall

An attempt to estimate the gas side mass transfer resistance during the wetted wall absorption experiments will be presented in this section. The gas side resistance will be calculated as a percentage of the overall resistance to mass transfer. In order to determine the overall mass transfer resistance, the overall mass transfer coefficient must firstly be determined. The overall mass transfer coefficient is calculated from the specific absorption rate and the log-mean partial pressure driving force (LMPD) for CO_2 in the gas phase according to (Luo, et al., 2012; Tsai, et al., 2008):

$$K_G = \frac{N_{CO_2}}{\left(P_{CO_2} - P_{CO_2,L}\right)_{LMPD}} \qquad \text{A 1}$$

where

$$\left(P_{CO_2}-P_{CO_2,L}\right)_{LMPD}=\frac{\left(P_{CO_2}-P_{CO_2,L}\right)_{\text{in}}-\left(P_{CO_2}-P_{CO_2,L}\right)_{\text{out}}}{\ln\left(\frac{\left(P_{CO_2}-P_{CO_2,L}\right)_{\text{in}}}{\left(P_{CO_2}-P_{CO_2,L}\right)_{\text{out}}}\right)} \qquad \text{A 2}$$

Under pseudo first order conditions the concentration of CO_2 falls to zero in the liquid phase, meaning $P_{CO_2,L}=0$, which simplifies equation A 2 somewhat. In the reaction kinetic study, it was found that the conversion of CO_2 in n-Propanol fell within the range of 93.89 – 99.95 %. For the purpose of this calculation, an average CO_2 conversion of 97.59 % will be used. Equation A 2 may now be expressed as:

$$\left(P_{CO_2}-P_{CO_2,L}\right)_{LMPD}=\frac{\left(0.9758P_{CO_2}\right)_{\text{in}}-\left(0.9758P_{CO_2}\right)_{\text{out}}}{\ln\left(\frac{\left(0.9758P_{CO_2}\right)_{\text{in}}}{\left(0.9758P_{CO_2}\right)_{\text{out}}}\right)}=0.9758\frac{\left(P_{CO_2,\text{in}}-P_{CO_2,\text{out}}\right)}{\ln\left(\frac{P_{CO_2,\text{in}}}{P_{CO_2,\text{out}}}\right)} \qquad \text{A 3}$$

Assuming ideal gas behaviour, the partial pressure of CO_2 may be calculated from the total pressure and the measured CO_2 vol% reading:

$$P_{CO_2}=\left(CO_2\ \text{vol}\%\right)\cdot P_{\text{dome}} \qquad \text{A 4}$$

and the following expression may be derived for the wetted wall column (Tsai, 2010):

$$K_G=\frac{N_{CO_2}}{\left(P_{CO_2}-P_{CO_2,L}\right)_{LMPD}}=\frac{\dot{V}_G}{0.9758\cdot RTa_{\text{WWC}}}\ln\left(\frac{\text{vol}\%\ CO_{2,\text{in}}}{\text{vol}\%\ CO_{2,\text{out}}}\right) \qquad \text{A 5}$$

where $\dot{V}_G$ is the volumetric gas flow rate, R the universal gas constant and a_{WWC} the area of the wetted wall surface in contact with the gas phase. Values of K_G obtained from evaluating equation A 5 under the conditions of this study, were found to be in the order of 10^{-11} - 10^{-10} kmol/Pa.m^2.s which agrees well with literature (Tsai, et al., 2008). The overall mass transfer resistance is calculated from the reciprocal of the overall mass transfer coefficient. Similarly, the gas phase mass transfer resistance is calculated from the reciprocal of the gas side mass transfer coefficient. The percentage contribution of the gas phase resistance to the overall mass transfer resistance may be calculated from:

$$\frac{K_G}{k_G} \times 100 \quad [\%] \qquad \text{A 6}$$

It is always best to measure the gas side mass transfer coefficient via a suitable method. One such method is the absorption of SO_2 into dilute aqueous solutions of NaOH (Tsai, 2010), which is a gas-film controlled process (Charpentier, 1981; Tsai, 2010). If no such experiments could be performed, then the gas side mass transfer coefficient must be estimated with the use of boundary layer theory.

In this study, the gas side boundary layer of the wetted wall column was assumed to be similar to that of a flat plate. The first calculation to be made would be to establish whether the gas flow over the wetted wall was laminar of turbulent in nature. For this the Reynolds number of the gas flow had to be calculated:

$$\mathrm{Re} = \frac{\rho_G \cdot u_{G,eff} \cdot h}{\mu_G} \qquad \text{A 7}$$

The gas phase physical properties used were that of N_2 at 25°C and 30°C. These properties are tabulated in **Table A 6**.

Table A 6 Gas Phase Physical Properties Used in Boundary Layer Calculations (Reid & Sherwood, 1966)

Temperature (°C)	Density (kg/m^3)	Viscosity x 10^5 (Pa.s)	$D_{CO2,N2}$ x 10^5 (m^2/s)
25	1.13	1.78	1.58
30	1.11	1.81	

The linear velocity used for determining the Reynolds number was calculated by assuming the hydraulic diameter for gas flow is 0.03 m. This is the distance from the wetted wall to the inner edge of the donut shaped gas distributor. Using this hydraulic diameter, the linear velocity of the gas phase was calculated to be in the order of 0.11 m/s. Since the liquid phase was moving at approximately the same velocity in the opposite direction, the effective linear velocity of the gas phase was calculated to be in the order of 0.21 m/s. The Reynolds number was calculated as a function of wetted wall column height (h) and the maximum calculated Reynolds number

was 1275. Since this value is well below 5 x 10^5, the flow was assumed to be laminar (Incropera & De Witt, 2002; Seader & Henley, 1998).

Under laminar flow conditions, the following equations are relevant to calculating the boundary layer properties (Incropera & De Witt, 2002; Seader & Henley, 1998):

$$\delta_{\text{Boundary Layer}} = \frac{5h}{\sqrt{\text{Re}_h}} \qquad \text{A 8}$$

$$Sh_h = \frac{k_G h}{D_{CO_2,N_2}} = 0.664 \cdot \text{Re}_h^{0.5}\, Sc^{0.333} \qquad \text{A 9.}$$

where

$$Sc = \frac{\mu_G}{\rho_G D_{CO_2,N_2}} \qquad \text{A 10}$$

From these equations a boundary layer profile along with the gas side mass transfer coefficient, k_G could be calculated. The calculated boundary layer profile is illustrated **Figure A 1**.

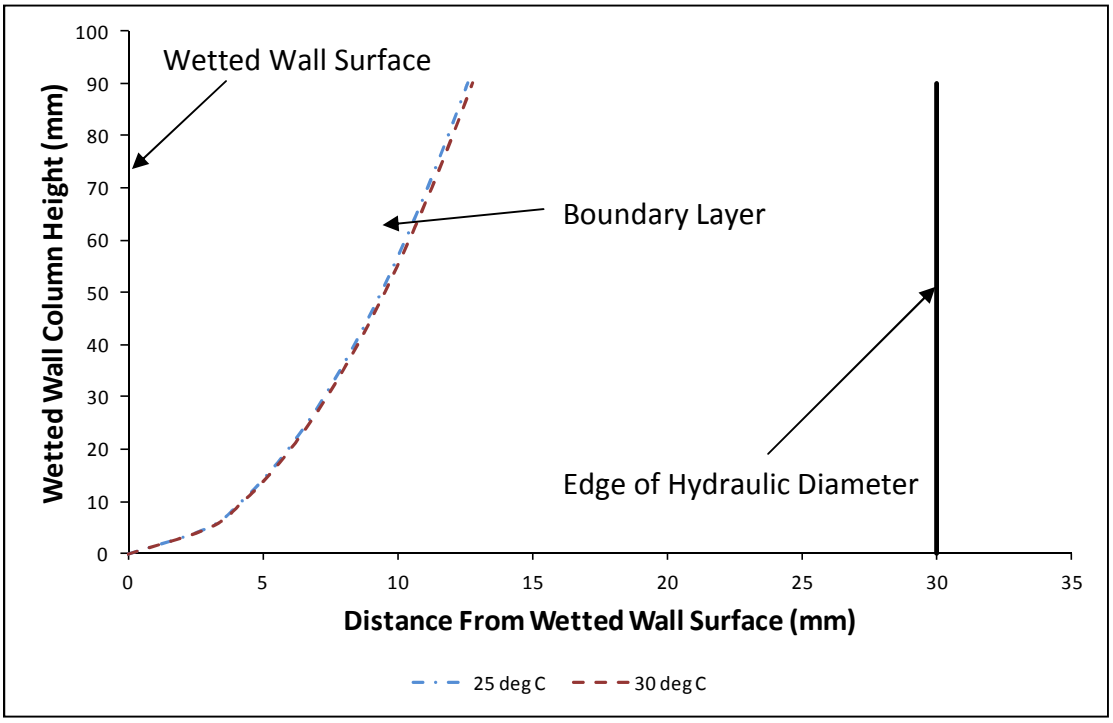

Figure A 1 Gas Phase Boundary Layer Profile

The boundary layer in **Figure A 1** is still in the developing phase when it reaches the top of the wetted wall, indicating that the resistance to mass transfer in the gas phase increases as the gas flows upwards. An average gas phase mass transfer coefficient will be used to determine the average gas phase mass transfer resistance. The average gas phase mass transfer coefficient, calculated from boundary layer theory, was in the order of 7 x 10^{-3} m/s for a 90 mm column height and 8.25 x 10^{-3} m/s for a 60 mm column height. The gas phase mass transfer coefficient has different units from the overall mass transfer coefficient. Before a direct comparison can be made, the units must firstly agree. The unit conversion may be done with the knowledge of the original form of the concentration driving force mass transfer coefficient:

$$k_G \equiv \frac{\text{kmol} \cdot \text{m}^3}{\text{m}^2 \cdot \text{s} \cdot \text{kmol}} \equiv \frac{\text{m}}{\text{s}}$$

which may be compared with the units of the overall mass transfer coefficient based on partial pressure driving force:

$$K_G \equiv \frac{\text{kmol}}{\text{m}^2 \cdot \text{s} \cdot \text{Pa}}$$

Therefore, if the pressure unit can be converted to a concentration unit, then the units of K_G can be converted to m/s in order for it to be comparable with k_G. From the ideal gas law, the following relationship may be derived:

$$1\text{Pa} \equiv RT \cdot \left(1\frac{\text{kmol}}{\text{m}^3}\right), \quad R = 8314\frac{\text{J}}{\text{kmol} \cdot \text{K}}$$

Therefore, if K_G is multiplied with RT, its units will be converted to m/s, making a comparison with the boundary layer theory derived k_G possible. The results from such a comparison at 25°C and an initial MEA concentration of 0.2 M in the liquid phase is tabulated in **Table A 7**

Table A 7 Gas Phase Resistance from Boundary Layer Theory for the Absorption of CO_2 into 0.2 M MEA solutions at 25°C on the Wetted Wall

h_{column} (mm)	N_{CO2} x 10^4 (mol/m^2.s)	P_{CO2} (kPa)	LMPD (Pa)	K_G x10^{10} (kmol/m^2.s.Pa)	K_G x10^3 (m/s)	k_G x 10^3 (m/s)	% Resistance
90	24.67	19.99	19.15	1.29	0.32	7.00	4.57
90	29.77	19.98	19.08	1.56	0.39	7.00	5.53
60	29.84	19.94	19.15	1.56	0.39	8.25	4.71
60	33.43	20.04	19.22	1.74	0.43	8.25	5.26
60	14.43	11.13	10.70	1.35	0.33	8.25	4.07
60	18.52	11.12	10.66	1.74	0.43	8.25	5.25
90	11.71	11.07	10.62	1.10	0.27	7.00	3.90
90	15.11	11.02	10.54	1.43	0.35	7.00	5.07
90	8.06	5.56	5.31	1.52	0.38	7.00	5.37
90	9.82	5.55	5.28	1.86	0.46	7.00	6.58
60	10.02	5.65	5.41	1.85	0.46	8.25	5.56
60	11.40	5.66	5.41	2.11	0.52	8.25	6.32

The gas phase resistance calculated in **Table A 7** is in the order of 3.90 – 6.32 %, indicating a low resistance to mass transfer in the gas phase. Considering all of the conditions investigated in this study, the calculated gas phase resistance was between 2.13 % and 8.81 %. Based on boundary layer theory, there was overall low gas phase resistance under the absorption conditions investigated in this study.

Appendix B BASIS FOR A NEW EFFECTIVE AREA THEORY AND NUMERICAL METHOD OF CALCULATION

This section will present the numerical technique proposed to determine effective interfacial mass transfer area under conditions where interfacial depletion and surface renewal of the liquid phase reactant is significant. Under these conditions, pseudo first order reaction kinetics is no longer valid and the more fundamentally derived reaction rate expression determined in this study must be incorporated. This section will start off by reintroducing the fundamental diffusion equation for reactive absorption. It will then show the expanded version of the diffusion equation by incorporating the reaction kinetics of the fast reaction of CO_2 with MEA in alcoholic solvents, determined in Chapter 4 of this study.

This fast reaction is suitable for the purpose of determining effective interfacial mass transfer area, since the absorption is only dependent upon the available effective area created by the presence of MEA at the gas-liquid interface. The method presented in this section will be applicable for all CO_2/MEA reactive absorption experiments carried for the purpose of calculating the effective interfacial mass transfer area for all types of structured and random packing. From the reaction kinetic study it was concluded that the rate expressions are valid over a wide concentration range, including pseudo first order conditions.

B.1 Formulation of the Proposed Approach to Determine Effective Interfacial Mass Transfer Area

This section will introduce the fundamental diffusion equations incorporating the reaction kinetics of CO_2 with MEA in alcoholic solvents. It will also show how the physiochemical properties required for solving the reactive diffusion equation was estimated. The proposed method is similar to the strategies followed in literature to determine the reaction kinetics of CO_2 with MEA in aqueous solvents using either a wetted wall (Bosch, et al., 1989) or a laminar

jet absorber (Aboudheir, et al., 2003). In their respective studies, they assumed the entire interfacial area to represent the effective area for mass transport and were thus able to derive the reaction kinetic parameters from the total absorption rate. In this study, the reaction kinetic parameters were determined separately as shown in Chapter 3 and Chapter 4 and now the same diffusion equations can be solved to determine the effective area from the total absorption rate.

B.1.1 The Fundamental Reactive Diffusion Equations

When a gas reactively absorbs into a liquid with constant diffusivity and density, the absorption is governed by the following expression (Astarita, 1967; Aboudheir, et al., 2003):

$$D_i \nabla^2 C_i = u \cdot \nabla C_i + \frac{\partial C_i}{\partial t} + r_i \qquad \text{B 1}$$

Equation 7.1 states that the molecular transport in the liquid film is subject to the sum of the convection rate $\left(u \cdot \nabla C_i\right)$, the accumulation rate $\left(\partial C_i / \partial t\right)$ and the reaction rate $\left(r_i\right)$. The following assumptions were made regarding the absorption of a reactive gas (CO_2) into a liquid film flowing down a wetted wall column (all assumption in agreement with literature (Bosch, et al., 1989; Aboudheir, et al., 2003)):

- A constant diffusivity and density in the liquid phase was assumed due to the low amount of CO_2 absorbing, thereby not affecting the liquid phase physical properties appreciably.
- Penetration or Surface Renewal Theory applies
- The penetration depth of the CO_2 molecules is much smaller than the liquid film thickness (Astarita, 1967). This implies that the liquid film may be considered to be infinitely deep with a flat surface.
- The diffusion of CO_2 in the direction of liquid flow is negligible.
- Insignificant convection movements in the liquid film. The liquid is assumed to be quiescent (Danckwerts, 1970).

Based on these assumptions, equation B 1 may be simplified to the general form of equation 2.15:

$$D_i \frac{\partial^2 C_i}{\partial x^2} = \frac{\partial C_i}{\partial t} + r_i \qquad 2.15$$

Equation 2.15 may be specialized for the case of CO_2 reactively absorbing into alcoholic solutions of MEA by incorporating either the fundamental reaction rate expressions derived in section 4.3.1 or the shortened fundamental rate expressions derived in section 4.3.2. These models were derived from the zwitterion reaction mechanism of equation 3.3 and its simplified syntax form of equation 4.1, which is reintroduced here:

$$\begin{aligned} &1)\ CO_2 + RNH_2 \underset{k_2}{\overset{k_1}{\rightleftharpoons}} RNH_2^+COO^- \\ &2)\ RNH_2^+COO^- + RNH_2 \underset{k_4}{\overset{k_3}{\rightleftharpoons}} RNHCOO^- + RNH_3^+ \end{aligned} \qquad 3.3$$

$$\begin{aligned} &CO_2 + RNH_2 \underset{k_2}{\overset{k_1}{\rightleftharpoons}} Z \\ &Z + RNH_2 \underset{k_4}{\overset{k_3}{\rightleftharpoons}} 2S \end{aligned} \qquad 3.9$$

The resulting equations are presented as follows:

Fundamental Rate Expressions:

The fundamental rate expressions should be used under conditions where surface depletion of MEA in the liquid phase becomes appreciable. This system may be selected to determine the effective interfacial mass transfer area created by the liquid phase under such conditions. The governing absorption equations are:

$$D_{CO_2,L} \frac{\partial^2 C_{CO_2}}{\partial x^2} = \frac{\partial C_{CO_2}}{\partial t} + \left(-k_1 C_{CO_2} C_{RNH_2} + k_2 C_Z\right) \qquad B\ 2$$

$$D_{RNH_2,L} \frac{\partial^2 C_{RNH_2}}{\partial x^2} = \frac{\partial C_{RNH_2}}{\partial t} + \left(-k_1 C_{CO_2} C_{RNH_2} + k_2 C_Z - k_3 C_Z C_{RNH_2} + k_4 C_S^2\right) \qquad B\ 3$$

$$D_{Z,L}\frac{\partial^2 C_Z}{\partial x^2}=\frac{\partial C_Z}{\partial t}+\left(k_1 C_{CO_2} C_{RNH_2}-k_2 C_Z-k_3 C_Z C_{RNH_2}+k_4 C_S^2\right) \quad \text{B 4}$$

$$D_{S,L}\frac{\partial^2 C_S}{\partial x^2}=\frac{\partial C_S}{\partial t}+\left(k_3 C_Z C_{RNH_2}-k_4 C_S^2\right) \quad \text{B 5}$$

The reaction rate constants of equations B 2 - B 5 are tabulated in **Table 4.5**.

Shortened Fundamental Rate Expressions:

The shortened fundamental rate expressions may be used under conditions where surface depletion of MEA is moderate, but still significant. It is a simplified form of the fundamental model, assuming reaction equilibrium to be achieved rapidly. This equation is suitable for use under conditions where pseudo first order kinetics is no longer valid, but surface depletion of MEA is not excessive. The governing absorption equations are:

$$D_{CO_2,L}\frac{\partial^2 C_{CO_2}}{\partial x^2}=\frac{\partial C_{CO_2}}{\partial t}+\left(-k_1 C_{CO_2} C_{RNH_2}^2+k_2 C_S^2\right) \quad \text{B 6}$$

$$D_{RNH_2,L}\frac{\partial^2 C_{RNH_2}}{\partial x^2}=\frac{\partial C_{RNH_2}}{\partial t}+2\left(-k_1 C_{CO_2} C_{RNH_2}^2+k_2 C_S^2\right) \quad \text{B 7}$$

$$D_{S,L}\frac{\partial^2 C_S}{\partial x^2}=\frac{\partial C_S}{\partial t}+\left(k_1 C_{CO_2} C_{RNH_2}^2+k_2 C_S^2\right) \quad \text{B 8}$$

The reaction rate constants for equations B 6 - B 8 are tabulated in **Table 4.8**.

Initial and Boundary Conditions

The partial differential equations formulated in this section can only be solved given the applicable initial and boundary conditions. The initial and boundary conditions for the reactive absorption of CO_2 into alcoholic solutions of MEA incorporating the fundamental rate expression model may be expressed as:

$$@\, x\geq 0,\ t=0\ :\ \left\{\begin{array}{c} C_{CO_2}=0 \\ C_{RNH_2}=C_{RNH_2,0} \\ C_j=0 \end{array}\right\}\ j\in\{Z,S\} \quad \text{B 9}$$

$$@\, x=0,\ \mathrm{t}>0\ :\ \left\{\begin{array}{c} C_{CO_2}=C_{CO_2,i}=\dfrac{P_{CO_2,i}}{H_{CO_2,[RNH_2]}} \\ \dfrac{\partial C_j}{\partial x}=0 \end{array}\right\}\ j\in\{RNH_2,Z,S\} \qquad \text{B 10}$$

$$@\, x\to\infty,\ t>0\ :\ \left\{\begin{array}{c} C_{RNH_2}=C_{RNH_2,0} \\ C_j=C_{j,L} \end{array}\right\}\ j\in\{CO_2,Z,S\} \qquad \text{B 11}$$

The initial and boundary conditions for the reactive absorption of CO_2 into alcoholic solutions of MEA incorporating the shortened fundamental rate expression model may be expressed as:

$$@\, x\geq 0,\ t=0\ :\ \left\{\begin{array}{c} C_{CO_2}=0 \\ C_{RNH_2}=C_{RNH_2,0} \\ C_j=0 \end{array}\right\}\ j\in\{S\} \qquad \text{B 12}$$

$$@\, x=0,\ \mathrm{t}>0\ :\ \left\{\begin{array}{c} C_{CO_2}=C_{CO_2,i}=\dfrac{P_{CO_2,i}}{H_{CO_2,[RNH_2]}} \\ \dfrac{\partial C_j}{\partial x}=0 \end{array}\right\}\ j\in\{RNH_2,S\} \qquad \text{B 13}$$

$$@\, x\to\infty,\ t>0\ :\ \left\{\begin{array}{c} C_{RNH_2}=C_{RNH_2,0} \\ C_j=C_{j,L} \end{array}\right\}\ j\in\{CO_2,S\} \qquad \text{B 14}$$

Once a solution is obtained, the effective area available for absorption may be calculated from the CO_2 concentration gradient at the gas liquid interface (Aboudheir, et al., 2003). Rearranging equation 2.22 yields:

$$a_e=\frac{n_{CO_2}}{-D_{CO_2,L}\left(\dfrac{\partial C_{CO_2}}{\partial x}\right)_{x=0}} \qquad \text{B 15}$$

The solution of equation B 15 gives the effective area available for mass transfer. The method used to estimate it from absorption rate data and the solution of the partial differential equation presented in this section will be discussed in section B.2. Before that can be done, the physiochemical data required in the partial differential equations, initial and boundary conditions must firstly be estimated.

B.1.2 Physiochemical Properties and Initial and Boundary Conditions

Due to the reactivity of MEA with CO_2, physiochemical properties such as the diffusivity and solubility of CO_2 into alcoholic solutions of MEA cannot be measured directly. These properties are best estimated with the use of an analogy with a non-reacting gas of similar molecular configuration, molecular volume and electronic structure (Littel, et al., 1992(a)). The most popular gas used for this purpose is N_2O (Laddha, et al., 1980; Sada, et al., 1986; Oyevaar, et al., 1989; Li & Lai, 1995; Xu, et al., 2013).

Absorption experiments with N_2O were not performed in this study, which means that the physiochemical properties used were estimated from literature data. The procedure followed to estimate the physiochemical data required to solve the partial differential equations in this section is documented in section B.4. The diffusivity and solubility data used are tabulated in **Table B 1** and **Table B 2**.

Table B 1 Diffusivities Used in the Partial Differential Equations of Section B.1.1

T (°C)	$D_{CO2,0.2\ M} \times 10^5$ (cm^2/s)	$D_{CO2,0.08\ M} \times 10^5$ (cm^2/s)	$D_{MEA,n\text{-}Prop} \times 10^5$ (cm^2/s)	$D_{Z,n\text{-}Prop} \times 10^5$ (cm^2/s)	$D_{S,n\text{-}Prop} \times 10^5$ (cm^2/s)
25	1.29	1.34	0.80	0.80	0.80
30	1.43	1.49	0.83	0.83	0.83

Table B 2 Solubility Data Used in the Partial Differential Equations of Section B.1.1

T (°C)	$H_{CO2,\ n\text{-}Prop}$ x 10^3 (kPa.dm^3/mol)	$H_{CO2,\ 0.2\ M}$ x 10^3 (kPa.dm^3/mol)	$H_{CO2,\ 0.08\ M}$ x 10^3 (kPa.dm^3/mol)
25	1.108	1.048	1.048
30	1.194	1.174	1.175

The diffusion coefficients of **Table B 1** are of the same order in magnitude as the values used in literature for aqueous MEA solvents (Versteeg, et al., 1990; Bosch, et al., 1989). The boundary values for CO_2 at $x = 0$ may be calculated from the partial pressure of CO_2 for a given absorption experiment and the applicable Henry's law coefficient for the bulk MEA liquid concentration, given in **Table B 2**.

The initial conditions applicable to the solution of the differential equations in this chapter are dependent upon the liquid phase concentrations of all species before gas absorption. If it is assumed that the liquid phase contains only MEA (at its initial concentration) and the alcohol of choice, which is the recommended initial liquid condition for effective area determination, then the initial concentrations of the other species are zero. The boundary conditions in the bulk liquid phase are dependent upon knowledge of the equilibrium concentrations of the product species and the absorbing gas, CO_2. The boundary condition for MEA in the bulk of the liquid will be its initial concentration in the bulk liquid phase. The conversion data of CO_2 for the various [MEA]:[CO_2] of this study is given in **Table 3.8**. From the CO_2 conversion, the equilibrium concentrations of both the zwitterion and salt products can be calculated with the use of the reaction stoichiometry. These equilibrium values are assigned as the boundary values for $x \to \infty$. Some of the initial and boundary conditions values to be used for determining the effective area achieved on the wetted wall column used in this study are tabulated in section B.4.

B.2 Solving the Reactive Diffusion Equation Numerically in Matlab®

The *pdepe*© algorithm in Matlab® solves parabolic and elliptic partial differential equations in one dimension, provided the initial and boundary conditions are available for the solution. The general form of a parabolic-elliptic partial differential equation is given in equation B 16

$$c\left(x,t,u,\frac{\partial u}{\partial x}\right)\frac{\partial u}{\partial t}=x^{-m}\frac{\partial}{\partial x}\left(x^{m}f\left(x,t,u,\frac{\partial u}{\partial x}\right)\right)+s\left(x,t,u,\frac{\partial u}{\partial x}\right) \qquad \text{B 16}$$

The algorithm can solve a system of partial differential equations in one space variable (x) and for a time variable (t). Equation B 16 shows a partial differential equation after discretization (taking it from a second order partial derivative to a first order partial derivative) in terms of the space variable was performed. The discretization in space results in ordinary, instead of higher order, partial differential equations with respect to the space variable, which Matlab® can solve using one of its *ode*© algorithms. The integrated ordinary partial differential equations serve as approximate solutions at certain points in time. The *pdepe*© algorithm then provides the added solution in space.

For the purpose of this study, the following changes and simplifications to equation B 16 are made:

1. $c\left(x,t,u,\frac{\partial u}{\partial x}\right)=1$. This implies that the equation has no elliptical elements and is thus only representative of a set of parabolic partial differential equations.
2. $m=0$. This implies that the surface of absorption is approximated as a slab.
3. $s\left(x,t,u,\frac{\partial u}{\partial x}\right)=r_i$. This is known as the source term, for which an applicable reaction rate expression will be used.
4. $u=C_i$. This will specify that the solution to the partial differential equations will be given in terms of concentration profiles in both time and space.

Application of the above simplifications and changes transforms equation B 16 into the set of partial differential equations given in section B.1.1. In order to solve this set of equations, the initial and boundary condition values must be provided in the correct form. Matlab® uses matrices in all its calculations, so the initial and boundary conditions must be provided in matrix form. The initial and boundary conditions (equations B 9 - B 11) applicable to the CO_2/MEA

reactive system for the fundamental reaction rate expression model (equations B 2 -B 5) are formulated as follows:

Initial Conditions $(t=0, x \geq 0)$

$$C_{j,0} = \begin{bmatrix} 0 \\ C_{RNH_2,L} \\ 0 \\ 0 \end{bmatrix} \qquad \text{B 17}$$

Left Boundary Conditions $(t \geq 0, x=0)$

$$\begin{bmatrix} C_{CO_2,i} - \left(\dfrac{P_{CO_2}}{H_{CO_2,[RNH_2]}} \right) \\ 0 \\ 0 \\ 0 \end{bmatrix} + \begin{bmatrix} 0 \\ 1 \\ 1 \\ 1 \end{bmatrix} \cdot \times \begin{bmatrix} D_{CO_2,[RNH_2]} \dfrac{\partial C_{CO_2}}{\partial x} \\ D_{RNH_2,L} \dfrac{\partial C_{RNH_2}}{\partial x} \\ D_{Z,L} \dfrac{\partial C_Z}{\partial x} \\ D_{S,L} \dfrac{\partial C_S}{\partial x} \end{bmatrix} = \begin{bmatrix} 0 \\ 0 \\ 0 \\ 0 \end{bmatrix} \qquad \text{B 18}$$

Right Boundary Conditions $(t \geq 0, x \to \infty)$

$$\begin{bmatrix} C_{CO_2} - C_{CO_2,L} \\ C_{RNH_2} - C_{RNH_2,L} \\ C_Z - C_{Z,L} \\ C_S - C_{S,L} \end{bmatrix} + \begin{bmatrix} 0 \\ 0 \\ 0 \\ 0 \end{bmatrix} \cdot \times \begin{bmatrix} D_{CO_2,[RNH_2]} \dfrac{\partial C_{CO_2}}{\partial x} \\ D_{RNH_2,L} \dfrac{\partial C_{RNH_2}}{\partial x} \\ D_{Z,L} \dfrac{\partial C_Z}{\partial x} \\ D_{S,L} \dfrac{\partial C_S}{\partial x} \end{bmatrix} = \begin{bmatrix} 0 \\ 0 \\ 0 \\ 0 \end{bmatrix} \qquad \text{B 19}$$

The initial and boundary conditions (equations B 12 - B 14) applicable to the CO_2/MEA reactive system for the shortened fundamental reaction rate expression model (equations B 6 - B 8) are formulated as follows:

Initial Conditions $\left(t=0, x \geq 0\right)$

$$C_{j,0} = \begin{bmatrix} 0 \\ C_{RNH_2,L} \\ 0 \end{bmatrix} \qquad \text{B 20}$$

Left Boundary Conditions $\left(t \geq 0, x=0\right)$

$$\begin{bmatrix} C_{CO_2,i} - \left(\dfrac{P_{CO_2}}{H_{CO_2,[RNH_2]}} \right) \\ 0 \\ 0 \end{bmatrix} + \begin{bmatrix} 0 \\ 1 \\ 1 \end{bmatrix} \cdot \times \begin{bmatrix} D_{CO_2,[RNH_2]} \dfrac{\partial C_{CO_2}}{\partial x} \\ D_{RNH_2,L} \dfrac{\partial C_{RNH_2}}{\partial x} \\ D_{S,L} \dfrac{\partial C_S}{\partial x} \end{bmatrix} = \begin{bmatrix} 0 \\ 0 \\ 0 \end{bmatrix} \qquad \text{B 21}$$

Right Boundary Conditions $\left(t \geq 0, x \to \infty\right)$

$$\begin{bmatrix} C_{CO_2} - C_{CO_2,L} \\ C_{RNH_2} - C_{RNH_2,L} \\ C_S - C_{S,L} \end{bmatrix} + \begin{bmatrix} 0 \\ 0 \\ 0 \end{bmatrix} \cdot \times \begin{bmatrix} D_{CO_2,[RNH_2]} \dfrac{\partial C_{CO_2}}{\partial x} \\ D_{RNH_2,L} \dfrac{\partial C_{RNH_2}}{\partial x} \\ D_{S,L} \dfrac{\partial C_S}{\partial x} \end{bmatrix} = \begin{bmatrix} 0 \\ 0 \\ 0 \end{bmatrix} \qquad \text{B 22}$$

The bulk liquid phase concentration $\left(C_{j,L}\right)$ of CO_2, the zwitterion and salt products may be calculated from the conversion data in **Table 3.8**. The initial and boundary condition values for some of the wetted wall reactive absorption rate experiments are tabulated in section B.5. In order to obtain an optimum solution to the set of partial differential equations, the size of the space and time domain mesh must be provided. This is not an easy task and at the time of publication of this study, the optimum mesh for this specific system, was not yet obtained. This will form a major part of future work in this particular avenue of research.

Solutions for aqueous based CO_2/MEA reactive systems are available (Aboudheir, et al., 2003) so the problem of defining the optimum mesh size has already been solved. The details of the mesh sizes used in their study, was not provided in the publication. A representation of the

expected concentration profiles to be obtained from the optimum solution to the set of partial differential equations is illustrated in **Figure B 1**. It was drawn based on the expected solution obtained using the shortened fundamental model rate expressions as source term in the system of partial differential equations. **Figure B 1** is based on the results obtained for the reactive absorption of CO_2 into aqueous solutions of MEA at similar CO_2 partial pressures and MEA liquid phase concentrations used in this study (Aboudheir, et al., 2003).

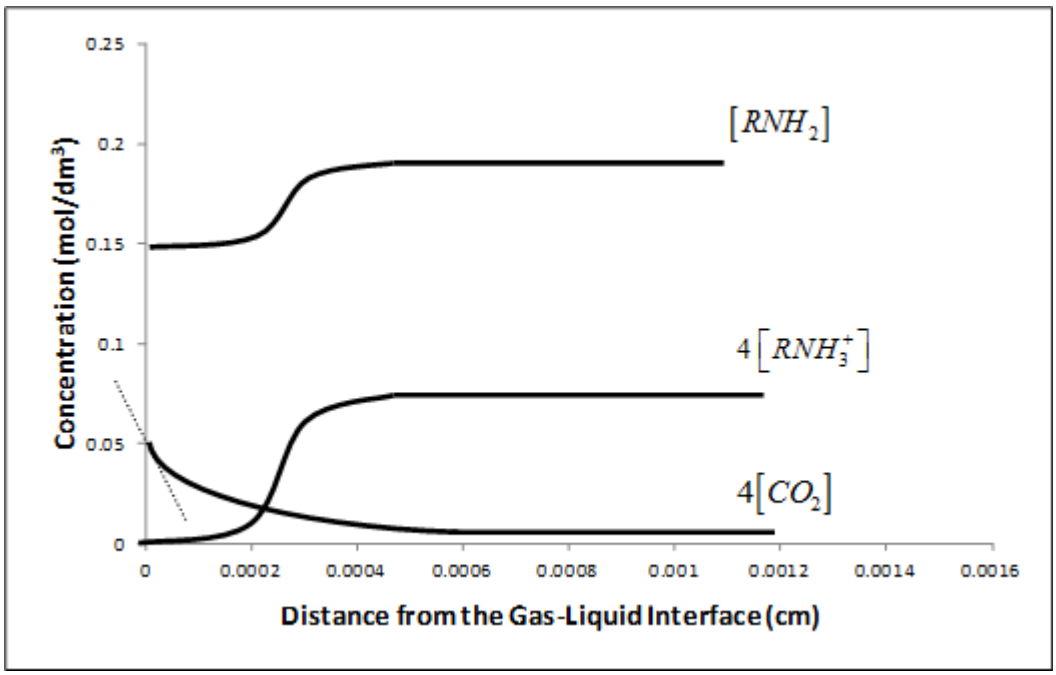

Figure B 1 Expected Concentration Profiles based on a Solution using the Shortened Fundamental Model.

From **Figure B 1** the surface depletion of MEA may be noticed. Under these conditions the pseudo first order rate expression is no longer valid. If the effective area available for mass transfer is to be calculated under these conditions, the fundamental or shortened fundamental rate expression developed in this study will have to be used. The effective area of gas liquid contacting devices, such as structured packing and random packing may be calculated provided the total absorption rate of CO_2 is known (which is a measured quantity) and the slope of the CO_2 concentration profile at the interface is accurately determined (see equation B 15).

The slope of the CO_2 concentration profile is indicated by the dashed line in **Figure B 1**. It is best calculated numerically with the use of the forward finite-difference approximation (Barakat & Clark, 1966; Aboudheir, et al., 2003) depicted in equation B 23:

$$\left(\frac{\partial C_{CO_2}}{\partial x}\right)_{x=q-1} = \frac{-\left(C_{CO_2}\right)_{q+2}^{n} + 4\cdot\left(C_{CO_2}\right)_{q+1}^{n} - 3\cdot\left(C_{CO_2}\right)_{q}^{n}}{2\Delta x} \quad O\left(\Delta x^2\right) \qquad \text{B 23}$$

where $O\left(\Delta x^2\right)$ denotes the magnitude of the error in the approximation. It may therefore be seen that in order to minimize the error, the step sizes in the space mesh must be selected to be as small as possible. The optimum mesh size selection must, however, keep computational time in mind as well. As previously mentioned, this will form part of future research. At the gas liquid interface where $x = 0$, thus $q = 1$ the slope may be calculated from equation B 24:

$$\left(\frac{\partial C_{CO_2}}{\partial x}\right)_{x=0} = \frac{-\left(C_{CO_2}\right)_{3}^{n} + 4\cdot\left(C_{CO_2}\right)_{2}^{n} - 3\cdot\left(C_{CO_2}\right)_{1}^{n}}{2\Delta x} \qquad \text{B 24}$$

where $\Delta x = x_{\text{mesh point 3}} - x_{\text{mesh point 1}}$. The calculated effective area values must be subject to some form of validations study. It is recommended that the interfacial area values obtained from systems where pseudo first order kinetics were assumed valid, serve as a validation data set. This should provide for adequate validations, since the method used to calculate effective area under pseudo first order conditions were also derived from the diffusion equations presented in this section (see section 5.2.1). Under pseudo first order conditions, the source term of the set of partial differential equations will be the pseudo first order rate expression. The results obtained from this proposed method, may be compared to the results obtained using the method described in section 5.2.3.

B.3 Estimating the Required Physiochemical Properties for the Use in the New Effective Area Theory

The N_2O analogy for estimating the solubility (in terms of the Henry's law coefficient, H_i) of CO_2 in a solution of water containing a certain concentration of amine may be expressed as (Xu, et al., 2013):

$$H_{CO_2,\text{Amine}} = \left(\frac{H_{CO_2,H_2O}}{H_{N_2O,H_2O}}\right) H_{N_2O,\text{Amine}} \qquad \text{B 25}$$

Equation B 25, therefore, states that the measured solubility of N_2O into a solution containing a certain concentration of amine, multiplied by the ratio of the solubility of CO_2 to N_2O in solutions of pure solvent, is equal to the solubility of CO_2 in the same concentration amine solution. Since solubility is a function of temperature, all solubility experiments must be carried out at the same temperature. It is therefore logical to deduce that the analogy will hold for any solvent (Sada, et al., 1986) and thus the following equations results for the use of 0.08 M and 0.2 M MEA solutions of n-Propanol (the solutions used in Chapter 6):

$$H_{CO_2,0.08\text{ M }RNH_2} = \left(\frac{H_{CO_2,\text{n-Prop}}}{H_{N_2O,\text{n-Prop}}}\right) H_{N_2O,0.08\text{ M }RNH_2} \qquad \text{B 26}$$

$$H_{CO_2,0.2\text{ M }RNH_2} = \left(\frac{H_{CO_2,\text{n-Prop}}}{H_{N_2O,\text{n-Prop}}}\right) H_{N_2O,0.2\text{ M }RNH_2} \qquad \text{B 27}$$

The solubility of N_2O in alcoholic solutions of MEA was not experimentally determined in this study, but was estimated from data available in literature. Although there is an abundance of data available for aqueous solution of MEA (Li & Lai, 1995) no data for MEA/n-Propanol solutions could be found. The solutions nearest resembling MEA/ n-Propanol found, was that of Di-ethanolamine (DEA)/2-Propanol (Sada, et al., 1986). The data presented in that study was of a combined physiochemical form of diffusivity and solubility. The data was determined from absorption measurement carried out at 30°C using a cylindrical wetted wall column, similar to the one used in this study. The physiochemical data were found to be:

$$\left(\frac{\left(D_{CO_2,\text{2-Prop}}\right)^{1/2}}{H_{CO_2,\text{2-Prop}}}\right)_{30°C} = 4.35\times10^{-12}\ \frac{\text{mol}}{\text{Pa}\cdot\text{cm}\cdot\text{s}^{1/2}} \qquad \text{B 28}$$

$$\left(\frac{\left(D_{N_2O,\text{2-Prop}}\right)^{1/2}}{H_{N_2O,\text{2-Prop}}}\right)_{30°C} = 5.39\times10^{-12}\ \frac{\text{mol}}{\text{Pa}\cdot\text{cm}\cdot\text{s}^{1/2}} \qquad \text{B 29}$$

Dividing equation B 28 by equation B 29 and rearranging yields:

$$\left(\frac{H_{CO_2,\text{2-Prop}}}{H_{N_2O,\text{2-Prop}}}\right)_{30°C} = 1.24\left(\frac{D_{CO_2,\text{2-Prop}}}{D_{N_2O,\text{2-Prop}}}\right)^{1/2}_{30°C} \qquad \text{B 30}$$

If it is assumed that the same correlation is valid for n-Propanol and that the correlation is independent of temperature for the temperature range of 25 - 30°C, then the following may be deduced:

$$\left(\frac{H_{CO_2,\text{n-Prop}}}{H_{N_2O,\text{n-Prop}}}\right)_{25°C\text{ or }30°C} = 1.24\left(\frac{D_{CO_2,\text{n-Prop}}}{D_{N_2O,\text{n-Prop}}}\right)^{1/2}_{25°C\text{ or }30°C} \qquad \text{B 31}$$

They then proceeded to collect physiochemical data for N_2O in various concentrations of DEA in 2-Propanol $\left(0\ \text{M} \le [DEA] \le 2\ \text{M}\right)$ at 30°C. If it is assumed that the physiochemical data for MEA/n-Propanol will be equal to the physiochemical data for DEA/2-Propanol, then the following expressions result:

$$\left(\frac{D^{0.5}_{N_2O,L}}{H_{N_2O}}\right)_{0.08\text{ M MEA}} = 0.983\cdot\left(\frac{D^{0.5}_{N_2O,L}}{H_{N_2O}}\right)_{\text{n-Prop}} \qquad \text{B 32}$$

$$\left(\frac{D^{0.5}_{N_2O,L}}{H_{N_2O}}\right)_{0.2\text{ M MEA}} = 0.972\cdot\left(\frac{D^{0.5}_{N_2O,L}}{H_{N_2O}}\right)_{\text{n-Prop}} \qquad \text{B 33}$$

It can now be seen that in order to be able to evaluate equations B 26 and B 27, the diffusivity of CO_2 and N_2O in n-Propanol and the diffusivity of N_2O in MEA/n-Propanol solutions will be required. The equation recommended in literature for the estimation of the diffusivity of these

gasses in organic solutions was derived by Fuller, Schettler and Giddings (Reid & Sherwood, 1966; Charpentier, 1981):

$$D_{AB} = \frac{KT}{\mu_{AB} \bar{V}_A^{1/3}} \qquad \text{B 34}$$

$$K = 8.2\times10^{-8}\left(1+\frac{3\bar{V}_B}{\bar{V}_A}\right)^{2/3} \qquad \text{B 35}$$

where $\bar{V}_i$ is the molal volume of species i at its normal boiling point (Reid & Sherwood, 1966). The molal volumes of the species used in this study are tabulated in **Table B 3**.

Table B 3 Molal Volumes

Species	Molal Volume (cm^3/mol)
n-Propanol	81.4
CO_2	34
N_2O	36.4
MEA	73.4

The calculated diffusivities are tabulated in **Table B 4**.

Table B 4 Calculated Diffusivities

T (°C)	$D_{CO2,n\text{-}Prop}$ x 10^5 (cm^2/s)	$D_{N2O,n\text{-}Prop}$ x 10^5 (cm^2/s)	$D_{MEA,n\text{-}Prop}$ x 10^5 (cm^2/s)	$D_{N2O,0.2\ M}$ x 10^5 (cm^2/s)	$D_{N2O,0.08\ M}$ x 10^5 (cm^2/s)
25	1.47	1.49	0.80	1.26	1.29
30	1.73	1.53	0.83	1.40	1.43

The calculated diffusivities are in agreement (the same order of magnitude) with the values used in literature for aqueous systems (Versteeg, et al., 1990). The solubility data of CO_2 in pure n-Propanol was taken from literature (Tokunaga, 1975). The calculated solubility values of CO_2 and N_2O are tabulated in **Table B 5**.

Table B 5 Solubility Data for CO_2 and N_2O

T (°C)	$H_{CO2,\ n\text{-}Prop}$ x 10^3 (kPa.dm^3/mol)	$H_{CO2,\ 0.2\ M}$ x 10^3 (kPa.dm^3/mol)	$H_{CO2,\ 0.08\ M}$ x 10^3 (kPa.dm^3/mol)	$H_{N2O,\ n\text{-}Prop}$ x 10^3 (kPa.dm^3/mol)	$H_{N2O,\ 0.2\ M}$ x 10^3 (kPa.dm^3/mol)	$H_{N2O,\ 0.08\ M}$ x 10^3 (kPa.dm^3/mol)
25	1.108	1.048	1.048	0.897	0.849	0.849
30	1.194	1.174	1.175	0.906	0.891	0.892

B.4 Examples of Initial and Boundary Conditions Values for Determining the Effective Mass Transfer Area of the Wetted Wall Column

Example initial and boundary condition values for use in the solution of the partial differential equation of section B.1.1 are presented in **Table B 6** and **Table B 7**. The solubility of CO_2 in the various solutions of MEA was calculated with the use of the Henry's Law coefficients tabulated in **Table B 5**. The diffusivities of the zwitterion and salt product was assumed to be equal to that of MEA, which is why only the diffusivity of MEA is tabulated. This is consistent with the practice in literature (Versteeg & van Swaaij, 1988).

Table B 6 Diffusivity and Solubility Data to be used as Initial and Boundary Condition Values

T = 25°C [MEA] = 0.2 M				
[MEA]:[CO_2]	**D_{CO2} x 10^5 (cm^2/s)**	**$D_{MEA,n\text{-}Prop}$ x 10^5 (cm^2/s)**	**P_{CO2} (kPa)**	**P_{CO2} /H_{CO2} x 10^2 (mol/dm^3)**
11	1.34	0.80	19.88	1.90
19	1.34	0.80	10.96	1.05
38	1.34	0.80	5.52	0.53
T = 25°C [MEA] = 0.08 M				
[MEA]:[CO_2]	**D_{CO2} x 10^5 (cm^2/s)**	**$D_{MEA,n\text{-}Prop}$ x 10^5 (cm^2/s)**	**P_{CO2} (kPa)**	**P_{CO2} /H_{CO2} x 10^2 (mol/dm^3)**
37	1.37	0.80	2.25	0.21
19	1.37	0.80	4.44	0.42
4	1.37	0.80	19.91	1.90

Table B 7 Bulk Liquid Concentrations to be used as Initial and Boundary Condition Values

T = 25°C [MEA] = 0.2 M				
[MEA]:[CO_2]	**$C_{CO2,L}$ x 10^4(mol/dm^3)**	**$C_{RNH2,L}$ (mol/dm^3)**	**$C_{Z,L}$ x10^4(mol/dm^3)**	**$C_{S,L}$ x10^4 (mol/dm^3)**
11	3.79	0.20	3.12	1.83
19	2.09	0.20	1.60	1.01
38	1.05	0.20	0.74	0.51
T = 25°C [MEA] = 0.08 M				
[MEA]:[CO_2]	**$C_{CO2,L}$ x 10^4(mol/dm^3)**	**$C_{RNH2,L}$ (mol/dm^3)**	**$C_{Z,L}$ x10^4(mol/dm^3)**	**$C_{S,L}$ x10^4 (mol/dm^3)**
37	0.43	0.08	0.30	0.21
19	0.85	0.08	0.65	0.41
4	3.80	0.08	3.46	1.83

B.5 Conclusions and Future Work Identified

A numerical method for calculating effective interfacial mass transfer area from the absorption rate of CO_2 into alcoholic solutions of MEA is proposed in Appendix B. The method may be applied to absorption rates measured for separation column internals such as random and structured packing material provided the initial and boundary values for the set of partial differential equations are known. A method for calculating the physiochemical properties required in the boundary conditions values are also presented in this chapter.

It is recommended that the N_2O analogy for estimating the diffusivity and solubility of CO_2 in MEA/alcohol solutions be further developed. This will require measurements of absorption rates of N_2O into MEA/alcohol solutions using the wetted wall column experimental set-up developed in this study. It is further recommended that a mesh optimization study is performed to enable an optimum solution to the set of partial differential equations presented in this study to be found. Validation of the method may then be done by comparing its results under pseudo first order reaction conditions with available effective area correlations.

Appendix C MECHANICAL DRAWINGS AND SCHEMATICS OF THE EQUIPMENT USED

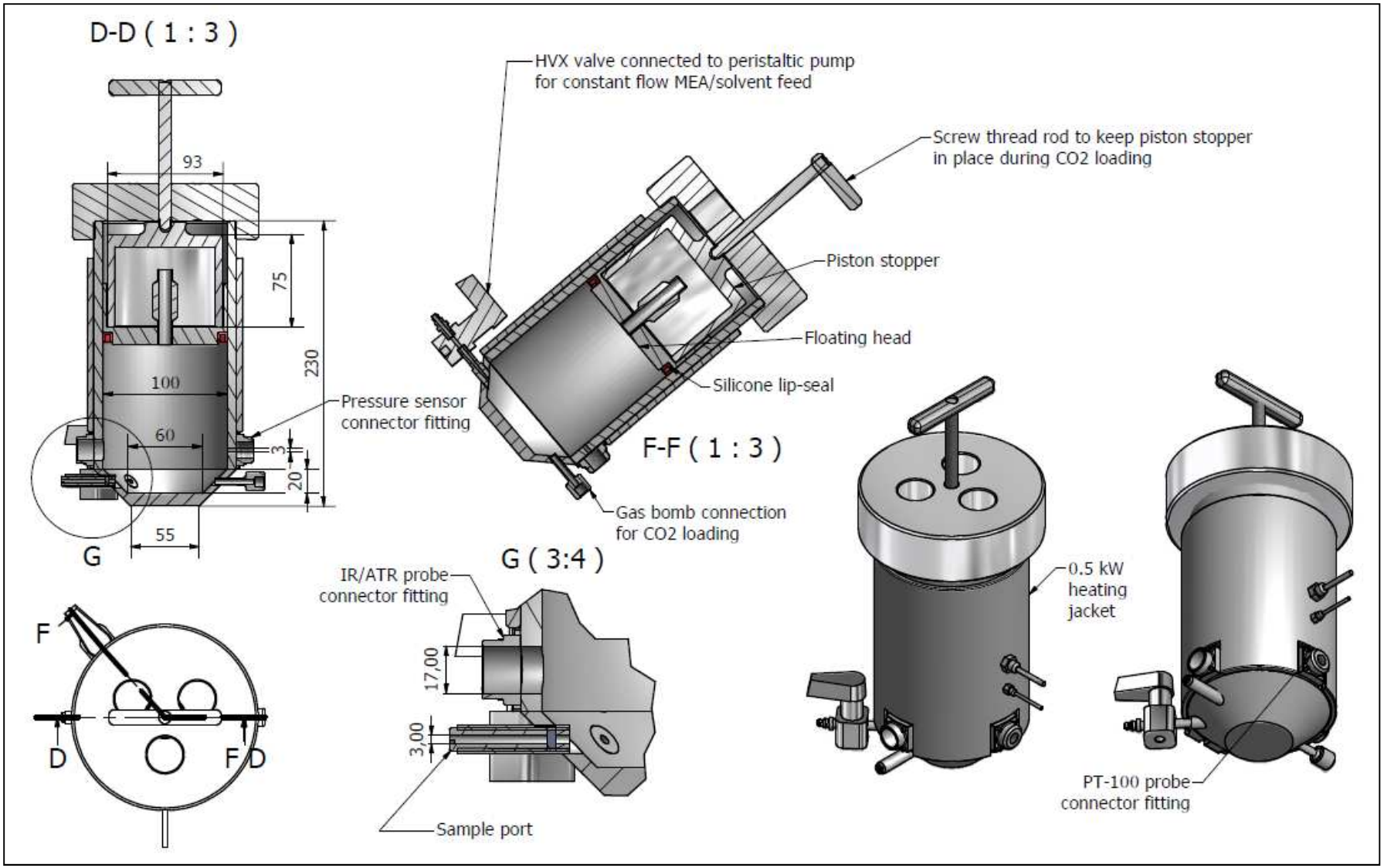

Figure C 1 Dimensioned Mechanical Drawing of Semi-batch Reactor

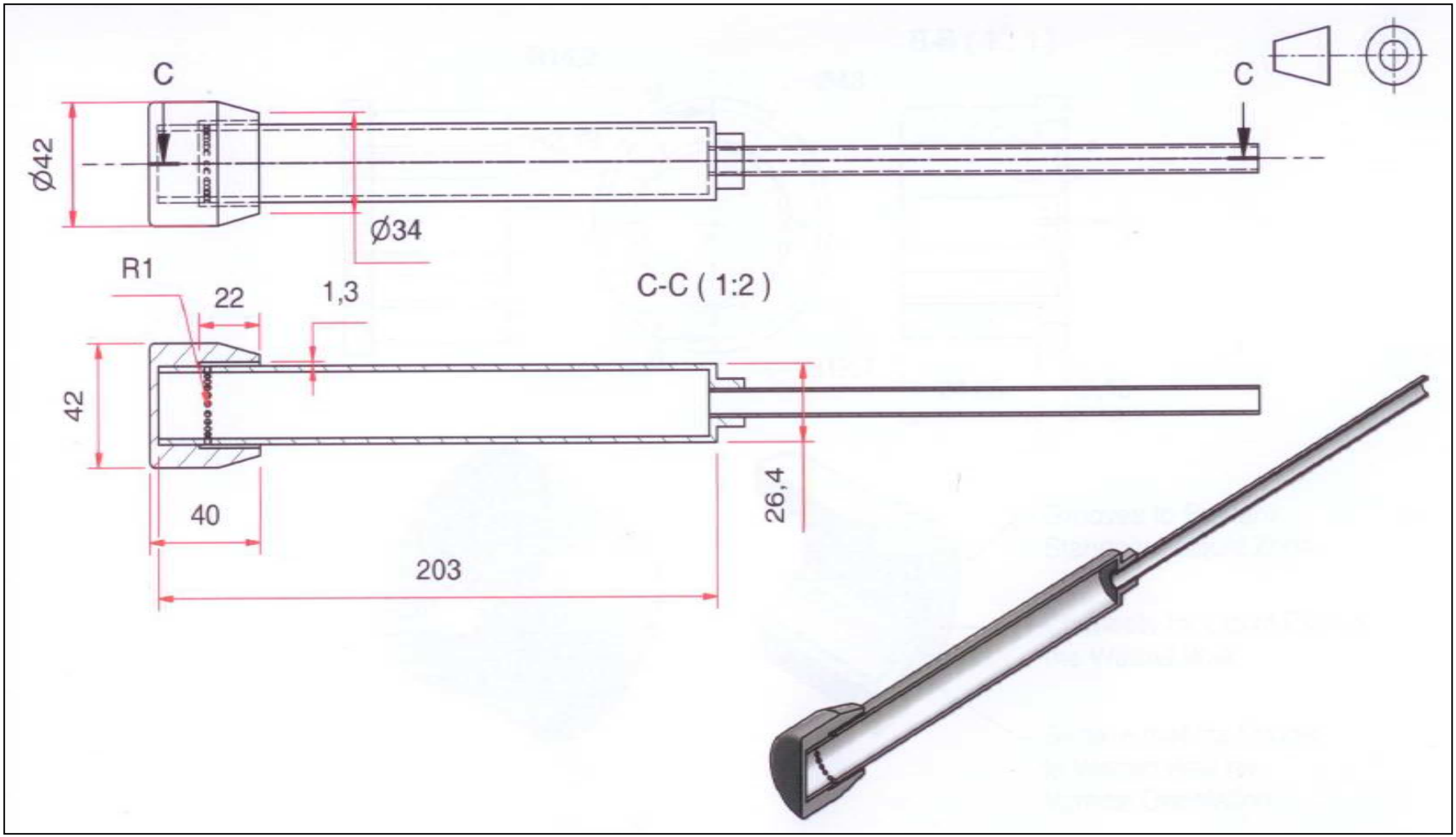

Figure C 2 Dimensioned Mechanical Drawing of Wetted Wall

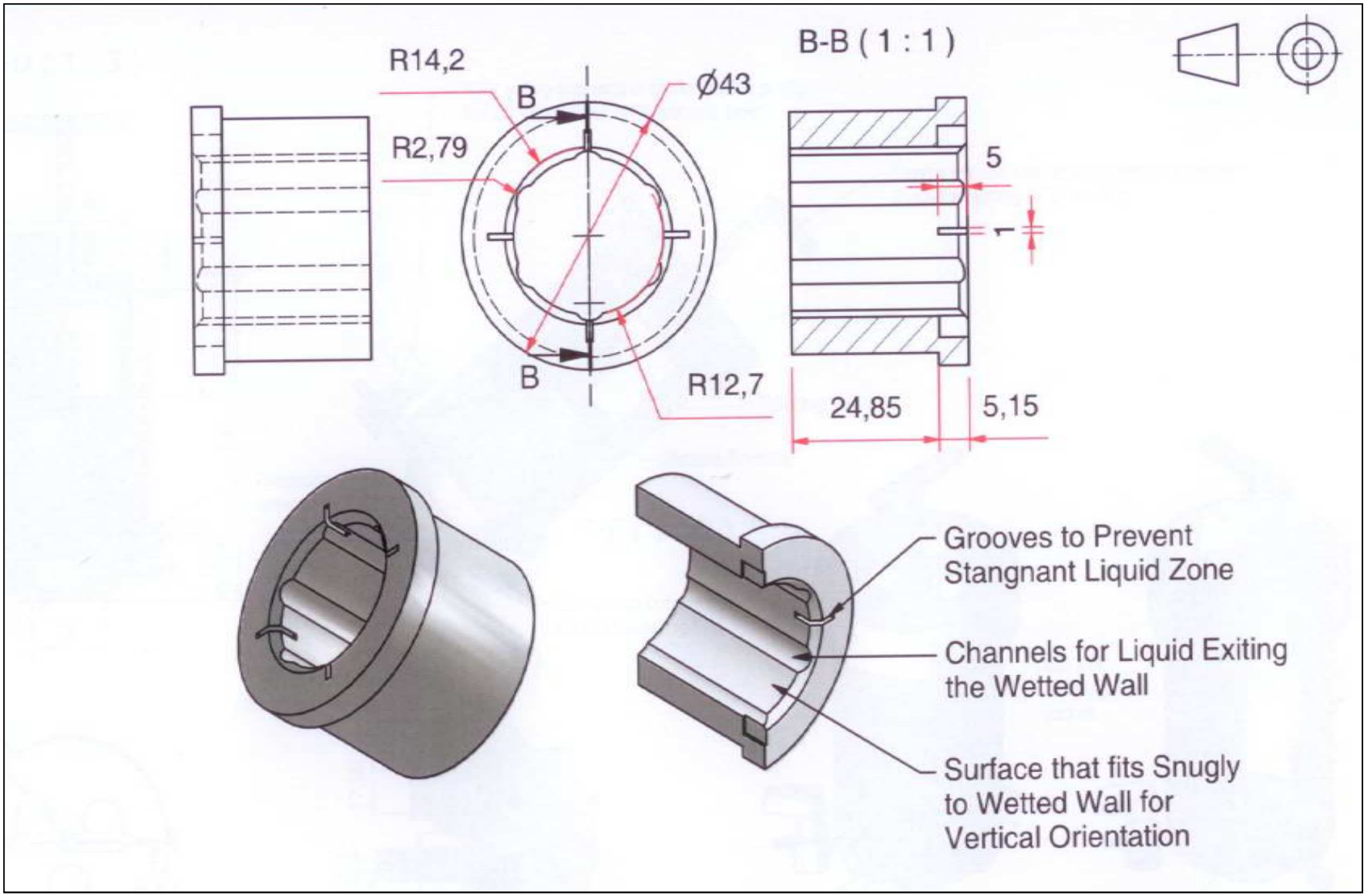

Figure C 3 Dimensioned Mechanical Drawing of Wetted Wall Exit Collar

Appendix D EQUIPMENT SPECIFICATIONS

D.1 Nicolet 6700 Spectrometer Specifications

THE NICOLET 6700 FT-IR ADVANCED GOLD SPECTROMETER

- 0.1 cm^{-1} resolution
- Integrated Scan Buttons
- Dual source, dual detector Gold optics
- ETC Everglo source with Rest, Stabilized and Turbo Modes
- Near-IR source
- Talon interchangeable beamsplitter system
- High speed USB 2.0 interface
- Accepts all Smart Accessories and many others
- Capability for hyphenated techniques including infrared microscopy, GC/IR, TGA/IR and an FT-Raman
- Internal beamsplitter storage case for additional beamsplitters
- Software control for multiple detectors, filters, polarizer available.
- Spectrometer driver and help
- Sealed and Desiccated windows (KBr) standard

The system includes OMNIC 8 software with the following enhanced productivity features:

- SOP workflows for execution through the Integrated Scan Button panel or OMNIC
- Toolbar including OMNIC Macros\Basic to compile your routine tasks into simple push button operations
- QCheck correlation for QC/QA verification of samples against one or many reference spectra; includes standard correlation and unique high sensitivity compare with pass/fail thresholds
- System Performance Verification (SPV) automatically monitors system status including:

- Hardware Diagnostics to ensure key system components are working properly
- Performance Verification, based on ASTM E1421, to test and document system operation
- System Suitability to ensure analysis consistency, including your sampling accessory
- Spectral Quality Checks ensure your sample is collected as you expect
- Scheduled Maintenance monitor warns operator when Preventative Maintenance is due
- Optional ValPro system qualification testing and documentation

Quantitative and qualitative method development (TQ Analyst - EZ Edition) and prediction including:

- Tools needed to develop calibrations and then perform predictions using Beer-Lambert and Classical Least Squares
- Tools needed to perform predictions (but not to build calibrations) using Discriminant Analysis, Partial Least Squares (PLS) and Principle Component Analysis (PCR)
- Infrared spectral interpretation with online interpretation guide

OMNIC™ 8.0 also includes the following extensive list of standard tools:

- Easy to set up parameters, live display of data collection, and spectral data preview
- Customizable toolbar, menu, and options with user logins and password protection
- Display capabilities: zoom, roll, stack, overlay, offset and interactive display tools
- Data processing: baseline correction (automatic and manual), smooth, blank and straight line, first and second derivative, curve fitting, spectral math, subtract line, first and second derivative, curve fitting, spectral math, subtract (manual and automatic)
- Data conversion and corrections: Kubelka Munk, Kramers Kronig, Photoacoustic, ATR correction including settings for crystal material, reflections, angle and sample refractive index
- Spectral Search: high-resolution library generation,customizable information fields, single or multi- region search, library management, with over 1400 spectra in included libraries

- Spectral peak picking and labeling
- Non-editable audit trail history log
- Direct conversion of JCAMP and other vendors spectral files and user libraries
- Spectral group statistical analysis: variance, average, and range
- Peak analysis tools: peak area, peak height, cursor, annotation
- Automatic atmospheric suppression to remove H2O and CO2 interferences (no standards needed)
- Full-featured report generator and electronic laboratory notebook
- Extensive on-line help and tutorials

System also includes:

- Nicolet X700 English Language Kit
- Power Cord Indian 250v
- Desiccated KBr Window Kit
- KBr Optics and Gasket, for external beam
- DLaTGS Detector w/KBr window (12,500-350 cm-1)
- Liquid N_2 Cooled MCT-High D* Detector with CdTe window (11,700 - 800 cm-1)
- System Performance Verification with Internal Standards
- Validation wheel includes NIST traceable standards of polystyrene and NG-11 glass
- Motor and wheel mount for automated operation
- Enables SPV in OMNIC 8.0 or higher
- For routine quality assurance
- Standard Purged System including Purge Regulator

D.2 Axiom DPR-207 IR Probe Inspection and Test Report

Prod_QC\Axiom\Forms\HPM-A:AF1-3
Form SF1-3, Rev. B (2/9/07)

INSPECTION AND TEST REPORT

Axiom Analytical INCORPORATED

Product Line: DPR-207

Customer: STELLENBOSCH UNIVERSITY	Test Report No: 210073
Customer PO No: 20182	Serial Number: 101213

CONFIGURATION

ATR Element Material:	ZNSE	Seal Material:	Kalrez 3675
Beam Pick-off Model:	3.5 INCHES	Configured for spectrometer model:	THERMO FISHER SCIENTIFIC
		Option:	OPT.DP27-SI-TF1, DSR-207

TEST RESULTS

Spectrometer Used: BRUKER CUBE

MEASUREMENT:	SPECIFICATION	MEASURED VALUE	SPECTRUM
Transmission @ 2500 CM^{-1}:	>2 %	2.65 %	210073-1
Acetone Absorbance @ 1713 CM^{-1}:	>0.8 AU	0.87 AU	210073-4

PACKAGE CONTENTS

- [x] INSTRUCTION MANUAL
- [x] TRANSMISSION SPECTRUM
- [x] ACETONE ABSORBANCE SPECTRUM
- [x] ALLEN WRENCH SET (1)
- [x] SLIDING TAPERED JOINT FASTENED ON PROBE (1)
- [x] SCREWS FOR APPROPRIATE BASEPLATE
- [x] APPROPRIATE BASEPLATE FOR SPECTROMETER

COMMENTS:

TESTS CONDUCTED BY: A.N.V DATE: 7-30-10

QUALITY CONTROL AUDIT BY: DATE: 8/2/10

D.3 1188HD Camera CCU and 1188 Camera Head with Coupler

Input Electrical Ratings:

100 – 240VAC ± 10% (0.6A) @ 47 – 63Hz

Total Shipping Weight

13 lbs. (6.0 kg)

Dimensions

Camera Console: 12.5" w × 3.3" h × 15.25" d (31.8 cm w × 8.4 cm h × 38.7 cm d)

Camera Head Cable to Camera Console

10.3 ft (3.15 m) sealed cable

20.7 ft (6.30 m) cable extension available

Enhancement

16 levels (switchable)

Classification

Class I Equipment

Type BF Applied Part

Water Ingress Protection, IPX0—Ordinary Equipment

Continuous Operation

Complies with Laser Product Standards

Class 1 Laser Product

Contains four 850-mm laser diodes

This product complies with IEC 60825-1:1993+A1:1997+A2:2001. This product complies with 21CFR, Subchapter J, Parts 1040.10 and 1040.11, except for deviations pursuant to Laser Notice No. 50, dated July 26, 2001.

Electromagnetic Compatibility

Like other electrical medical equipment, the 1188HD Camera requires special precautions to ensure electromagnetic compatibility with other electrical medical devices.

Note: The 1188HD Camera has been designed and tested to comply with IEC 60601-1-2:2001 requirements for EMC with other devices.

SDC Classic

Technical Specifications

Operating temperature: 10 – 40°C, Operating humidity: 3 0 – 75% RH, Transport/storage temperature: -20° – 60°C, Transport/storage humidity: 10 – 85% RH

System Type

MPEG -1 or -2 compression engine with full IP encoding

Video Inputs

Input Resolution

(1) S-Video: (NTSC) 720 × 480,

(1) Composite: (PAL) 720 × 576

(1) DVI: (SXGA) 1280 × 1024,

(XGA) 1024 × 768,

(720p) 1280 × 720

(1) RGBHV

(via DVI-I connectors)

Video Outputs

Same as video inputs

Audio

Stereo line and microphone input, (2) speaker outputs

Image Resolution

Progressive scan image capture; same as video input resolution

Disc Capacity

50 images and 50 video files, with auto cutoff for CD (600 MB), DVD (4GB), or none (8 GB, maximum case size permitted)

File Format

Images: Bitmap (BMP), JPEG, Videos: MPEG-1 and MPEG-2, 27 Disc Recording Formats: CD-R, DVD-R, DVD+R (single session), DVD+RW

USB, NTFS format supported MAC users will only have read capabilities

Remote Control

Wireless infrared, camera-head triggering

D.4 Hauppauge Colossus Recording Card

Hardware encoder

- H.264 AVCHD video encoder
- AC-3 recording from AC-3 source
- AAC audio encoding from PCM source

- Recording datarate: from 1 to 20 Mbits/sec (user selectable in the ArcSoft ShowBiz application)
- Recording format:
- up to 1080i from component video (YCrCb or YPrPb)
- NTSC: 720p60, 1080i60, 480i60, 480p60
- PAL: 720p50, 1080i50, 576p50, 576i50, 480p50, 480i50 - Note: the video input format determines the recorded format. For example, 1080i input records at 1080i, 720P records at 720P, etc. Any other format conversions needs to be done with the MediaConvert program (supplied).
- NTSC or PAL supported

System Requirements

Note: when playing back video recordings made with the Colossus, a fast CPU and at least 256MB of graphics memory are needed.

- Processor Requirements (minimum for HD playback): Dual core CPU 2.0GHz or faster
- Windows 7 (32 and 64-bit), Windows Vista or Windows XP service pack 2 (32-bit).
- Graphics with 256MB memory (or greater)
- PCI Express x1 slot
- Sound card for audio playback
- CD-ROM drive for installing the Colossus software

Bundled software applications

- **ArcSoft *"ShowBiz"*** for video recording and authoring and burning of your TV recordings onto a Blu-ray DVD compatible disc
- **Hauppauge WinTV v7 application**, with support for the Hauppauge remote control and IR blaster
- **Input and outputs**
- Note: video input on Component and HDMI sources is limited to 1080i
- A/V cable input adapter with:

- Component video input
- Left/ Right RCA audio input
- A/V cable output adapter with loop through audio and video:
- Component video output
- Left/ Right RCA audio output
- Optical audio input and loop through output
- HDMI input (Note: for use with un-encrypted HDMI video sources)
- IR Blaster output

D.5 CO_2 Concentration Analyser Calibration Certificate

Dräger South Africa (Pty) Ltd
1969/003553/07

Unit 1, Cor Willow Rd & Cecil Morgan St,
Stikland, 7530

P O Box 3677, Tyger Valley, 7536
Tel +27 21 945 4241/5
Fax +27 21 945 4246

St. Peter's Square, Cnr. Waterford Place &
Witkoppen rd. Kloeve Hill Park, Sandton

PO Box 68601, Bryanston, 2021
Tel +27 (0) 11 465 9959
Fax +27 (0) 11 465 6953

Dräger

GAS CALIBRATION CERTIFICATE

NUMBER: C2947

Works Order No: 1401 Product Ref: 5546

Owners Name: University of Stellenbosch

Submitted for test by: University of Stellenbosch

Instrument Type: PIR 7200

Serial Number: ARBH-0185

Sensor Type	Part Number	Serial No	Cal Gas	Batch No	Expiry Date	Alarm 1	Alarm 2	STEL	TWA
IR CO2	n/a	n/a	2% Vol CO2	1266866	Mar 2013	n/a	n/a	n/a	n/a

Calibrated at: Sea Level

Next Calibration: 17 October, 2012

Calibration Verified

Functional Inspection

Visual Checked

CALIBRATED AND CHECKED Wayne Baguley

DRÄGER S.A. (PTY) LTD
Unit 1
Cor Willow & Cecil Morgan St
Stikland - 7530
P O Box 3677, Tyger Valley, 7536
Tel 021 945 4241 / Fax: 021 945 4246

Signature:

Date: 17 April, 2012

THIS CERTIFICATE IS INVALID UNLESS OVERSTAMPED

The issue of this certificate does not imply any warranty in respect of any instrument as to its fitness for use once the instrument has left the Company's premises save that at the time of calibration it conformed to manufacturer's standard operating specifications under simulated test conditions using the test gases above. This instrument is required to be periodically re-calibrated in accordance with these standard manufacturer specifications.

Appendix E DATA OF THE REACTION KINETIC STUDY

E.1 Derivation of the Pseudo Steady State Hypothesis Reaction Rate Expression

Starting with equation 3.2:

$$1)\ CO_2 + R'R''NH \underset{k_2}{\overset{k_1}{\rightleftharpoons}} R'R''NH^+COO^-$$
$$2)\ R'R''NH^+COO^- + R'R''NH \underset{k_4}{\overset{k_3}{\rightleftharpoons}} R'R''NCOO^- + R'R''NH_2^+ \qquad 3.2$$

which, for the primary amine, MEA, may be written as:

$$1)\ CO_2 + RNH_2 \underset{k_2}{\overset{k_1}{\rightleftharpoons}} RNH_2^+COO^-$$
$$2)\ RNH_2^+COO^- + RNH_2 \underset{k_4}{\overset{k_3}{\rightleftharpoons}} RNHCOO^- + RNH_3^+ \qquad 3.3$$

Assuming that the two salt products are always present in equal molar amounts, the rate of disappearance of amine in terms of only one of the products may be given as:

$$-r_{RNH_2} = k_1[CO_2][RNH_2] - k_2\left[RNH_2^+COO^-\right] + k_3\left[RNH_2^+COO^-\right][RNH_2] - k_4\left[RNH_3^+\right]^2 \quad (1)$$

The rate of disappearance of CO_2 is:

$$-r_{CO_2} = \frac{\left(-r_{RNH_2}\right)}{2} \quad (2)$$

The Pseudo Steady State Hypothesis (PSSH) states that the nett reaction rate of the zwitterion at reaction equilibrium is zero:

$$r_z = 0 = k_1[CO_2][RNH_2] - k_2\left[RNH_2^+COO^-\right] - k_3\left[RNH_2^+COO^-\right][RNH_2] + k_4\left[RNH_3^+\right]^2$$

Rearranging yields:

$$\left[RNH_2^+COO^-\right] = \frac{k_1[CO_2][RNH_2] + k_4\left[RNH_3^+\right]^2}{k_2 + k_3[RNH_2]} \quad (3)$$

substituting (3) into (1) and rearranging:

$$-r_{RNH_2} = \frac{2\left(k_1 k_3 [CO_2][RNH_2]^2 - k_2 k_4 \left[RNH_3^+\right]^2\right)}{k_2 + k_3 [RNH_2]} \quad (4)$$

Substituting (2) into (4) and rearranging and lumping the rate constants, yields equation 3.4:

$$-r_{CO_2} = \frac{k'''[CO_2][RNH_2]^2 - k_4 \left[RNH_3^+\right]^2}{1 + k''[RNH_2]} \quad 3.4$$

where $k'' = \frac{k_3}{k_2}$ and $k''' = k_1 k''$.

E.2 Reaction Kinetic Experimental Parameters

The experimental parameters for the reaction kinetic study are tabulated in **Table E 1**.

Table E 1 Experimental Parameters for n-Propanol

[MEA]:[CO2] = 5:1									
T (°C)	**25**			**30**			**35**		
Run#	5_1	5_2	5_3	5_1	5_2	5_3	5_1	5_2	5_3
$m_{CO2,\ loaded}$ (g)	0.518	0.573	0.535	0.545	0.547	0.502	0.548	0.466	0.569
$m_{MEA,\ charged}$ (g)	3.77	3.89	3.78	3.88	3.81	3.55	3.94	3.27	3.83
F_{MEA} (mol/s)	0.00649	0.0059	0.0064	0.0068	0.0073	0.0065	0.0075	0.0058	0.0068
[MEA]:[CO_2] = 10:1									
T (°C)	**25**			**30**			**35**		
Run#	10_1	10_2	10_3	10_1	10_2	10_3	10_1	10_2	10_3
$m_{CO2,\ loaded}$ (g)	0.518	0.51	0.523	0.516	0.52	0.523	0.508	0.533	0.554
$m_{MEA,\ charged}$ (g)	6.95	7.15	6.96	7.24	7.25	7.27	7.17	7.43	7.85
F_{MEA} (mol/s)	0.0115	0.0077	0.0094	0.00856	0.0089	0.00979	0.0105	0.0108	0.0112

E.3 Fundamental Model Estimated Rate Constants

The estimated rate constant of the fundamental model for each of the experimental runs selected for modelling is tabulated in

Table E 2 Fundamental Model Estimated Rate Constants for Experimental Run# 25_5_1

	k_1 ($dm^3.mol^{-1}.s^{-1}$)	k_2 (s^{-1})	k_3 ($dm^3.mol^{-1}.s^{-1}$)	k_4 ($dm^3.mol^{-1}.s^{-1}$)
Best fit	352	9	66	95
Upper Bound (95%)	450	19	128	143
Median	330	10	72	130
Lower Bound (5%)	286	4	27	33

Table E 3 Fundamental Model Estimated Rate Constants for Experimental Run# 25_5_2

	k_1 ($dm^3.mol^{-1}.s^{-1}$)	k_2 (s^{-1})	k_3 ($dm^3.mol^{-1}.s^{-1}$)	k_4 ($dm^3.mol^{-1}.s^{-1}$)
Best fit	288	55	91	117
Upper Bound (95%)	347	96	223	188
Median	319	47	126	89
Lower Bound (5%)	236	13	83	48

Table E 4 Fundamental Model Estimated Rate Constants for Experimental Run# 25_5_3

	k_1 ($dm^3.mol^{-1}.s^{-1}$)	k_2 (s^{-1})	k_3 ($dm^3.mol^{-1}.s^{-1}$)	k_4 ($dm^3.mol^{-1}.s^{-1}$)
Best fit	327	8	53	123
Upper Bound (95%)	431	25	97	219
Median	332	12	78	139
Lower Bound (5%)	327	7	49	95

Table E 5 Fundamental Model Estimated Rate Constants for Experimental Run# 25_10_1

	k_1 ($dm^3.mol^{-1}.s^{-1}$)	k_2 (s^{-1})	k_3 ($dm^3.mol^{-1}.s^{-1}$)	k_4 ($dm^3.mol^{-1}.s^{-1}$)
Best fit	340	6	49	169
Upper Bound (95%)	514	27	73	213
Median	337	6	49	163
Lower Bound (5%)	243	3	34	144

Table E 6 Fundamental Model Estimated Rate Constants for Experimental Run# 25_10_2

	k_1 ($dm^3.mol^{-1}.s^{-1}$)	k_2 (s^{-1})	k_3 ($dm^3.mol^{-1}.s^{-1}$)	k_4 ($dm^3.mol^{-1}.s^{-1}$)
Best fit	330	27	32	149
Upper Bound (95%)	330	30	34	178
Median	330	29	30	168
Lower Bound (5%)	323	27	28	165

Table E 7 Fundamental Model Estimated Rate Constants for Experimental Run# 25_10_3

	k_1 ($dm^3.mol^{-1}.s^{-1}$)	k_2 (s^{-1})	k_3 ($dm^3.mol^{-1}.s^{-1}$)	k_4 ($dm^3.mol^{-1}.s^{-1}$)
Best fit	320	11	53	160
Upper Bound (95%)	424	28	88	257
Median	337	15	70	154
Lower Bound (5%)	301	6	21	132

Table E 8 Fundamental Model Estimated Rate Constants for Experimental Run# 30_5_1

	k_1 ($dm^3.mol^{-1}.s^{-1}$)	k_2 (s^{-1})	k_3 ($dm^3.mol^{-1}.s^{-1}$)	k_4 ($dm^3.mol^{-1}.s^{-1}$)
Best fit	458	36	107	216
Upper Bound (95%)	571	71	349	448
Median	469	40	115	232
Lower Bound (5%)	451	19	99	197

Table E 9 Fundamental Model Estimated Rate Constants for Experimental Run# 30_5_2

	k_1 ($dm^3.mol^{-1}.s^{-1}$)	k_2 (s^{-1})	k_3 ($dm^3.mol^{-1}.s^{-1}$)	k_4 ($dm^3.mol^{-1}.s^{-1}$)
Best fit	412	26	137	222
Upper Bound (95%)	975	66	964	997
Median	485	13	65	270
Lower Bound (5%)	336	8	19	225

Table E 10 Fundamental Model Estimated Rate Constants for Experimental Run# 30_5_3

	k_1 ($dm^3.mol^{-1}.s^{-1}$)	k_2 (s^{-1})	k_3 ($dm^3.mol^{-1}.s^{-1}$)	k_4 ($dm^3.mol^{-1}.s^{-1}$)
Best fit	473	5	92	249
Upper Bound (95%)	860	54	106	348
Median	473	5	84	244
Lower Bound (5%)	430	1	59	228

Table E 11 Fundamental Model Estimated Rate Constants for Experimental Run# 30_10_1

	k_1 ($dm^3.mol^{-1}.s^{-1}$)	k_2 (s^{-1})	k_3 ($dm^3.mol^{-1}.s^{-1}$)	k_4 ($dm^3.mol^{-1}.s^{-1}$)
Best fit	479	20	40	262
Upper Bound (95%)	502	27	56	355
Median	474	18	50	262
Lower Bound (5%)	442	15	38	246

Table E 12 Fundamental Model Estimated Rate Constants for Experimental Run# 30_10_2

	k_1 ($dm^3.mol^{-1}.s^{-1}$)	k_2 (s^{-1})	k_3 ($dm^3.mol^{-1}.s^{-1}$)	k_4 ($dm^3.mol^{-1}.s^{-1}$)
Best fit	433	41	154	216
Upper Bound (95%)	640	114	222	402
Median	471	85	111	243
Lower Bound (5%)	397	8	31	162

Table E 13 Fundamental Model Estimated Rate Constants for Experimental Run# 30_10_3

	k_1 ($dm^3.mol^{-1}.s^{-1}$)	k_2 (s^{-1})	k_3 ($dm^3.mol^{-1}.s^{-1}$)	k_4 ($dm^3.mol^{-1}.s^{-1}$)
Best fit	471	14	154	252
Upper Bound (95%)	637	77	169	534
Median	479	11	64	271
Lower Bound (5%)	315	5	39	207

Table E 14 Fundamental Model Estimated Rate Constants for Experimental Run# 35_5_1

	k_1 ($dm^3.mol^{-1}.s^{-1}$)	k_2 (s^{-1})	k_3 ($dm^3.mol^{-1}.s^{-1}$)	k_4 ($dm^3.mol^{-1}.s^{-1}$)
Best fit	650	10	349	303
Upper Bound (95%)	727	80	343	340
Median	658	67	195	318
Lower Bound (5%)	608	16	160	216

Table E 15 Fundamental Model Estimated Rate Constants for Experimental Run# 35_5_2

	k_1 ($dm^3.mol^{-1}.s^{-1}$)	k_2 (s^{-1})	k_3 ($dm^3.mol^{-1}.s^{-1}$)	k_4 ($dm^3.mol^{-1}.s^{-1}$)
Best fit	522	28	239	343
Upper Bound (95%)	664	227	355	391
Median	643	162	207	307
Lower Bound (5%)	411	55	155	177

Table E 16 Fundamental Model Estimated Rate Constants for Experimental Run# 35_5_3

	k_1 ($dm^3.mol^{-1}.s^{-1}$)	k_2 (s^{-1})	k_3 ($dm^3.mol^{-1}.s^{-1}$)	k_4 ($dm^3.mol^{-1}.s^{-1}$)
Best fit	599	28	356	337
Upper Bound (95%)	691	366	525	482
Median	643	158	180	324
Lower Bound (5%)	400	50	73	33

Table E 17 Fundamental Model Estimated Rate Constants for Experimental Run# 35_10_1

	k_1 ($dm^3.mol^{-1}.s^{-1}$)	k_2 (s^{-1})	k_3 ($dm^3.mol^{-1}.s^{-1}$)	k_4 ($dm^3.mol^{-1}.s^{-1}$)
Best fit	628	55	276	348
Upper Bound (95%)	825	160	382	351
Median	660	79	190	310
Lower Bound (5%)	407	18	160	133

Table E 18 Fundamental Model Estimated Rate Constants for Experimental Run# 35_10_2

	k_1 ($dm^3.mol^{-1}.s^{-1}$)	k_2 (s^{-1})	k_3 ($dm^3.mol^{-1}.s^{-1}$)	k_4 ($dm^3.mol^{-1}.s^{-1}$)
Best fit	636	31	263	307
Upper Bound (95%)	727	116	258	350
Median	660	72	175	331
Lower Bound (5%)	616	38	153	279

Table E 19 Fundamental Model Estimated Rate Constants for Experimental Run# 35_10_3

	k_1 ($dm^3.mol^{-1}.s^{-1}$)	k_2 (s^{-1})	k_3 ($dm^3.mol^{-1}.s^{-1}$)	k_4 ($dm^3.mol^{-1}.s^{-1}$)
Best fit	655	11	321	328
Upper Bound (95%)	721	93	365	359
Median	659	45	189	328
Lower Bound (5%)	527	12	160	270

Appendix F DATA OF THE REACTIVE ABSORPTION STUDY

F.1 Wetted Wall Experimental Data

The reactive absorption rates measured on the wetted wall experimental set-up is tabulated in **Table F 1** - **Table F 4**.

Table F 1 Reactive Absorption Data for [MEA] = 0.2 mol/dm^3, T = 25°C, P = 104 kPa

[MEA] = 0.2 mol/dm^3										
h_{column} (mm)	T_L (°C)	T_G (°C)	V_L (cm^3/s)	t_c (s)	V_G (cm^3/s)	P_{CO2} (kPa)	CO_2 in (vol %)	CO_2 out (vol%)	n_{CO2} x 10^5 (mol/s)	N_{CO2} x 10^4 (mol/m^2.s)
90	25.8	25.5	0.874	1.19	76.33	19.88	19.21	18.71	1.71	23.60
90	25.4	25.2	1.345	0.89	76.13	19.87	19.22	18.61	2.08	28.69
60	25.3	25	1.016	0.72	76.43	19.83	19.18	18.78	1.37	28.28
60	24.9	25.1	1.345	0.60	76.32	19.93	19.22	18.77	1.54	31.85
60	24.8	24.7	1.016	0.72	80.00	11.06	10.67	10.48	0.63	13.00
60	24.8	24.8	1.345	0.60	81.35	11.05	10.65	10.40	0.83	17.07
90	24.8	24.7	0.874	1.19	79.63	11.00	10.60	10.37	0.78	10.74
90	24.7	24.5	1.345	0.89	80.56	10.96	10.56	10.25	1.03	14.13
90	24.7	24.7	0.874	1.19	81.56	5.52	5.32	5.16	0.52	7.13
90	24.7	24.7	1.345	0.89	81.91	5.52	5.31	5.11	0.65	8.89
60	24.9	24.7	1.016	0.72	81.74	5.61	5.40	5.27	0.42	8.64
60	24.9	24.6	1.345	0.60	81.93	5.63	5.41	5.26	0.48	10.01

Table F 2 Reactive Absorption Data for [MEA] = 0.2 mol/dm^3, T = 30°C, P = 104 kPa

[MEA] = 0.2 mol/dm^3										
h_{column} (mm)	T_L (°C)	T_G (°C)	V_L (cm^3/s)	t_c (s)	V_G (cm^3/s)	P_{CO2} (kPa)	CO_2 in (vol %)	CO_2 out (vol%)	n_{CO2} x 10^5 (mol/s)	N_{CO2} x 10^4 (mol/m^2.s)
60	30.4	30.1	1.016	0.70	76.24	5.62	5.40	5.30	0.31	6.51
60	30.9	30.2	1.345	0.58	76.56	5.66	5.44	5.32	0.38	7.82
90	30.8	31	0.874	1.16	76.91	5.62	5.40	5.29	0.35	4.81
90	30.7	30.8	1.345	0.87	76.86	5.61	5.39	5.27	0.40	5.44
90	30.8	30.9	0.874	1.16	78.94	11.17	10.73	10.58	0.49	6.74
90	30.7	30.6	1.345	0.87	78.89	11.16	10.72	10.54	0.59	8.06
60	30.8	30.7	1.016	0.70	78.93	11.17	10.73	10.60	0.42	8.75
60	30.8	30.9	1.345	0.58	78.94	11.16	10.72	10.58	0.46	9.40
60	30.6	30.8	1.016	0.70	81.99	20.23	19.40	19.20	0.68	14.00
60	30.2	30	1.345	0.58	82.01	20.13	19.30	19.06	0.81	16.82
90	30.4	30	0.874	1.16	81.96	20.13	19.28	19.00	0.95	13.14
90	30.3	30.1	1.345	0.87	82.03	20.26	19.42	19.07	1.19	16.35

Table F 3 Reactive Absorption Data for [MEA] = 0.08 mol/dm^3, T = 25°C, P = 104 kPa

[MEA] = 0.08 mol/dm^3										
h_{column} (mm)	T_L (°C)	T_G (°C)	V_L (cm^3/s)	t_c (s)	V_G (cm^3/s)	P_{CO2} (kPa)	CO_2 in (vol %)	CO_2 out (vol%)	n_{CO2} x 10^5 (mol/s)	N_{CO2} x 10^4 (mol/m^2.s)
90	26.2	26.5	0.874	1.18	76.33	2.27	2.16	2.07	0.30	4.13
90	26.2	26.5	1.345	0.89	76.13	2.27	2.16	2.05	0.36	4.99
60	25.9	26.2	1.016	0.71	76.43	2.24	2.14	2.07	0.24	4.87
60	26	26.3	1.345	0.59	76.32	2.24	2.13	2.05	0.27	5.52
60	25.5	25.7	1.016	0.71	80.00	4.48	4.26	4.15	0.38	7.93
60	25.7	25.9	1.345	0.59	81.35	4.47	4.26	4.16	0.35	7.31
90	25.8	25.8	0.874	1.18	79.63	4.47	4.26	4.14	0.41	5.71
90	25.3	25.7	1.345	0.89	80.56	4.49	4.28	4.17	0.38	5.30
90	25	25.4	0.874	1.18	81.56	20.04	19.18	18.85	1.14	15.80
90	24.9	25.3	1.345	0.89	81.91	19.91	19.09	18.74	1.22	16.73
60	24.8	25.4	1.016	0.71	81.74	19.98	19.07	18.75	1.11	23.06
60	24.8	25.4	1.345	0.59	81.93	20.01	19.15	18.82	1.15	23.72

Table F 4 Reactive Absorption Data for [MEA] = 0.08 mol/dm^3, T = 30°C, P = 104 kPa

[MEA] = 0.08 mol/dm^3										
h_{column} (mm)	T_L (°C)	T_G (°C)	V_L (cm^3/s)	t_c (s)	V_G (cm^3/s)	P_{CO2} (kPa)	CO_2 in (vol %)	CO_2 out (vol%)	n_{CO2} x 10^5 (mol/s)	N_{CO2} x 10^4 (mol/m^2.s)
60	30.8	30.8	1.016	0.69	81.71	19.86	19.02	18.85	0.57	11.87
60	30.9	31	1.345	0.58	81.81	19.80	18.98	18.78	0.67	13.93
90	31.2	31.5	0.874	1.15	81.94	20.02	19.25	19.02	0.77	10.69
90	31.1	31.5	1.345	0.86	81.93	20.02	19.19	18.92	0.91	12.54
90	31.2	31.7	0.874	1.15	78.23	4.55	4.36	4.27	0.29	4.00
90	31	31.4	1.345	0.86	79.15	4.55	4.37	4.28	0.29	4.04
60	30.9	31.3	1.016	0.69	77.94	4.53	4.34	4.29	0.16	3.32
60	30.7	31.1	1.345	0.58	78.26	4.53	4.35	4.28	0.23	4.65
60	30.4	30.8	1.016	0.69	76.13	2.18	2.10	2.04	0.19	3.89
60	30.4	30.8	1.345	0.58	77.12	2.23	2.15	2.12	0.10	1.96
90	30.2	30.6	0.874	1.15	77.04	2.25	2.16	2.12	0.13	1.75
90	30.2	30.7	1.345	0.86	76.83	2.25	2.16	2.09	0.22	3.05